Synthesis of Plasmonic Thin Film for Multi-Functional Photonic Applications

Thesis Submitted in Partial Fulfillment for the Award of Degree

Doctor of Philosophy

By

Sobhan Hazra

SCHOOL OF MATERIALS SCIENCE AND TECHNOLOGY
INDIAN INSTITUTE OF TECHNOLOGY
(BANARAS HINDU UNIVERSITY) VARANASI
VARANASI – 221005
INDIA

Roll No. - 20111522

2025

Dedicated

To

My Beloved Family

CERTIFICATE

It is certified that the work contained in the thesis titled ***"SYNTHESIS OF PLASMONIC THIN FILM FOR MULTI-FUNCTIONAL PHOTONIC APPLICATIONS"*** by ***"SOBHAN HAZRA"*** has been carried out under my supervision and that this work has not been submitted elsewhere for a degree.

It is further certified that the student has fulfilled all the requirements of Comprehensive, Candidacy, and SOTA for the award of a Ph.D. degree.

Date: 03/09/2025

Place: Varanasi

Bpal 03/09/25

Prof. Bhola Nath Pal

(Supervisor)

Professor/आचार्य
School of Materials Science & Technology/पदार्थ विज्ञान एवं प्रौद्योगिकी स्कूल
Indian Institute of Technology/भारतीय प्रौद्योगिकी संस्थान
(Banaras Hindu University), Varanasi/काशी हिन्दू विश्वविद्यालय, वाराणसी

DECLARATION BY THE CANDIDATE

I, **SOBHAN HAZRA**, certify that the work embodied in this Ph.D. thesis is my own bonafide work carried out by me under the supervision of **Prof. BHOLA NATH PAL** for a period from **December 2020** to **April 2025** at the **SCHOOL OF MATERIALS SCIENCE AND TECHNOLOGY**, Indian Institute of Technology (Banaras Hindu University) Varanasi, Varanasi, India. The matter embodied in this Ph.D. thesis has not been submitted for the award of any other degree/diploma. I declare that I have faithfully acknowledged and given credits to the research workers wherever their works have been cited in my work in this thesis. I further declare that I have not willfully copied any other's work, paragraphs, text, data, results, *etc*., reported in journals, books, magazines, reports dissertations, thesis, *etc*., or available at websites and have not included them in this thesis and have not cited as my own work.

Date: 03/09/2025

Sobhan Hazra

Place: Varanasi (Sobhan Hazra)

CERTIFICATE BY THE SUPERVISOR

This is to certify that the above statement made by the candidate is correct to the best of my knowledge.

B Pal

Prof. Bhola Nath Pal
Professor/आचार्य
School of Materials Science & Technology/पदार्थ विज्ञान एवं प्रौद्योगिकी स्कूल
Indian Institute of Technology/भारतीय प्रौद्योगिकी संस्थान
(Banaras Hindu University), Varanasi/काशी हिन्दू विश्वविद्यालय, वाराणसी
Supervisor

Prof. Chandan Upadhyay
Coordinator / समन्वयक
School of Materials Science & Technology / पदार्थ विज्ञान एवं प्रौद्योगिकी स्कूल
Indian Institute of Technology / भारतीय प्रौद्योगिकी संस्थान
(Banaras Hindu University) / काशी हिन्दू विश्वविद्यालय, वाराणसी
Coordinator

COPYRIGHT TRANSFER CERTIFICATE

Title of the Thesis: "Synthesis of Plasmonic Thin Film for Multi-Functional Photonic Applications"

Candidate's Name: Mr. Sobhan Hazra

Copyright Transfer

The undersigned hereby assigns to the Indian Institute of Technology (Banaras Hindu University) Varanasi, Varanasi all rights under copyright that may exist in and for the above thesis submitted for the award of the *Doctor of Philosophy*.

Date: 03/09/2025

Sobhan Hazra

Place: Varanasi (Sobhan Hazra)

Note: However, the author may reproduce or authorize others to reproduce materials extracted verbatim from the thesis or derivative of the thesis for the author's personal use provided that the source and the Institute's copyright notice are indicated.

Acknowledgements

As I look back on this journey, I am filled with immense gratitude for the many individuals who have supported me, both directly and indirectly, throughout my time at IIT (BHU). Expressing my thanks is not just a formality, but a heartfelt act of appreciation.

First and foremost, I extend my deepest gratitude to my supervisor, Prof. Bhola Nath Pal. His trust, insightful guidance, and steady support have been instrumental in shaping my work. I will always cherish the memories of his patience, encouragement, and dedication to my progress. His mentorship has left a lasting impact, and I am truly thankful for his unwavering commitment.

I am equally grateful to the members of my RPEC committee, Prof. P. Maiti from the School of Materials Science and Technology, and Dr. Somak Bhattacharyya from the Department of Electronics, (IIT-BHU). Their constructive feedback and thoughtful critiques have broadened the horizons of my research. My thanks also go to the coordinator, Dr. Chandan Upadhyay of the School of Materials Science and Technology for providing essential instrumental facilities, and to Dr. Ravi Panwar (DPGC convener) for his valuable insights and warm support.

I extend my sincere appreciation to all the faculty members of the department: Prof. D. Pandey, Prof. R. Prakash, Prof. P. Maiti, Prof. C. Rath, Prof. A. K. Singh, Prof. C. Upadhyay, Dr. S. K. Mishra, Dr. A.K. Mishra, Dr. S. Singh, Dr. N. Kumar, Dr. R. Panwar, Dr. A. Kumar and Dr. U. Shankar. Their guidance and encouragement have been vital throughout the course of my research.

I would also like to express my sincere gratitude to Prof. Sandip Chatterji, Dr. Praveen Chandra Pandey and Dr. Pradip Kumar Roy for their constant guidance, valuable insights, and unwavering support throughout the course of my research. Their expertise and encouragement have been instrumental in helping me navigate challenges and explore new perspectives, and I deeply appreciate their contributions to my academic journey. I would also like to extend my sincere gratitude to my collaborators Dr. Sudip Mukherjee (IIT BHU), Prof. Parasuraman Swaminathan (IIT Madras), Dr. Monalisa Pal (Banaras Hindu University), Dr. Ashish Kumar Mishra (IIT BHU), Prof. Jahar Sarkar, Dr. Sudip Kumar Batabyal (Amrita University), Dr. Biplab Kumar Kuila (BHU), Dr. Debanjan Guin (BHU), Ms. Lipi Pradhan, Ms. Baishali Banerjee Thakurta, Ms. Shukla Majhi, Ms. Swapnika Suresh, Ms. Priyanka Jhangra, Ms. Ummiya Qumar, Ms. Neelam Gupta, Ms. Anamika and Mr. Jay Prakash Bijarniya.

I am also deeply thankful to the CIFC at IIT (BHU) for their assistance with the characterization of my samples, and to the administrative staff and authorities of IIT (BHU) for their support during my stay.

A special note of thanks to my senior labmates: Dr. Satya Veer Singh, Dr. Anand Sharma, Dr. Nitesh Kumar Chourasia, Dr. Vishwas Acharya, Dr. Nila Pal, Dr. Utkarsh Pandey, and Dr. Priyanka Chetri, as well as Dr. Pawan Kumar Ojha, Dr. Piyali Maity, Dr. Labanya Ghosh and Dr. Swati Suman. Their guidance and camaraderie have been invaluable. I also extend my heartfelt thanks to my labmates: Mr. Rajarshi Chakraborty, Mr. Sandeep, Mr. Pijush Kanti Aich, Mr. Akhilesh Kumar Yadav, Mr. Subarna Pramanik, Mr. Radhe Shyam, Mr. Pushpendra Prakash Maurya, Mr. Chinmoy Pan, Mr. Piyush Kumar, Mr. Harendra Singh Chauhan, Mr. Rohan Kumar, Mr. Roshan Singh, Mr. Chetan Singh, Mr. Shashank Prasad, Mr. Tanish Jain and Mr. Himanshu Singodia for their insightful discussions and support throughout my research.

A noteworthy thanks to Mr. Jaydeep Gupta, Mr. Prosun Mandal, Mr. Subham Sekhar Mandal, Dr. Nilesh Kumar for their constant support throughout my research work.

I am fortunate to have friends like Mr. Tapas Das, Mr. Rittik Parui, Mr. Souvik Jana, Mr. Akash Ghosh, Mr. Sukhendu Maity, Mr. SK Parvej Ali, Mr. Satyajit Khutia, Mr. Ashes Shit, Mr. Shubhranil Maity, Mr. Debraj Mahato, Mr. Biswajit Manna and my batchmates, who have made my time here more enjoyable and offered their support during challenging moments.

Words cannot fully express my gratitude to my family. My parents, Mr. Samarendra Hazra and Mrs. Kalpana Hazra, my paternal grandparents, Late Mr. Anil Kumar Hazra and Mrs. Arati Hazra, my wife Mrs. Payel Das Hazra, uncles and aunts, Mr. Samar Hazra and Mrs. Tapati Hazra, Mr. Manoj Kumar Shaw and Mrs. Shipra Shaw, My Sisters Mrs. Tumpa Hazra Pakhira and Mrs. Pampa Hazra Mandal, my brothers Mr. Prasenjit Hazra, Mr. Soumya Hazra, their constant encouragement, love, and unwavering belief in me have been the bedrock of my strength.

Date: 03/09/2025

Sobhan Hazra

Place: Varanasi

(Sobhan Hazra)

Contents

List of Figures

List of Tables

Abbreviations

MNPs	Metal nanoparticles
LSPR	Localized surface plasmon resonance
NMNPs	Non-metallic nanoparticles
Au	Gold
Ag	Silver
Cu	Copper
Pt	Platinum
Pd	Palladium
SnO_2	Tin Oxide
TiO_2	Titanium dioxide
ZnO	Zinc oxide
Ag_2S	Silver Sulfide
Cu_2S	Copper Sulfide
WS_2	Tungsten sulfide
MoS_2	Molybdenum oxide
PbS	Lead sulfide
CdS	Cadmium sulfide
CdSe	Cadmium selenide
Fe_2O_3	Iron oxide
EM	Electromagnetic
SPR	Surface plasmon resonance
SPPs	Surface plasmon polaritons

LSPs	Localized surface plasmons
NIR	Near infrared region
SERS	Surface Enhanced Raman Spectroscopy
fs	femtoseconds
ps	picoseconds
ns	nanoseconds
DOS	Density of states
F_E	Fermi energy
Φ_{SB}	Schottky barrier
HTL	Hole transport layer
Φ_M	Metal work-function
χ_s	Semiconductor electron mobility
EQE	External quantum efficiency
TCF	Transparent conductive film
ITO	Indium tin oxide
CNTs	Carbon nanotubes
ROSs	Reactive oxygen species
ICMO	Ion-conducting metal oxide
LTO	$Li_4Ti_5O_{12}$
XRD	X-Ray Diffraction
CB	Conduction Band
PVD	Physical Vapor Deposition
THR	Transparent Heat Reflector

M-S-M	Metal-semiconductor-metal
POSCs	Plasmonic Organic Solar Cells
ETL	Electron transport layer
PCE	Power conversion efficiency
R6G	Rhodamine 6G
I-V	Current-voltage
I-t	Current-time
PMMA	Polymethyl methacrylate
P3HT	Poly(3-hexylthiophene)
$PC_{71}BM$	[6,6]-phenyl-C_{71}-butyric acid methyl ester
PEDOT:PSS	Poly(3,4-ethylenedioxythiophene) polystyrene sulfonate
2-MEA	2-methoxy ethanol
DI	Distilled water
n^+-Si	n-doped silicon
GIXRD	Grazing incidence X-ray diffraction
PL	Photoluminescence Spectra
AFM	Atomic force microscopy
HR-SEM	High resolution scanning electron microscopy
EDX	Energy dispersive x-ray spectroscopy
HR-TEM	High resolution transmission electron microscopy
Φb	Barrier Height
η	Ideality factor
J-V	Current density-voltage

V_{oc}	Open circuit voltage
J_{SC}	Short circuit current density
IQE	Internal quantum efficiency
FTO	Fluorine tin oxide
SAED	Selected area diffraction pattern
TC	Transparent conductor
P_c	Percolation thresold
P	Percolation
P_∞	Percolation probability
BHJ	Bulk Heterojunction
OPVs	Organic photovoltaics
OSCs	Organic solar cells
CT	Charge transfer
VB	Valance band
HOMO	Highest occupied molecular orbital
LUMO	Lowest unoccupied molecular orbital

PREFACE

Nanomaterials have drawn significant attention in recent years due to their numerous potential applications. These materials have been developed for various purposes, including improved chemical and colloidal stability, fabrication of photovoltaic devices and prevention of bacterial infection. Besides, tailoring the optical properties of nanomaterials, it's possible to apply different nanomaterials for various advanced photonic technologies. Particularly, thin films of metal nanoparticles have garnered significant attention in modern opto-electronics due to their ability to enhance light-matter interactions through localized surface plasmon resonance. These thin films, typically made from metal NPs like Ag, Au, and Cu are used to improve device efficiency in applications such as transparent conductors, solar cells, transparent heat reflectors, photodetectors, biosensors, and anti-bacterial coating. Their sensitivity to environmental changes makes them ideal for chemical and biological sensing, while their light-trapping capabilities enhance energy harvesting and photonic applications. As electronics continue to miniaturize and demand higher performance, plasmonic thin films offer a scalable, cost-effective solution with promising integration into next-generation technologies like quantum computing, wearable devices, and flexible electronics. With advancements in solution-based fabrication techniques, their future in energy-efficient systems, healthcare diagnostics, and photonics is particularly bright.

Researchers are increasingly interested in plasmonic thin film devices fabricated via solution-processed techniques because they offer a groundbreaking combination of cost and performance. The coast-effectiveness, scalability, and versatility, particularly suitable for large-area and flexible device applications. Solution processes such as spin-coating, dip-coating, and inkjet printing allow for the mass production of high-performance plasmonic devices without the need for expensive equipment or controlled environments, unlike sputtering, lithography techniques etc. Solution processing also allows seamless integration of plasmonic nanoparticles with other materials, enhancing their optical and electrical properties, thus paving the way for high-performance, low-cost devices in industries ranging from renewable energy to healthcare. As research continues, the ability to fabricate these

devices with precision and scalability is positioning solution-processed plasmonic thin films as a transformative technology in modern electronics.

To address the higher cost of these photonic technologies, we have introduced a novel cost-efficient technique where an ion-conducting metal oxide (ICMO) ceramic is used as initial material. This ceramic contains some light ions like Li^+, Na^+, K^+ etc. and these mobile ions can move through the crystal channel easily. By taking advantage of these mobile ions, we have chemically implanted conducting ions like Ag or Cu inside the dielectric matrix. This new innovation helps to fabricate plasmonic thin film with much more stability, making it feasible for multi-functional photonic applications. To utilize this phenomena, I have successfully fabricated an ion conducting dielectric $Li_4Ti_5O_{12}$ initially and then by doing surface chemistry we have developed an Ag-TiO_2 plasmonic thin film. Using Ag-TiO_2 thin film, I have successfully fabricated a narrowband plasmonic hot electron based photodetector in photoconductor geometry. Device shows a very high detectivity with conclusive evidence of hot electron generation from the plasmonic part.

Furthermore, by employing surface engineering with an ultra-thin plasmonic layer and Ag-TiO_2 thin film, I have successfully developed flexible transparent conductors, transparent heat reflectors, plasmonic solar cells, photodetectors, and active SERS substrates using a low temperature solution process and subsequent physical vapor deposition technique.

A concise overview of the subsequent thesis chapters is presented in the following section.

Chapter 1 provides a brief description of nanomaterials and their growing importance in modern technology. Owing to their unique stability, optical tunability, and multifunctional applications, nanomaterials have been widely explored in energy, healthcare, and photonics. In particular, thin films of metallic nanoparticles (Ag, Au, Cu) utilize localized surface plasmon resonance to enhance light–matter interactions, improving the performance of solar cells, sensors, transparent conductors, and antibacterial coatings. Their scalability, sensitivity, and light-harvesting capabilities make them highly promising for next-generation photonic, healthcare, and flexible electronic systems.

Chapter 2 provides a detailed synthesis process of a popular ion-conducting metal oxide dielectric $Li_4Ti_5O_{12}$ (LTO), plasmonic Ag-TiO_2 thin film, semiconducting precursor solution like SnO_2, TiO_2, SnO_2 NPs, ZnO NPs, TiO_2 NPs, and preparation of polymeric solution like PMMA, P3HT, $PC_{71}BM$ by solution process technique whereas devices are fabricated via spin coating and thermal evaporation technique. The detailed study of material and device characterization are explained in a very concise manner. The characterization techniques of XRD, UV-Visible, photo-luminescence, Raman, FE-SEM, AFM, HR-TEM, semiconductor parameter analyzer, EQE measurement unit along with reflectance and transmission measurement unit, etc. has been explained elaborately.

Chapter 3 discusses the development of Ag-TiO_2 thin film from an ion-conducting dielectric Lithium Titanium Oxide ($Li_4Ti_5O_{12}$) material via an in-situ growth technique and its application as a hot electron based plasmonic photodetector. The X-ray diffraction (XRD) measurement has been performed to confirm the phase of the material. UV-visible, and PL spectroscopy has been used to study the optical absorption and luminescence of active Ag-TiO_2 material. HR-SEM and HR-TEM has been performed to calculate the Ag NPs size and the composition of the material. This Ag-TiO_2 nano-Schottky junction has a low barrier height, high interface area with least interface state that enables efficient hot electron transfer to the conduction band (CB) of TiO_2, which is realized in the EQE data. This EQE data shows an intense photocurrent formation in the region of plasmonic absorption of Ag NPs, indicating the primary contribution of hot electrons on photocurrent production. This photodetector has been fabricated in a glass substrate in photoconductor geometry that shows a peak detectivity of 3.19×10^{11} Jones at 420 nm with a response time of ~2 sec.

Chapter 4 is separated into two sections; the first section discusses the development of Ag nanostructured based flexible transparent conductor and its application as a self-biased plasmonic photodetector and the second section focuses on the fabrication of a cost-effective Ag/Ag-TiO_2 flexible transparent heat reflector for energy-efficient smart window applications.

4.1 Flexible Transparent Conductors with a Percolated Ag Nanostructure and its Application as Efficient Self-Bias Plasmonic Photodetector

A percolated Ag nanostructured-based transparent conductor has been deposited by physical vapor deposition (PVD) technique where lateral growth of Ag has been enhanced by a pre-deposited Ag-TiO_2 thin film. This Ag-TiO_2 film has embedded Ag nanoparticles (NPs) within TiO_2 thin film which is grown in a low temperature (100˚C) solution processed technique that includes $Li_4Ti_5O_{12}$ (LTO) thin film deposition by a sol-gel method followed by ion-exchange ($Li^+ \rightarrow Ag^+$) process to yield an Ag-TiO_2 thin film. The percolated Ag network has appeared as soon film mass-thickness reaches close to 10 nm, resulting in an abrupt drop of electrical resistivity of the film. This percolated Ag nanostructured thin film (10 nm Ag/Ag-TiO_2/plastic) has resistivity of ~ 50 ohm/□ and an average visual transmittance of >70% up to 450 nm. In higher wavelength range, transparency gradually reduces, and it reaches to ~50% at 600 nm which is mostly due to the plasmon absorption of this film. By utilizing its combined optical transparency and surface plasmon absorption, this film has been used to develop plasmonic hot electron photodetectors where Ag-thin film works as transparent electrode as well as plasmon induced photo-excited hot electron generation. Device has been fabricated on a highly doped n type Si (n^+-Si) with a metal-semiconductor-metal (M-S-M) device geometry. External quantum efficiency (EQE) data reveal that photocurrent of this device is mostly generated in the plasmonic absorption region with a peak detectivity of 2.84×10^{12} Jones at 510 nm under -3V external bias. Besides, the device shows fast response with a response time of ~25 ms.

4.2 Cost Efficient Ag/Ag-TiO_2 Coating Based Flexible Transparent Heat Reflector for Energy-Saving Smart Window

This work has demonstrated a mass-producible and low-cost transparent heat reflector (THR) fabrication method on a flexible substrate by using a per-deposited silver nanostructures thin film which is grown in two step deposition method. Initially, polycrystalline LTO thin film has been grown on a plastic substrate by a low temperature processed sol-gel technique. Afterword, mobile Li^+ of LTO thin film has been replaced by Ag^+ by an ion-exchange method to form Ag-TiO_2 thin film. In the second step, 10 nm Ag has been deposited on top of Ag-TiO_2 thin film by thermal evaporation. This bilayer THR has IR/NIR reflectivity of ~85-90% in combination with its visible transmittance of ~50-70%. For higher environmental stability of this THR, a polymer film (PMMA) has been coated on top of this

Ag/Ag-TiO_2 coating. To realize the practical application of this THR, a prototype box with one transparent glass window coated with this THR film has been developed and its internal temperature has been investigated during daytime. A reduction of internal temperature of ~6-7˚C has been observed due to this THR coating w.r.t the reference uncoated box, indicating its plausibility as energy-saving smart window applications.

Chapter 5 is also categorized into two subparts; the first part discusses about the development of visible to IR active highly transparent Au-Ag bimetallic conducting film and its application as an efficient plasmonic photodetector on plastic substrate, and the next part I demonstrated an enhanced energy conversion plasmonic organic solar cell using this Au-Ag bimetallic transparent conducting film as a back electrode.

5.1. Visible to IR Active Highly Transparent Au-Ag Bimetallic Conducting Film and its Application as an Efficient Plasmonic Photodetector on Plastic Substrate

This section of this chapter demonstrated a gold (Au)-based transparent conductor by PVD technique where nano-porous of Au-Ag bimetallic nanostructured has been enhanced by a pre-deposited Ag-TiO_2/SnO_2 or ZnO NPs thin film. This Ag-TiO_2 thin film is an Ag NPs embedded TiO_2 thin film that has been grown over SnO_2 or ZnO NPs which leads to a percolated nano-porous-like structure. Prior to this, the surface morphology of the film shows a clear transition from spherical nanoparticles to percolated nano-porous Au-Ag bimetallic nanostructure with random hole formation that results in an abrupt jump of electrical conductivity when deposition reaches to 4 nm mass thickness of Au. This percolated nano-porous structure thin film (4 nm Au/Ag-TiO_2/SnO_2 or ZnO NPs /plastic) has a low resistivity of ~ 5-10 ohm/□ and an average visual transmittance around 75-80 % in the visible region. This film has been used to develop a metal-semiconductor-metal (M-S-M) plasmonic hot electron photodetector where Au-Ag thin film works as a photo-excited hot electron generation. External quantum efficiency (EQE) data reveal that photocurrent of this device is mostly generated in the plasmonic absorption region with a peak detectivity of 1.6×10^{13} Jones at 750 nm under -2V external bias. Besides, the device shows fast response with a response time of ~33 ms.

5.2. Au-Ag Bimetallic Transparent Conducting Thin Film for Boosting Energy Conversion Efficiency of Organic Solar Cell

Here, I discussed a new approach for enhancing the power conversion efficiency through an inverted plasmonic organic solar cells (POSCs) in a cost-effective way. As an alternative to ITO, I used our developed Au-Ag bimetallic transparent conducting film to back the electrode. A P3HT or a blended P3HT:$PC_{71}BM$ organic polymer are used as an active material of this device whereas PEDOT: PSS and SnO_2 NPs are used as hole transport and electron transport layer respectively. The device with 120-140 nm thick active layer shows a remarkable power conversion efficiency of 7.8% for P3HT and 11.17% for blended P3HT:$PC_{71}BM$ bulk heterojunction solar cells which are record efficiency with this materials combination that become possible due to enhancement of open circuit voltage by double, ensuring a tandem cell formation. This research offers a fresh, simple method to develop innovative plasmonic nanoparticles for enhancing the efficiency of OSCs.

Chapter 6 presents a straightforward method to fabricate a porous Au-Ag bimetallic nano-film on an inexpensive plastic substrate to detect SERS signal. Hollow and porous percolated nanostructures hold significant importance in SERS due to their intrinsic EM hotspots, multipolar resonance, and other factors. Au-Ag bimetallic film is fabricated via the same method as mentioned in the earlier chapter. This flexible substrate demonstrates effective SERS-based sensing, detecting Rhodamine 6G (R6G) dye and Vitamin B_{12} down to 1 pM and 1 nM concentrations, respectively. The porous nature of the nano thin film aids in dispersing the analytes, thus lowering particle density for single molecule optical detection and enabling low-concentration measurements.

Chapter 7 summarizes the key outcomes presented in the thesis. Furthermore, the final part includes a brief outline of prospective research possibilities related to the current thesis.

List of journals and books used to bind up the thesis has been given at the end of the thesis as references

Chapter 1

Introduction & Literature Review

Chapter 1

This chapter provides a general review of the global field of nanomaterials, particularly plasmonic metal nanoparticles (MNPs), and their properties and applications. In the beginning, a brief introduction of nanotechnology and nanomaterials has been given, which motivates the inherent capacity to impact manufactures now and hereafter with some examples. Notably, plasmonic thin films have garnered significant attention in modern photonics due to their ability to enhance light-matter interactions through localized surface plasmon resonance (LSPR). This enables superior optical, electronic, and sensing properties at the nanoscale. Herein, photoexcitation and relaxation of charge carriers within plasmonic NPs are discussed briefly. This chapter deliberates an overview of the plasmonic MNPs, which has some important photonic applications in the field of solar cells, plasmonic photodetector, transparent conductor, memristor, heat reflector, gas sensor, bio sensor, as well as bio-imaging. These MNPs require a specialized fabrication procedure for their preparation. At the end of this chapter, these materials are discussed in detail with their properties and applications, alongside motivation and the scope of the thesis.

1.1 Nanotechnology

The term “nanotechnology” was first introduced by Prof. Norio Taniguchi of Tokyo Science University Japan in 1974.[1-3] At this scale, unique properties and behaviors emerge, enabling the design and creation of materials, devices, and systems with enhanced functionalities. Nanotechnology encompasses various applications across diverse sectors, including electronics, medicine, energy, and materials science.[4-10] Researchers manipulate and control materials at the nanoscale to exploit novel characteristics, such as increased surface area, improved conductivity, and enhanced reactivity. The potential benefits of nanotechnology include advancements in drug delivery, more efficient energy storage, and the development of smaller and more powerful electronic components.[11-13]

However, ethical and safety considerations accompany the rapid progress in nanotechnology, necessitating careful exploration of its societal implications.

1.2 Nanomaterials

Nanomaterials are the fundamental components of the nanoscience and nanotechnology fields. Research and development processes associated with this are expanding rapidly around the globe. In 1959, physicist and scientist Richard Feynman developed the term "nanomaterial".[14, 15] Nanomaterials have typical particle dimensions between 1 and 100 nm. Furthermore, nanomaterials belong to a class of materials restricted in the bulk materials domain. Nanomaterials exhibit qualities that are completely distinct from their bulk counterparts. The characteristics of these materials are investigated using a precise length scale, which is generally in the nanoscale range. When bulk material is shrunk below the nanometer scale, its physical characteristics alter significantly. The properties of nanomaterials change due to the significant increase in surface-to-volume ratio, leading to high surface tension, which is shown in **Figure 1.1.** This tension causes rapid melting. As particle size reduces, the number of surface atoms increases, impacting free energy and enhancing electronic, optical, mechanical, and thermodynamic properties.[16-18] Surface atoms play a significant role in governing nanoparticle properties. Reducing NP size affects atomic energy levels as the system becomes more constrained, leading to strong variations in optical and electrical properties due to changes in the density of electronic energy levels, known as the quantum size effects.[19, 20] This effect is observed more prominently in metal nanoparticles (MNPs) compared to non-metallic nanoparticles (NMNPs) due to the absence of a band gap and the Fermi level's position in metals.[21] Designing at the nanoscale is crucial for developing new products that replace existing chemicals and materials with enhanced performance and potential cost savings. This also benefits the environment by reducing material usage. Additionally, nanotechnology offers opportunities to organize and improve fabrication processes.

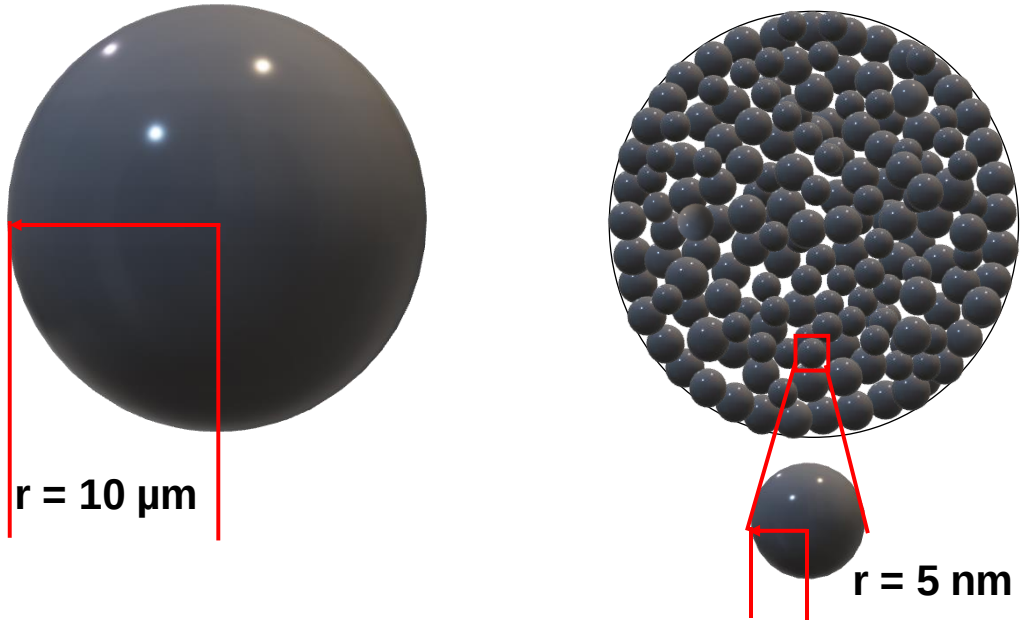

Figure 1.1 Schematic illustration of the difference in surface to volume ratio between a bulk microsphere and microsphere formed by NPs.

1.3 Classification of Nanomaterials

Nanomaterials are generally classified into two major categories: MNPs and NMNPs. The MNPs, such as gold (Au), silver (Ag), copper (Cu), nickel (Ni), platinum (Pt), and palladium (Pd) etc. and their alloys with combination of bi-metal like Ag-Au, Ag-Cu, Cu-Ni and so on are composed of metal components only. Due to their small size and large surface area, these MNPs show unusual electrical, optical, and catalytic properties. On the Other hand, NMNPs, such as tin oxide (SnO_2), titanium dioxide (TiO_2), zinc oxide (ZnO), silver sulfide (Ag_2S), copper sulfide (Cu_2S), tungsten sulfide (WS_2), molybdenum oxide (MoS_2), lead sulfide (PbS), cadmium sulfide (CdS), cadmium selenide (CdSe) and iron oxide (Fe_2O_3), consist of metal atoms bonded to oxygen or Sulphur. These NPs are known for their excellent chemical stability, magnetic properties, and wide range of applications in energy saving smart windows, photodetection, photo-catalysis and biomedical fields.[22-28]

1.3.1 Metal Nanoparticles

A widely recognized definition of a nanomaterial describes it as a material with a structure where at least one of its phases exhibits a nanometre-scale size in at least one dimension. Based on this definition, nano-objects can be categorized into three distinct groups:

I. 1D nanoscale objects (e.g., thin films)
II. 2D nanoscale objects (e.g., nanowires, nanorods and nanotubes)
III. 3D nanoscale objects (e.g., nanoclusters or nanoparticles)

The journey of synthesizing MNPs started in 1856 when Michael Faraday successfully reduced gold chloride with phosphorus, creating gold colloids that exhibited a stable ruby red color. These samples, some of which are still preserved in the Faraday Museum in London.[29] The increasing significance of MNPs in modern science has driven the development of new techniques and enhancements in nanoparticle manufacturing, leading to particles with remarkable properties. One of the most notable properties of MNPs is their optical behavior, which differs greatly from that of single molecules or bulk materials. When reduced to nanoscale, metals like Au and Ag absorb visible light very strongly. These optical characteristics have been known for a long time and were first explained by Mie theory in 1908. This theory, grounded in Maxwell's equations, calculates the particle extinction spectra based on the material's dielectric function and particle size within the visible light wavelength range. Since its introduction, Mie theory has been extensively applied.[30, 31] Typically, standard colloidal results in roughly spherical particles, and a variety of optical methods are used to characterize the spectra of these NPs.

1.3.2 Non-Metallic Nanoparticles

Non-metals or metal oxides are pivotal in various fields due to their ability to form a wide range of compounds with diverse structural geometries and electronic properties, ranging from metallic to insulating. They are essential in technological applications such as microelectronics, sensors, fuel cells, and catalysts.[32-35] In nanotechnology, NMNPs exhibit unique properties, which are not seen in bulk materials, driven by their small size and high surface area, which introduce significant changes in structural and electronic

characteristics. As the particle size decreases, structural changes occur due to increased surface energy, which can lead to modifications in lattice parameters, thermodynamic stability, and even phase transitions. These changes, along with quantum size effects, alter the electronic properties, including band gaps and conductivity. The surface properties of nanostructured oxides are also profoundly affected, with enhanced chemical reactivity and unique absorption due to the presence of under-coordinated atoms and vacancies, making them highly valuable for catalytic and other chemical processes.

1.4 Various Synthesis Technique of Metallic/Non-Metallic Nanoparticles

The fabrication of MNPs has seen diverse techniques, reflecting the significant role of NP preparation in science and technology. Two primary strategies for developing materials at the nanometer scale are the top-down and bottom-up approaches, which are shown in **Figure 1.2**. The term “nanotechnology” was discovered by Professor Norio Taniguchi of Tokyo University in 1974 to describe highly precise ultrafine dimensions, introducing the top-down approach, which involves physical and chemical methods to obtain atomic-scale materials by removing material from bulk substances. This method, however, is not ideal for producing uniform small particles. About a decade later, K. Eric Drexler introduced the bottom-up approach, which assembles atoms into nanostructures and can yield more uniform particles. The top-down method's drawback is the significant removal of material, while the bottom-up method can suffer from poor monodispersity due to the challenge of maintaining consistent growth rates for all nanoparticles. Various techniques exist to fabricate different types of nanomaterials, such as colloids, clusters, powders, tubes, wires, thin films, and rods, depending on the target material and nanostructure type. NPs can be synthesized by growing, shaping, or self-assembling materials through physical, chemical, biological, or hybrid methods. The top-down approach includes methods like electron beam lithography and photolithography, while the bottom-up approach encompasses physical, chemical, and biological methods, including electrochemical, seeding, and thermal and photochemical reduction methods, with electrochemical and photochemical methods capable of producing uniform nanorods.[36-39]

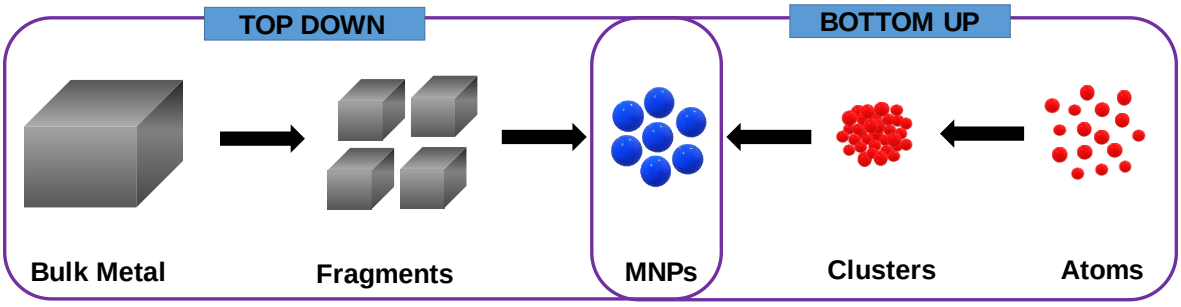

Figure 1.2 Schematic presentation of top-down and bottom-up approach for the synthesis of metal/metal oxide NPs.

Chemical methods have several advantages over physical methods: they are relatively easy and economical, can be conducted at low temperatures, produce large quantities of material, and do not require sophisticated equipment. These methods allow for the preparation of materials in various compositions and are extensively used for synthesizing nanomaterials. In this context, capping materials such as surfactants or polymers are utilized to prevent the aggregation of MNPs in solution. Various shapes, including spheres, cubes, wires, rods, tubes, triangular prisms, tetrahedral NPs, and quantum dots, have been synthesized from metals like Au, Ag, Cu, Pt, etc. and metal oxides like SnO_2, ZnO, TiO_2, etc., using different reduction techniques and capping agents. NPs can also be developed using a combination of physical and chemical methods. Therefore, the choice of fabrication procedures depends on the desired physical and chemical properties, such as size, dispersion, mixture homogeneity, and optical properties. Both physical and chemical methods can result in environmental contamination and toxicity. In contrast, biological approaches, specifically green synthesis, are environmentally friendly and less toxic. Still, for the fabrication of opto-electronic devices, physical and chemical methods are superior as they allow making precious NP size, shape and morphology, which is very much crucial for photonic applications.[40-42] The various approaches and methods for NP synthesis are summarized in **Figure 1.3**.

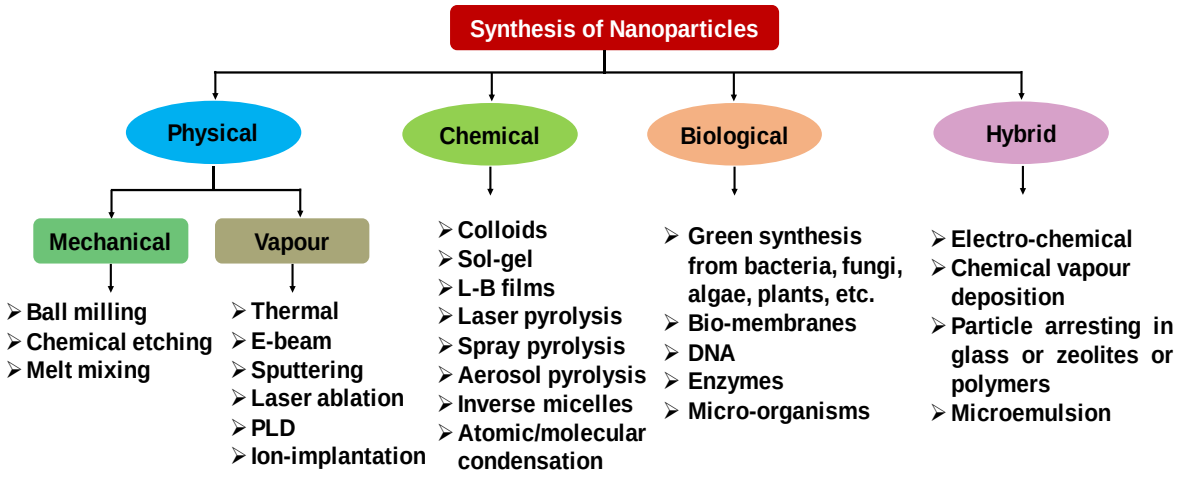

Figure 1.3 Schematic of different synthesis routes for the fabrication of nanomaterials.

In 1951, John Turkevitch reported the synthesis of spherical Au NPs using the citrate reduction method. This technique, which involves reducing Au ions in solution with citrate ions, has become a widely used method for producing Au NPs due to its simplicity and effectiveness. Turkevitch's method remains a fundamental approach in the field of nanotechnology for the preparation of Au NPs.[43, 44] An admired method for creating highly spherical and non-spherical NPs is the seeding system. Typically, spherical NPs are initially developed and then added to a growth solution containing additional metal ions and surfactants to promote anisotropic particle growth. This process often involves seeds fabricated using sodium borohydride, a strong reducing agent. The growth solution employs a weaker reducing agent to partially reduce the metal salt, allowing only the catalyzed reduction on the NP surface. A schematic comparison between in-situ and ex-situ methodologies is shown in **Figure 1.4**.

The stabilization of MNPs can be achieved through various approaches. In ex-situ fabrication, NPs are dispersed in a solid or liquid medium after their synthesis using different chemical methods. This approach provides stabilization but poses a risk of reaggregation over time. In contrast, in an in-situ fabrication, MNPs are grown directly within the stabilizing medium, which is of great interest due to its technological advantages.[45]

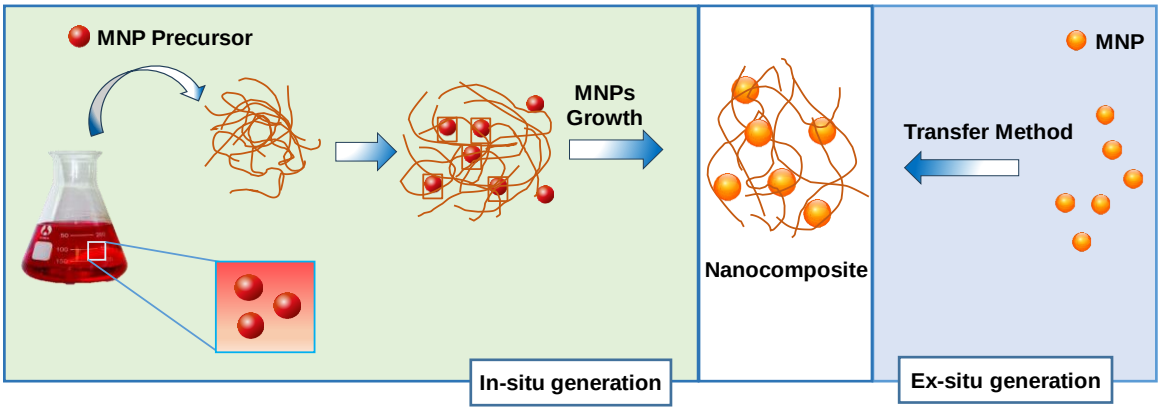

Figure 1.4 Schematic presentation of in-situ and ex-situ methodology for NP synthesis.

1.5 Plasmonic Metal Nanoparticles

The investigation of optical phenomena related to the electromagnetic (EM) behavior of metals has driven the rapid growth of a promising research area known as plasmonics. The intense interaction between EM fields and plasmonic NPs creates new opportunities for technologies that leverage photophysical processes, enhanced by this light-matter interaction. The interaction of these metallic NPs with incoming light causes a collective oscillation of free electrons known as plasmon to become dominant, resulting in the surface plasmon resonance (SPR).[46, 47] Many of these electrons participate in the SPR, resulting in high absorption, scattering, and near-field amplification at the plasmonic NPs natural frequency, which is also known as plasma frequency.[47] Novel metals, including Au, Ag, Cu, Ni, or their bimetallic nano-film, can be employed as free electron systems whose electrical and optical properties are determined only by the conduction electrons. According to the Drude-Lorentz model, metals are considered plasmas because they contain equal numbers of positive ions and conduction electrons.[48] So, in the presence of an incoming plane EM wave, charge displacement occurs within this plasma. Volume or Bulk plasmons are the cases discussed by Pines and Bohm,[49] visualized in **Figure 1.5a)**. So, bulk plasmon is the outcome of the generation of forward and backward EM waves (due to charge displacements caused by an incoming plane EM wave), resulting in the formation of an energy gap.[50] The energy of the bulk plasmon[51] is given by **equation 1.1**-

$$E_{bulk} = \hbar\omega_p \text{ ------- } \mathbf{(1.1)}$$ where ω_p is the plasma frequency

In the context of metal thin film with finite dimensions and different surrounding dielectric materials, their collective oscillations are known as surface plasmon polaritons (SPPs) or surface plasmons. The resonant interaction of optical waves with free electrons in a metal can generate surface-bound EM modes, often known as surface plasmons, which are typically excited at the interface of a noble metal and a dielectric. These surface plasmons have maximum field intensity at the metal-dielectric interface, with evanescent waves penetrating the surrounding dielectric, making them highly sensitive to refractive index changes near the metal surface, as shown in **Figure 1.5b)**. Localized surface plasmons (LSPs) arise when light hits MNPs or metal nanostructures. As the light wavelength is substantially larger than the nanostructure, a plasmon oscillates around it, as shown in **Figure 1.5c)**. When light interacts with MNPs or nanostructures, the conduction electrons on their surface oscillate collectively at a particular frequency, known as plasma frequency.[52]

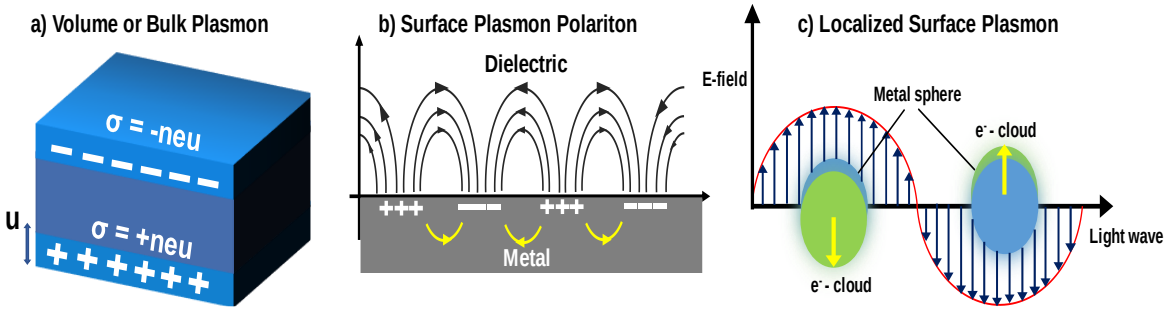

Figure 1.5 Comparative diagrams of **a)** volume or bulk Plasmon, **b)** surface plasmon polariton, and **c)** localized surface plasmon.

LSPR is one primary characteristic of plasmonic MNPs like Ag, Au, Cu, etc. that are widely used in varieties of applications. This effect is typically excited by direct illumination without requiring a specific angle that satisfies the resonance condition, with maximum field intensity at the metal-dielectric interface, decaying exponentially away from it. The light absorption by MNPs originates from the coherent oscillation of conduction band electrons caused by interaction with external EM radiation. In MNPs, a disturbance-like interaction with EM radiation displaces the equilibrium of the negatively charged electron cloud and the positively charged ion cloud, depicted in **Figure 1.6**. This disturbance causes electrons to

oscillate back and forth, creating collective oscillations, which result in strong absorption in the visible to near infrared (NIR) region.[53, 54]

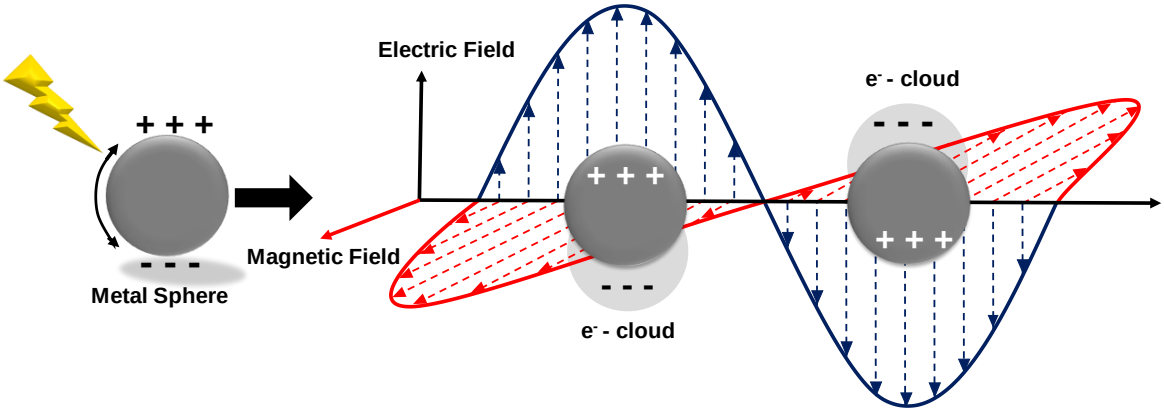

Figure 1.6 Schematic representations of the LSPR effect in plasmonic MNPs.

The illumination of a metallic nanostructure triggers a series of complicated processes in different time scales, leading to various possible outcomes.[55] These include the rapid internal relaxation or ejection of hot carriers, the generation of strong optical near-fields, and the re-emission of photons. The initial stage in hot carrier excitation begins with photon absorption (**Figure 1.7a)**), where the probability of absorption is related to the square of the local electric field inside the metal. In metallic nanostructures, light absorption is further amplified by the LSPR effect.[56, 57] This enhancement results in an antenna-like effect, allowing the structure to collect light from an area larger than its actual size.[58, 59] Consequently, these MNPs or nanostructures act as an EM hotspot. The concentrated light field generated by this effect has been extensively studied and applied in surface-enhanced processes such as surface-enhanced Raman spectroscopy (SERS), surface photochemistry, and the photoexcitation of nearby quantum emitters.[60, 61] In nanostructures, plasmon resonances can be damped non-radiatively by generating hot electron-hole pairs through Landau damping or radiatively by photon re-emission (**Figure 1.7b)**). Landau damping is a purely quantum mechanical phenomena that transfers a plasmon quantum into a single electron–hole pair excitation within a timescale (τ) ranging from 1 to 100 femtoseconds (fs).[62] The plasmon-induced electric field, acting as a time-dependent perturbation on the metal's conduction electrons, facilitates transitions from occupied to unoccupied electronic states. However, because the transition matrix elements for electron–hole pair formation are

relatively small, the most likely direct outcome of plasmon decay is the creation of a single electron–hole pair, with a possible carrier distribution illustrated in **Figure 1.7b)**. The distribution of charge carriers depends on multiple factors, including plasmon energy, particle size, plasmon mode symmetry, and the material's electronic structure and density of states.[63] Landau damping contributes to the imaginary part of a metal's dielectric permittivity in the visible spectrum. Understanding this imaginary component is crucial for optimizing hot carrier generation. For example, adjusting a subradiant plasmon mode to energy levels where the imaginary component of the permittivity is high allows for the optimization of hot carrier production. This tuning can be achieved by leveraging the geometric tunability of LSPRs in MNPs or by designing composite structures composed of noble metals combined with metals exhibiting strong intraband transitions. Following plasmon decay, the hot electrons rapidly redistribute their energy among lower-energy electrons through electron–electron scattering mechanisms, such as Auger transitions.[64] While hot carrier relaxation dynamics have been well studied for extended surfaces, little is known about these processes at the nanoscale. For extended MNP surfaces, time-resolved studies[65] suggest that relaxation times range between 100 fs and 1 picosecond (ps), leading to the formation of a high-temperature Fermi–Dirac-like distribution with an elevated effective electron temperature (**Figure 1.7c)**). Hot electrons are those electrons that are not in thermal equilibrium with the atomic lattice of the substance. These hot electrons follow a Fermi distribution but exhibit an increased effective temperature. In the final stage, heat is transferred from the metallic nanostructure to its surroundings, a process that occurs over a timescale ranging from 100 ps to 10 nanoseconds (ns), depending on factors such as material composition, particle size, and the thermal conductivity of the ambient atmosphere (**Figure 1.7d**).

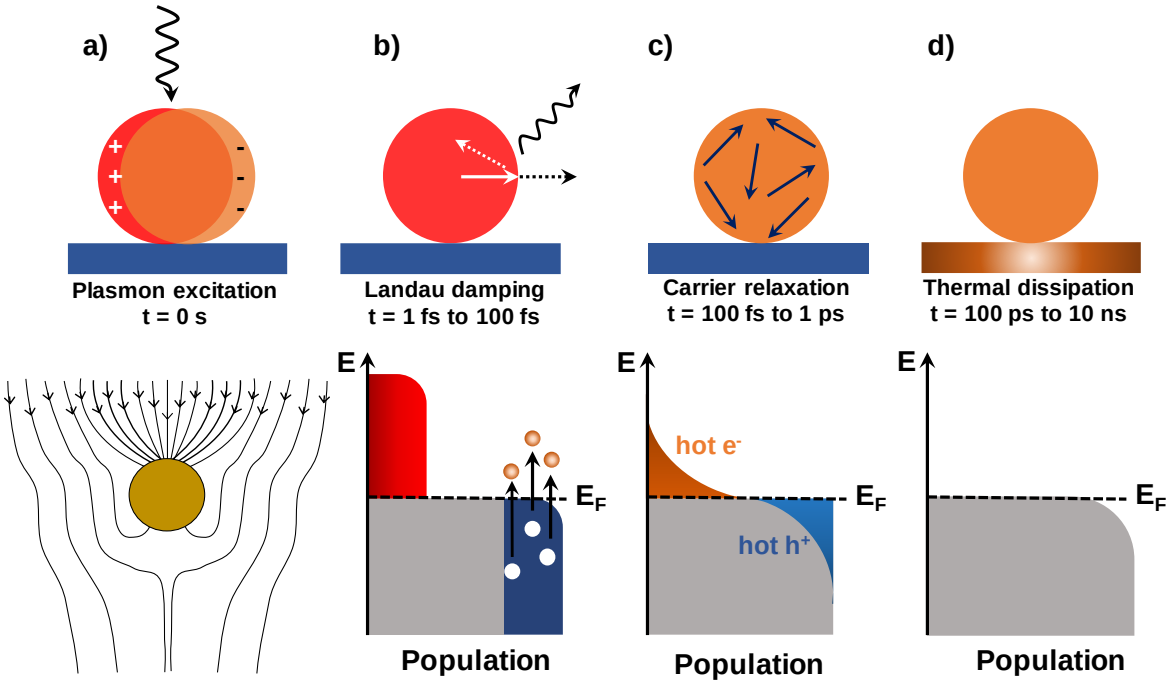

Figure 1.7 a) Excitation of a LSPs redirects the Poynting vector, channeling the flow of light toward and into the NP. Following plasmon excitation, the distribution of electronic states changes, with hot electrons appearing in the orange regions above the Fermi energy (E_F) and hot holes occupying the blue regions below E_F. **b)** Within the first 1–100 fs after Landau damping, electron–hole pairs form a thermal distribution that undergoes decay either by photon re-emission or through carrier multiplication driven by electron–electron interactions. During this brief period, the hot carrier distribution remains highly non-thermal. **c)** hot carriers undergo energy redistribution through electron–electron scattering processes, occurring within a timescale of 100 fs to 1 ps. **d)** Thermal conduction facilitates the transfer of heat from the metallic structure to its surroundings over a longer timescale, ranging from 100 ps to 10 ns.

Following light absorption and LSPR excitation in these nanostructures, EM decay occurs on a fs timescale. This decay can occur either radiatively, by emitting photons, or non-radiatively, by transferring energy to hot electrons, as illustrated in **Figure 1.8a)**. In the non-radiative pathway, surface plasmons initially decay into single-electron excited states, which may subsequently lead to photoemission if the electron's energy surpasses the work function of the material.[66-69] Non-radiative decay in noble-metal nanostructures can occur via

intraband excitations within the conduction band or interband excitations involving transitions between other electronic bands (such as d bands) and the conduction band. In Ag, the d band energy levels are positioned 4 eV below the Fermi energy level, allowing only intraband excitations. Conversely, Au exhibits significant interband excitations under light exposure due to the shorter energy gap of 2.4 eV between its d-states and the Fermi level.[70, 71] Since Ag only undergoes intraband transitions, hot electrons can be efficiently excited above the Fermi energy within the same band, making it more favourable for hot electron collection to the conduction band of metal-oxide at the metal–semiconductor interface compared to Au. However, Au remains the most stable plasmonic nanoparticle among noble metals. When a bi-metallic Ag–Au nanostructure is illuminated, it experiences fewer interband excitations than Au alone, as its d-states are shifted further from the Fermi level. This provides enhanced stability along with improved charge carrier collection. Once photo excited, electrons dissipate energy through electron–electron and electron–phonon interactions, ultimately converting into heat. An electron-donor solution or a hole-transporting layer (HTL) is required to promote hole transfer to the counter electrode in order to maintain charge balance and electrical current. **Figure 1.8b)** illustrates the parabolic density of states (DOS) in the conduction band of a plasmonic nanostructure where the Fermi energy is used as a function of energy.[72-74] A highly effective method for capturing these hot electrons is the formation of a Schottky barrier with a suitable semiconductor. **Figure 1.8c)** presents a Schottky barrier between a plasmonic nanostructure and an n-type semiconductor, such as titanium dioxide (TiO_2). Due to its high DOS in the conduction band, TiO_2 serves as an excellent electron-accepting metal oxide, enabling rapid electron injection. Hot electrons with energies exceeding the Schottky barrier energy (Φ_{SB}) can be transferred into the semiconductor, with emission efficiency depending on their energy.[75] Following electron injection into the adjacent semiconductor, the plasmonic nanostructure becomes positively charged due to electron depletion. An electron-donor solution or a hole-transporting layer (HTL) is required to promote hole transfer to the counter electrode in order to maintain charge balance and electrical current.

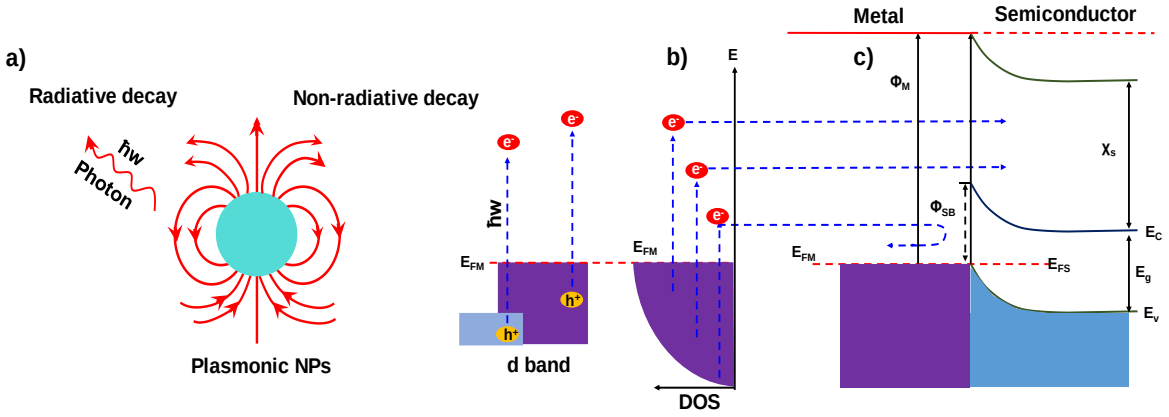

Figure 1.8a) LSPs decay either radiatively, by emitting photons, or non-radiatively, by exciting hot electrons **b)** plasmonic energy conversion excites electrons from occupied energy levels above the Fermi energy **c)** hot electrons with sufficient energy overcome the Schottky barrier $\Phi_{SB} = \Phi_M - \chi_S$ and are injected into the conduction band E_c of a neighboring semiconductor. where Φ_M represents the metal's work function and χ_S denotes the semiconductor's electron affinity.

These novel MNPs can be easily combined with other materials (e.g., zinc, titanium, tin, silicon, carbon, and various polymers) for photonic applications.[76, 77] Their synthesis is generally environmentally friendly compared to other nanomaterials. The plasmonic properties of noble MNPs, especially their large scattering and absorption cross-sections, strong field enhancement, and the ability to form various reproducible morphologies, make them superior to many other nanomaterials. These optical properties enable a wide range of applications in imaging and sensing, associated with enhanced chemical signals, which is schematically shown in **Figure 1.9**. The reproducibility of their fabrication protocols and tunable optical properties makes metallic plasmonic NPs dominant in both theoretical study and practical applications within the field of plasmonics.[78-84]

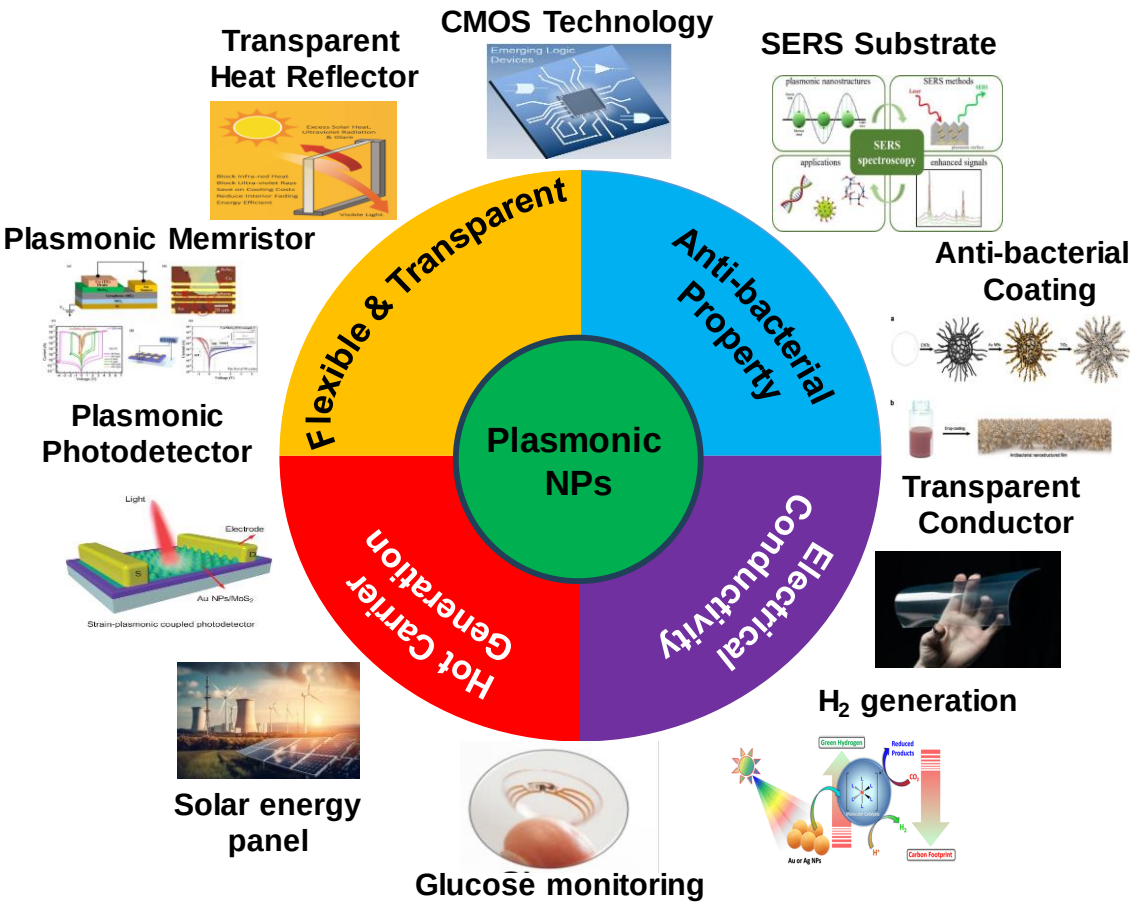

Figure 1.9 Schematic presentation of wide-range photonic applications of plasmonic NPs.

1.5.1 SPR Band Position of Plasmonic MNPs

Both Au and Ag NPs have plasmonic resonance in the visible range with strong absorption at wavelengths of ~ 520-550 nm and ~ 420-480 nm, respectively.[85] The spectrum position depends on diverse factors like size, shape and surrounding dielectric medium. These SPR bands of MNPs can be tuned by varying their size range of 1 – 100 nm. In **Figure 1.10**, we can observe that a single broad plasmon absorption band breaks into two plasmon bands as the shape changes from a sphere to a rod. The peak is caused by transverse plasmon resonance along the shorter axis at a shorter wavelength and longitudinal plasmon resonance along the longer axis at a higher wavelength. It is observed that nanorods of Au exhibit two SPR peaks, one for the transverse mode and another for longitudinal mode, which can be tuned in the spectral region depending on their aspect ratio.[86] Along with the different

shapes and sizes of the particles, surface plasmon resonance depends on Rayleigh scattering, charge transfer interactions, changes in the local refractive index and agglomeration of metal NPs. Due to their broad applications of plasmonic NPs with different shapes, they have been synthesized by various routes such as sphere, cubes, rods, bimetallic core-shell, and so on.[85, 87-89]

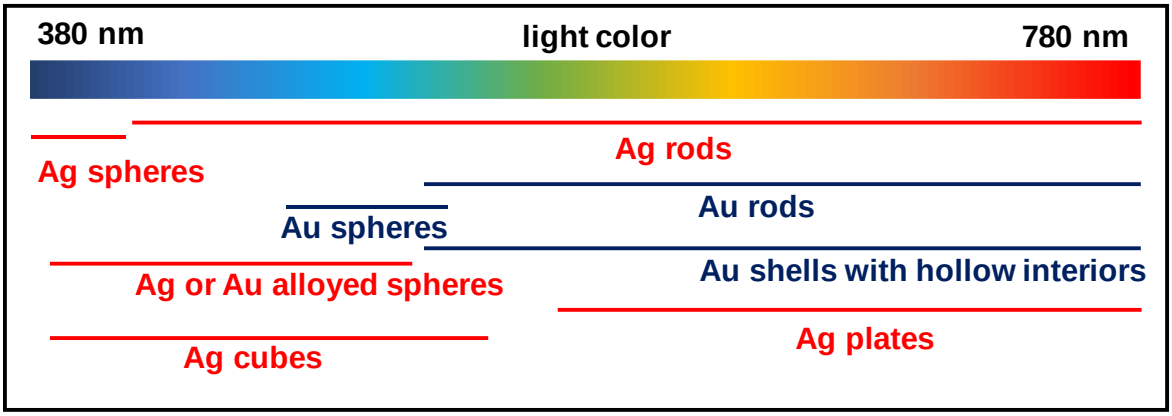

Figure 1.10 Schematic of SPR band position of plasmonic (Ag or Au) MNPs.

1.6 Properties of Plasmonic MNPs

Plasmonic MNPs are renowned for their unique optical properties, primarily due to the LSPR effect, where conduction electrons oscillate in resonance with incident light. This leads to strong light absorption, scattering, and enhanced EM fields.[76, 90] Beyond optical properties, these materials also exhibit significant catalytic activity due to their high surface area and active sites, which are enhanced by the LSPR effect, enabling efficient energy transfer and boosting reaction rates. These NPs have various forms, such as mono-metallic, bi-metallic nanocomposite, metal/semiconductors nanocomposite, etc. The physical and chemical properties of these nanostructured materials are closely related to their shape, size and chemical composition.[91-96] By changing their size, it is possible to tune their different physical properties, including optical, mechanical, electronic, magnetic, photo-catalytic, etc., which are listed in **Figure 1.11**.

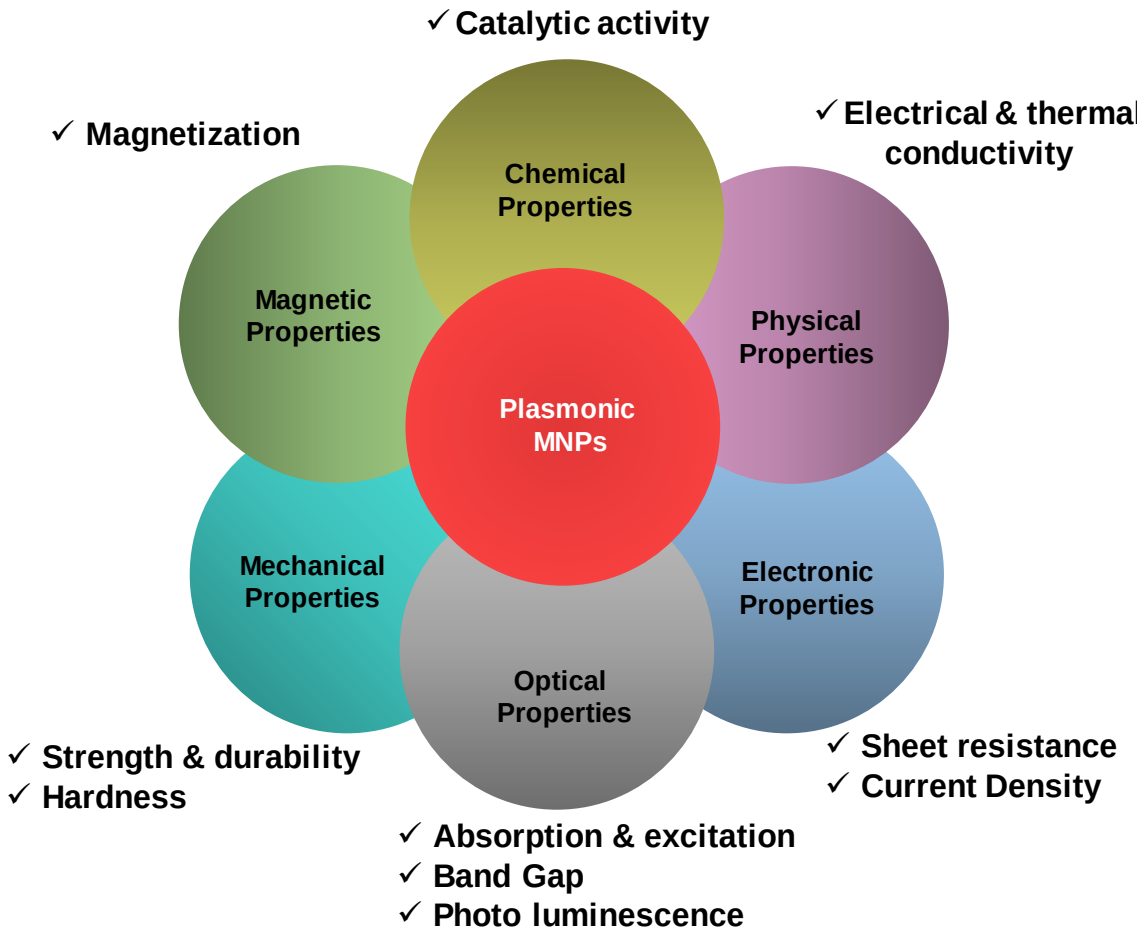

Figure 1.11 Schematic illustrations of different size dependent physical properties of plasmonic MNPs.

1.7 Different Applications of Plasmonic Thin Films

Plasmonic thin films of metal, metal-oxide semiconductor or their nanocomposite have drawn significant attention due to their strong potential applications. These materials have been fabricated for numerous applications like plasmonic photodetector, solar cell, transparent conductor, transparent heat reflector, memristor, SERS, photocatalysis, gas sensor, biosensors, energy storage device, therapeutic and drug delivery, anti-bacterial coating, etc.[97-105] A few applications are explored below in detail.

1.7.1 Plasmonic Photodetector

A photodetector is an electronic device that converts a light (photons) signal into an electrical signal and works by absorbing photons, which generate charge carriers (electrons and holes) within the material, leading to a measurable current or voltage. A plasmonic photodetector leverages the interaction between light and free electrons in metal nanostructures, known as plasmonics, to enhance its performance. By concentrating light into very small volumes and increasing the local EM field, these photodetectors achieve higher light absorption, leading to a stronger photocurrent and improved photo-detectivity. These devices can be designed in three different geometries, such as photoconductors, photodiodes, and phototransistors, as illustrated in **Figure 1.12**. The performance of a plasmonic photodetector is typically evaluated using key parameters, including external quantum efficiency, responsivity, detectivity and transient time response curve. A high-performance plasmonic photodetector should have high detectivity and responsivity with fast response. Whereas external quantum efficiency tells the spectra sensitivity of the device at a particular wavelength range. The key device parameters are discussed in the following section.

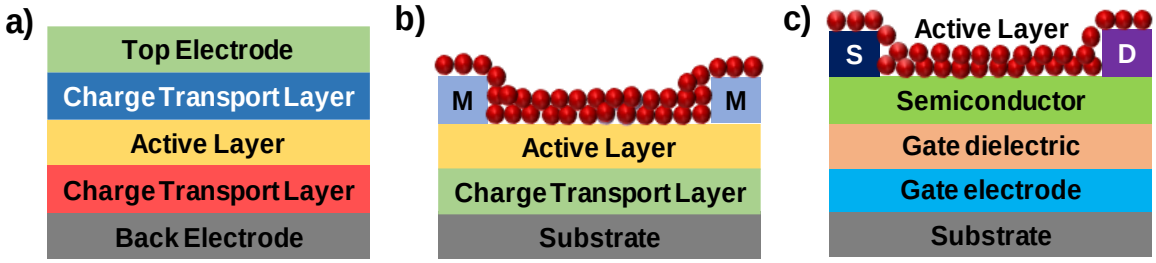

Figure 1.12 Schematic representation of different photodetector geometry **a)** photodiode **b)** photoconductor **c)** phototransistor.

External Quantum Efficiency (EQE)

EQE is the ratio of the number of charge carriers generated and collected by a photodetector to the number of incident photons on the device and measures the effectiveness of converting incoming photons into an electrical signal[106] and is given by the **equation 1.2-**

$$\mathbf{EQE} = \frac{\mathbf{J_{ph}}}{\mathbf{e\phi}} = \frac{\mathbf{J_{ph}} \times \mathbf{h\nu}}{\mathbf{eP_o}} \quad \text{---------- (1.2)}$$

where **h**, **ν**, **c**, $\mathbf{P_o}$, **e**, **ϕ**, $\mathbf{J_{ph}}$ and **λ** is plank constant, frequency, speed of light, output power, electronic charge, the flux of incident photon, photocurrent density and wavelength of the incident light respectively.

Responsivity (R_λ)

Responsivity is a measure of a photodetector's ability to convert incident light into an electrical signal, expressed as the output current or voltage per unit of incident light power.[106] It can be derived from EQE and is given by using **equation 1.3**-

$$R_\lambda = \frac{hc \times EQE}{e\lambda} \quad \text{---------- (1.3)}$$

Detectivity (D^*)

The detectivity of a photodetector quantifies its signal-to-noise ratio within a 1 Hz bandwidth, normalized to the detector's area. This critical parameter determines the sensitivity of the device. Taking into account that the primary source of noise originates from the device's dark current, the detectivity[107] can be expressed mathematically as shown in **Equation 1.4**-

$$D^* = R_\lambda/(2eJ_d)^{1/2} \text{---------- (1.4)}$$

where $\mathbf{J_d}$ denote the dark current density

1.7.2 Plasmonic Solar Cells

Photovoltaics have strong potential to play a crucial role in addressing environmental issues by providing sustainable energy solutions. In recent years, research has focused on.[108-110] For optimal light absorption, photovoltaic layers need to be sufficiently thick. However, indirect band gap materials like crystalline silicon require high-quality production to ensure effective carrier diffusion through thick layers. Currently, around 60-70% of solar cells use crystalline silicon wafers, which are typically 200-300 µm thick, and these wafers account for about 40% of the total cost of the solar cell.[111] In recent years, organic & perovskite

photovoltaics have developed in different research groups throughout the world. Still, power conversion efficiency needs to improve for that photovoltaics. Plasmonic NPs based photovoltaics has driven significant research into thin-film solar cells, in which film thickness is usually 1-2 μm and can be deposited on low-cost substrates such as glass or plastic. However, the major challenge with thin-film solar cells is their inefficient absorption of near band gap light.[112] The progress of solar cells are categorized in four different generations by the development of different materials, which is schematically presented in **Figure 1.13**.

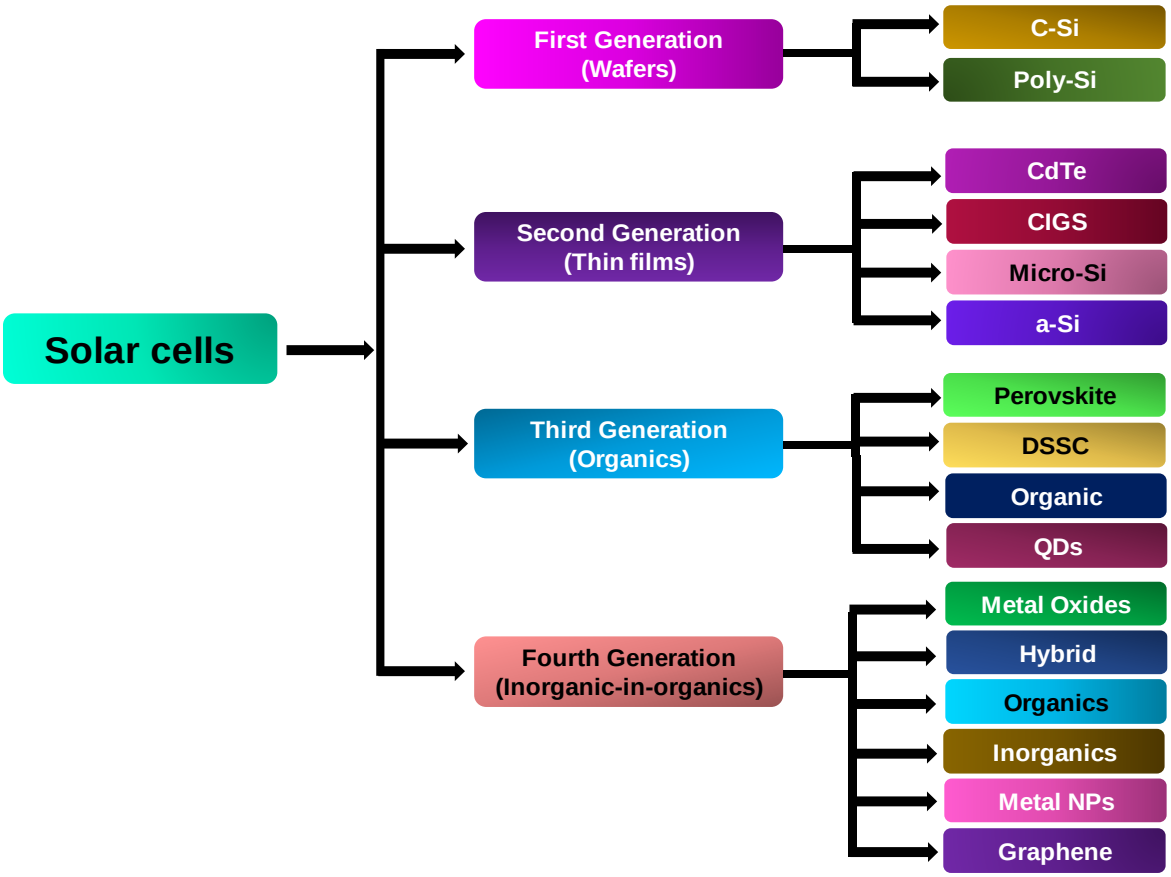

Figure 1.13 Schematic of four different generation solar cells with different materials.

Plasmonic NPs can significantly enhance the efficiency of solar cells by increasing the absorption of light in the active material.[113] These NPs exhibit LSPR, where the conduction electrons resonate with incident light and enhance strong EM fields around the NPs. This resonance enhances the local light intensity, broadening the absorption spectrum

and enabling the solar cell to capture more sunlight across various wavelengths. Additionally, plasmonic NPs scatter light, increasing the optical path length within the active layer, which is particularly beneficial in thin-film solar cells. This scattering effect enhances the probability of photon absorption, leading to greater exciton (electron-hole pair) generation. Besides, plasmonic NPs also produce "hot electrons" that are injected into the conduction band of the active material and contribute to additional photocurrent generation. The size, shape, and distribution of the NPs are essential to optimizing these effects without introducing recombination sites that could negate the benefits. Overall, plasmonic NPs play a key role in improving light absorption, enhancing charge carrier generation, and increasing the power conversion efficiency (PCE) of solar cells, especially in organic and perovskite thin-film photovoltaic devices.

1.7.3 Transparent Conductor & Heat Reflector

Transparent and flexible conductors play a vital role in the advancement of efficient, stretchable, and wearable optoelectronic devices.[114, 115] At the core of these systems lies transparent conductive film (TCF), which must maintain both high optical transparency in the visible spectrum and excellent electrical conductivity, even under significant strain deformation. A key challenge in developing flexible and stretchable electronics is the creation of cost-effective TCFs. Till now, indium tin oxide (ITO) has been the most widely used transparent conductor, offering high transmittance (>90%) and low sheet resistance (10–25 Ω/sq).[116, 117] However, ITO is inherently brittle and susceptible to cracking.[118] Additionally, the limited availability of indium, along with the high-cost sputtering techniques used in ITO film fabrication, makes it less suitable for low-cost and large-area applications.[119] For instance, in photovoltaics, the use of ITO in TCFs accounts for more than 50% of the total material and processing expenses. To address these limitations, alternative TCF materials and cost-efficient solution-phase coating processes are urgently required to enable the production of affordable, flexible electronics. Several emerging materials, including conductive polymers, metal grids, carbon nanotubes (CNTs), graphene, metal/metal-oxide interfaces, and random networks of metal nanowires (such as silver and copper nanowires), are being explored as potential next-generation replacements for ITO.[120-122] Solution processed plasmonic material shows emerging merits because of

their low cost, ease of scalable fabrication, and flexible/stretchable/wearable features to fabricate transparent conductors and heat reflectors.[123, 124] Transparent heat reflectors mainly reflect light in NIR/IR region and allow visible light to pass through the film, which is strongly applicable for the development of energy efficient smart windows.[125, 126] Fabrication of these novel TCF materials is possible via low-cost physical methods, including spin-coating, drop-casting, spraying, dip-coating techniques alongside with thermal or sputtering deposition techniques. However, these solution-processed techniques are difficult to scale up and are frequently employed for laboratory demonstrations. There is a pressing demand for a large-scale, large-area fabrication technique with industrialized potential.

1.7.4 Plasmonic Memristor

Plasmonic memristors, which combine the unique properties of plasmonic nanostructures and memristive behavior, hold significant promise for advanced applications in neuromorphic computing, high-density data storage, and optical signal processing.[127, 128] The integration of plasmonic nanostructures, such as metal NPs or nanowires, into memristive devices enhances their functionality by enabling strong light-matter interactions at the nanoscale. This results in the possibility of light-assisted switching, where optical signals can modulate the resistance states of the memristor, thereby enabling faster and more energy-efficient data processing. In neuromorphic computing, plasmonic memristors can mimic synaptic behavior with high precision, offering potential for artificial neural networks that process information similarly to the human brain but with much greater speed and efficiency. Additionally, the plasmonic enhancement can lead to more pronounced and stable resistive switching, improving the performance and reliability of the memristor. In optical signal processing, the ability to control memristive states with light opens avenues for integrated photonic circuits, where data can be processed and stored optically, significantly reducing the energy consumption and enhancing the speed of optical communications.

1.7.5 Surface Enhanced Raman Spectroscopy (SERS) Substrate

SERS is a highly sensitive and selective vibrational spectroscopy technique that leverages the inelastic scattering of photons by molecular species. Its advantages, including ultra-sensitivity, non-destructiveness, speed, and fingerprinting capabilities, make it ideal for analytical and sensing applications.[129, 130] Despite its potential, the high cost and low reproducibility of SERS signals limit its broader application. Developing versatile, stable, flexible and reusable nano-engineered SERS substrates offers a promising solution to these challenges. In recent time, plasmonic SERS-active nano-substrates with varied morphologies have gained significant attention due to their ability to create dense hot spots, enhanced stability, tunable morphology, and surface functionalization.

1.7.6 Chemical and Bio-Sensors

Chemical and biosensors are devices designed to detect and quantify specific chemical substances or biological entities, often at extremely low concentrations. These sensors are essential for a number of applications, such as industrial process control, food safety, healthcare diagnostics, and environmental monitoring.[131-133] Chemical sensors typically detect analytes like gases, pH, ions, or organic compounds, while biosensors are tailored for biological molecules such as glucose, proteins, DNA, or pathogens. The performance of these sensors hinges on their sensitivity, selectivity, and ability to produce rapid and reliable results, often necessitating the detection of trace amounts of analytes in complex matrices. Plasmonic materials have emerged as a transformative technology in the development of advanced chemical and biosensors. These materials exhibit LSPR and collective oscillations of surface electrons that occur when illuminated by light at specific wavelengths. This resonance amplifies the local EM fields near the material's surface, significantly enhancing the detection capabilities of sensors. When incorporated into chemical or biosensors, plasmonic materials enable ultra-sensitive detection by boosting signal intensities and allowing for the real-time monitoring of molecular interactions at the sensor surface. This sensitivity, combined with the ability to functionalize plasmonic surfaces for specific target recognition, makes plasmonic materials ideal for creating highly responsive and selective

sensors, pushing the boundaries of detection limits and enabling new applications in diagnostics and environmental monitoring.

1.7.7 Anti-bacterial Coating

Plasmonic MNPs like Ag, Au, and Cu are known for their unique antibacterial properties, largely driven by their ability to harness LSPR effect. Upon exposure to light, especially in the UV-Visible range, the excitation of plasmons leads to the formation of reactive oxygen species (ROS) such as hydroxyl radicals, superoxide anions, and singlet oxygen. These ROS can disrupt bacterial cell membranes, damage intracellular components like DNA and proteins, and ultimately lead to bacterial cell death. Furthermore, the small size and high surface area of plasmonic NPs enable them to penetrate bacterial cells more efficiently, enhancing their antimicrobial effects. In addition to oxidative stress, Ag^{+}/Au^{+} released from Ag/Au based plasmonic NPs, interact with bacterial enzymes and disrupt essential biological processes. These properties make plasmonic NPs highly suitable for applications in antibacterial coatings for medical devices, wound dressings, water filtration systems, food packaging, and even air filtration systems, providing a non-toxic, efficient, and long-lasting antibacterial strategy that is increasingly important in the fight against antibiotic-resistant bacteria.[134-137]

1.8 Motivation and Scope of the Thesis

Nanotechnology is the emergent technology of different areas of electronics and opto-electronics including display, sensor, photovoltaics and many other photonic applications. These materials have been developed for various purposes, including improve chemical and colloidal stability, fabrication of photovoltaic devices, prevention of bacterial infection, enhancement of photoluminescence, etc. which enables advanced photonic technologies. Particularly, plasmonic thin films have garnered significant attention in modern opto-electronics due to their ability to enhance light-matter interactions through LSPR. This enables superior optical, electronic, and sensing properties at the nanoscale. These thin films, typically made from metal NPs like Ag, Au, and Cu are used to improve device efficiency in applications such as transparent conductors, solar cells, transparent heat reflectors,

photodetectors, biosensors, and anti-bacterial coating. Their sensitivity to environmental changes makes them ideal for chemical and biological sensing, while their light-trapping capabilities enhance energy harvesting and photonic applications. As electronics continue to miniaturize and demand higher performance, plasmonic thin films offer a scalable, cost-effective solution with promising integration into next-generation technologies like quantum computing, wearable devices, and flexible electronics. With advancements in solution-based fabrication techniques, their future in energy-efficient systems, healthcare diagnostics, and photonics is particularly bright.

Researchers are increasingly interested in plasmonic thin film devices fabricated via solution-processed techniques because they offer a groundbreaking combination of cost-effectiveness, scalability, and versatility, particularly for large-area and flexible applications. Solution processes such as spin-coating, dip-coating, and inkjet printing allow for the mass production of high-performance plasmonic devices without the need for expensive equipment or controlled environments, unlike sputtering or lithography techniques. Solution processing also allows seamless integration of plasmonic nanoparticles with other materials, enhancing their optical and electrical properties, thus paving the way for high-performance, low-cost devices in industries ranging from renewable energy to healthcare. As research continues, the ability to fabricate these devices with precision and scalability is positioning solution-processed plasmonic thin films as a transformative technology in modern electronics.

To address the higher cost of these photonic technologies, We have introduced a novel cost-efficient technique where an ion-conducting metal oxide (ICMO) ceramic is used as initial material. This ceramic contains some light ions like Li^+, Na^+, K^+, etc. and these mobile ions can move through the crystal channel easily. By taking advantage of these mobile ions, We have chemically implanted conducting ions like Ag or Cu inside the dielectric matrix. This innovation helps to fabricate plasmonic thin film with much more stability, making it feasible for multi-functional photonic applications. To utilize this phenomena, We have successfully fabricated an ion conducting dielectric $Li_4Ti_5O_{12}$ initially and then by doing surface chemistry, we have developed an Ag-TiO_2 plasmonic thin film. Using Ag-TiO_2 thin film, We have successfully fabricated a narrowband plasmonic hot electron-based photodetector

in photoconductor geometry. The device shows a very good detectivity with conclusive evidence of hot electron generation from the plasmonic part. This approach shows a record detectivity of a plasmonic photodetector with a photoconductor geometry.

Furthermore, by employing surface engineering with an ultra-thin plasmonic layer and Ag-TiO_2 thin film, I have successfully developed flexible transparent conductors, transparent heat reflectors, plasmonic solar cells, photodetectors, and active SERS substrates using a low temperature solution process and physical vapor deposition technique.

From the next chapter onward, the thesis carries forward detailed studies encompassing material characterization and device engineering, systematically addressing the experimental investigations and their outcomes in a structured manner.

Chapter 2

Experimental Methods:

Material Synthesis, Analysis with Device Fabrication, and Performance Evaluation

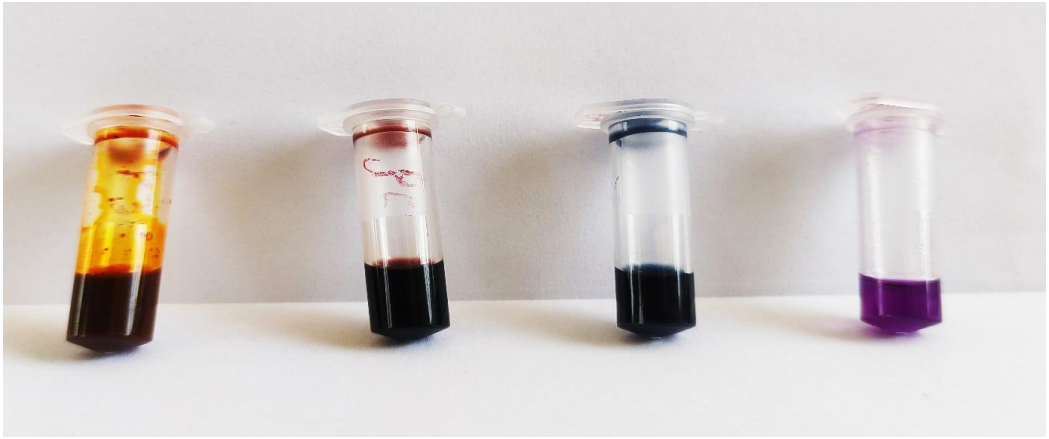

Chapter 2

In this chapter, I explore a variety of experimental methodologies integral to this thesis, including materials synthesis, characterization techniques, device fabrication processes, and device performance assessments. The materials synthesis section highlights three distinct approaches for producing ion-conducting oxide dielectrics, metal oxide semiconductors, and organic polymeric materials. The characterization of these materials, primarily in thin-film form, encompasses a comprehensive suite of analytical techniques. The device fabrication section covers the development of thin film heterostructure photodetectors, transparent conductors, transparent heat reflectors, SERS substrate, and organic photovoltaics. Finally, the electrical characterization focuses on critical analyses, including current-voltage (I-V), current-time (I-t), EQE, and SERS measurement, offering key insights into device behavior and performance.

2.1 Materials Synthesis

In this thesis work, mainly three different types of materials have been synthesized via low-cost solution process method. These materials have included i) ion-conducting dielectric, ii) metal-oxide semiconductor, and iii) organic polymeric materials. The ion-conducting dielectric material is used as an initial material to synthesize plasmonic Ag-TiO_2 thin films. Various kinds of metal oxide semiconductors like SnO_2, SnO_2 NPs, ZnO, ZnO NPs, TiO_2 and TiO_2 NPs have been synthesized for different device applications. A non-conducting polymer, polymethyl methacrylate (PMMA), has been used as a protective layer for some particular devices. Organic dye rhodamine 6G (R6G) and vitamin B_{12} have been used as analytic molecules for SERS experiments. Organic polymer poly(3-hexylthiophene) (P3HT) and [6,6]-phenyl-C_{71}-butyric acid methyl ester ($PC_{71}BM$) are used as an active material. Conducting polymer poly(3,4-ethylenedioxythiophene) polystyrene sulfonate (PEDOT: PSS) is used as a HTL for the fabrication of photovoltaic devices. The solution process

method allows uniform molecular-level reactions, which allow single-compound thin film formation. The detailed synthesis process is outlined below.

2.1.1 Synthesis of Ion-Conducting Dielectric $Li_4Ti_5O_{12}$ Precursor Solution

An ion-conducting dielectric ($Li_4Ti_5O_{12}$) thin film has been deposited on a plastic substrate by a solution-processed technique. A two-step process has been adapted to produce a thin layer of $Li_4Ti_5O_{12}$. Initially, we take lithium acetate dihydrate [$LiOOCCH_3.2H_2O$] (acquired from Alfa-Aesar, 99% extra pure] and titanium (IV) butoxide [$Ti(OC_4H_9)_4$] (acquired from Sigma-Aldrich, >97% pure) as precursor chemicals. Different molarity solutions of both are prepared in 2-methoxy ethanol (2-MEA) solvent and stirred each for 1 h at 700 r.p.m, and then both solutions are added in a 4:5 volume ratio to prepare a precursor solution of $Li_4Ti_5O_{12}$ ceramic product. The mixture is then vigorously stirred for the next 1 h at 700-800 r.p.m under ambient atmospheric conditions to yield a clear, transparent, and homogeneous solution. The synthesis step is schematically present in **Figure 2.1**.

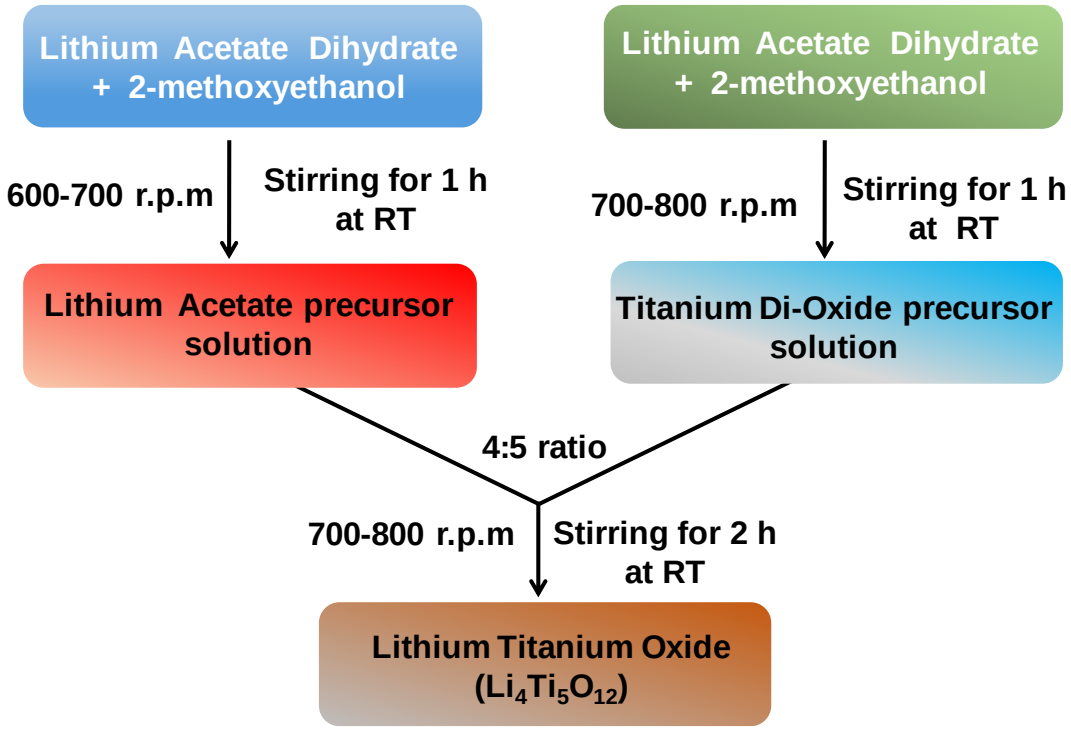

Figure 2.1 Synthesis of ion-conducting dielectric $Li_4Ti_5O_{12}$ by solution process route.

2.1.2 Synthesis of SnO_2 Precursor Solution

The Solution process SnO_2 has been employed as a metal-oxide semiconductor channel layer for photodetector fabrication. Different concentration precursor solution has been prepared by dissolving tin chloride [$SnCl_2$] (99.99%, obtained from Sigma Aldrich) in 2-MEA solvent, and the solutions are stirred for 30 minutes at 700-800 r.p.m before spin coating.

2.1.3 Synthesis of Precursor Solution of SnO_2 NPs

For the synthesis of SnO_2 NPs, at first, a required amount of tin chloride is mixed in distilled water to make 300 mM concentration precursor solution. During this solution preparation, cetrimide (Cetyl Trimethyl Ammonium Bromide) (CTAB) (purchased from Aseschem) is added that works as a reacting agent. This mixture was then stirred for 2 h to obtain a clear solution. To grow SnO_2 NPs, sodium borohydrate (NaBH4, 98% extra pure crystals, purchased from SRL) are added in this solution dropwise that forms a white precipitation of SnO_2 NPs. White part of this mixture is then cleaned by a centrifuge at 10000 r.p.m for 5 minutes and dried in a preheated hot plate at 60˚C for overnight. Then SnO_2 NPs are dispersed it in methanol to make the final SnO_2 NPs solution. Detailed synthesis process is schematically present in **Figure 2.2**.

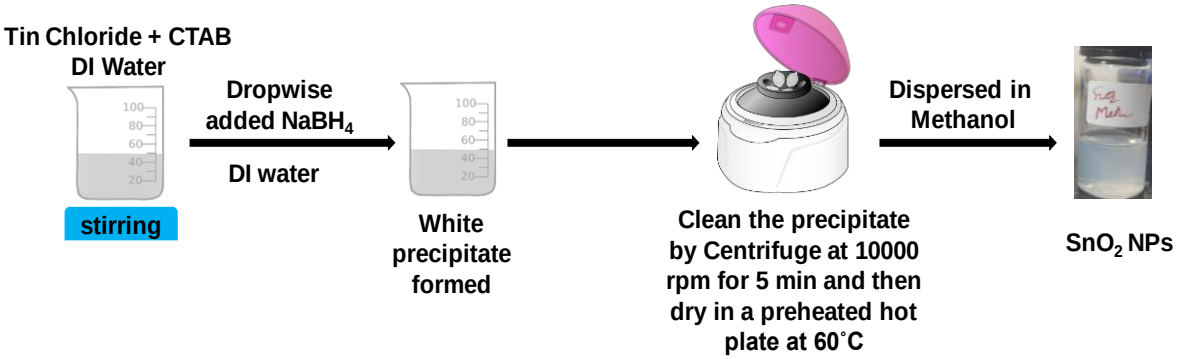

Figure 2.2 Schematic representation for the synthesis of SnO_2 NPs by solution process method.

2.1.4 Synthesis of Precursor Solution of ZnO NPs

For the preparation of colloidal ZnO NPs with a concentration of 20 mg/ml, zinc acetate dihydrate (purchased from Sigma-Aldrich, 99% pure) and potassium hydroxide (KOH) have been selected as the precursor salts. Each salt is individually dissolved in methanol and heated at 60°C for 10 min. The KOH solution is then injected into the Zinc acetate solution, resulting in the rapid clouding of the mixture. After 30 minutes, it clarified and stirred for 3 h at the same temperature. The solution is left undisturbed for 4 h to allow particle precipitation under normal atmospheric conditions. The clear top solution is carefully decanted, redissolved in methanol, and set aside for 16 h. The subsequent steps involve centrifuging the solution with the addition of acetone and rinsing with methanol, repeated three times. Finally, methanol is added to the remaining NPs in the centrifuge tube, followed by sonication. After allowing for any precipitation, the top solution constitutes the synthesized colloidal ZnO NPs. Detailed synthesis process is schematically present in **Figure 2.3**.

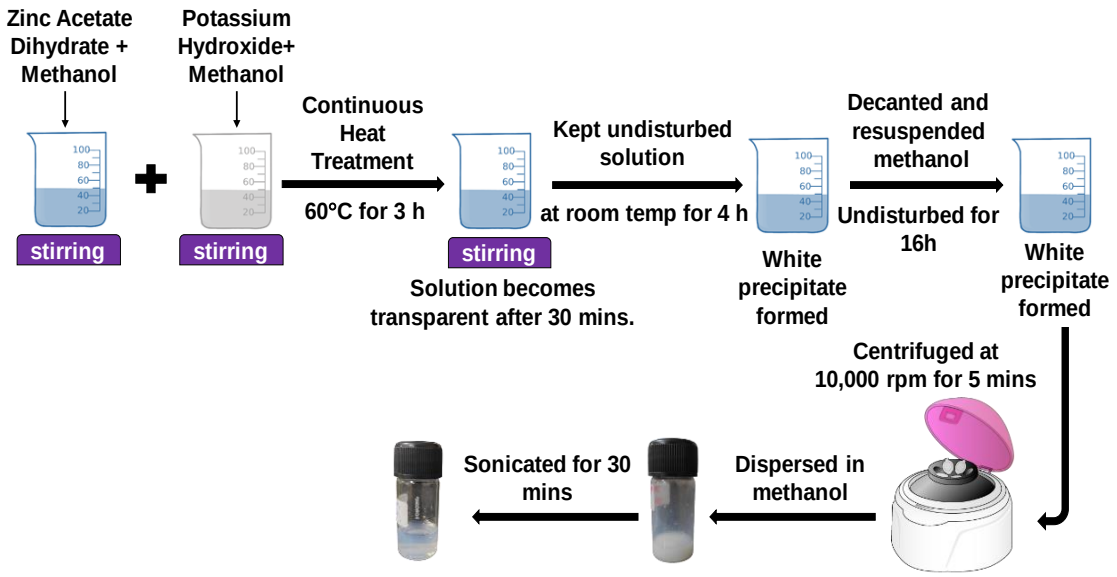

Figure 2.3 Schematic representation for the synthesis of ZnO NPs by solution process method.

2.1.5 Synthesis of Precursor Solution of TiO_2

To prepare the TiO_2 thin film via sol-gel method, 100 mM concentration of titanium (IV) butoxide [$Ti(OC_4H_9)_4$] (acquired from Sigma-Aldrich, >97% pure) solution is prepared by dissolving it in 2-MEA solvent and stirred at room temperature around 30 min at 600 r.p.m to prepare a transparent precursor solution.

2.1.6 Preparation of Precursor Solution of TiO_2 NPs

For the preparation of TiO_2 NPs, 18NR-T transparent titanium paste has been used as a source material which is dispersed in ethanol to prepare a colloidal solution of concentration 100 mg/ml. A stable colloidal solution is obtained after mixing it through an ultra-sonication process for 30 minutes. Then the solution is left for 10 minutes at room temperature before spin coating.

2.1.7 Preparation of PMMA Solution

A PMMA precursor solution is prepared by dissolving powder of PMMA (Sigma-Aldrich, molecular weight ~350,000), in chloroform solvent (SRL, extrapure AR). The dissolved process involved vigorous magnetic stirring at 1200 r.p.m for 4-5 h at room temperature. Subsequently, the prepared solution has been left undisturbed for 30 minutes to stabilize the solution before spin coating.

2.1.8 Preparation of PEDOT: PSS Solution

1.2 WT% of PEDOT; PSS solution is prepared by adding 80 ml DI water with pure solution and then sonicate it for 1 hr. using ultra-sonicator for 30 min. The solution is then stored in a cool & dark place before spin coating.

2.1.9 Preparation of P3HT Solution

Solution of P3HT polymer is prepared by dissolving the required amount of P3HT powder (Sigma-Aldrich) in chlorobenzene (Sigma-Aldrich). Prepared solution is stirred at 600-700 r.p.m at 60˚C for 1 h and then probe sonicate for 5 min to ensure proper mixing before spin coating the solution.

2.1.10 Preparation of $PC_{71}BM$ Solution

Solution of $PC_{71}BM$ organic polymer is prepared by dissolving the required amount of $PC_{71}BM$ powder (Sigma-Aldrich) in chlorobenzene solution. Prepared solution is probe sonicate for 30 min to ensure proper mixing.

2.1.11 Preparation of blended P3HT: $PC_{71}BM$ Solution

Solution of P3HT and P3HT: $PC_{71}BM$ are blended (1:1 ratio) in the same wt % and then probe sonicate it for 1 hr. at room temperature for proper mixing. After that, the mixture is stored at a cool and dark place for 20 min before use.

2.1.12 Solution Preparation of R6G Dye & Vitamin B_{12} Biomolecules

A parent solution with concentrations of 10^{-3} M for R6G and vitamin B_{12} is prepared using Milli-Q water. This solution is prepared through ultrasonic processing for a duration of 4-5 hours at ambient temperature. Subsequently, through the method of serial dilution, the concentrations of R6G and vitamin B_{12} are varied in the range from 10^{-6} M to 10^{-12} M which are derived from their respective initial concentration.

2.2 Substrate Cleaning Process

In device fabrication, the substrate cleaning process is a critical initial step to ensure the removal of contaminants from the surface of materials like silicon wafers, glass or plastic substrates. Effective cleaning is vital for the success of subsequent fabrication stages. The subsequent sections provide an explanation of the cleaning process for all the devices used in this thesis.

2.2.1 Glass Substrate Cleaning

For the device fabrication, borosilicate glass has been utilized as substrate. A widely adopted glass cleaning process is illustrated in the flow chart presented in **Figure 2.4**. At the beginning glass substrates of size 15 mm ×15 mm are kept inside piranha solution (concentrated H_2SO_4 and H_2O_2 in a 3:1 ratio) for 15 min to eliminate organic residues from the substrate's surface.[138] The substrates are then washed by using DI water for 10 minutes

with the help of an ultrasonic bath. Subsequently, substrates are transferred to a 2-propanol solution and kept inside an ultrasonic bath for 10 minutes, followed by a drying process with an air-blower.

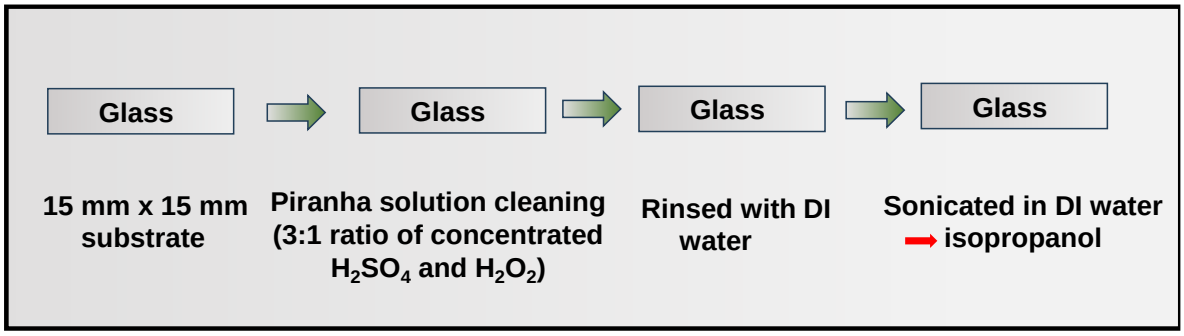

Figure 2.4 Schematic presentation of three-step solution cleaning of glass substrates.

2.2.2 Silicon Substrate cleaning

For the fabrication of thin-film devices, highly n-doped Si (n^+-Si) is also used as both substrates and bottom electrodes. For cleaning, a widely used three- step solution cleaning process is adopted, illustrated in **Figure 2.5**. Initially, the surfaces are cleaned with a soap solution (Extran) and subsequently rinsed with DI water. Following this, the substrates undergo a series of steps involving immersion in different media (such as DI water, acetone, and isopropanol) and ultra-sonication for 10 minutes in each step. The substrates are then dried by passing air and placed in a plasma cleaning chamber at 20 W for 10 minutes.[139] Plasma treatment enhances the hydrophilic nature of the surface and also removes residual organic materials, ensuring the fabrication of pinhole-free films.

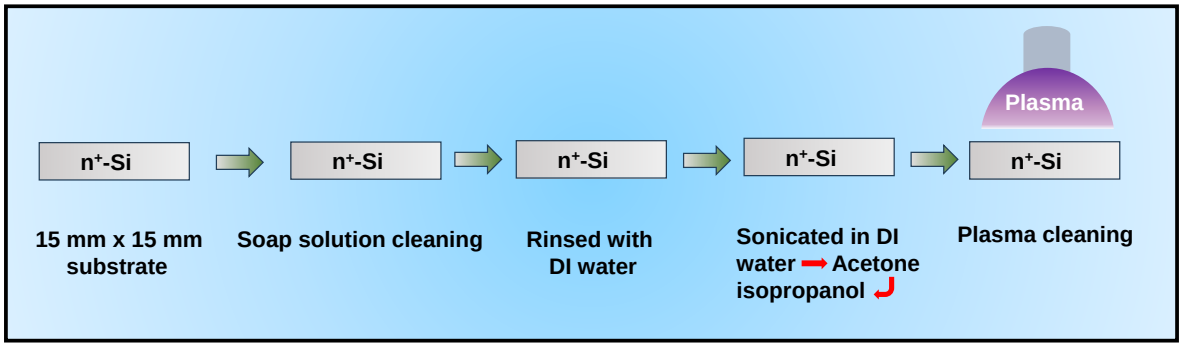

Figure 2.5 Schematic presentation of four-step solution cleaning step of traditional silicon cleaning followed by plasma treatment.

2.2.3 PET Substrate Cleaning

For flexible device fabrication, plastic PET substrates are used, and its step-by-step cleaning process is identical like silicon substrate cleaning process. At first, plastic substrate is cleaned with soap solution and then ultra-sonicate those substrates by DI water, acetone and isopropanol respectively each for 15-20 minutes. After that, the substrates are dried properly with an air-blower. Then those dried substrates are placed in an oxygen plasma cleaner at 20 W power for 10 minutes. This process is highly effective in removing organic and inorganic residues from the substrate's surface.

2.3 Device Fabrication

The subsequent sections provide a brief outline of all different device fabrication process used in this thesis.

2.3.1 Ag-TiO_2 Based Heterostructure Photoconductor

This photodetector has been fabricated on a glass substrate in a photoconductor geometry and the fabrication steps of this device has been shown schematically in **Figure 2.6**. At first, glass substrates are cleaned, and the cleaning process is described in **Section 2.2.1**. These clean glass substrates are spin-coated with a 300 mM SnO_2 precursor solution for 40 s at 4000 rpm and transferred on a preheated hot plate at 100°C. The substrates are then annealed for half an hour at 500°C to form the crystalline SnO_2 thin film. To get the desired thickness of SnO_2 layer, this process is repeated 3 times. A TiO_2 layer is then deposited on top of the SnO_2 film in a similar process. Therefore, the precursor solution of TiO_2 is spin-coated for 50 s at 5000 rpm and annealed at 500°C for 30 min to grow a highly crystalline layer. The photoactive Ag-TiO_2 nano-Schottky junction thin film has been grown on top of this glass/SnO_2/TiO_2 substrate. For this Ag-TiO_2 thin film deposition, antecedent solution of LTO is spin-coated over these substrates for 30 s at 3000 rpm and then annealed at 550°C for 1 hr. to form a crystalline surface. Those crystallization films are submerged in a 100 mM $AgNO_3$ solution for 1 hr. to exchange Li^+ of LTO film with Ag^+ of the solution that forms $Ag_4Ti_5O_{12}$. Following this ion-exchange procedure, the samples are rinsed with DI water to eliminate any remaining $AgNO_3$ from the surface of the film. After washing, the substrates are immersed in a 300 mM $NaBH_4$ solution at ambient temperature for 1 hr. which changes

the color of the substrate from transparent to yellowish. Throughout this process, Ag^{+} has been transformed to metallic silver (Ag^{0}) to make Ag-NPs, and the initial $Ag_4Ti_5O_{12}$ crystal is transformed to TiO_2 to form the final Ag-TiO_2 nano-Schottky junction thin film. **Equations** (**2.1** & **2.2**) show the chemical processes of this ion exchange and reduction procedure, respectively. After reduction, the films are cleaned by dipping inside DI water to eliminate any remaining $NaBH_4$ solution from the surface of the film.[140] Finally, silver electrodes (electrode area ~ 0.84×0.84 mm^2) are deposited by thermal evaporation on top of this glass/SnO_2/TiO_2/Ag-TiO_2 film through a shadow mask process.

Ion-exchange and reduction reaction:

$$Li_4Ti_5O_{12} + 4\,AgNO_3 \xrightarrow{Li^+ \longrightarrow Ag^+} Ag_4Ti_5O_{12} + 4\,LiNO_3 \qquad \text{-------} \quad (2.1)$$

$$Ag_4Ti_5O_{12} + NaBH_4 \xrightarrow{Ag^+ \longrightarrow Ag^0} 4Ag\text{-}5TiO_2 + NaBO_2 + 2H_2 \qquad \text{------} \quad (2.2)$$

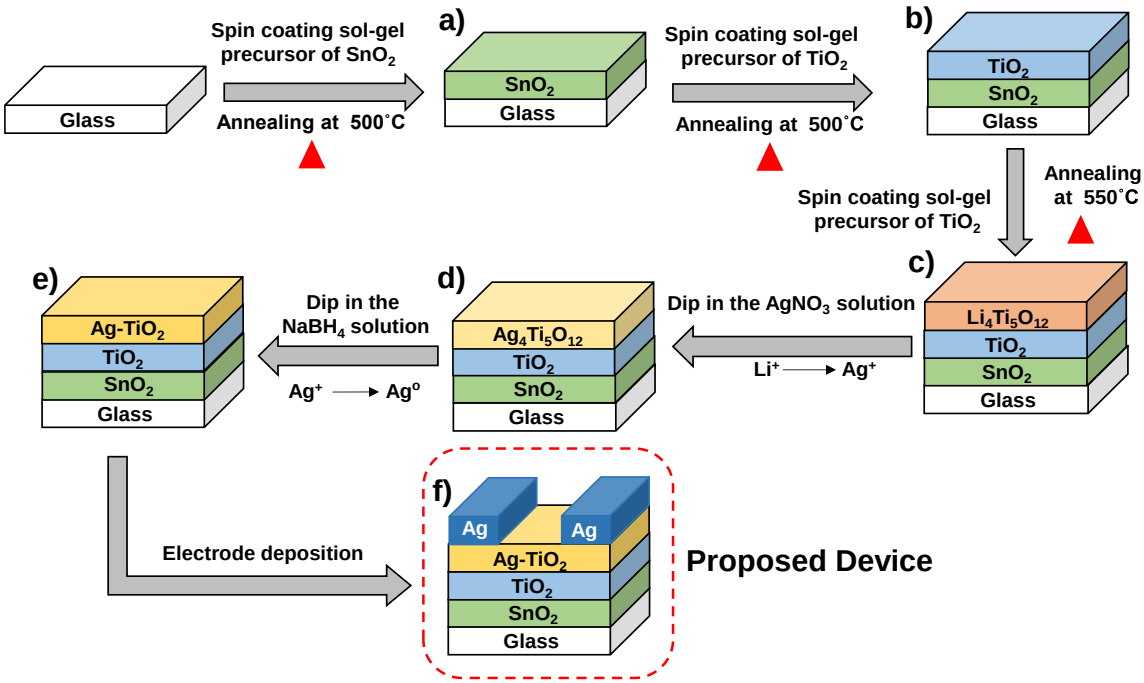

Figure 2.6 Depicts the six-step growth process of an in situ grown Ag-TiO_2 thin film-based photodetector : **a)** SnO_2 thin layer on glass substrate via spin coating of a sol-gel precursor followed by annealing **b)** spin coating of TiO_2 thin film precursor followed by annealing at 500°C **c)** spin coating of LTO precursor and 1 hr. annealing at 550 °C to achieve polycrystalline LTO thin film **d)** Li^+ ions are exchanged with Ag^+ ions in an ion-exchange

process to form $Ag_4Ti_5O_{12}$ **e)** reduction process which reduces Ag^+ ions into Ag^0 to form Ag-TiO_2 thin film containing Ag NPs inside the TiO_2 matrix **f)** finally Ag electrode is deposited on top for electrical contact.

2.3.2 Ag/Ag-TiO_2 based Transparent Conductor (TC) & Transparent Heat Reflector (THR) Film

The TC & THR thin film has been fabricated on a plastic PET substrate which is schematically presented in **Figure 2.7**. In this fabrication process, at the beginning, plastic substrates (20×20 mm^2) are cleaned, and cleaning process is mentioned in **Section 2.2.3**. Then the precursor solution of LTO is spin-coated over the clean substrates for 30 s at 3000 rpm and immediately kept on a hot plate at 100^{o}C. Subsequently, UV light of intensity ~ 9 W/m^2 is illuminated from that top side of the hotplate and keep it for 1 hr. This combined heating and UV illumination enable us to deposit crystalline LTO thin film at 100^{o}C. However, without using UV light, it is required 550^{o}C annealing to achieve this crystalline phase of LTO where we can't use common plastic PET as a substrate. These crystalline LTO films are then immersed in a 100 mM $AgNO_3$ solution for 1 hr. where Ag^+ of the solution are exchanged with Li^+ of the film that convert LTO thin film to $Ag_4Ti_5O_{12}$ thin film which subsequently convert to Ag-TiO_2 film due to the formation of Ag cluster inside oxide film. The reduction of Ag^+ to Ag^0 occurs due to the unstable nature of $Ag_4Ti_5O_{12}$. Moreover, the residual part of the oxide film also converted to TiO_2, resulting an Ag-TiO_2 thin film. These individual Ag NPs and TiO_2 phases have been identified through XRD study which is discussed later. Following the ion-exchange process, the samples are rinsed with DI water to wash any excess $AgNO_3$ from the film's surface. The chemical reaction of this process is illustrated in **Equation 2.3**. After that, 10 nm Ag thin film is deposited on the top of the Ag-TiO_2 thin film using a thermal evaporator to get a TC or THR film. Finally, a very thin layer of PMMA polymer is deposited over the 10 nm Ag/Ag-TiO_2 film by the spin-coating method (75 mg/mL,1000 rpm for 30 s) to provide better chemical and air stability of the prepared film.

Ion-exchange reaction:

$$Li_4Ti_5O_{12} + 4AgNO_3 \xrightarrow{Li^+ \longrightarrow Ag^+} \begin{matrix} Ag_4Ti_5O_{12}\ (unstable) + 4LiNO_3 \\ \downarrow \\ Ag\text{-}TiO_2\ (stable) \end{matrix} \quad \text{-------} \quad (2.3)$$

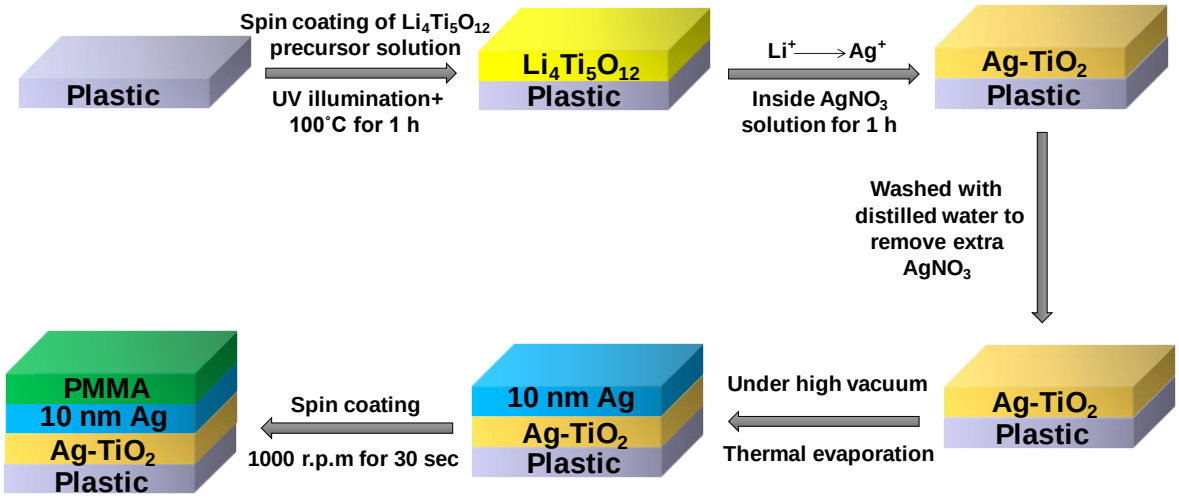

Figure 2.7 Schematic presentations of lateral growth of 10 nm Ag/Ag-TiO_2/plastic TC or THR film through low temperature annealed (100˚C) process. PMMA is used as a top layer to protect the film from oxidization.

2.3.2.1 10 nm Ag/Ag-TiO_2 TC Film based self-bias Photodetector Device

Furthermore, these fabricated 10 nm Ag/Ag-TiO_2 TC thin film have been used as transparent electrode to develop plasmonic photodetectors in a photodiode geometry which is schematically represented in **Figure 2.8**. For this device fabrication, n^+-Si has been taken as an initial substrate. At first, traditional n^+-Si substrates are properly cleaned, and the cleaning process is described in **Section 2.2.2**.100 mM precursor solution of LTO is spin coated over the clean substrate for 30 s at 3000 rpm followed by a drying process at 100°C on a hot plate. Then UV light has been illuminated by keeping the samples on a hot plate at 100°C for 1 hr. to form the crystalline LTO thin film. After that, samples are dipped in a 100 mM $AgNO_3$ solution for 1 hr. where Ag^+ of the solution are exchanged with Li^+ of LTO thin film. Following the ion-exchange procedure, the samples washed with DI water to remove any excess $AgNO_3$ from the film's surface. Finally,10 nm Ag is deposited in selected areas of the ion-exchanged thin film through a shadow mask by using a thermal evaporator technique.

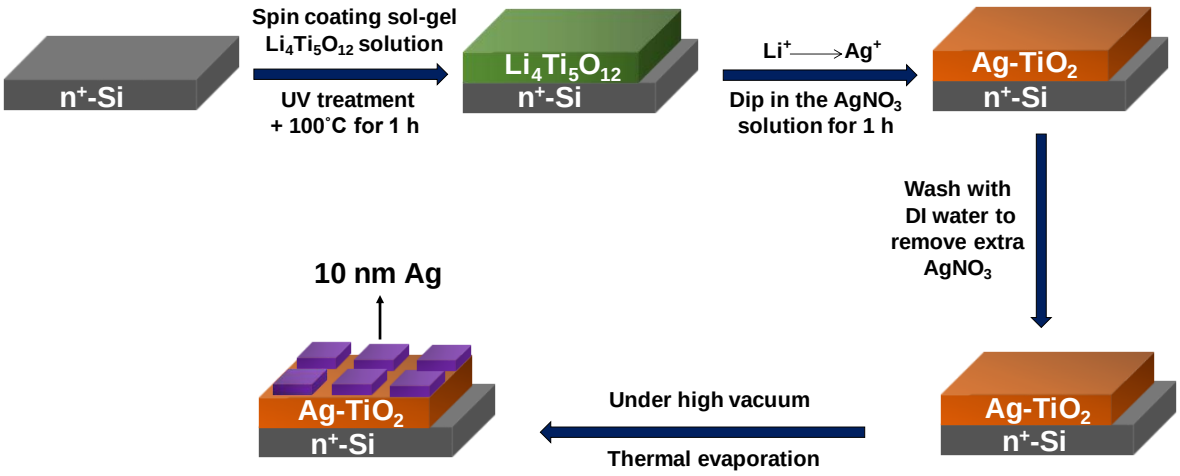

Figure 2.8 Schematic presentation of the proposed photo-diode device using fabricated 10 nm Ag/Ag-TiO_2 thin film as a transparent electrode.

2.3.3 Bimetallic Au-Ag based TC & SERS Active Thin Film

The bimetallic Au-Ag TC thin film has been fabricated on a plastic PET substrate which is schematically presented in **Figure 2.9**. The cleaning process is mentioned in **section 2.2.3**. At first, the precursor solution of as prepared SnO_2 NPs is spin-coated over the clean PET substrates for 30 s at 3000 rpm and immediately kept on a hot plate at 100^{o}C for next 30 min. After that, film is cooled to room temperature and then spin-coated with LTO precursor solution at 3000 rpm for 30 s. Then again, film is kept in a pre-calibrated hot plate for next 1 hr. under UV light explorations. UV light of intensity ~ 0.9 mW/cm^2 is illuminated from that top side of the hotplate. This combined heating and UV illumination enable us to deposit crystalline LTO thin film at 100^{o}C. After that, same ion-exchange procedure has been done where Ag^+ of the solution are exchanged with Li^+ of LTO thin film, to form Ag-TiO_2 thin film. The whole process is mentioned earlier in **Section 2.3.2**. The chemical reaction of this process is illustrated earlier in **Equation 2.3**. Finally, 4 nm Au thin film is deposited on the top of the film using a thermal evaporation technique to get the final Au-Ag based bimetallic TC thin film, which is also used as an active SERS substrate.

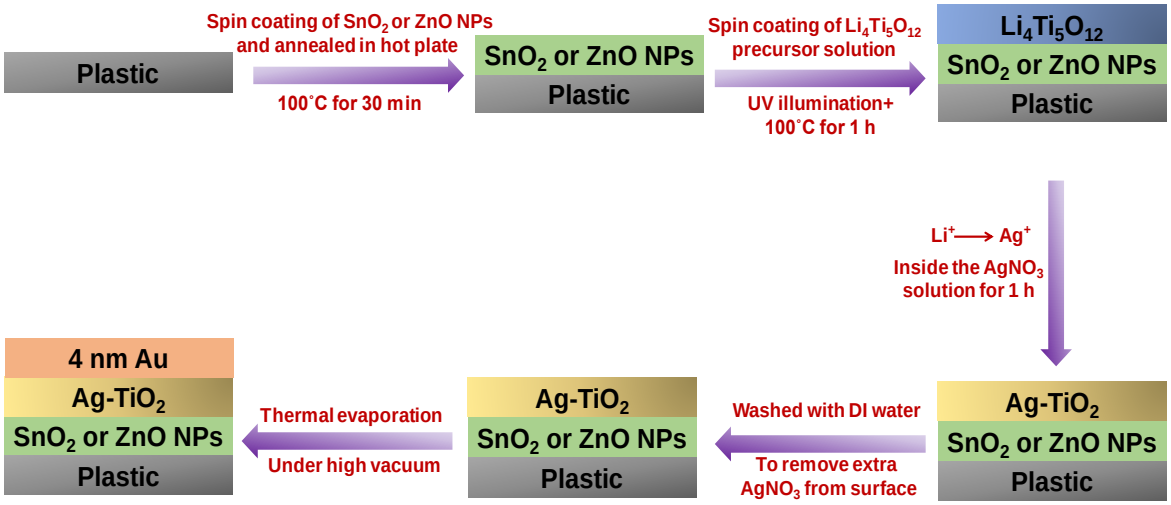

Figure 2.9 Schematic presentation of fabricated Au-Ag bimetallic TC thin film on plastic PET substrate via low temperature (100^{o}C) synthesis route

2.3.3.1 Bimetallic Au-Ag based TC Film for Self-Bias Photodetector

The Au-Ag bi-metallic TC film is further used for the fabrication of flexible plasmonic photodetectors in a photodiode geometry (step-by-step device configuration is shown in **Figure 2.10**). Initially, plastic PET has been taken as a substrate. The whole cleaning process is mentioned in **Section 2.2.3**. Following the earlier step, we have developed Au-Ag bimetallic TC film at top of the plastic substrate which is mentioned earlier in **Section 2.3.3**. And after that a very thin layer of TiO_2 NPs is spin coated in a specific area at 3000 rpm for 30 s and followed by annealed at 100°C for 30 min to make the film crystalline. In next step, for better transport of charge carrier to the top electrode, SnO_2 NPs is coated over it at 3000 rpm for 30 s and followed by annealed at 100°C for 30 min. Finally, LiF/Al is deposited as a top metal electrode with specific mask design to develop flexible plasmonic photodetector with photo diode geometry.

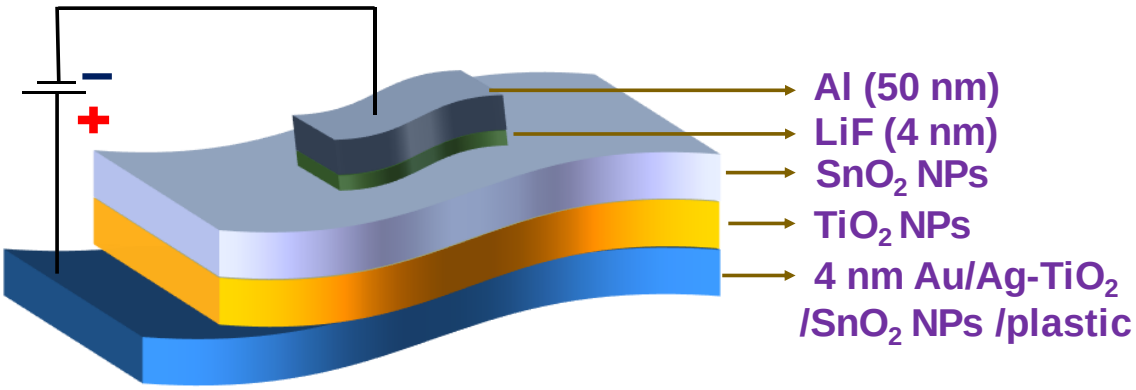

Figure 2.10 Schematic diagram of hierarchical architecture of Au-Ag TC film based flexible photodetector device.

2.3.3.2 Bimetallic Au-Ag TC Film for Plasmonic Organic Solar Cell

Furthermore, as synthesized Au-Ag bimetallic TC thin films have been used as a transparent back electrode to develop inverted plasmonic organic solar cells (device structure shown in **Figure 2.11**). Device is fabricated on plastic substrate (cleaning process is described in **Section 2.2.3)**. Firstly, using the initial step we developed an Au-Ag-based bimetallic TC film onto the plastic substrate. Next, as a HTL layer, PEDOT: PSS of 1.2 wt% is spin-coated at 1500 rpm for 40 s and annealed at 120˚C for 30 min under vacuum chamber. Now, as an active layer,15 mg/ml of only P3HT and blended P3HT:$PC_{71}BM$ (weight ratio 1:1) polymeric solution are used. Each solution is spin-coated at 1000 rpm for 60 s to get the desired thickness of the active layer and after spin coating sample is immediately annealed at 130˚C under vacuum chamber for 30 min. Next, as an ETL, SnO_2 NPs is spin-coated at 3000 rpm for 30 s and annealed at 120˚C for 30 min. Finally, 4 nm LiF/80 nm Al is deposited using thermal evaporator for top electrode. Here, LiF is used as an interfacial electron ejecting layer which also helps to reduce the overall work function of Al electrode.

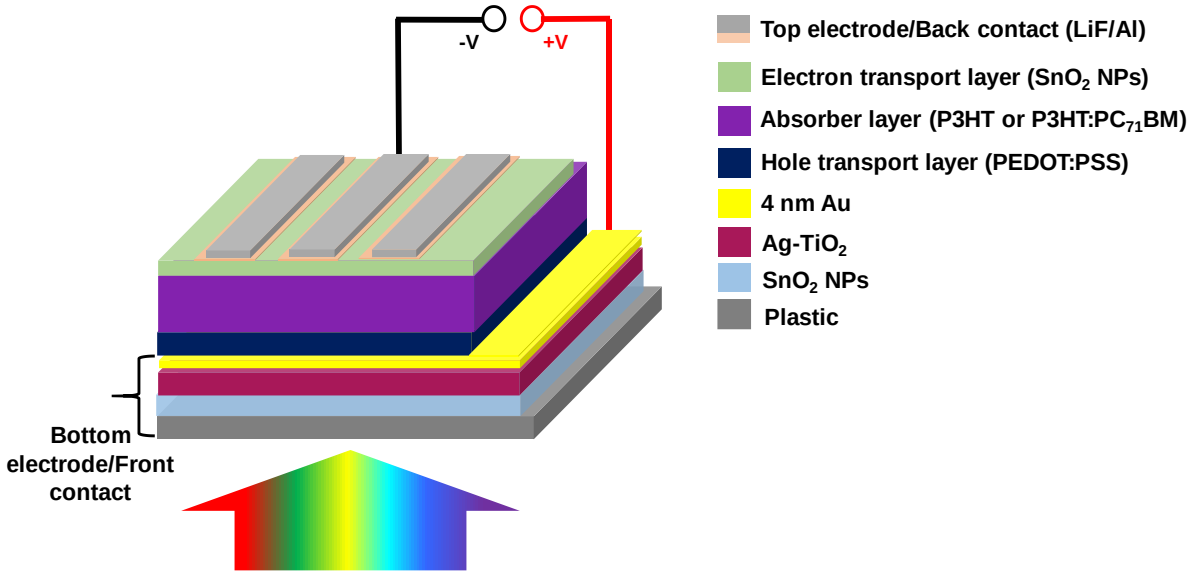

Figure 2.11 Schematic diagram of Plasmonic Organic Solar cells using Au-Ag bimetallic TC film as a back electrode.

2.4 Material Characterization

2.4.1 X-Ray Diffraction

A wide angle grazing Incidence X-Ray Diffraction (GIXRD) integrated with a multi-temperature chamber and a graphite monochromator with Cu-Kα radiation is performed using a Rigaku SmartLab system (wavelength of 0.154 nm) has been utilized to analyze the X-Ray Diffraction of as-prepared thin film samples. The generator has operated at 45 kV and 200 mA. The samples have been held on the sample holder, and the scans have been performed at a diffraction angle ranging from 20° to 60°, at a scan rate of 2°/min.

2.4.2 UV-Vis Spectroscopy

The UV-Visible spectroscopic properties of the prepared thin films have been measured using the JASCO V-770 spectrophotometer. This UV-Visible spectroscopy technique has been applied to evaluate the optical absorption of prepared plasmonic thin films.

2.4.3 Reflectance & Transmittance Spectra

Reflectance and transmittance study of plasmonic thin films have been studied by using an external quantum efficiency cum reflectance/transmission measurement set-up (Enlitech QE-R EQE).

2.4.4 Photoluminescence Spectroscopy

Photoluminescence (PL) spectra of the prepared thin films within the wavelength range of 300-550 nm have been measured using the F-4600 FLSPECTOROPHOTOMET. Using this technique, we can detect the emitted photons of plasmonic thin films at different wavelengths.

2.4.5 Surface Enhanced Raman Spectroscopy

The vibrational characteristics of SERS substrates are studied by Raman spectroscopy using an AIRIX Corp. STR 300 spectrometer, with a 532 nm excitation laser, 100× objective lens and 1200 cm^{-1} gratings. To avoid degradation of analyte biomolecules, low laser power (0.69 mW for 633 nm and 1.15 mW for 532 nm) is used for SERS study.

2.4.6 Atomic Force Microscopy

The surface morphology study of plasmonic thin films is essential to understanding the metal/dielectric interface, which plays a crucial role in the performance of thin-film photonic technologies. The rough interface acts as a transport barrier, hindering the transportation of charge carriers in semiconductors. Therefore, creating a high-quality plasmonic thin film with very low roughness is crucial. An atomic force microscopy instrument with powerful nanoscale resolution has been used to investigate the surface roughness of the prepared plasmonic thin film. The distance between the cantilever tip and the sample's surface has determined the operating mode of the atomic force microscope (AFM). The NT-MDT multimode AFM (Russia) (atomic scale resolution ~ 2 nm for HOPG), controlled by a Solver scanning microscope controller, has been used to scan the bulk surface morphology of the samples. The root mean square roughness of a plasmonic thin film has been calculated using the semi-contact mode of AFM. For this mode, a single-beam cantilever with a tip of length (l), width (w) and thickness (h) of 123 μm, 35 μm and 1.84 μm is mounted having a resonant frequency range between 240 to 255 kHz and a corresponding spring constant of 11.5 N/m.

2.4.7 High Resolution Scanning Electron Microscopy

The High-Resolution Scanning Electron Microscope (HR-SEM) is a type of electron microscope that uses a focused beam of electrons to scan the surface of a sample for image acquisition. Electrons interact with atoms in the sample, producing diverse signals that transmit information about the sample's surface topography and composition. The electron beam has been scanned in a raster pattern, and the combination of beam position and signal intensity has created an image. Generally, in SEM studies, secondary electrons generated by atoms stimulated by the electron beam have been detected using a secondary electron detector (Everhart-Thornley detector). The quantity of detectable secondary electrons, and hence the signal intensity, has been influenced by specimen topography and other factors. The HR-SEM model NANOSEM 450, FEITM, (resolution 100 nm in secondary electron imaging mode) has been utilized to examine the morphology and cross-sectional view of the samples. For the elemental analysis and color mapping, energy dispersive spectroscopy (EDX) studies have been performed using EDX analysis equipment attached with the HR-SEM instrument.

2.4.8 High Resolution Transmission Electron Microscopy

High resolution transmission electron microscopy (HR-TEM) is a method of imaging that allows the observation of a sample's crystallographic structure at the atomic level. In contrast to conventional microscopy, this does not use absorption to form images; instead, images are created through interference in the image plane. The electrons interact with the sample individually, and the electron wave passes via the imaging system, where phase change takes place. The recorded image does not directly represent the sample structure. Because of its extreme resolution, this approach is an excellent tool for exploring nanoscale material characteristics. The size of NP, particle distribution and crystallite nature of different NPs have been analyzed by HR-TEM, Tecnai G2 20 TWIN unit (point-to-point resolution 0.24 nm and a lattice resolution of 0.10 nm).

2.5 Electrical Characterization

2.5.1 Photoconductor: Current Vs Voltage (I-V) Characterization

Photoconductivity is an electro-optical phenomenon in which a material exhibits increased electrical conductivity upon absorbing EM radiation, such as UV-Vis or NIR light. Photoconductor is a two-terminal lateral device. When incident light interacts with the material, photons are absorbed by electrons in the valence band, exciting them to the conduction band and leaving behind holes. This process generates additional charge carriers in the form of electrons and holes, resulting in an overall increase in electrical conductivity. The enhancement in conductivity is thus directly attributed to photoexcitation in the carrier channel. Here, for the measurement of photoconductor, an Agilent B1500A semiconductor parameter analyzer is employed. Electrical contact with the device electrodes is established using a probe micromanipulator. All measurements are conducted under ambient atmospheric conditions. The formula for calculation of photocurrent generation is given in **Equation 2.4** and given by –

$$I_{ph} = I_{light} - I_{dark} \text{ ---------- (2.4)}$$

2.5.2 Photodiode: Current Vs Voltage (I-V) Characterization

A photodiode is a two terminal vertical device that converts incident light into an electrical current through the principle of the photoelectric effect. Unlike a photoconductor, which relies on increased conductivity due to photoexcitation, a photodiode operates as a two-terminal junction device, typically in reverse bias mode, to generate a photocurrent proportional to the intensity of incident EM radiation. When incident light interacts with the depletion region of the photodiode, photons are absorbed by electrons in the valence band, exciting them to the conduction band and generates electron-hole pairs. The built-in electric field of the depletion region facilitates the separation of these charge carriers, generating a photocurrent. This photocurrent is collected at the electrodes, leading to a measurable response. Considering the I–V curves, one can utilize the thermionic emission (TE) theory to calculate photodiode parameters. According to TE, using the experimental I-V graph we can calculate the main diode parameters such as ideality factor (n), barrier height (Φ_b), and saturation current (I_o). The relationship between I and V is represented by the following **Equations (2.5 & 2.6)[**141, 142**]**:

$$I = I_o \left[\exp\left(\frac{qV}{KT}\right) - 1\right] \text{ ---------- (2.5)}$$

$$I_o = AA^*T^2 \exp\left(-\frac{q\Phi_b}{KT}\right) \text{ ---------- (2.6)}$$

where A is the effective area of the photodiode, A^* is the effective Richardson constant, q is the electronic charge, T is the room temperature in K, and k is the Boltzmann constant.

Even though finding an ideal rectifier contact is impossible, an ideal diode has an ideality factor of 1. Higher values of n than unity are caused by a number of circumstances. The high ideality factor is often shown due to the complex interplay of carrier generation, recombination, mobility, surface effects, and temperature. These factors introduce deviations from the ideal diode equation. The experimental values of Φ_b and n are determined by **Equations** (**2.7 & 2.8**) as follows[141, 143]:

$$\Phi_b = \frac{KT}{q} \ln\left(\frac{AA^*T^2}{I_0}\right) \text{ ---------- (2.7)}$$

$$n = \frac{q}{KT}\left(\frac{dV}{d\ln I}\right) \text{ ---------- (2.8)}$$

For the measurement of the photodiode's I-V characteristics, the same Agilent B1500A semiconductor parameter analyzer is employed. Electrical contact with the device terminals is established using a probe micromanipulator. All measurements are conducted under ambient atmospheric conditions to evaluate the device's performance in real-world environments.

2.5.3 Photovoltaics devices: Current Density Vs Voltage (J-V) Characterization

The J-V characteristics of the fabricated solar cells are measured in both dark and illuminated conditions to evaluate their performance. These measurements are conducted using a solar simulator (Photoemission Inc., USA, Class AAA) under the standard Air Mass 1.5 Global (AM 1.5G) solar spectrum at room temperature, with an Keithley 2450 source meter applying as an external potential bias. In forward bias, electrons are injected from the photoanode into the device, while in reverse bias, electrons are injected from the counter electrode side. An ideal solar cell exhibits typical diode behavior under dark condition which is shown in

Figure 2.12 (red line). At low applied voltage, minimal or no current flows due to the low charge carrier density in the dark. As the applied voltage increases, charge density rises, leading to an upward shift in the quasi-Fermi level within the metal oxide. When the quasi-Fermi level aligns with the conduction band of the active material, electron transport to the back electrode becomes unhindered, increasing the dark current. This behavior confirms that dark current is primarily governed by electron-hole recombination, which dictates charge carrier dynamics in the absence of illumination.

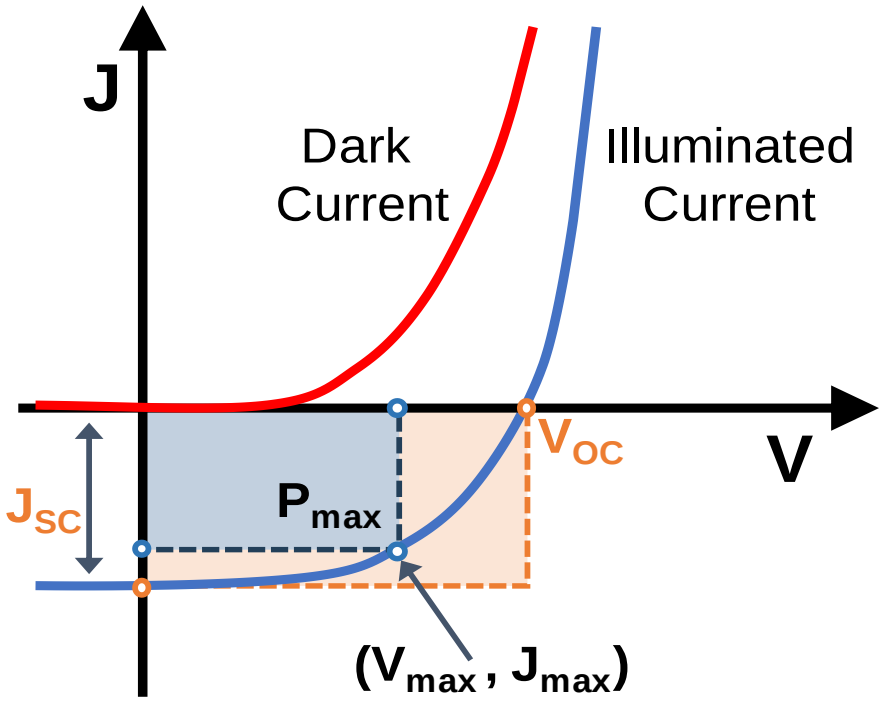

Figure 2.12 J-V curve of typical photovoltaics under dark (red line) and light (blue) illumination.

Under illumination, photocurrent is generated and flows opposite to the dark current, as shown in

Figure 2.12 (blue line). The J-V characteristics are governed by two competing processes: photocurrent generation and electron-hole recombination. At a low applied potential, most charge carriers are collected before recombination, resulting in a nearly constant photocurrent. As the applied potential increases, recombination dominates, reducing the photocurrent until it reaches zero, which is termed as open-circuit voltage (V_{oc}). At zero bias,

the photocurrent is termed the short-circuit current density (J_{sc}). The maximum of the power curve is called the maximum power point (P_{max}), and the corresponding voltage and current are denoted as J_{max} and V_{max}, described with **Equation 2.9.** The power conversion efficiency (PCE) is a key parameter for evaluating solar cell performance and is given by -

$$\mathbf{PCE} = \frac{\boldsymbol{P_{max}}}{\boldsymbol{P_{in}}} = \frac{\boldsymbol{J_{max} \times V_{max}}}{\boldsymbol{P_{in}}} \text{ ---------- (2.9)}$$

where P_{in} is the illuminated light intensity (100 mW/cm^2)

Another crucial parameter of a solar cell is the fill factor (FF), which represents the squareness of the I-V curve and is defined as (**Equation 2.10**)-

$$\mathbf{FF} = \frac{\boldsymbol{J_{max} \times V_{max}}}{\boldsymbol{J_{sc} \times V_{oc}}} \text{ -------- (2.10)}$$

Finally, utilizing all the factor, PCE is determined using **Equation 2.11** and is given by-

$$\mathbf{PCE} = \frac{\boldsymbol{J_{sc} \times V_{oc} \times FF}}{\boldsymbol{P_{in}}} \text{ -------- (2.11)}$$

2.5.4 Current Vs Time (I-t) Characterization

Transient photo response is another key parameter of a photodetector that implies how fast a device can respond to light and how promptly it can return to its original stage for detecting the next signal. Here, the transient response of photodetector device has been measured by measuring the current vs time (I-t) behaviour of the device. This is a two-probe measurement, and it has been utilized to calculate the response time (rise time and fall time) of the device under the influence of illumination of light. The time intervals needed for the photocurrent to increase from 10% to 90% of its peak value (τ_r) and for the response to decrease from 90% to 10% of its peak value (τ_f) are always used to define the device rise time (τ_r) and fall time (τ_f).

2.5.5 Quantum Efficiency Measurement

Quantum efficiency measures the ratio of collected charge carrier in the form of electrons to the number of incident photons. Quantum efficiency can be expressed as external quantum

efficiency (EQE) and internal quantum efficiency (IQE). The EQE measures how efficiently a photovoltaics or photodetector device converts incident photons into electrical current. The external quantum efficiency of a device generally follows the relation (**Equation 2.12**) [107]–

$$\mathbf{EQE\ (\%) = \eta_{abs} \times \eta_{gen} \times \eta_{coll}} \quad \text{---------- (2.12)}$$

Where η_{abs}, η_{gen} and η_{coll} are the absorption efficiency, e^{-}- h^{+} charge generation efficiency and charge collection efficiency of the charge transport layer, respectively.

Among these, η_{abs} has significant wavelength dependence. When a device is illuminated with light, electromagnetic waves flow through many layers of thin film devices and during this process, photons may be absorbed, reflected by the interface, followed by repeated reflections, or transmitted through the device. As a result, EQE tends to follow materials' optical absorption properties. However, this value includes photons lost through optical transmission and reflection.

While IQE measure excluded the losses due to the reflection of light, as a result IQE value is always greater compare to EQE value. IQE can be measured or extract from EQE value by using **Equation 2.13**-

$$\mathbf{IQE} = \frac{\mathbf{EQE}}{\mathbf{1-R}} \quad \text{---------- (2.13)}$$

where R is the reflectance of the device

Chapter 3

Solution-Processed Ag-TiO_2 Nanostructure-Based Schottky Junction Thin Films for Narrowband Hot-Electron Photodetectors

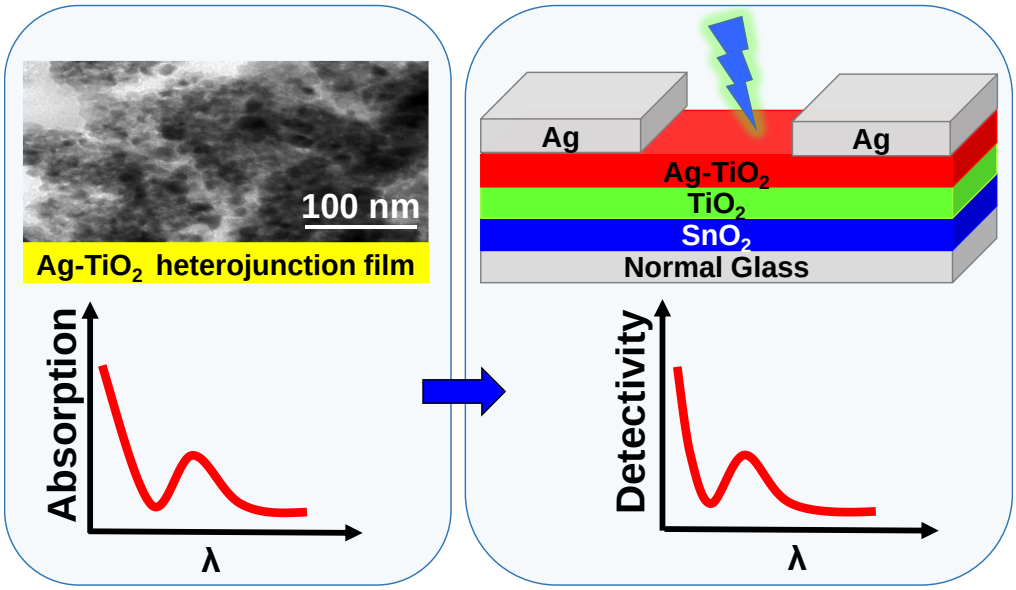

Chapter 3

This chapter mainly focuses on the results of plasmonic NPs based hot electron photodetector. It is not very easy to capture plasmonic hot electrons for photodetection in a photodetector. In this work, an in-situ grown Ag-TiO_2 nano-schottky junction thin film has been deposited by solution processed technique which contains a highly dense Ag NPs surrounded by TiO_2. This Ag-TiO_2 nano-Schottky junction has a low barrier height, high interface area with least interface state that enables efficient hot electron transfer to the CB of TiO_2, which is realized in the EQE data. This EQE data shows an intense photocurrent formation in the region of plasmonic absorption of Ag NP, indicating the primary contribution of hot electrons on photocurrent production. This photodetector has been fabricated in a glass substrate in photoconductor geometry that shows a peak detectivity of 3.19×10^{11} Jones at 420 nm with a response time of ~ 2 sec.

3.1 Introduction

Plasmonic hot-electrons are energetic electrons which are produced by the decay of surface plasmons in metal nanostructured materials.[144] A suitable combination of metal NP and semiconductor can form a low barrier height Schottky junction that can efficiently transfer plasmon induced hot electrons to the semiconductor, which convert photons to other forms of energy.[145, 146] A number of reports claim that the barrier height of these nano-Schottky junctions is much lower w.r.t their bulk combination, which also can be tuned by changing their nanostructure. These plasmatic hot electrons possess a broad range of applications, including photo-catalysis, photo-electrochemical water splitting, photovoltaic conversion, photodetection and so on.[147-150] The plasmonic hot electron-induced photocurrent needs to transfer to the semiconducting layer efficiently for its photovoltaic and photodetection application.[81, 151] Besides, the plasmonic absorption spectra depends on the shape and size of metal NPs and commonly shows a narrow band absorption for similar size metal

NPs.[152, 153] Therefore, a narrowband photodetector can be fabricated by efficient detection of a plasmonic hot electron and detection spectra can be tuned by varying the nanostructure.[154-156] However, due to the inefficient hot-electron charge transfer rate to the semiconducting layer, until now most of the plasmonic photodetectors show too poor detectivity to detect. In fact, most of the claim of plasmonic hot electron photodetector doesn't show EQE data to show the intense photocurrent generation in the plasmonic absorption region of the materials. Although, without showing this data, it's difficult to estimate the real contribution of hot electron in the overall photocurrent.

To date, most plasmonic hot electron photodetectors are based on Au/semiconductor Schottky diodes mainly because of the very high stability of Au nanoparticles.[157-159] Although, Ag NPs are very cost-effective metal and assumed to be a superior plasmonic element than Au because of their efficient surface plasmon effect. Besides, their plasmonic resonance wavelengths exist in the range of 400–480 nm and can have quite good stability. Hot electrons are formed in Ag nanocrystals through intraband excitation inside the conduction band (from occupied s-band to vacant s-band) due to its stronger intraband transition.[68, 72, 160] On the other hand, among different metal oxide semiconductors, n-type TiO_2 is considered as an attractive choice for various applications like electrochemical, photochemical and photovoltaic due to its extremely high physical and chemical durability.[161, 162] Besides, it is also commonly used as electron-accepting semiconductor in different heterostructure device where photo-generated electrons are required to separate promptly.[163, 164] Particular in Ag/TiO_2 heterostructure, energy band off-set for electron is quite low, which enable to transfer electron from Ag to the CB of TiO_2 very efficiently.[165] Therefore, Ag-TiO_2 heterostructure has been widely used for various applications including, photo-catalyst, photo-electro-catalysis, photodetectors, solar cell etc.[140, 166, 167] However, till now, there are very few reports where metal NPs are incorporated into TiO_2 nanostructures for the use of a plasmonic hot electron-based photodetector.[168] In most of the photodetector fabrication, expensive transparent electrode like indium tin oxide (ITO) or fluorine doped tin oxide (FTO) are used as substrate.[169] Besides, different physical vapor deposition techniques are used for such plasmonic photodetector fabrication which increases overall cast of fabrication.[170]

In this chapter, We fabricated an in-situ grown Ag-TiO_2 plasmonic hot electron photodetector fabrication through a solution processed technique where highly dense Ag NPs are embedded by TiO_2 semiconductor. To improve photodetector device performance, a TiO_2/SnO_2 heterojunction thin film is used as an underlying layer of this Ag-TiO_2 nanocrystals thin film. This photodetector has a fast response speed with a good narrowband detectivity that originated from plasmonic hot electron induced photocurrent and it is shown that the LSPR emission by Ag NPs and their subsequent transfer to the TiO_2 matrix by analyzing narrowband EQE of the device. To differentiate the removal of hot electrons by intraband excitation, EQE, absorption/reflection spectra and internal quantum efficiency (IQE) are investigated. An empirical model based on the energy band diagram has been proposed to explain the working principle and the underlying photo-physics of the device.

3.2 Experimental Section

3.2.1 Synthesis of Materials

The ion-conducting LTO dielectric, SnO_2, and TiO_2 semiconductors have been synthesized by a low-cost solution process technique. The detailed synthesis method is described in **Chapter 2 Sections 2.1.1, 2.1.2** and **2.1.5**, respectively.

3.2.2 Growth of Ag-TiO_2 Thin Film and Device Fabrication

The photodetector has been fabricated on a glass substrate in a photoconductor geometry and the fabrication steps of this device has been explained **Chapter 2 Section 2.3.1**, and schematically present in **Figure 2.6**. Four different type of device structure has been developed, which is shown in **Figure 3.1a-d)**. In each device, Ag electrodes (effective area ~ 0.84×0.84 mm^2) are deposited on top by thermal evaporation through a shadow mask technique.

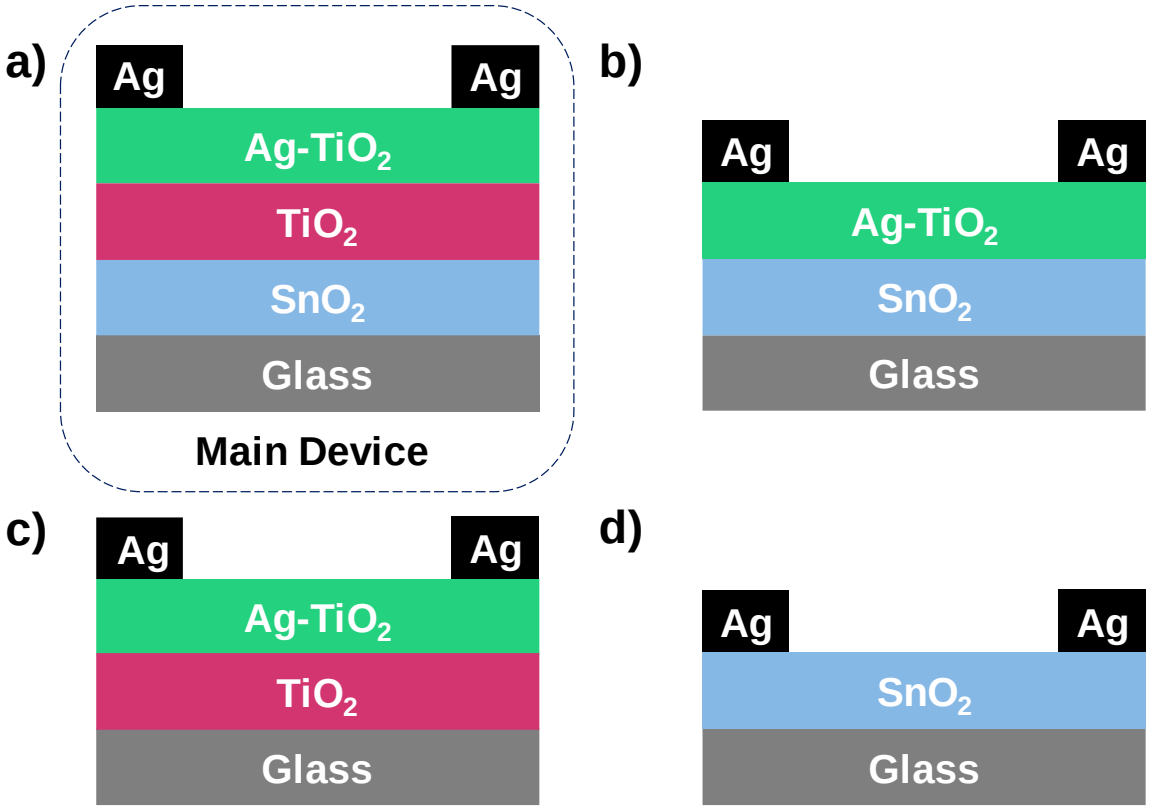

Figure 3.1 Schematic presentation of four different device structure **a)** Ag-TiO_2/TiO_2/SnO_2 layer (proposed device) **b)** with Ag-TiO_2/SnO_2 layer **c)** with Ag-TiO_2/TiO_2 layer **d)** with SnO_2 layer only**.**

3.3 Result and discussion

3.3.1 XRD, UV-Vis and PL Study

Step-by-step XRD pattern of Ag-TiO_2/TiO_2/SnO_2 thin films are depicted in **Figure 3.2a)**. The glass substrate is used as a reference, and the XRD data of the bare glass is subtracted from sample data to get the actual signal of the sample. The XRD pattern of the SnO_2 thin film annealed at 500˚C exhibits peaks generated from the (110), (101), (200), (211), and (310) planes which are located at 2θ of 26.31˚, 33.58˚, 37.55˚, 51.39˚ and 54.32˚ respectively (JCPDS file no. 411445). The thin-film XRD pattern of SnO_2/TiO_2 gives two additional intense peaks at 2θ ~25.01˚ and 47.76˚ which corresponds to (101) and (200) of TiO_2 (JCPDS file no. 2111272), indicating the anatase phase formation of TiO_2. Similarly, LTO/ SnO_2/TiO_2 film shows an additional intense peak at 2θ ~ 44.79˚ corresponds to LTO (400)

well matched with JCPDS file no. 490207. In case of multilayer device structure, we get all XRD peaks including the intense (111) & (200) planes of Ag NPs located at 2θ ~ 37.96˚ and 43.58˚ respectively (JCPDS file no. 897322). For optical studies, thin films of pure LTO, Ag-TiO_2, and Ag-TiO_2/TiO_2/SnO_2 are fabricated on a quartz substrate using the same conditions as used in photodetector fabrication. The normalized UV-Vis absorbance spectra of pure $Li_4Ti_5O_{12}$, Ag-TiO_2, and Ag-TiO_2/TiO_2/SnO_2 thin films spanning the optical spectral region of 300–800 nm are shown in **Figure 3.2b)**. The absorption spectrum of Ag-TiO_2 thin film demonstrates narrowband plasmonic absorption of Ag NPs with a plasmonic peak at 420 nm in visible range of spectra. This plasmonic absorption produces hot electrons which can be utilized for fabrication narrowband photodetectors. Furthermore, we investigated the optical transparency and reflectivity of Ag-TiO_2/TiO_2/SnO_2/glass stacked film which is shown in **Figure 3.2c)**, indicating an excellent optical transparency of 80-85% in the visible region. In addition, it also indicates that the reflectivity of the film is relatively higher (~35%) in the range of 300-400 nm compared to longer wavelength (~20%). The PL spectra of the Ag-TiO_2 thin film is shown in **Figure 3.2d)**, which is acquired in the range of 350-600 nm with an excitation wavelength of 350 nm, indicating the emission peaks around 405 nm (3.06 eV), which is related to a band-to-band transition of TiO_2 semiconductor in the UV region.

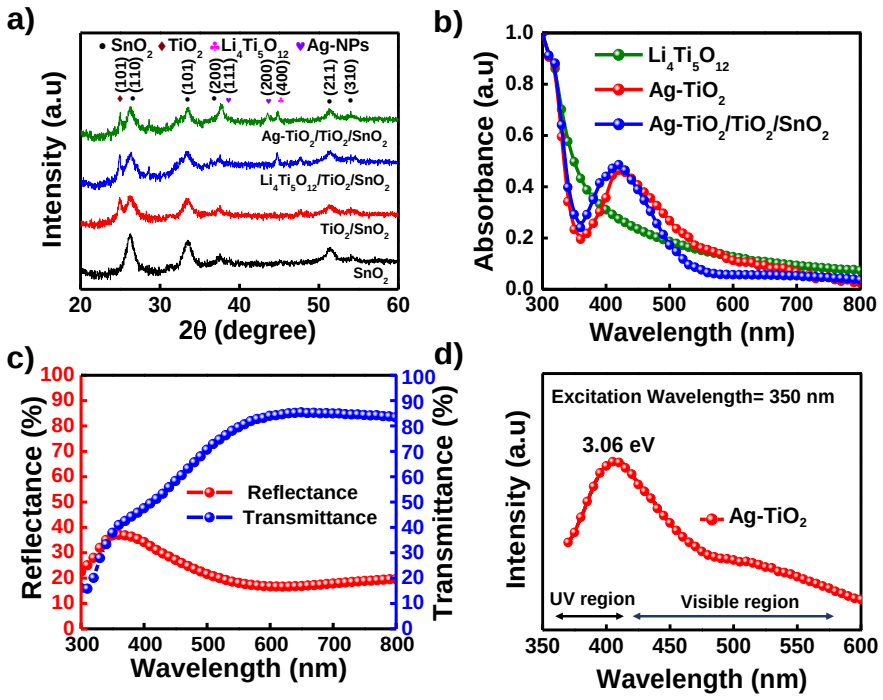

Figure 3.2a) Step-by-step XRD pattern of proposed thin film (Ag-TiO_2/TiO_2/SnO_2) **b)** UV-Vis absorption spectra of LTO,Ag-TiO_2 and Ag-TiO_2/TiO_2/SnO_2 thin films **c)** optical transparency and reflectance of Ag-TiO_2/TiO_2/SnO_2 **d)** PL emiossion spectra of Ag-TiO_2 with the excitation wavelength of 350 nm.

3.3.2 Surface Morphology (HR-SEM & HR-TEM) Study

The surface morphology of Ag-TiO_2 is studied in detail using HR-SEM, as illustrated in **Figure 3.3a)**. From this picture, it can be noted that the formation of densely packed bright spots, which originated from Ag NPs, is surrounded by relatively low intensity zones, indicating the growth of Ag NPs inside a TiO_2 matrix. This difference of contrast appears in the SEM image because of the difference in electron density. As Ag NPs have higher electron density, it becomes much brighter than TiO_2, and makes it easily distinguishable. This data also revealed that the particle sizes of Ag NPs are within the ranges between 5 to 35 nm with an average particle size of ~16 nm **Figure 3.3b)**. An energy-dispersive X-ray spectrometer (EDX) connected to the HR-SEM determines the chemical compositions of the metallic elements that clearly demonstrates the presence of Ag and Ti components within the thin film **Figure 3.3c)**. The color mapping of Ag-TiO_2 thin film is shown in the **Figure 3.3d)**, indicating the uniform distribution of Ag, Ti and O ions.

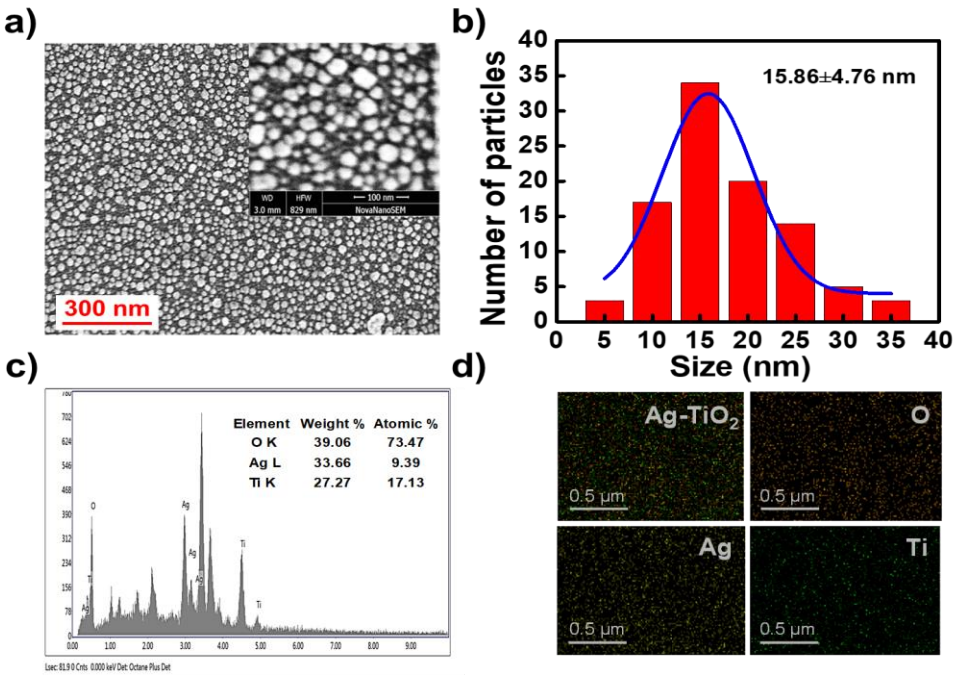

Figure 3.3a) HR-SEM image of Ag-TiO_2 thin film **b)** particle size distribution of Ag (NPs) inside TiO_2 thin film **c)** EDX elemental analysis **d**) color mapping image of Ag-TiO_2 thin film.

TEM analysis of the Ag (NPs)-TiO_2 nanocomposites has been performed for further structural analysis, as illustrated in **Figure 3.4**. For the TEM sample preparation, Ag-TiO_2 thin film is scratched out with the help of a clean glass slide and collected on a clean paper. Then, it is dissolved in isopropanol and dispersed with the help of a probed sonicator for a few minutes. Subsequently a 10 µL drop of this dispersed solution is collected into a TEM grid and used for further analysis. **Figure 3.4a)** shows that the Ag-NPs have been grown quite uniformly within the TiO_2 matrix. This data also shows that NPs are predominantly between 5 and 25 nm in size, with an average particle size of 15.2 nm, which is consistent with the HR-SEM study. The particle size distribution of Ag NPs inside TiO_2 matrix is shown in **Figure 3.4b)**. Higher magnification TEM analysis **Figure 3.4c)** of an Ag-TiO_2 sample indicates individual lattice fringe formation of Ag-NPs and TiO_2, implying their own co-existence. The average d-spacing of Ag-NPs and TiO_2 are 0.203, 0.241, and 0.352 nm, respectively which are corresponding to the Ag (200), Ag (111) and anatase TiO_2 (101) planes. All this spacing's are also defined by the selected area electron diffraction pattern (SAED), as shown in **Figure 3.4d)**. As shown earlier, the XRD pattern of the Ag-TiO_2 sample (**Figure 3.2a)**) also revealed the same set of planes.

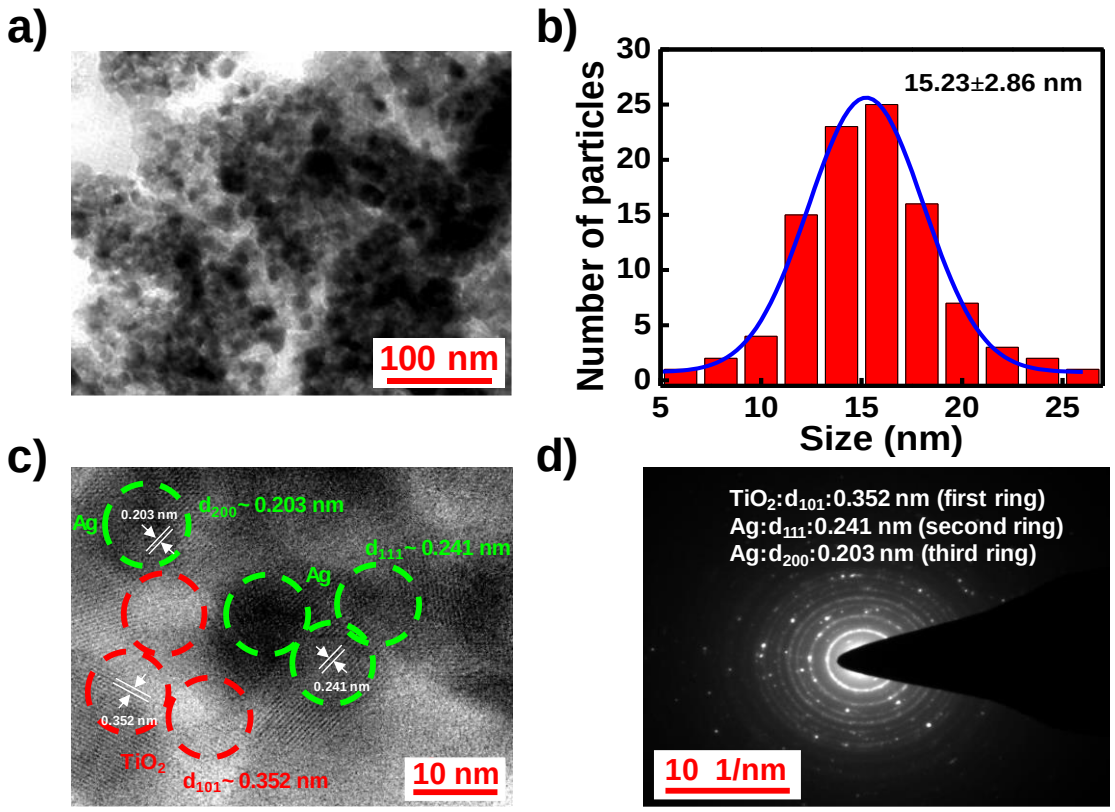

Figure 3.4a) TEM image of Ag-TiO_2 thin film **b)** distribution of particle size of Ag-NPs from TEM image analysis **c)** high-resolution image of Ag (NPs)-TiO_2, greenish ring suggests the lattice d-fringe of Ag NPs and reddish ring for TiO_2 **d)** SAED pattern of Ag (NPs)-TiO_2.

3.3.3 Photodetection Under Dark and Light

Top Ag electrodes of size 0.84 × 0.84 mm^2 which are separated by 200 µm, works as contacts for all electrical characteristics. The electrical current-voltage (I-V) characteristics of multi-layer heterojunction and single-layer photoconductors are measured at room temperature under dark and white lamp illumination conditions, as shown in **Figure 3.5a-d)** respectively. A high-power Xenon lamp that works as source of white light has been illuminated from the top of the device (inset of **Figure 3.5a-d)**). For heterojunction proposed device, light intensity has been varied from 20 W/m^2 to 800 W/m^2 and it is observed that under ±10 V external bias dark current density is ~10^{-3} A/cm^2 which increased by 416 times under the illumination of 800 W/cm^2 light. In comparison to that, under same light illumination (800 W/m^2), enhancement of current for Ag-TiO_2/SnO_2 and Ag-TiO_2/TiO_2 based device shows a

less photocurrent generation, indicating the crucial role of TiO_2/SnO_2 heterojunction as a bottom layer of the device. On the other hand, only SnO_2 semiconductor-based device shows ~two orders less photocurrent generation. For optimization, we varied the initial concentration of Ag-TiO_2 layer and 300 mM concentrated Ag-TiO_2 layer shows better photocurrent generation compared to others. I-V characteristics with different concentration of Ag-TiO_2 (100 mM, 200 mM, 500 mM) thin film is shown in **Figure 3.6a-c)**.

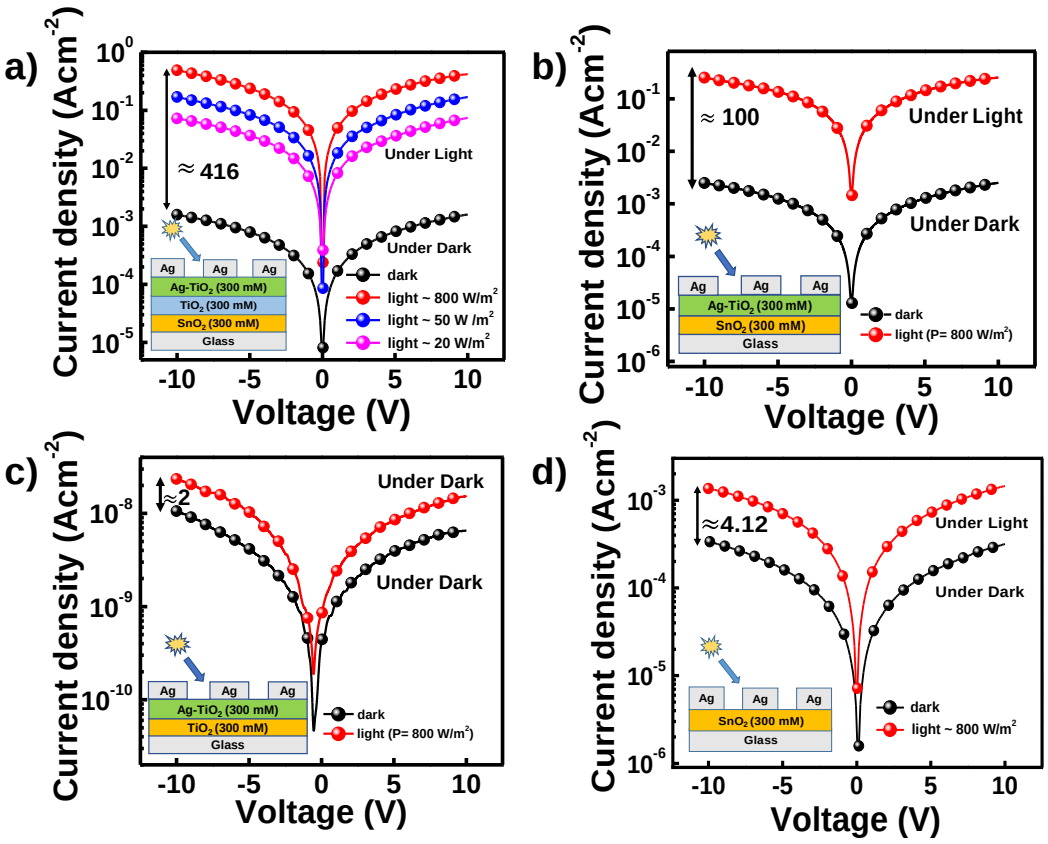

Figure 3.5 Semi-log I-V plot shows the photoconductivity of **a)** Ag-$TiO_2/TiO_2/SnO_2$ **b)** Ag-TiO_2/SnO_2 **c)** Ag-TiO_2/TiO_2 and **d)** SnO_2 based device under dark and light illumination.

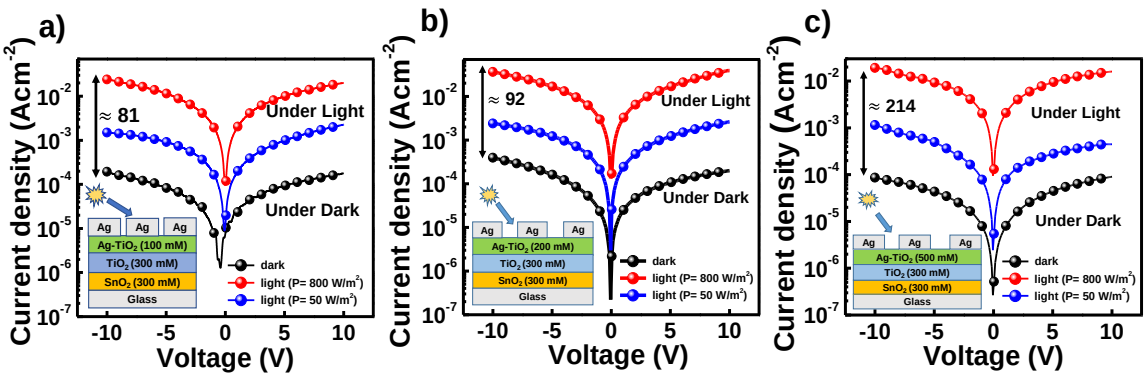

Figure 3.6 I-V plot for different concentration of Ag-TiO_2 layer **a-c)** 100,200 and 500 mM respectively under white light illumination at different intensities.

3.3.4 Experiment Evaluation of EQE & IQE and Role of Plasmon Excitation

Optical excitation must be separated from subsequent electronic transit and collection to experimentally analyze the significance of plasmonic hot electrons in device performance.[171] For this, we experimentally measure EQE within the wavelength range from 300 to 600 nm which describes the incident photon-to-photocurrent generation efficiency which is shown in **Figure 3.7a-d)** for main device (Ag-TiO_2/TiO_2/SnO_2/glass). From this spectrum, it can be noted that, there is a strong photocurrent spectrum in the range 400 to 480 nm with a peak at 420 nm. This spectrum is very much similar to the absorption spectra of Ag-TiO_2 thin film (**Figure 3.2b)**) where we found strong plasmonic absorption in the same region, indicating that the photocurrent of this device is generating mostly due to the hot electron generation from the Ag NPs. With 300 mM concentration of Ag-TiO_2 thin film, we get best photocurrent generation which match with I-V data as well. Here, we also provide different concentration (100,200, and 500 mM) Ag-TiO_2 based EQE data to understand the photocurrent generation more clearly with different thickness of active Ag-TiO_2 layer.

However, during illumination, some part of that incident light is reflected by the Ag-TiO_2/TiO_2/SnO_2 thin film which needs to be excluded to understand the role of the hot-electron generation in this plasmonic photodetector. Therefore, to recognize the contribution

of hot electron on the photocurrent generation of the device, IQE data has been extracted from the experimentally determined EQE data by using **Equation 2.13**.

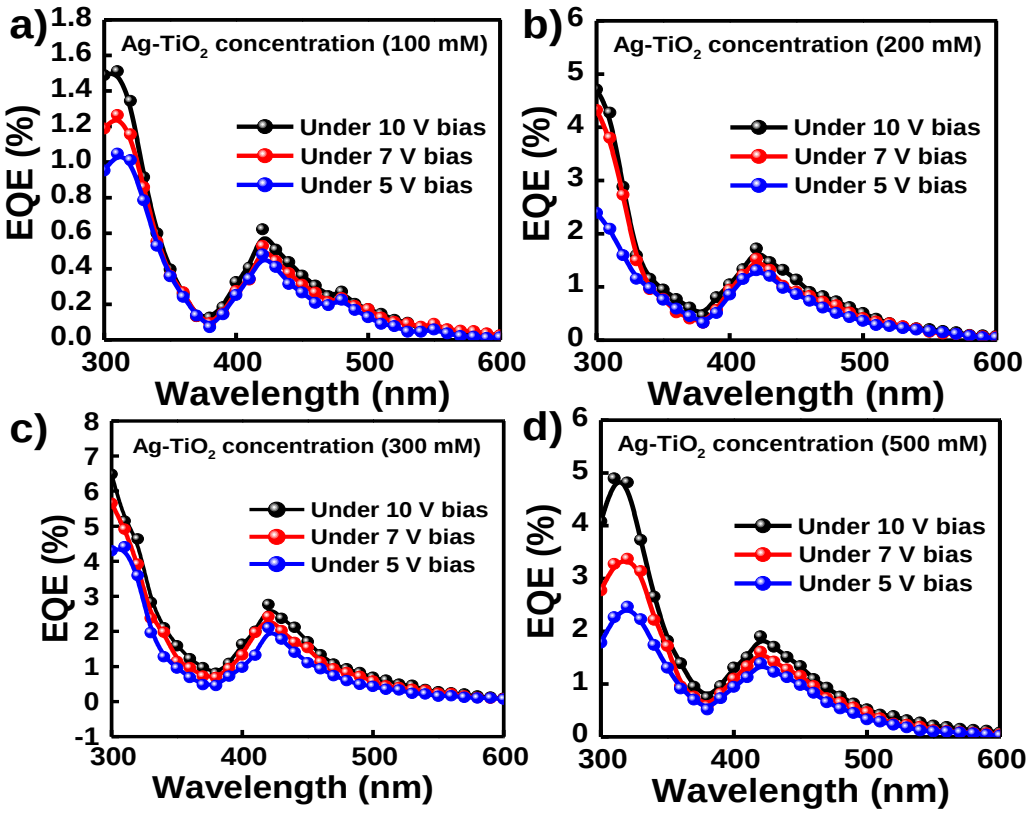

Figure 3.7a-d) EQE data of the plasmonic Ag-TiO_2 thin film based hot electron photodetector for different concentration of Ag-TiO_2 (100,200,300 & 500 mM).

The extracted IQE spectrum has been shown in **Figure 3.8a)**, indicating much stronger photocurrent generation in the plasmonic absorption spectra region. The maximum value of IQE is ~ 4.02% at 420 nm which is ~ 1.5 times of EQE value at the same wavelength.

Moreover, it has been observed the EQE of this device depends on the thickness of Ag electrodes and Ag with 30 nm thickness gives the highest photocurrent. As it is known that the transport of these hot carriers to an interface can occur either ballistically or via electron-electron and electron-phonon scattering, therefore the hot carrier collection by the electrodes also depends on it. It has been reported that when the thickness of such plasmonic strips becomes in the order of average mean path of hot carrier (~20 nm), collection of hot carriers

by the electrodes can be ballistically without much scattering. Therefore, in this photodetector, this optimum 30 nm Ag electrode thickness gives the highest photocurrent (**Figure 3.8b)**).

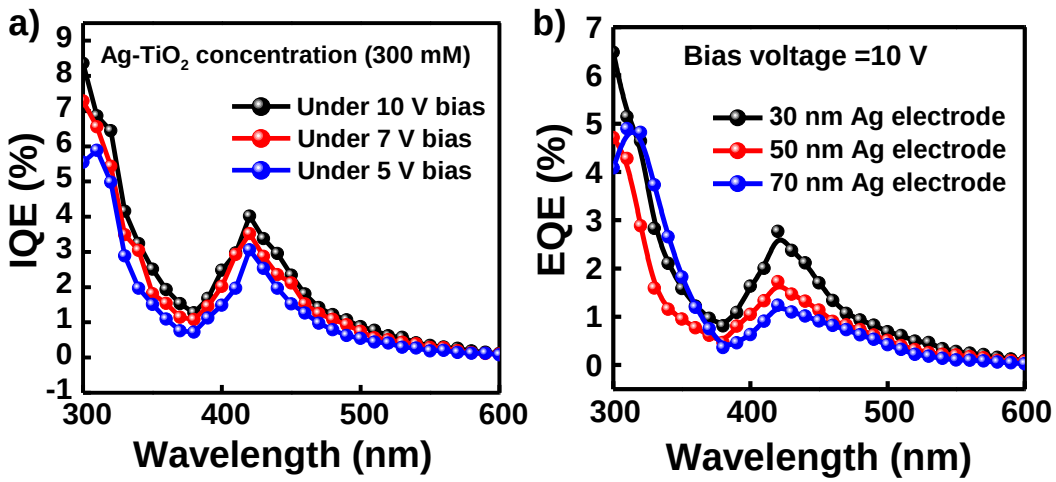

Figure 3.8a) Extracted IQE data of Ag-TiO_2 based hot electron photodetector **b)** EQE data for different thickness of Ag electrode.

In the photocurrent generation process, initially light is absorbed by the material followed by hot electron generation and subsequent transport to the electrodes which is schematically presented in **Figure 3.9a-c)**. Since, the hot electron of Ag NPs is generated from the intraband excitation (s-band) and Ag-TiO_2 Schottky junction has lower barrier height, therefore, hot electrons of Ag NPs can easily transfer to the conduction band of TiO_2. Particularly, this *in-situ* grown Ag-TiO_2 has a highly reduced interface state that enables an efficient charge transfer from Ag NPs to the CB of TiO_2 without much recombination loss. Again, it has been observed that an additional TiO_2 layer of this Ag-TiO_2 thin film generates much higher photocurrent in the device. One possible reason for this is due to the lack of TiO_2 contact in the vertical direction of the Ag-TiO_2 only thin film. Whereas an additional TiO_2 ensures a hot electron to get the Ag-TiO_2 interface during the charge transport to the SnO_2 layer. As soon as a hot electron reaches the SnO_2 layer, it increases the electron density of this semiconducting layer and is collected to the electrode under external bias due to its high electron mobility.

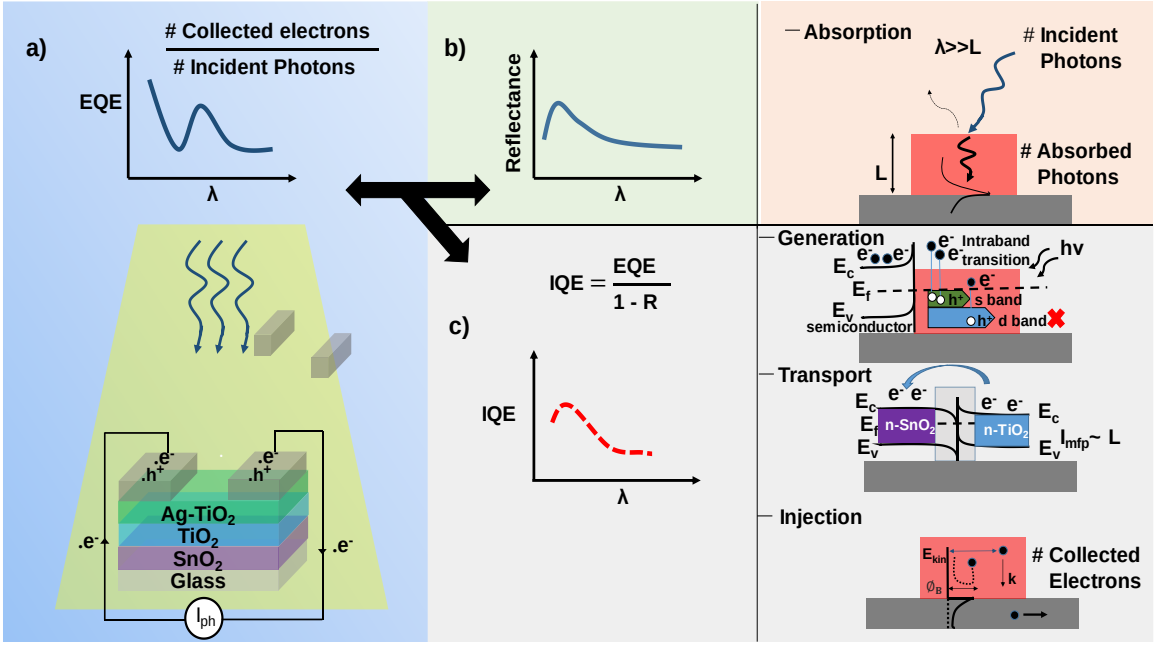

Figure 3.9 Steps of photocurrent generation **a)** EQE spectrum represents the wavelength (λ) - dependent photon-to-electron conversion probability **b)** reflectance data with the variance of different wavelength **c)** schematic representation of IQE which contribute to the carrier generation through intraband transition of Ag NPs. On the other hand, absorption spectrum of a metal nanostructure displaying a resonant plasmonic feature which can be engineered through photonic design. Plasmon excitation indeed yields high absorption in metallic nanostructure switch characteristic dimension L much smaller than the wavelength λ of the incident photon; illustrative IQE spectrum shows the generation of hot charge carriers through intraband transitions, propagation, and scattering of the hot carriers with energy-dependent mean free path (l_{mfp}), and injection of hot carriers with adequate kinetic energy (E_{kin}) and momentum (k) across the Schottky contact ($\emptyset_B$).

3.3.5 Photodetector Device Performance

Responsivity (R_λ) and detectivity (D*) are two key parameters to identify the quality of a photodetector. The EQE, is the photocurrent per photon whereas R_λ is the amount of photocurrent that a unit area photodetector generates when unit power of light is illuminated

on it. Responsivity of the device is calculated from EQE measurement by using **Equation 1.3**.

The change in photo-responsivity of this photodetector under various external biases is depicted in **Figure 3.10a)** for proposed device (Ag-TiO_2/TiO_2/SnO_2/glass) with 300 mM Concentration of Ag-TiO_2 thin film. This data indicates, under an external bias of 10 V, the maximum responsivity of 0.98 (A/W) at 420 nm can be achieved.

The specific detectivity, D*, of a photodetector is a measurement of the signal-to-noise ratio across a 1 Hz bandwidth normalized to the detector's area. It is an essential device parameter that can be used to identify the sensitivity of detectors. By considering the noise that comes mostly from the dark current of the device, detectivity can be measured by using **Equation 1.4.**

The variation of detectivities of proposed heterostructure device are shown in **Figure 3.10b)** under different external bias. The highest detectivity of this heterojunction photodetector is observed with a value of 3.19×10^{11} Jones at 420 nm under 10 V external bias. The peak position of detectivity at 420 nm, indicating the highest sensitivity of device, matches exactly with the plasmonic absorption peak. Therefore, the photocurrent of this device is mostly generated from the hot electron of Ag NPs.

Another important feature of photoconductors is the device's response speed that determines how fast the detector can measure the next signal. The instantaneous response of such devices is further investigated by lighting them with white light pulses of width and separation ~10 s while the device is subjected to a 10 V external bias, as illustrated in **Figure 3.10c)**. The time intervals needed for the photocurrent to increase from 10% to 90% of its peak value (τ_r) and for the response to decrease from 90% to 10% of its peak value (τ_f) are always used to define the device rise time (τ_r) and fall time (τ_f). **Figure 3.10d)** indicates the rise time of the device is ~ 1.2 s and whereas decay time is ~ 0.95 s. This data reveals that the device's rise and decay time responses are reasonably fast. Moreover, the device has been stored in an ambient atmosphere for months, although its photosensitivity and response speed remain almost the same.

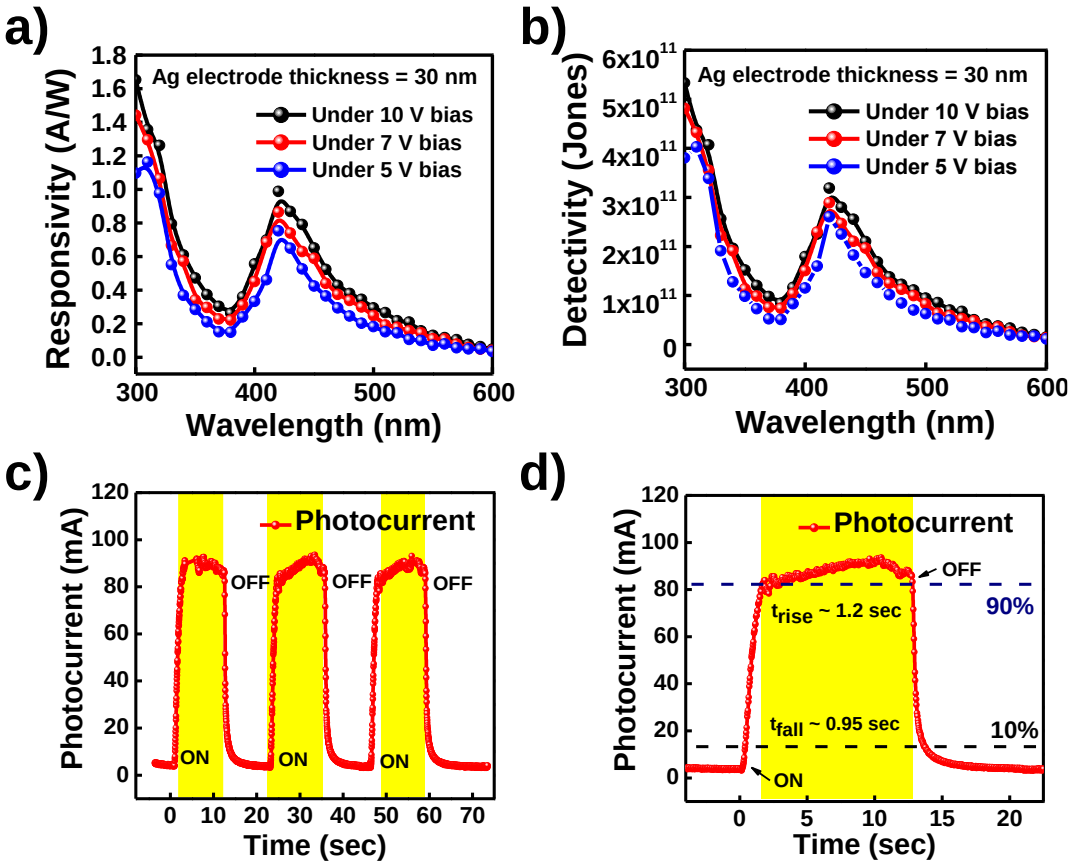

Figure 3.10 illustrates the performance of Ag-TiO_2/TiO_2/SnO_2/glass-based proposed lateral heterostructure photoconductor device **a)** extracted responsivity ($\mathbf{R_\lambda}$) vs wavelength **b)** extracted detectivity (D*) vs wavelength **c)** shows the instantaneous time response of the device **d)** indicates very fast rising and decaying time of ~1.2 s and ~0.95 s, respectively.

To compare the overall performance of our device, a summary of earlier reported works on this plasmonic photodetector is shown in **Table 3.1.** Previous works on hot electron based photodetector have mostly concentrated on responsivity (R_λ) of the photodetectors, while other important parameters of the hot electron photodetectors such as EQE (%), detectivity (D*) and response time (τ_r/τ_f) have not explored much. Out of diferent hot-electronbased photodtector, we found only one work on Ag/TiO_2 based material in photodiode geometry (Nanophotonics. 2019;8(7):1247-1254.) that have faster response time due to its photodiode gemetry. They didn't report the EQE and detectivity spectrum of the device in that paper,

but mention the peak detectivity value which is added in the table. In comparison to those reported hot-electron photodetectors, our Ag-TiO_2 based hot electron photodetector exhibits a higher responsivity whith higher detectivity value. Additionally, our strong narrowband response which can be utilized as colour sensitive photodetector.

Table 3.1 Comparison of the present Ag-TiO_2 based photodetector's device performance with that of other plasmonic hot-electron photodetectors

Device	**λ (nm)**	**EQE (%)**	**R (A/W)**	**D^*(Jones)**	**τ_r/τ_f**	**Ref.**
Ag-TiO_2/TiO_2/SnO_2	420	2.76%	0.98	3.19×10^{11}	1.2/0.95 s	This Work
Porous Ag/TiO_2	450	–	3.3×10^{-3}	9.8×10^{10}	112/24 µs	[165]
Ag/TiO_2 NTs/FTO	370	–	176.30	–	82/14 s	[172]
Porous Au/Si	–	–	3.5×10^{-3}	–	–	[173]
Au nanorods/Si	–	–	1.0×10^{-5}	–	–	[154]
Au/Pyramid-Si	1200	–	8.2×10^{-3}	1.8×10^{10}	–	[159]
Au/ $SrTiO_3$/Si	1350	–	3.7×10^{-4}	–	1 ms	[174]

3.4 Conclusions

In conclusion, in this chapter, we presented a highly efficient Ag-TiO_2 nano-heterostructure based hot electron photodetector, which had a narrowband response in the visible region with a fast response speed. Device has been fabricated in solution-processed techniques in photoconductor geometry. The responsivity, EQE and detectivity of this photodetector at 420 nm are calculated to be 0.98 A/W, 2.76% and 3.19×10^{11} Jones respectively, whereas transient photocurrent study indicates its rise and fall time are 1.2 s and 0.95 s respectively. The detectivity of this plasmonic photodetector has been compared with earlier reported works which reveal superior photosensitivity of this detector, which becomes possible due to the efficient hot electron transfer through the Ag-TiO_2 nano-heterostructure. Besides, using an underlying SnO_2 charge transport layer, photo-generated electrons are collected efficiently to the electrodes. Overall, device performance of this photodetector gives a visible way to fabricate narrowband photodetectors using plasmonic NPs.

Chapter 4

1st Part: Flexible Transparent Conductors with a percolated Ag nanostructure and its Application as Efficient Self-bias Plasmonic Photodetector

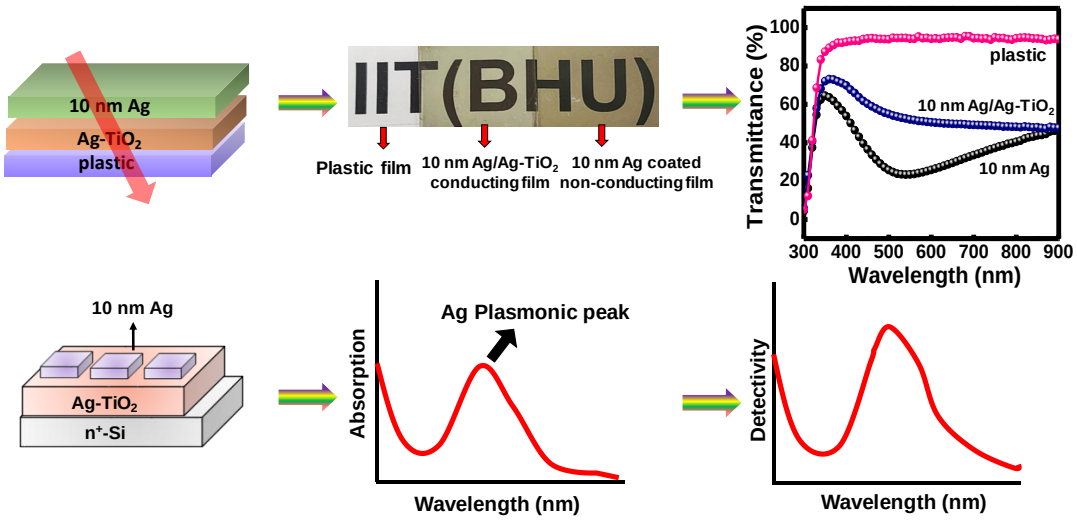

Chapter 4

This chapter mainly focuses on development of a percolated silver (Ag) nanostructured-based transparent conductor and used it for the applications of self-bias plasmonic photodetector. Device has been deposited by physical vapor deposition (PVD) technique where lateral growth of Ag has been enhanced by a pre-deposited Ag-TiO_2 thin film. This Ag-TiO_2 film has embedded Ag nanoparticles (NPs) within TiO_2 thin film which is grown in a low temperature (100˚C) solution processed technique that includes LTO thin film deposition by a sol-gel method followed by ion-exchange ($Li^+ \rightarrow Ag^+$) process to yield an Ag-TiO_2 thin film. The percolated Ag network has appeared as soon film mass-thickness reaches close to 10 nm, resulting in an abrupt drop of electrical resistivity of the film. This percolated Ag nanostructured thin film (10 nm Ag/Ag-TiO_2/plastic) has resistivity of ~ 50 ohm/□ and an average visual transmittance of >70% up to 450 nm. In higher wavelength range, transparency gradually reduces, and it reaches to ~50% at 600 nm which is mostly due to the plasmon absorption of this film. By utilizing its combined optical transparency and surface plasmon absorption, this film has been used to develop plasmonic hot electron photodetectors where Ag-thin film works as transparent electrode as well as plasmon induced photo-excited hot electron generation. Device has been fabricated on a highly doped n type Si (n^+-Si) with a metal-semiconductor-metal (M-S-M) device geometry. External quantum efficiency (EQE) data reveal that photocurrent of this device is mostly generated in the plasmonic absorption region with a peak detectivity of 2.84×10^{12} Jones at 510 nm under -3V external bias. Besides, the device shows fast response with a response time of ~25 ms.

4.1 Introduction

Until now, indium tin oxide (ITO) has mostly used as a transparent conductor (TC) that can achieve transparency (>90%) with quite excellent electrical conductivity.[116, 117] However, these ITO-based transparent electrodes (TEs) are quite expensive due to the use

of indium, which is one least abundant mineral on earth.[119] Besides, due to the inorganic nature of ITO, it has poor mechanical flexibility.[118] Relatively, carbon-based TC like carbon nanotube[175] and graphene[176] has higher mechanical flexibility with excellent optical transparency. Although, the electrical conductivity of these ITO or carbon based TCs are quite lower with respect to metals like Ag, Au, and Cu.[120] In contrast, metals have significant refractive index (n) that limit the development of metal based TEs. Among different metals, Ag has the least n (~0.05) in the visible range of light and has been widely studied for TC development.[177-179] Most of those studies are either Ag nanowire[121, 180, 181] based or oxide/Ag/oxide multi-stack thin film[122, 182] based where ~10 nm Ag film is commonly used. These Ag-based TCs have higher electrical conductivity than ITO with acceptable mechanical flexibility which could be an ideal TC electrode for flexible electronics.[123, 183] However, Ag nanostructured or Ag thin films have very strong plasmonic absorption which is a key barrier to achieve high optical transparency of those films.[124, 184] Besides, due to higher reactivity of Ag nanostructure, long term stability of these Ag-based TCs are not as good as ITO.[123, 185]

Although plasmonic absorption is a key bottleneck of developing metal based highly transparent conductors, it's useful for developing various optoelectronics devices including solar cell, plasmonic photodetector, memory device, sensors, and light emitting diodes.[186-189] A number of group claims that the plasmonic effect of electrode can add hot-electron induced photocurrent which can be beneficial for photocurrent generation of solar cell, photodetector and photo-electrochemical H_2 generation.[140, 190, 191] When electromagnetic waves (EMW) interact with a metal MNPs, part of that EMW is scattered and the rest of the part is absorbed by MNPs due to the SPR. This SPR absorption of MNPs increase whereas scattering reduces with reducing particle size. Besides, shape of MNPs, the relation of dielectric constant of MNPs and surrounding are also important parameters for SPR related absorption of MNPs.[81] Due to the SPR, MNPs either generate electron-hole pairs or go through radiative decay to the far field. Again, this generated electron-hole pair can produce hot-electron through non-thermal electron distribution via electron-electron scattering.[55, 192] To utilize this hot-electron for optoelectronics device application, a semiconductor-metal Schottky junction is required through which it can be injected to the semiconductor within a very short period of time (<100 fs), before non-

radiative energy relaxation of hot-electron through electron-phonon scattering. Besides, for efficient electron injection of this hot-electron in the Schottky junction, a low barrier height (Φ_b) Schottky junction is required.[193, 194] In plasmonic devices, this metal-semiconductor Schottky junction have been developed by varsities ways like; by depositing metal thin film on a nanostructured semiconductor surface followed by inert atmosphere annealing to form MNPs,[195] MNPs-metal oxide thin film,[196, 197] semiconductor-metal thin film heterojunction etc.[198, 199] In addition, several reports claims that the optoelectronics devices performance can be improved by using a plasmonic electrodes.[169] In a plasmonic photodetector, the contribution of hot electron is commonly realized from the EQE measurement that indicated a strong photocurrent generation in the plasmonic absorption region of MNPs. However, there are very limited reports that demonstrated the similarity of plasmonic absorption and EQE spectra of the device. Moreover, EQE values of those devices are also quite poor.

This section of the chapter has described a low cost deposition technique of Ag based TC film. For this, 10 nm Ag has been deposited on top of an Ag-TiO_2 thin film at low temperature (~100°C) to fabricate TC films, enables us to deposit this conducting film on a plastic substrate. The growth of Ag NPs inside TiO_2 matrix, helps in controlling the size and uniform distribution of Ag NPs throughout the plastic substrate. At the initial stage of Ag growth, it has been observed that the nucleation density of Ag NPs on this TC film is much higher than bare plastic substrate. However, after a critical size growth of those grains, granular film undergoes a solid-state dewetting process which makes it possible to deposit percolated finger-like Ag nanostructured thin film. The presence of metal-oxide TiO_2 layer offer structural support to ensure long-term stability and durability of this TC film. So, the combination of TiO_2 and Ag NPs leverages the strengths of both materials. As a consequence, the resistivity of the film dropped suddenly while optical transparency has been maintained ~70% in the violet-blue region. However, it drops to ~50-60% in the higher wavelength region of light due to the plasmonic absorption of the film. To analyze the surface phenomena of this percolated finger-like Ag nanostructured, we developed a percolation model which tells about the nature of percolation threshold during growth. Besides, this transparent-conducting Ag film has been used as a plasmonic electrode for developing high performance hot-electron photodetectors. Device has been fabricated on a

n^+-Si substrate that shows extremely high detectivity with fast response speed. The UV-Vis absorption spectra of Ag based TC film shows a strong SPR absorption, has an excellent spectral matching with the EQE spectra of the photodetector, implying the major contribution of hot-electron in the photocurrent generation of the device.

4.2 Experimental Section

4.2.1 Synthesis of Materials

The synthesis process for $Li_4Ti_5O_{12}$ via low temperature solution process technique has been explained in **Chapter 2 Chapter 2 Section 2.1.1.** PMMA is used as a protective coating for TC film. The solution is prepared by standard method, reported in **Chapter 2 Section 2.1.7**.

4.2.2 Fabrication of TC Film

The Ag/Ag-TiO_2 based TC film has been fabricated on a flexible PET substrate and the fabrication steps has been explained **Chapter 2 Section 2.3.2**, and schematically present in **Figure 2.7**. For fabrication of a photodetector, these optimized 10 nm Ag/Ag-TiO_2 TC thin film have been used as transparent electrode to develop plasmonic photodetectors in a photodiode geometry which is schematically present in **Figure 2.8**.

4.3 Result and discussion

4.3.1 XRD Analysis of Thin Films

For the crystal phase identification of thin films, we prepared XRD samples on a plastic substrate. **Figure 4.1** shows the XRD patterns of LTO, Ag-TiO_2, 10 nm Ag/Ag-TiO_2, and 10 nm Ag thin film on bare plastic substrate. In the thin-film XRD pattern of LTO, two intense peaks at $2\theta \sim 35.55^o$ and 43.3^o have been observed which come from the reflection planes of (311) and (400) respectively (JCPDS file no. 490207). The XRD pattern of Ag-TiO_2 thin film shows three intense peaks at $2\theta \sim 25.1^o$, 37.72^o and 43.7^o which corresponds to anatase TiO_2 (101), Ag (111) and Ag (200) respectively. These intense broad peaks of Ag NPs are confirming the formation of Ag NPs inside TiO_2 matrix after ion-exchange process. The prepared TC film (10 nm Ag/Ag-TiO_2) shows similar peak positions with much higher intensity at $2\theta \sim 25.1^o$, 37.72^o, and 43.7^o corresponding to TiO_2 (101), Ag (111), and Ag

(200) respectively. As a reference, we did an XRD analysis of 10 nm Ag film on a bare plastic substrate, which shows peak positions at 2θ ~ 37.72º and 43.7º corresponding to Ag (111) and Ag (200) respectively (JCPDS file no 897322).

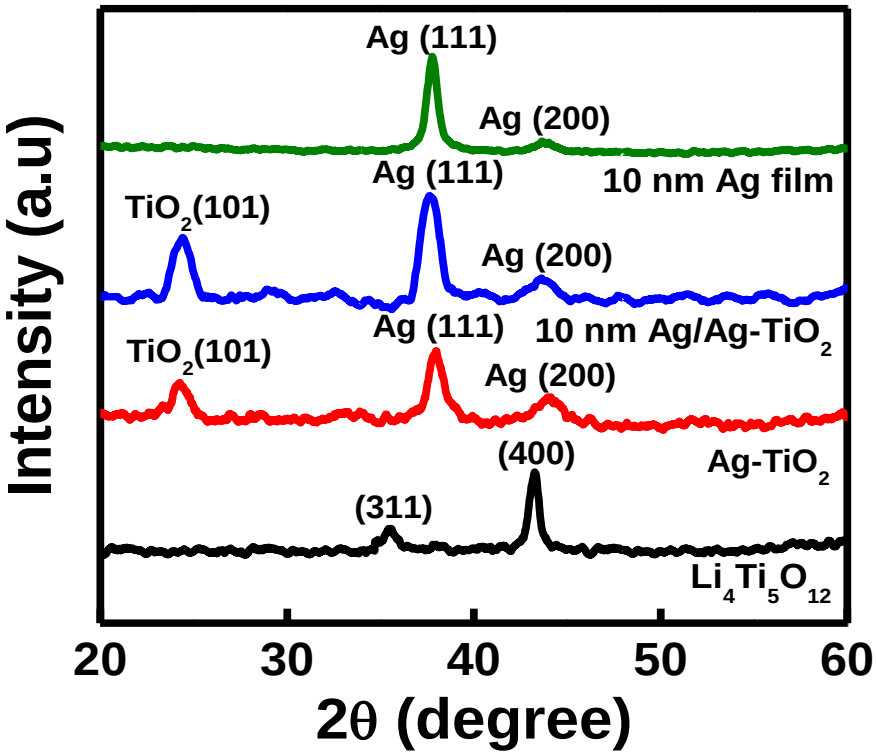

Figure 4.1 XRD pattern of step-by-step growth of TC film deposited on plastic substrates.

4.3.2 Electrical and optical characterization of TC Film

To measure the electrical resistivity of as prepared TC films, parallel Ag electrodes (thickness ~50 nm) of separation 0.45 mm have been deposited over the film. **Figure 4.2a)** depicts the semi-log plot of current density vs voltage (J-V) graphs of Ag/Ag-TiO_2 thin films with different Ag film thickness varying from 10 nm to 14 nm. This data implies that conductivity of 14 nm Ag/Ag-TiO_2 film is ~ one order higher w.r.t the 10 nm Ag film/Ag-TiO_2 film. Besides, it is observed that a large amount of current is achievable by applying a relatively modest voltage of 0.05 V. Besides, to test the film flexibility, we have examined the conductivity test with different bending cycles of (10 nm Ag/Ag-TiO_2) thin film which is shown **Figure 4.2b)**. This study indicates that conductivity of the film remains almost unaltered even after 100 cycles of bending with a fixed value of bending radius 4 mm, suggesting that film is highly durable for the fabrication of high performance flexible opto-

electronic devices. We have also coated a very thin layer of PMMA polymer as a protective layer on the top of the film to enhance the durability from humidity, oxidation, and abrasion. Following PMMA coating, an experiment is conducted to visualize the influence of the film's performance. After coating, films electrical conductivity and optical transparency (PMMA/10 nm Ag/Ag-TiO_2/plastic) data shows almost similar performance compared to uncoated PMMA film (**Figure 4.2c**). Besides, resistance vs temperature of (10 nm Ag/Ag-TiO_2) samples has been measured by four probe methods. The sample shows moderate drop in resistance up to 200 K which indicates fully metallic behavior of the TC film (**Figure 4.2d**).

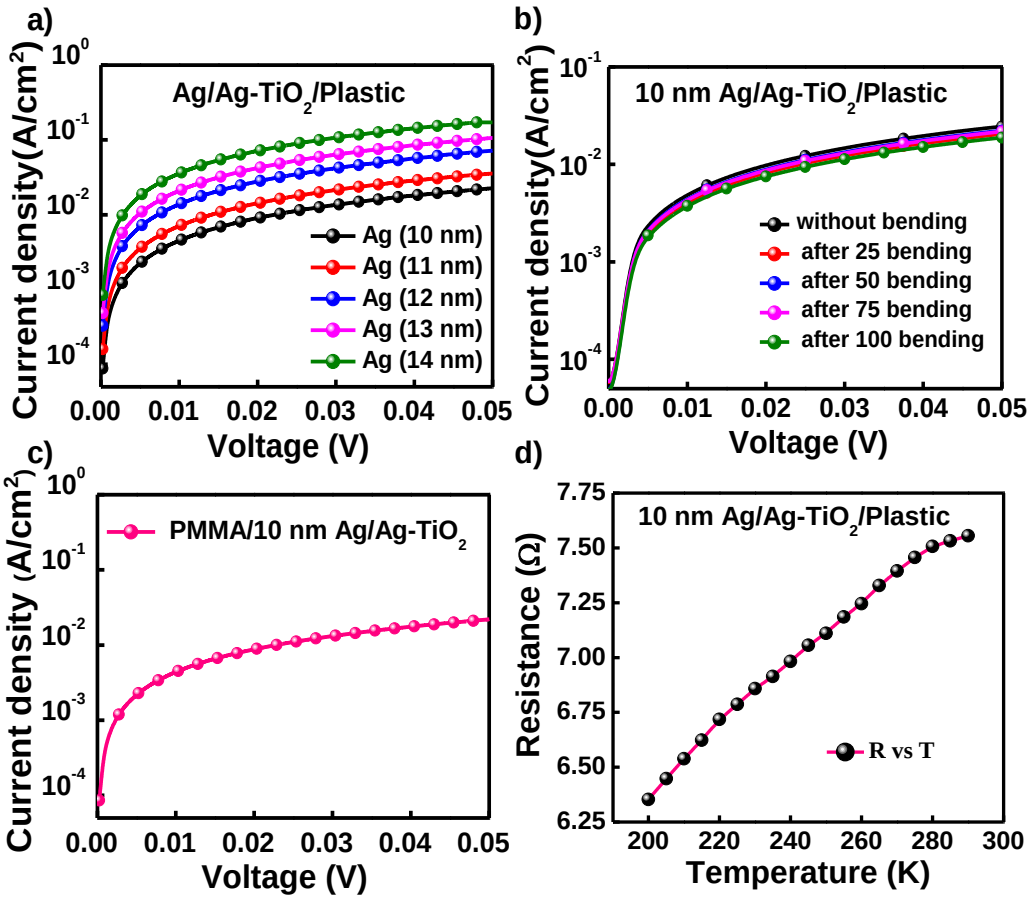

Figure 4.2a) Semi-log graph of electrical current density vs voltage of Ag/Ag-TiO_2 based TC film with Ag film thickness varying from 10 nm to 14 nm **b)** exhibits mechanical stability up to 100 bending cycles **c)** performance of TC film with PMMA as a protecting layer and **d)** variation of resistance and temperature under four probe measurement upto 200 K.

The optical transmittance of Ag/Ag-TiO_2 film for different Ag film thickness has been investigated, depicted in **Figure 4.3a)**. This data implies that 10 nm conducting film has an excellent optical transparency of 73-70 % in the blue region of 380 - 400 nm which is reduced to ~ 50 % for longer wavelengths of light. The reduction of transparency at higher wavelength is mainly due to the plasmonic absorption of Ag/Ag-TiO_2 thin film. With PMMA coat, film shows almost same transparency as compared to original TC film (**Figure 4.3b)**). The phenomena of conductivity and transparency are interconnected, leading to a trade-off. The precise form of this dependency is defined by the impact of varying deposition conditions on the electro-optical characteristics of these layers. However, under ideal circumstances, both sheet resistance (R_{sh}) and transparency (T) are greatly affected by the film thickness. **Table 4.1** shows the combined electrical and optical data of these prepared TC films. **Figure 4.3c)** represents the variance of sheet resistance and visible transmittance with the film thickness. Therefore, it can be concluded that the electrical conductivity of the film increases with increasing Ag thickness, but also it reduces the optical transparency (**Figure 4.3c)**).

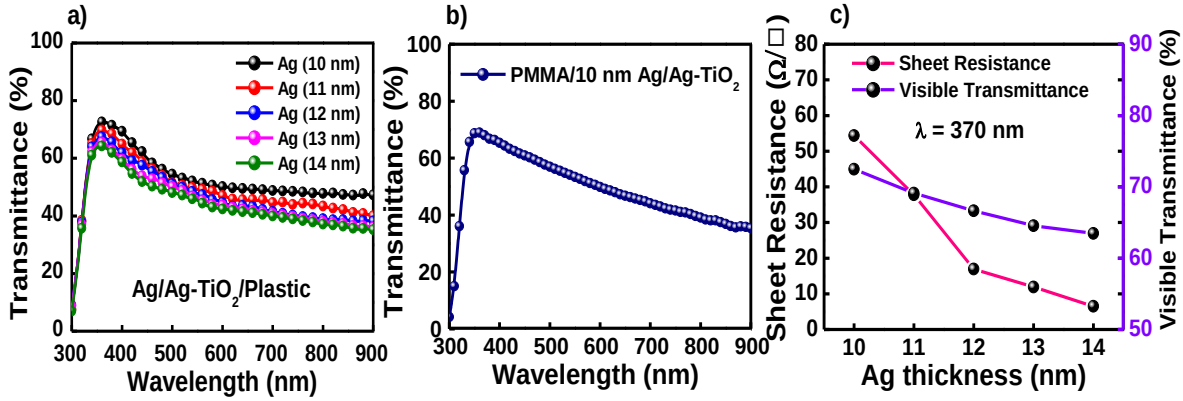

Figure 4.3a) Optical transparency of TC film with different Ag film thickness **b**) optical transparency of TC film with PMMA protecting layer, and **c)** variation of sheet resistance and visible transmittance under different Ag film thickness.

Table 4.1 Electrical Sheet Resistance and Visible Transmittance data of (Ag/Ag-TiO_2) based transparent conducting films by altering the thickness of Ag film.

The thickness of Ag film (nm)	Sheet Resistance (Ω/□)	Visible Transmittance (%) λ= 370 nm	Visible Transmittanc (%) λ= 500 nm
10	54.36	72.46 %	54.49 %
11	37.79	69.11 %	51.47 %
12	16.93	66.64 %	51.15 %
13	11.91	64.56 %	50.28 %
14	6.51	63.48 %	48.12 %

4.3.3 Surface Morphology (HR-SEM, AFM & HR-TEM) Study

HR-SEM is performed to look at the surface morphological structure of Ag/Ag-TiO_2 thin film. During Ag film deposition, morphological changes of film surface have been depicted in **Figure 4.4**. It has been observed when 10 nm Ag is deposited on top of Ag-TiO_2 film by thermal evaporation, individual Ag islands are percolated to interconnected finger-like structure (**Figure 4.4c)**),whereas demonstrate the earlier development stages of the film which consist of individual compact islands separated by nano-gaps (**Figure 4.4a&b)**). Because of these morphological changes, suddenly conductivity of the 10 nm Ag film increases by several order and transparency of the film also increases. This sudden variation of surface morphology originated from the swiftly merge of separated islands into a bigger one which are finally interconnected. Again, this morphology is not a fully coalesced structure, rather it is creating percolation structure with minimal wiping.[200] As long as film thickness reaches to 10 nm, the effective coverage area for this percolated film becomes quite high (~70%). This is because the empty channels between the elongated structures are quite thin in comparison to the width of the structures. With further deposition of Ag, those channels are mostly filled as shown in **Figure 4.4d)**, resulting in a complete continuous film.

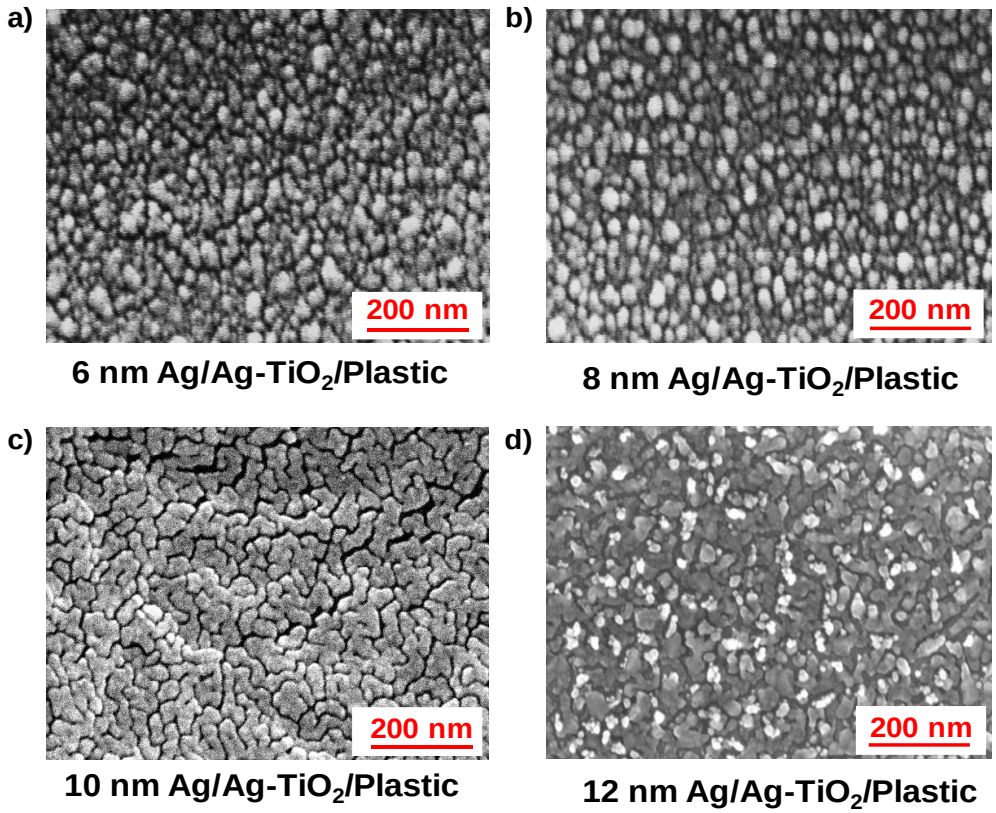

Figure 4.4 FE-SEM photographs of Ag/Ag-TiO_2 thin film at room temperature. Each photograph's average film thickness is listed below. **a&b)** early stage of growth and coalescence of islands **c)** percolating structures **d)** overgrowth percolated structures.

Moreover, TiO_2 metal-oxide also play an important role to reach this percolation threshold at very low thickness of Ag deposition. TiO_2 has a high surface energy, which help Ag NPs nucleate more easily. When Ag is deposited onto the TiO_2 surface, the high surface energy sites on TiO_2 act as nucleation centers, promoting the initial formation of Ag NPs. Besides, TiO_2 stabilize tiny Ag NPs by preventing their agglomeration, leading to a more uniform distribution, which promote better electrical conductivity & visual transparency of the film. For comparison, a set of reference Ag thin films of different mass-thickness (6, 8, 10 and 12 nm) have been grown on bare plastic substrates. The HR-SEM pictures of those films (**Figure 4.5a,b,c&d)**) show that all films are composed of individual isolated islands and doesn't show any conductivity variation up to 14 nm of mass-thickness deposition of Ag, which implies the key role of underlying Ag-TiO_2 thin film for percolated Ag growth.

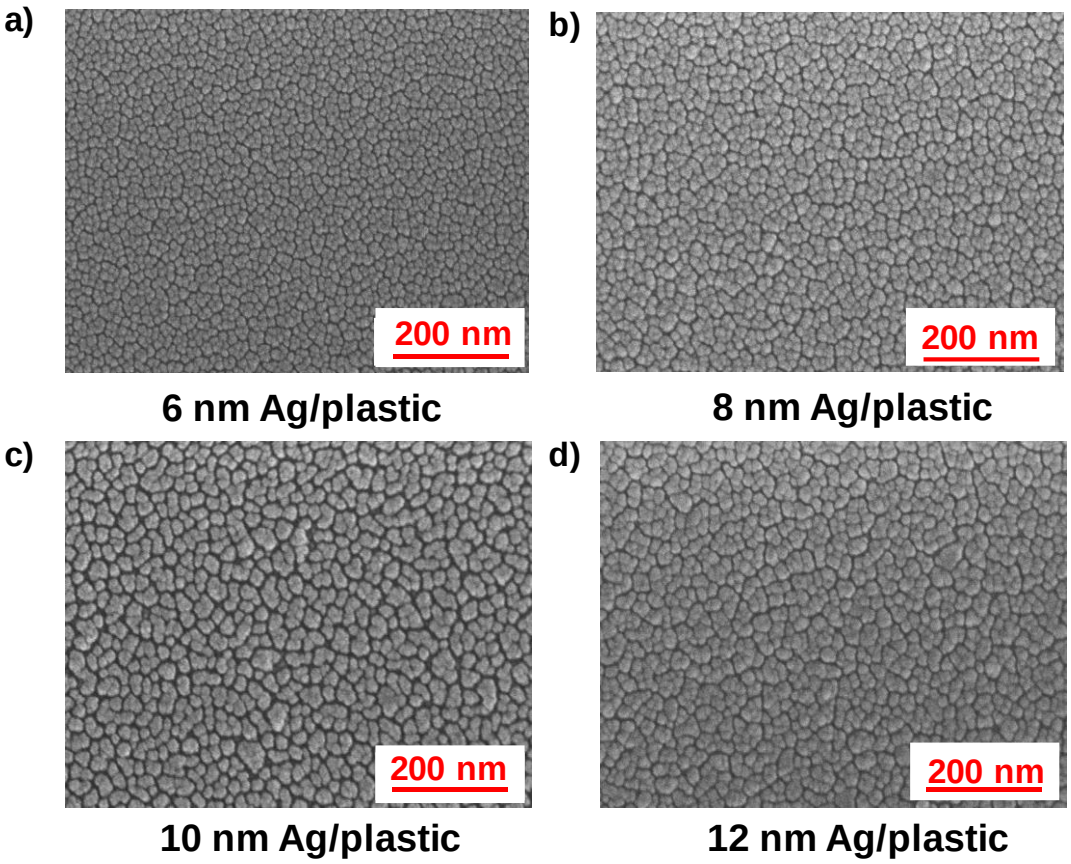

Figure 4.5 SEM images of evaporated Ag on bare plastic at ambient temperature. The surface morphology of Ag film of mass thickness **a)** 6 nm **b)** 8 nm **c)** 10 nm and **d)** 12 nm, which shows the compact separate Ag islands.

An energy- dispersive X-ray spectrometer (EDX) attached to the HR-SEM instrument is used to figure out the contents and amount of metallic elements in 10 nm Ag/Ag-TiO_2 sample is shown in **Figure 4.6a&b)**, which confirms the presence of Ag, Ti, and O uniformly throughout the film. Moreover, the cross-sectional SEM image Ag/Ag-TiO_2 film is shown in **Figure 4.6c)** and obtained thickness of the Ag film is ~ 10 nm and Ag-TiO_2 is ~ 20 nm. The thickness of the Ag film is similar to the recorded thickness obtained from the DTM thickness monitor (~10 nm) of the PVD unit.

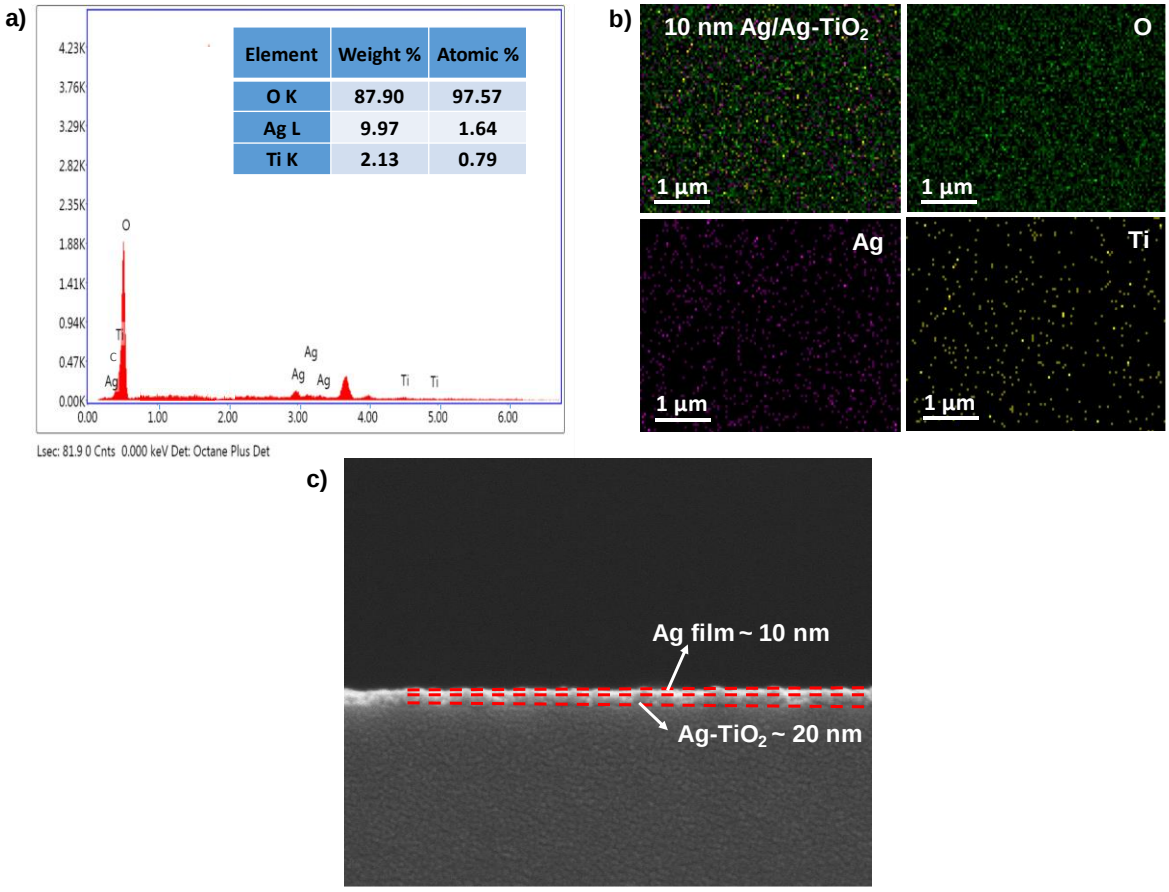

Figure 4.6a) Energy dispersive spectra of 10 nm Ag/Ag-TiO_2/plastic thin film, with the elemental composition determined by EDS displayed in the inset **b)** EDS mapping of (i) 10 nm Ag/Ag-TiO_2 thin film (ii) O, (iii) Ag and (iv) Ti **c)** cross-section SEM image of TC film to determine the thickness of the each individual layer.

AFM is used to describe the surface morphology in more detail, specifically to recognize the surface roughness (R_{rms}). An unconventional surface roughness is observed with increasing Ag film thickness on plastic substrates. It is found that in the lower thickness of Ag film (6 nm Ag/Ag-TiO_2), surface r.m.s roughness ~ 3.6 nm is quite high. However, it decreases to ~ 2.8 nm as soon mass-thickness reaches to 8 nm. Most interestingly, the film roughness reduces to ~ 1.75 nm as soon as mass-thickness of Ag reaches to 10 nm which becomes possible due to the flat finger-like percolated network formation as shown in **Figure 4.7a&b)**.

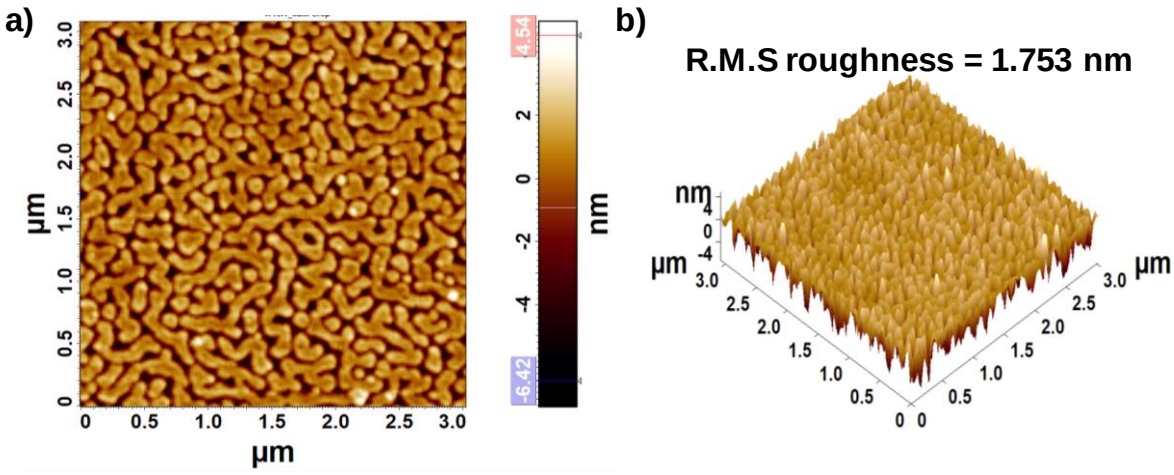

Figure 4.7a) 2-D and **b)** 3-D AFM image of 10 nm Ag/Ag-TiO_2 film ($R_{r.ms}$ ~ 1.75 nm) on plastic PET substrate.

Although, this roughness increases gradually if further growth of Ag film is continued. Besides, the reference 10 nm Ag on plastic substrate also shows high roughness of around ~ 5.2 nm. Surface morphology and their roughness value for different Ag thickness ((6,8,12 nm Ag/Ag-TiO_2) samples and reference (Ag 10 nm/plastic) sample is shown in supplementary data in (**Figure 4.8a,b,c&d)**) and **Table 4.2** . From this study, it is clear that Ag is initially forming individual isolated islands or clusters that have larger vertical growth, resulting in its higher roughness. However, after 8 nm mass-thickness of Ag deposition, lateral growth dominates and finally an abrupt change of surface morphology is evolved as soon this thickness reaches to 10 nm that reduces the surface roughness significantly. This phenomenon is comparable to the thin film dewetting of thin film which normally required higher temperature to evolve such structure.[201, 202] Although in this study, it appears during room temperature Ag growth during physical vapor deposition when grain size of Ag crosses a critical size.

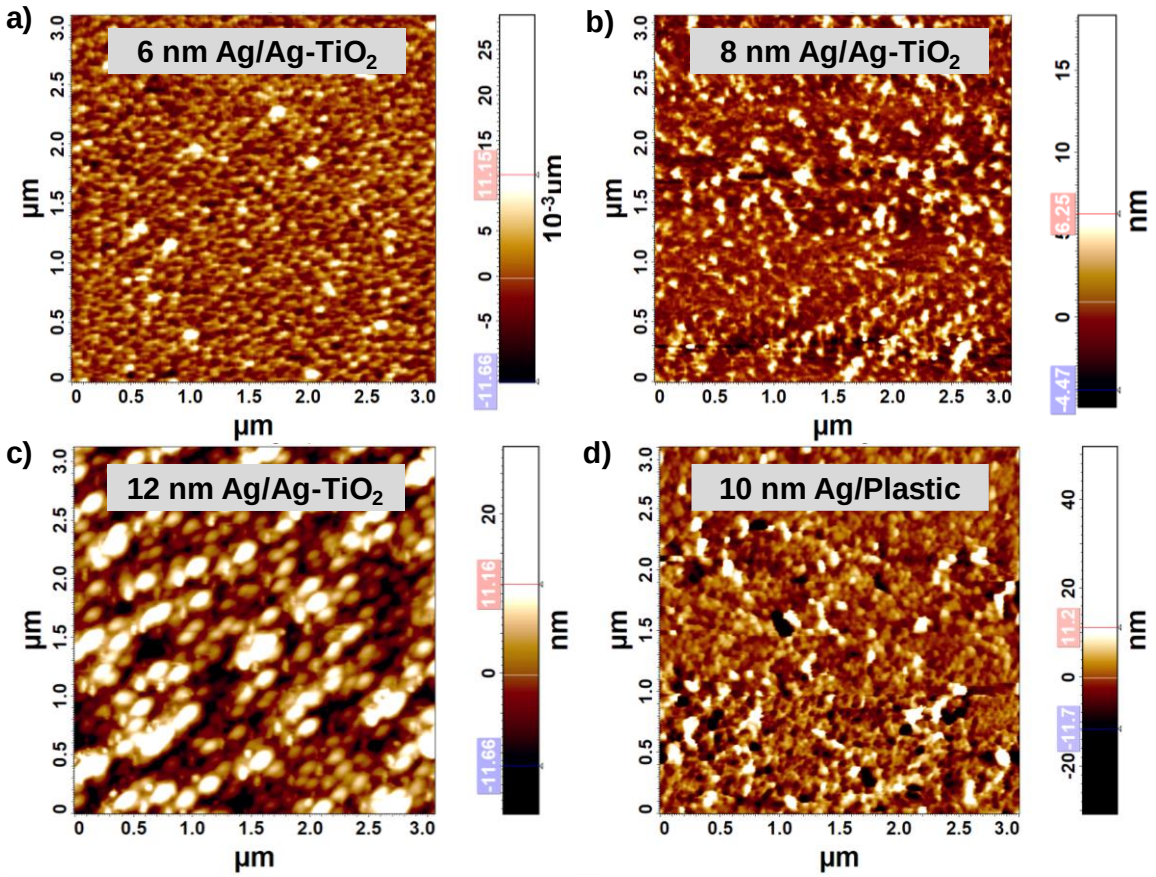

Figure 4.8 2D AFM image of prepared Ag film on Ag-TiO_2 thin film with thickness of **a)** 6 nm **b)** 8 nm and **c)** 12 nm. **d)** AFM image of 10 nm Ag on bare plastic.

Table 4.2 R.M.S Roughness Value for Different Mass Thickness of Ag film

Ag Film	R.M.S Roughness
6 nm Ag/Ag-TiO2/Plastic	3.59
8 nm Ag/Ag-TiO2/Plastic	2.83
10 nm Ag/Ag-TiO2/Plastic	1.75
12 nm Ag/Ag-TiO2/Plastic	6.93
10 nm Ag/Plastic	5.23

The Newman-Ziff cluster algorithm which is a theoretical simulation model based on 2-D square lattice has been used to understand the nature of growth around percolation.

According to their model, when the percolation threshold (P_C) reaches ~ 0.6, percolation starts.[203] The SEM image of 10 nm Ag/Ag-TiO_2 film has been taken as input of this algorithm where the effective coverage area for this percolated film has been considered as P_C (~ 0.7) that determined by ImageJ software. Outcome of this simulation has given the variation of mean cluster size (S) with percolation (P), percolation probability (P_∞) vs P which have been shown in **Figure 4.9**. **Figure 4.9a)** shows as soon as the P approaches the critical threshold, the S value undergoes a rapid transition where isolated clusters start merging together to form larger clusters. This sudden emergence of larger clusters leads to the huge gain in the mean cluster size (S) before network formation. On the other hand, P_∞ vs P plot provides a visual representation of how the probability of percolation evolves as a function of the fraction of occupied sites in **Figure 4.9b)**. According to our SEM data this plot typically exhibits a point at which the percolation probability sharply increases from 0 to 1 (Figure 4.4**c)**), indicating sudden variation of the structure.

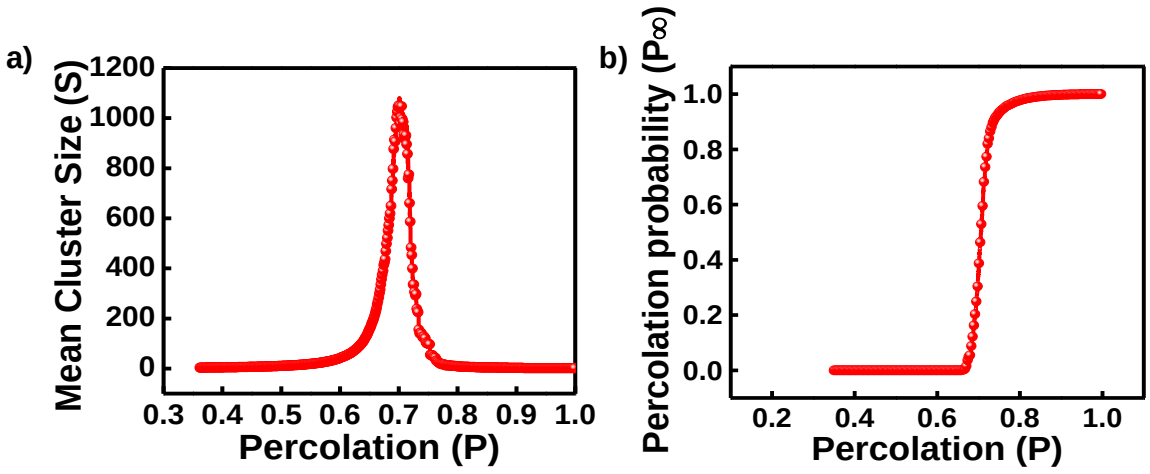

Figure 4.9 Computer-generated Newman-Ziff cluster algorithm data **a)** shows the variation of mean cluster size (S) vs percolation (P) **b)** shows the variation of percolation probability (P_∞) vs Percolation (P). Each point represents the average of 100 distinct arrangements.

TEM analysis of the 10 nm Ag/Ag-TiO_2 TC film is performed for particle size distribution, as illustrated in **Figure 4.10**. For sample preparation, entire film is scratched out with the help of a clean biological surgical blade and collected on a plastic microtube. After the sample is collected, it is dissolved in isopropyl alcohol and dispersed it for 5 minutes in a probed sonicator. Subsequently, a diluted 10 µL drop of this dispersed solution is collected

into a copper coated TEM grid and dried out on a vacuum desiccator for 2 h before characterizing the sample. The Ag NPs have grown within the TiO_2 matrix quite consistently, as seen in **Figure 4.10a)**. From HR-SEM investigation, these results demonstrate that most of the NPs have a size between 5 and 18 nm, with an average particle size of 10.62 nm (**Figure 4.10b)**). Individual lattice d-fringe of Ag NPs and TiO_2 is shown by HR-TEM image (**Figure 4.10c)**) of as prepared sample, suggesting their separate persistence. The average d spacings of Ag NPs and TiO_2 are 0.214, 0.245, and 0.355 nm, respectively, which correspond to the Ag (200), Ag (111), and anatase TiO_2 (101) planes. All these spacings are also defined by the selected-area electron diffraction (SAED) pattern **Figure 4.10d)**, which is well matched with the same set of planes of XRD for 10 nm Ag/Ag-TiO_2 film (Figure 4.1).

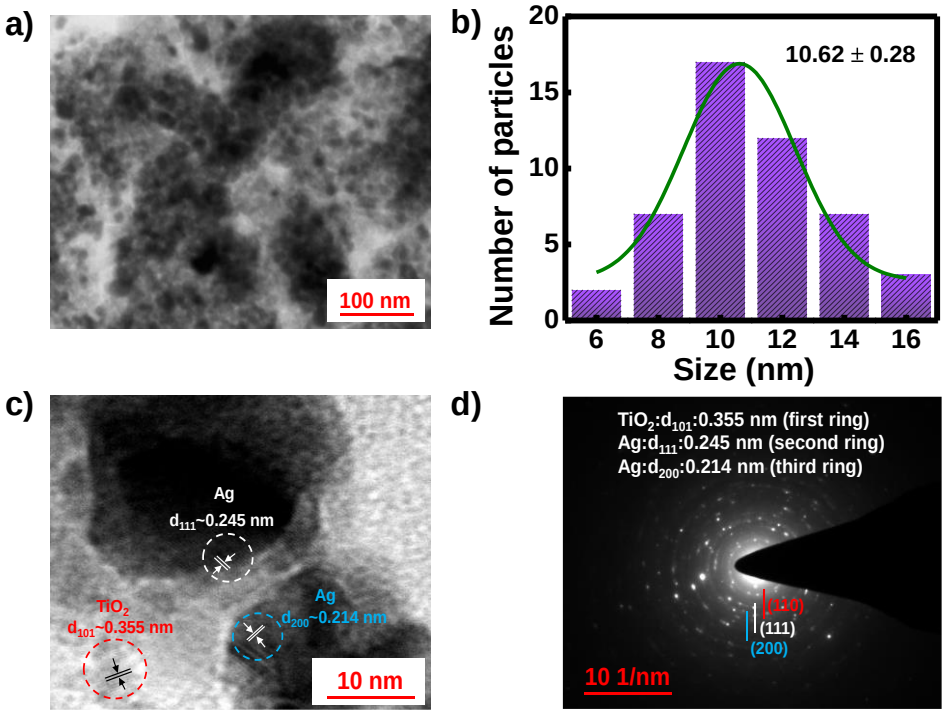

Figure 4.10a) TEM image of 10 nm/Ag-TiO_2 **b)** particle size distribution fitting curve calculated from TEM image **c)** HR-TEM image, the white and bluish ring suggests the lattice d fringe of Ag NPs and reddish ring is of TiO_2 **d)** SAED pattern of 10 nm Ag/Ag-TiO_2 material.

4.3.4 Hydrophilicity test of the 10 nm Ag/Ag-TiO_2/plastic sample

The surface morphology of the fabricated 10 nm Ag/Ag-TiO_2/plastic films are correlated with its macroscopic wettability by measuring equilibrium contact angle (θe) using a host of sessile liquid droplets of constant volume (10 µl), as depicted in **Figure 4.11a)**. The θe of water, ethylene glycol (EG), and N, N-Dimethylformamide (DMF) evolve over time to reach equilibrium values. For a substrate, θe>90° indicates poor wettability and hydrophobicity, while θe<90° indicates good wettability and hydrophilicity. The apparent macroscopic contact angles for different liquid droplets are shown in **Figure 4.11b,c&d)**, with real-time droplet images. The 10 nm Ag/Ag-TiO_2 film on plastic is hydrophilic for all test liquids due to the high surface energy attributed to Ag and TiO_2, which attract polar solvents more strongly. Exposure to UV light during the film development generates hydroxyl groups on the surface, facilitating hydrogen bond formation with polar solvents and resulting in decreased contact angles. Surface roughness also influences wettability; smoother surfaces allow liquids to spread more easily, reducing contact angles. The equilibrium contacts angle for water, EG, and DMF are 58.23°, 42.73°, and 27.34°, respectively. EG and DMF have lower surface tensions than water, leading to easier spreading on the film surface. The surface tension values of the test liquids are sourced from literature, as listed in below (**Table 4.3**).

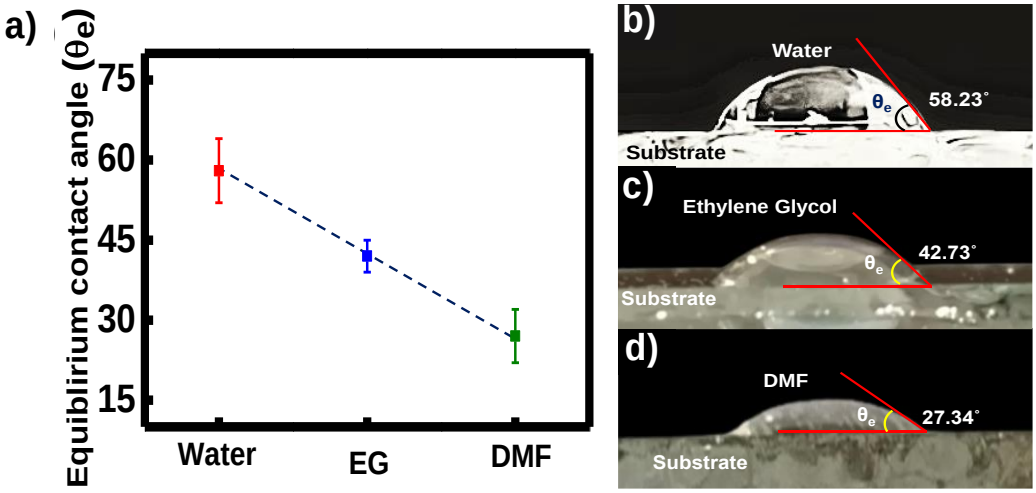

Figure 4.11a) Variation in the equilibrium contact angles, θe with test liquids arranged in decreasing order (L – R) of their liquid–vapour surface tension, γ_l for substrates of specific 10 nm Ag/Ag-TiO_2 film; Real time droplet images on film showing contact angles with **b)** water, **c)** EG, and **d)** DMF respectively.

Table 4.3 Surface Tension Value of Test Liquids

Test Liquid	Water	Ethylene Glycol	DMF
Surface Tension (mN/M)	72	47.7	37.1

4.3.5 UV-Absorption Study

The **Figure 4.12a&b)** shows the picture of comparative transparency of the 10 nm Ag/Ag-TiO_2 sample w.r.t references. Visible transmittance of the conducting film is over 70% where reference (Ag coated plastic) sample shows poor visible transmittance below 60% (**Figure 4.12c)**). Normalized UV-Vis absorption spectra of LTO and 10 nm Ag/Ag-TiO_2 thin films spanning in the 300-900 nm wavelength range are shown in **Figure 4.12d)**. This data indicates the absorption of LTO thin film is in the UV-region (300-350 nm) only whereas the absorption data of 10 nm Ag/Ag-TiO_2 thin film shows an extended absorption in the visible range with an Ag plasmonic peak at 510 nm. The broadening of plasmonic absorption originated due to the large variation of Ag nanostructure of the film morphology.

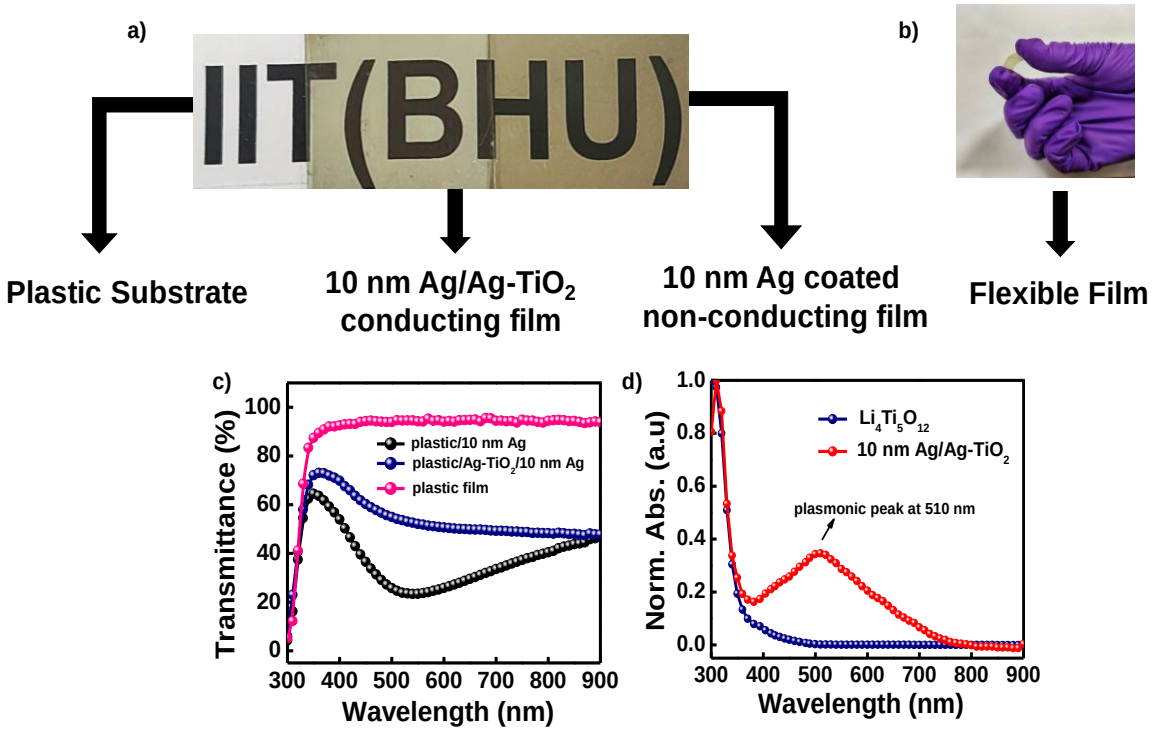

Figure 4.12a) Comparison of optical transparency with plastic substrate, 10 nm Ag/Ag-TiO_2 transparent conducting film and 10 nm Ag coated non-conducting film **b)** image of flexible transparent conducting film **c&d)** optical transparency & UV-Vis absorption spectra of 10 nm Ag/Ag-TiO_2 thin films with reference sample.

4.3.6 Photocurrent Generation under Light

As mentioned earlier, plasmonic photodetectors have been fabricated on top of n^+-Si, where 10 nm Ag/Ag-TiO_2 film works as top electrode with an active area of 0.84×0.84 mm^2 and n^+-Si works as a bottom electrode. Besides, photocurrent of this device is generated from the hot electron generating due to the LSPR of percolated Ag nanostructure. The surface conduction electrons of Ag-NPs that collectively oscillate in response to incident light, leading to enhanced EM fields near the NPs.[55, 81] This enhanced EM field leads to the absorption of incident photons resulting the generation of hot electrons. During electrical characterization of the device, white light of different intensity has been illuminated from the top side of the device that partly transmits and partly absorbed by Ag/Ag-TiO_2 electrode due to the semi-transparent nature and plasmonic absorption of the electrode respectively. **Figure 4.13a)** shows the device configuration where 10 nm Ag/Ag-TiO_2 is used as a transparent electrode. **Figure 4.13b&c)** linear & semi-log plot of electrical current-voltage parameters of this plasmonic photodetector device under dark and light. Linear I−V characterization data ensures the device is a diode in nature. From this semi-log plot, it is clear that the device is rectifier in nature and reverse photocurrent increases with light intensity. When the light intensity is varied from 0 to 400 W/m^2, reversed bias current at 3 V increases from ~8×10^{-6}A to ~2×10^{-3}A, which 265 times w.r.t the dark current. Furthermore, it has been observed that the reverse bias photocurrent variation is nearly linear with the incident light intensity (**Figure 4.13d)**).

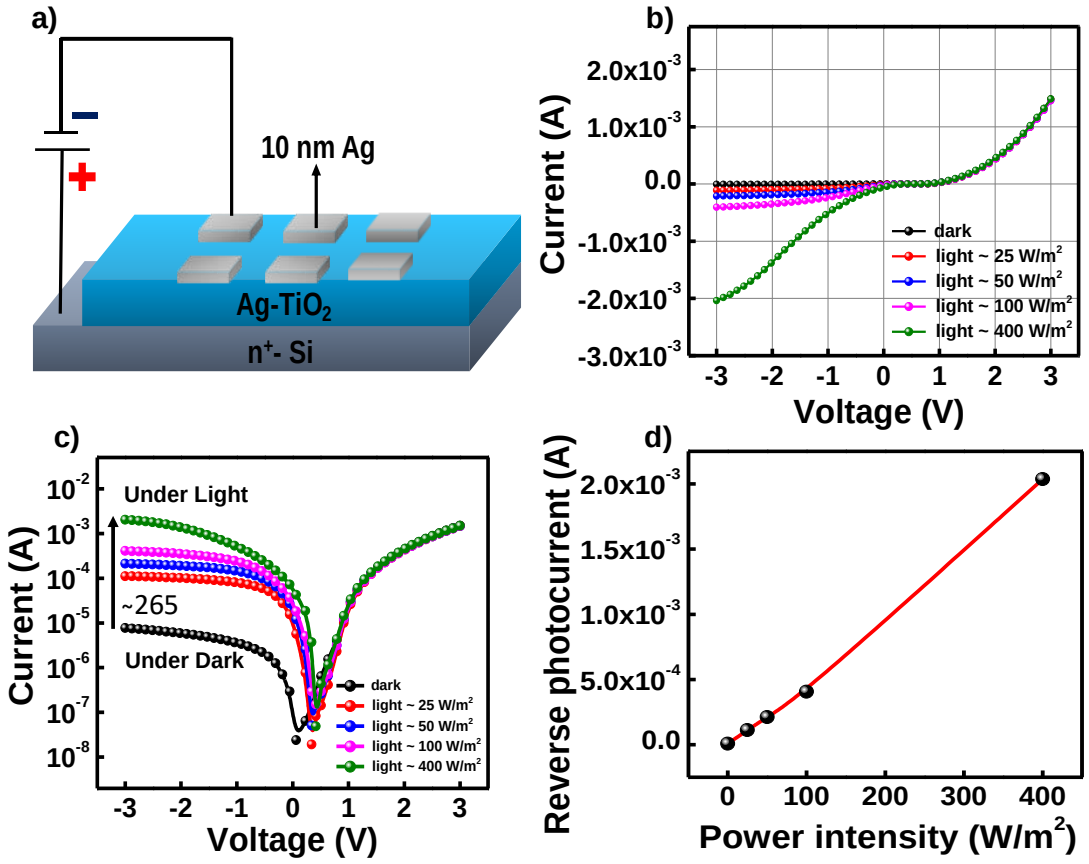

Figure 4.13a) shows device configuration (10 nm Ag/Ag-TiO_2/n^+-Si) **b&c)** linear & semi-log plot which shows immense photocurrent generation of photodiode under dark and light condition **d)** reverse photocurrent vs power intensity curve which shows linear increment of photocurrent generation.

Barrier height and ideality factor of the proposed device under dark and light condition is calculated using **Equation 2.7** and **2.8** respectively. The calculated value of ideality factor and barrier height under dark circumstances are 1.96 and 0.82 eV respectively. Detailed calculation and plots under dark and different light intensities are given in **Figure 4.14a&b)** and **Table 4.4**. Under dark, the ratio of forward bias to reverse bias current at 2 V is ~100. **Figure 4.14c)** shows schematic representations of the relative energy band structure, band bending, and charge separation of the devices under illumination. As soon, light is illuminated, Ag NPs present at top Ag/Ag-TiO_2 electrode exhibit LSPR, leading to strong EM field enhancement near the metal surface, generates hot-electron due to the plasmonic

absorption and subsequently transfers to the conduction band (CB) of TiO_2 and finally reaches to the CB of n^+-Si due to favorable energy band alignment. This rapid charge transfer reduces recombination losses, enhancing the photocurrent generation, thereby improving the photo-response. Hole, on the other hand, is collected by the Ag electrode itself. This generates electron-hole pairs and are separated due to the built-in electric field within the photodiode structure and the different work functions of the electrode materials.

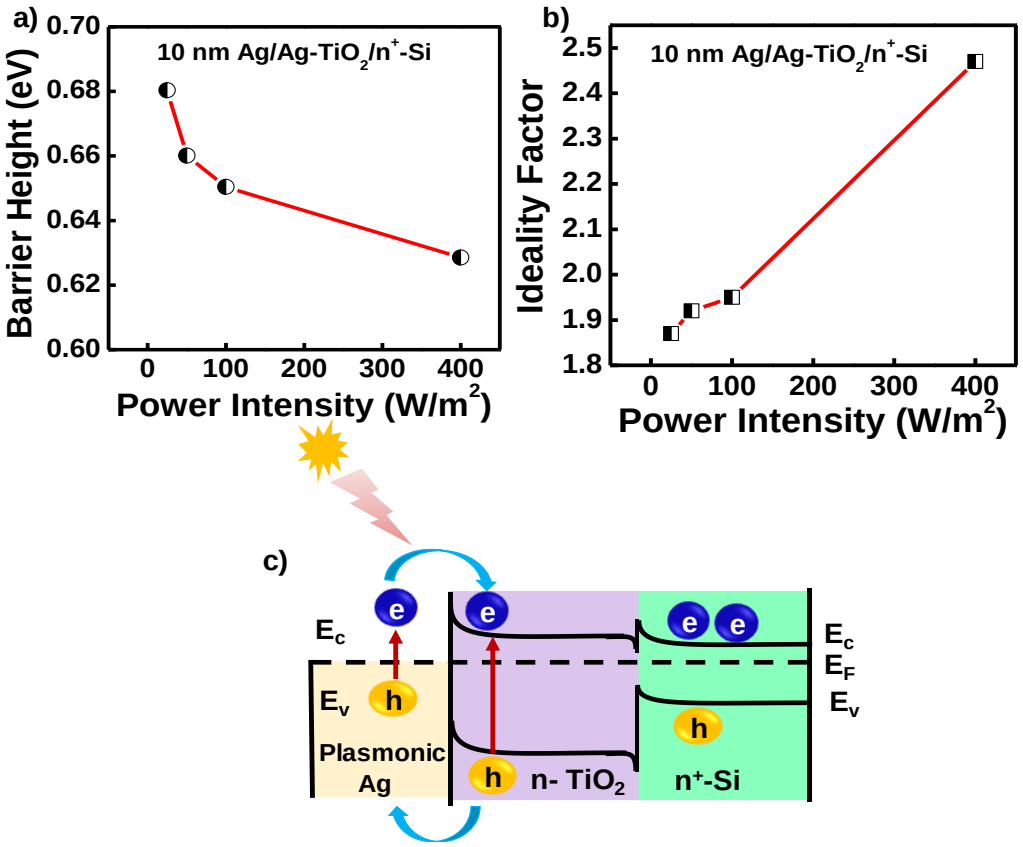

Figure 4.14a) experimental barrier height vs power intensity (Φ_b–P) and **b)** ideality factor vs power intensity (n-P) curve of the 10 nm Ag/Ag-TiO_2/n^+-Si photodiode **c)** band alignment, band bending and charge separation of this hetero-structure photodiode devices.

Table 4.4 Calculated Φ_b and n under dark and different light intensities

Light Intensity (W/m^2)	Barrier Height (Φ_b)	Ideality Factor (n)
0	0.82	1.96
25	0.68	1.87
50	0.66	1.92
100	0.65	1.95
400	0.62	2.47

4.3.7 EQE, Responsivity, Detectivity and Role of Plasmon Induced Hot Electron

The EQE values under different external bias have been measured in the wavelength range of 300 to 1100 nm, as shown in **Figure 4.15a)**. This data implies that EQE value reaches ~ 42.54% at 510 nm under -3V external bias. It can be noted that the EQE spectra of this device is quite similar to the absorption spectra of the Ag/Ag-TiO_2 film (**Figure 4.12d)**) with exactly same peak position (510 nm) which indicates the photocurrent is mostly generated from the plasmon driven hot electron generation. Responsivity and detectivity of the device is calculated from EQE measurement by using **Equation 1.3** and **1.4** respectively. The variation of photo-responsivity under different external biases is depicted in **Figure 4.15b)**. These results show that a maximum responsivity of 15.28 (A/W) can be achieved at 510 nm with an external bias of -3V. As a plasmonic photodetector, this responsivity data is reasonably higher than earlier reports. Besides, detectivity is another fundamental device parameter that suggests the device sensitivity with respect to the minimum signal that can be detected by the photodetector. The variation of the device's detectivities is shown in **Figure 4.15c)**. The highest detectivity of this heterojunction photodetector that has been calculated is of 2.84×10^{12} Jones at 510 nm under -3 V external bias. It is worth mentioning that the plasmonic absorption peak coincides perfectly with the peak of the detectivity at 510 nm, indicating the hot electron of the Ag NPs is primarily responsible for this device's photocurrent generation.

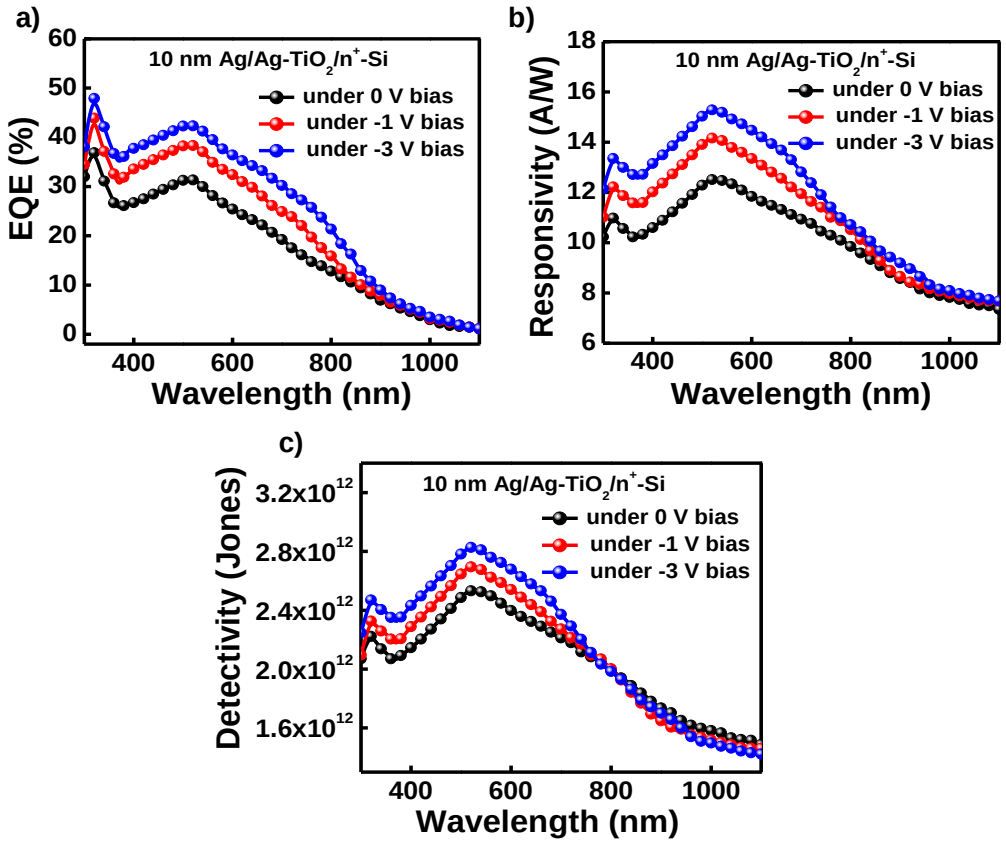

Figure 4.15 illustrates the performance of (10 nm Ag/Ag-TiO_2/n^+-Si) heterostructure photodiode device **a)** EQE vs wavelength **b)** extracted R_λ vs wavelength **c)** extracted D* vs wavelength.

4.3.8 Transient Time Response

Beside device photosensitivity, transient photo response is another key parameter of a photodetector that implies how fast a device can respond and how promptly it can back to its original stage for detecting the next signal. To determine the photo-response of these devices a white light pulse of width and separation of ~ 5 s is illuminated on the device. During this study, the device is subjected to -1V external bias. Photocurrent of the device increases with light intensity, as shown in (**Figure 4.16a)**). Moreover, this transient photocurrent data which is shown in **Figure 4.16b)**, reveals that the device's rise and decay time are ~ 12.36 ms and ~ 12.64 ms respectively, indicating the device has fast photo response and recovery time. Faster transient times are necessary for high-speed applications like optical communication and real-time photography because they indicate a quicker response to changes in light

intensity. A consistent transient response over multiple cycles indicates stable performance, which is important for long-term use in practical applications. Moreover, effective transient response analysis also aids in optimizing the self-bias mechanism to reduce power consumption and boosts energy efficiency of the device. Furthermore, devices are stored in an ambient atmosphere for a few months, although its photosensitivity and transient time remains almost the same, indicating its very high atmospheric stability.

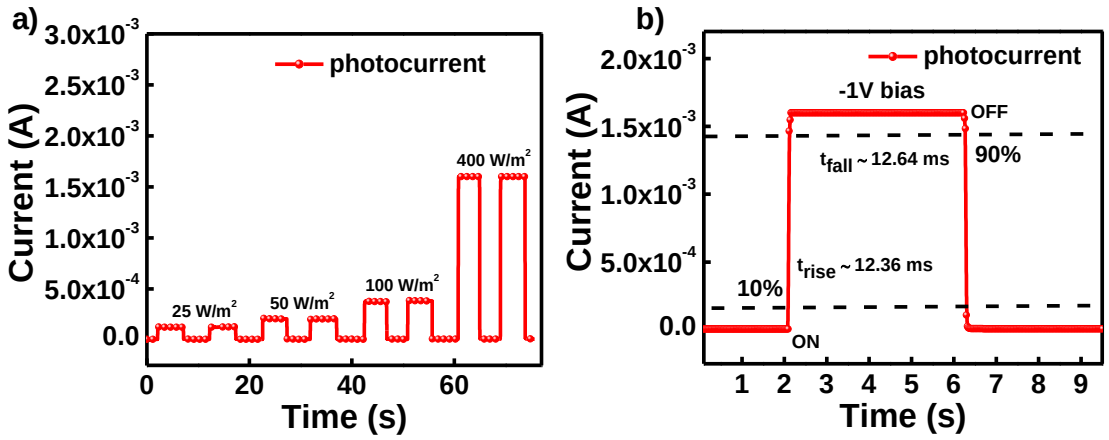

Figure 4.16a) shows the time response of the device **b)** single cycle time response data with rising and decaying times of ~ 12.36 ms and ~ 12.64 ms, respectively.

For a comprehensive assessment of our device's performance, a summary of previously published work on photodetectors based on plasmonic hot electrons is presented in **Table 4.5**. It can be noted that earlier investigations into hot-electron photodetectors have primarily focused on spectral response (R_λ) and the rise-to-fall time ratio (t_{rise}/t_{fall}). Although, important parameters of the hot electron photodetectors are the EQE and D* spectra analysis from where contribution of the hot-electron can be realized, have not been explored in most of the reports. Again, in our previous work on the Ag-TiO_2 based hot-electron photoconductor device (ACS Applied Nano Materials 2023, 6 (16), 15119−15127) photo response is very slow with poor EQE (2.76%) and detectivity (3.19×10^{11}). In comparison to other reported hot-electron photodetectors, this (10 nm Ag/Ag-TiO_2/n^+-Si) plasmonic hot-electron photodetector exhibits a higher responsivity, higher detectivity with extremely fast response speed.

Table 4.5 Comparison of the performance of the current plasmonic hot electrons photodetector with that of other similar devices employing plasmonic hot electrons

Device	λ (nm)	EQE (%)	R (A/W)	D^*(Jones)	τ_r/τ_f	Ref.
10 nm Ag/Ag-TiO_2 / n^+- Si	510	42.54%	15.28	2.82×10^{12}	12.3/12.6 ms	This Work
Ag-TiO_2/TiO_2/ SnO_2/glass	420	2.76%	0.98	3.19×10^{11}	1.2/0.95 s	[106]
Porous Ag/TiO_2/Ti	450	–	3.3×10^{-3}	9.8×10^{10}	112/24 µs	[165]
Ag/TiO_2 NTs/FTO	370	–	176.30	–	82/14 s	[172]
Porous Au/Si	–	–	3.5×10^{-3}	–	–	[173]
Au nanorods/Si	–	–	1.0×10^{-5}	–	–	[154]
Au/Pyramid-Si	1200	–	8.2×10^{-3}	1.8×10^{10}	–	[159]

4.4 Conclusions

In conclusion, a sol-gel derived synthesis technique has been developed to deposit LTO thin film on mechanically flexible plastic substrate at low temperature by combined heating (at 100˚C) and UV illumination. Then, the loosely bound Li^+ of this thin film has been replaced by Ag^+ through an ion-exchange process that forms an Ag-TiO_2 thin film. A thermally evaporated 10 nm Ag has been deposited on top of this Ag-TiO_2 thin film, which shows high electrical conductivity (50 ohm/□) and over a 70% average visible transmittance in the range

of 350-450 nm wavelength. This high electrical conductivity of the film appears due to the higher lateral growth of Ag during thermal evaporation w.r.t reference clean plastic substrate. A growth mechanism has been proposed to understand this Ag NPs induced lateral growth of the film. This film also shows a vibrant plasmonic absorption that limits the transparency of the film. By utilizing combined optical transparency and plasmonic absorption features of this thin film, a plasmonic photodetector has been fabricated on top of a n^+-Si substrate where, 10 nm Ag/Ag-TiO_2 thin film works as plasmonic electrode and n^+-Si substrate as counter electrode. Device shows a very high photosensitivity in the visible region. It has been observed that the EQE spectra of this device has a great similarity with the absorption spectra of 10 nm Ag/Ag-TiO_2 thin film. Same absorption and EQE peak position (510 nm) reveals that the contribution of plasmonic hot electron is highly responsible for the photocurrent generation of the device. Device shows very high EQE, photo responsivity, and detectivity of values 42.54%, 15.28 A/W, and 2.84×10^{12} Jones, respectively at (510 nm). Moreover, devices show extremely fast photo response with a rise and decay times of 12.36 ms and 12.64 ms respectively. Overall performance of this plasmonic photodetector is significantly higher than the previously reported article, that gives a visible way to fabricate reliable hot electron-based photodetectors.

Chapter 4

2nd Part: Cost Efficient Ag/Ag-TiO_2 Coating Based Flexible Transparent Heat Reflector for Energy-Saving Smart Window

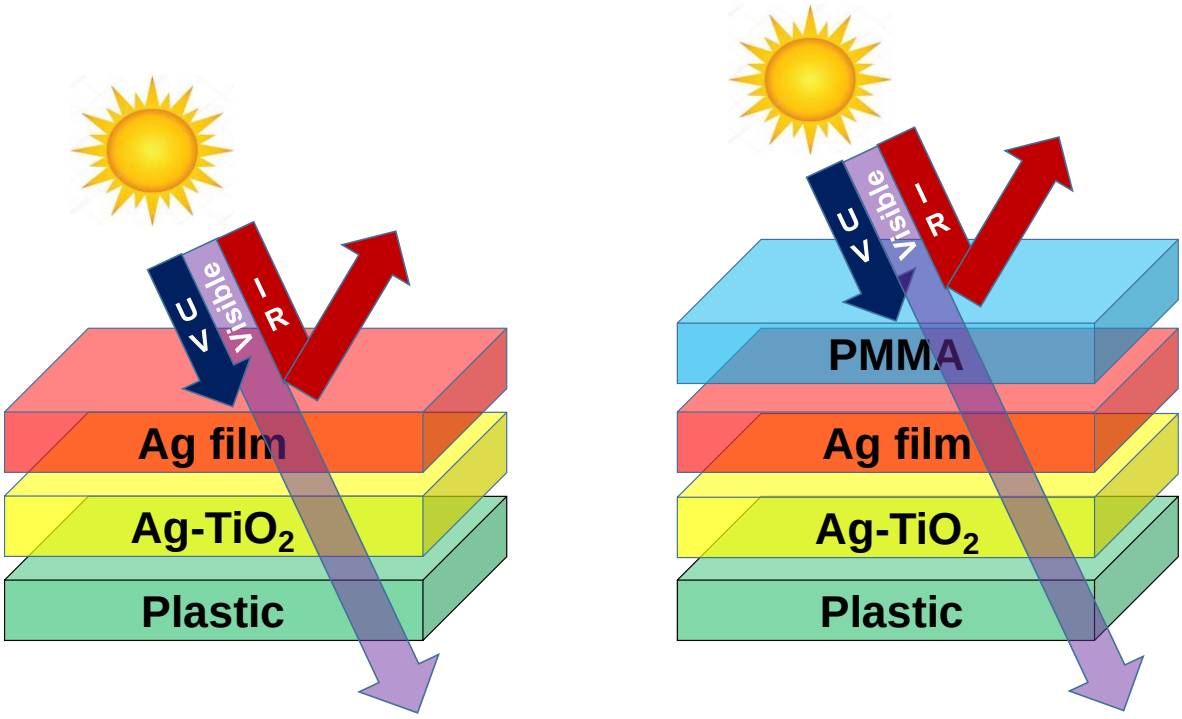

This work is a continuation of chapter 4 first part for the development of a mass-producible and low-cost transparent heat reflector (THR) on a flexible PET substrate by using a per-deposited Ag nanostructures thin film which is grown in two step deposition method. Initially, a polycrystalline LTO thin film has been grown on a plastic substrate by a low temperature processed sol-gel technique. Afterword, mobile Li^+ of LTO thin film has been replaced by Ag^+ by an ion-exchange method to form Ag-TiO_2 thin film. In the second step, 10 nm Ag has been deposited on top of Ag-TiO_2 thin film by thermal evaporation. This bilayer THR has IR/NIR reflectivity of ~85-90% in combination with its visible transmittance of ~50-70%. For higher environmental stability of this THR, a polymer film (PMMA) has been coated on top of this Ag/Ag-TiO_2 coating. To realize the practical application of this THR, a prototype box with one transparent glass window coated with this THR film has been developed and its internal temperature has been investigated during daytime. A reduction of internal temperature of ~6-7˚C has been observed due to this THR coating w.r.t the reference uncoated box, indicating its plausibility as energy-saving smart window applications.

4.5 Introduction

The major source of contemporary global warming and environmental degradation is the utilization of fossil fuels.[204-206] One way to significantly reduce worldwide energy usage is to develop and implement an efficient cooling or heating system that maintains interior comfort using minimal electricity.[207, 208] The design of next-generation smart windows holds a long-term influence on the environment's sustainability,[209] energy consumption efficiency[210, 211] and human health behavior. THR coating has a high reflectivity in NIR/IR radiation with high transmittance in the visible region.[212-215] Heat flux mainly quantifies the amount of thermal energy transferred per unit time through a unit area. Heat flux through a material, particularly in the context of windows, depends significantly on the position of the visible (380-760 nm) to NIR/IR (700-2500 nm) bands. It is known that the heat flux from visible light is significantly lower compared to NIR. In earlier work, it has been demonstrated that approximately ~50-60% of heat flux of solar irradiation exists in the

NIR region compared to the visible region (~10-15%).[216, 217] Therefore, it's very important to develop a NIR/IR reflecting coatings to a window for blocking heat transmission through the glass during daytime, saving energy for air conditioning cooling cost throughout the summer.[218, 219] Simultaneously, sufficient transmission efficiency in the visible spectrum of the window is required to ensure optimum visibility which can reduce the daytime electric cost of light. Traditional glass windows not only enable the visible light to pass through it, but also allow heat transmission through it, which in turn increases the indoor temperature. Therefore, THR materials must be highly transparent in the visible region (350-650 nm) and should have a high NIR/IR reflectivity (700-5000 nm).[125, 126, 220, 221]

Till now a number of concepts have been introduced to develop high performance THR. Among them sandwiching a thin layer of metal in between two dielectrics in a dielectric/metal/dielectric (DMD) is the most successful approach.[222, 223] However, the fabrication cost of these multilayer stacked structures is not economical in most of the cases. These DMD structure are mostly developed based on different physical vapor deposition like sputtering, e-beam evaporation and also frequently include expensive materials like Au for its optimum reflectivity spectra in NIR/IR region, but its potential is limited by its steep cost.[224] Besides, thermo-chromic materials[225-229] have also been widely studied because of their temperature dependent transmission/reflection properties. Although the performance of such thermo-chromic materials as THR depends on their phase transition temperature.[230] Among different thermo-chromic materials, doped vanadium dioxide (VO_2)[231-236] is widely investigated due to their insulator-to-metal transition that changes the transmission/reflection spectra of this material. It has been observed that foreign cations like W^{6+}, Nb^{5+}, Ti^{4+}, can greatly reduce the transition temperature and make it a promising material for practical application.[237-240] Though, fine tuning of color change in such thermo-chromic materials is a difficult task. On the other hand, Ag has a high IR reflectivity and lower market price compared to Au, is much desirable for the low-cost transparent heat reflecting window application.[241-243]

In this section of this chapter, a low cost and mass-producible fabrication method of Ag-nanostructured based THR has been reported. A percolated Ag film has been grown during thermally deposited Ag film on an Ag-TiO_2 thin film with a critical mass-thickness of 10

nm. This Ag-TiO_2 film is an Ag nanoparticle embedded TiO_2 thin film that has been deposited on a plastic substrate by a solution processed technique in two individual steps. During thermally grown Ag film on Ag-TiO_2 coated substrate, at a critical mass-thickness of 10 nm, Ag nanostructure becomes percolated. This 10 nm Ag/Ag-TiO_2/plastic shows a visible transmittance of around ~50-70% with an average ~85% reflection in the NIR/IR region. To realize its practical application as THR, a prototype box with one transparent wall coated with this Ag/Ag-TiO_2 film has been developed and its internal temperature has been investigated during daytime. A reduction of internal temperature of ~6-7˚C has been observed due to this coating w.r.t the reference uncoated box.

4.6 Experimental Section

4.6.1 Preparation of Precursor Materials

The synthesis process for LTO via low temperature solution process technique has been explained in **Chapter 2 Chapter 2 Section 2.1.1.** PMMA is used as a protective coating for THR film. The solution is prepared by standard method, reported in **Chapter 2 Section 2.1.7**.

4.6.2 Fabrication of THR Film

The Ag/Ag-TiO_2 based THR film has been fabricated on a flexible PET substrate and the fabrication steps has been explained **Chapter 2 Section 2.3.2**, and schematically present in **Figure 2.7**.

4.7 Results and Discussion

4.7.1 Structural Evaluation (XRD analysis)

Step-by-step XRD analysis of THR film is similar with previous work and discussed earlier in **Chapter 4 Section 4.3.1**.

4.7.2 Surface Analysis (HR-SEM, AFM & HR-TEM)

Surface morphology of Ag/Ag-TiO_2 thin film of different Ag thickness is studied by HR-SEM and AFM. HR-TEM study is done to understand the average particle size of Ag NPs formation within the THR film. Detail study of morphological changes is explained in **Chapter 4 Section 4.3.3**.

4.7.3 Optical Study (Reflectance & Transmittance Spectra)

The optical transmittance and reflectance of Ag/Ag-TiO_2 film for different thickness of Ag film ranging from 10 nm to 14 nm is presented in the **Figure 4.17a&d)** with a fixed thickness of Ag-TiO_2 film. From the reflectance spectra, it can be observed that the reflectance of all these films has reached around ~ 85 % in the range above 1000 nm long with a transparency ~ 70 % in the blue region and ~ 50-60 % in the rest of the visible region. It is also noticed that the increasing thickness of Ag from 10 nm to 14 nm makes it more IR/NIR reflecting while visible transmittance decreases simultaneously. In the visible wavelengths, the transmittance spectra are influenced by absorption of light in the Ag thin film due to plasmonic absorption, which is associated with the interband electronic transitions, due to the excitation of electrons from the d-band to the fermi surface. By increasing the thickness of the Ag layer, larger number bound electrons are excited and therefore transmission reduces further. However, the surface coverage by Ag film increases a bit that results in a small enhancement of reflectance, both in UV-Vis and NIR region. Furthermore, reflectance spectra have been measured up to 5000 nm by a FTIR spectrophotometer. This study indicates the reflection spectra is very flat in the higher wavelength range and reached around 90% as shown in **Figure 4.17b)**. Similar reflectance and transmission studies have been performed with protective PMMA coated Ag/Ag-TiO_2 film with different thickness of Ag layer ranging from 10 nm to 14 nm which is shown in **Figure 4.17c&e)**. In this work PMMA coating has been utilized for the long-term environmental stability of the Ag/Ag-TiO_2 coating. It has been observed that an uncoated Ag/Ag-TiO_2 film starts oxidizing after 3-4 days and affects its optical properties like transmission & reflectance. High visible transmittance and IR/NIR reflectance are the key factors for designing a transparent heat reflector. For this clarification, a graphical presentation has been provided in **Figure 4.17f)**, which shows the transmittance at λ=375 nm and reflectance at λ=1800 nm with different thickness of Ag film. As shown in this figure, transmittance of these Ag/Ag-TiO_2 films

remain within ~ 65-70 % whereas reflectance remains ~ 85-90 %. Moreover, with increasing thickness of Ag, transmission decreases and reflectance increases.

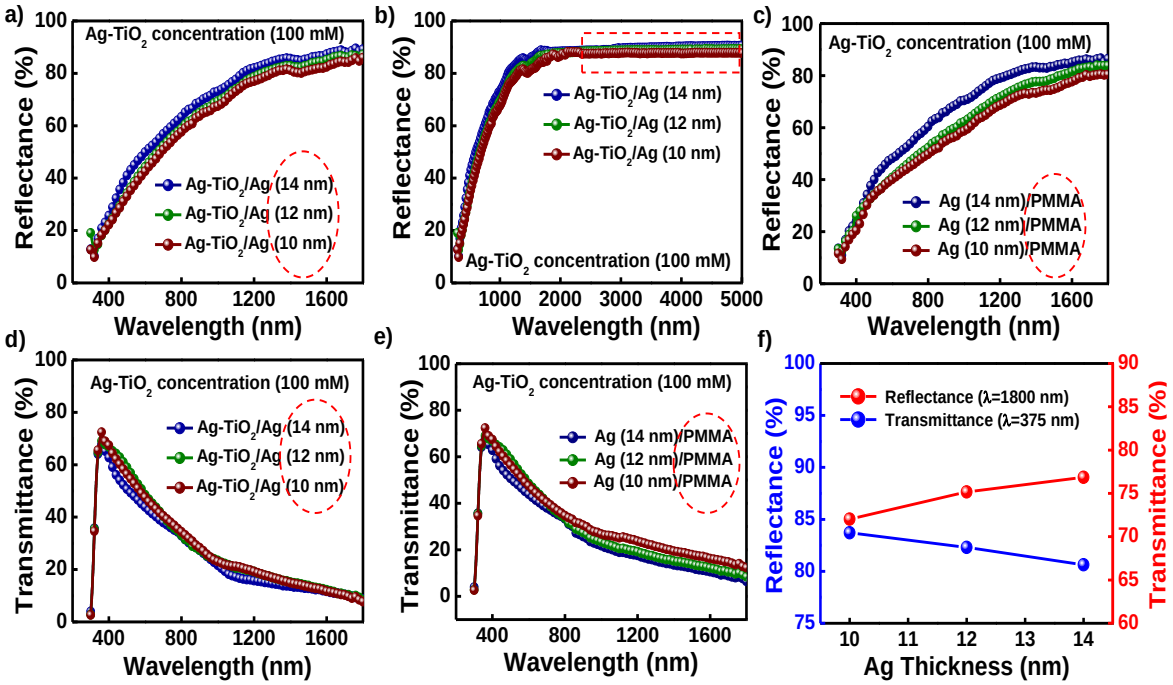

Figure 4.17a) Reflectance spectra of Ag/Ag-TiO_2 film with different thickness of Ag layer ranging from 10 nm to 14 nm **b)** extended reflectance spectra of the film upto far infrared region (5000 nm) **c)** reflectance spectra of the film with PMMA as a protecting layer **d&e)** transmittance spectra of THR film without and with protecting layer **f)** varience of reflectance (λ= 1800 nm) and transmittance (λ=375 nm) spectra ranging from 10 nm to 14 nm thickness of Ag film with fixed Ag-TiO_2 film thickness.

For comparative study with and without coated PMMA over the film as a top matrix, shows optical reflectance and transparency data over the time span of 7 days for a particular wavelength, which is shown in (**Figure 4.18a&b**). However, such oxidation (or color change) is not observed in a 6-month-old PMMA coated Ag/Ag-TiO_2 THR film. Besides, this film is more stable under mechanical bending and also protects the Ag/Ag-TiO_2 coating from mechanical scratching.

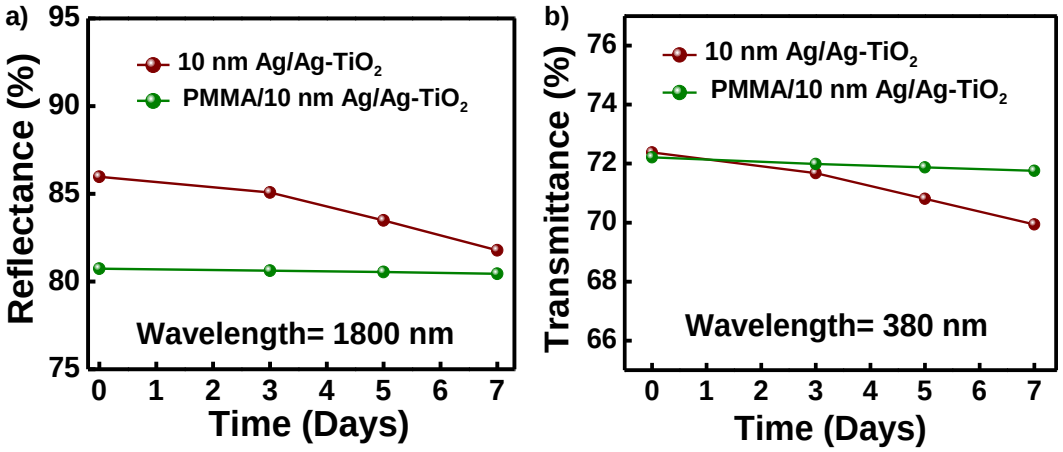

Figure 4.18a&b) Stability comparision of reflectance (at R = 1800 nm) and transmittance (at T= 380 nm) data of 10 nm Ag/Ag-TiO_2 coated THR film with and without PMMA matrix.

To optimize the optical properties of THR, a detailed investigation has been performed by varying the thickness of Ag-TiO_2 layer. From this study, it has been identified that the optimized Ag-TiO_2 layer can be obtained from the LTO precursor concentration of ~100 mM. The cross-sectional SEM study of this Ag-TiO_2 thin film (LTO concentration ~ 100 mM) indicates its thickness of ~ 20 nm (**Figure 4.6c)**). The variation of reflectance and transmittance spectra with different thickness of Ag-TiO_2 layer and fixed thickness of Ag film (10,12&14 nm) is shown in **Figure 4.19a,b,c,d,e&f)**.

To identify the role of Ag-TiO_2 film for THR fabrication, a comparative reflectance and transmission data of 10 nm Ag thin film grown on bare plastic and Ag-TiO_2 coated plastic film are provided in **Figure 4.20a&b)** respectively. In this presentation, reflectance and transmission data of bare plastic film is also provided as reference. This data clearly shows 10 nm Ag film that grown on a bare plastic film has a very poor reflectance in NIR/IR region (~20%) w.r.t the Ag/Ag-TiO_2 layer (~80-85%), whereas the reflectance of bare plastic is only ~16% throughout the spectra. Similarly, comparative transmission data shows that the 10 nm Ag film that grows on Ag-TiO_2 layer has a very poor transmission in the IR/NIR region (~30% at 800 nm)) and its gradually decreasing with wavelength (~20% at 1800 nm).

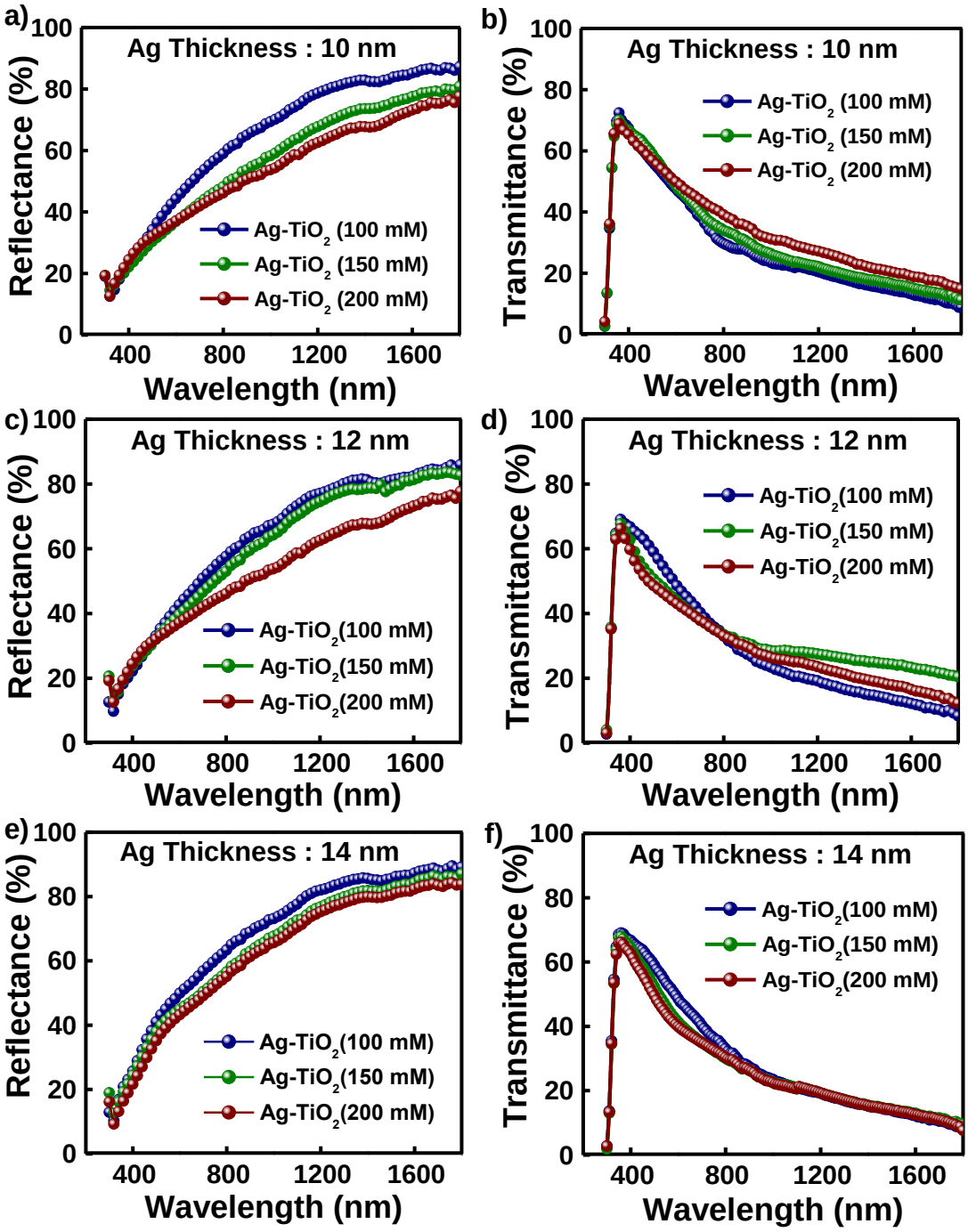

Figure 4.19a,b,c,d,e&f) Reflectance & transmittance spectra of 10,12&14 nm Ag/Ag-TiO_2 THR film with different thickness of Ag-TiO_2 layers varying approximately from 20 nm to 40 nm.

In contrast to that, the 10 nm Ag film on bare plastic shows very high transmission in the NIR/IR region with a dip in the visible region. That dip originated from the strong plasmonic absorption from the granular Ag film that grows on bare plastic, shows that the transmission of the bare plastic substrate is ~ 90% throughout the spectra. The reflectance and transmission data of relatively lower thickness Ag/Ag-TiO_2 film have presented in **Figure 4.20c&d)** respectively. From Figure 4.20**c)** it's very clear that the reflectance of 6 and 8 nm Ag film is very poor (~20%) throughout the spectra whereas reflectance of 10 nm Ag film is very high (~70-85%) in NIR/IR region which is totally different from lower thickness Ag films. The transmission data of these films shows that 6 nm Ag film in NIR/IR region is very high (~60-80%), while 8 nm Ag film has relatively lower transmittance (~40% in NIR/IR region). On the other hand, the transmission of 10 nm Ag film in NIR/IR region is very poor which is due to their high reflecting properties.

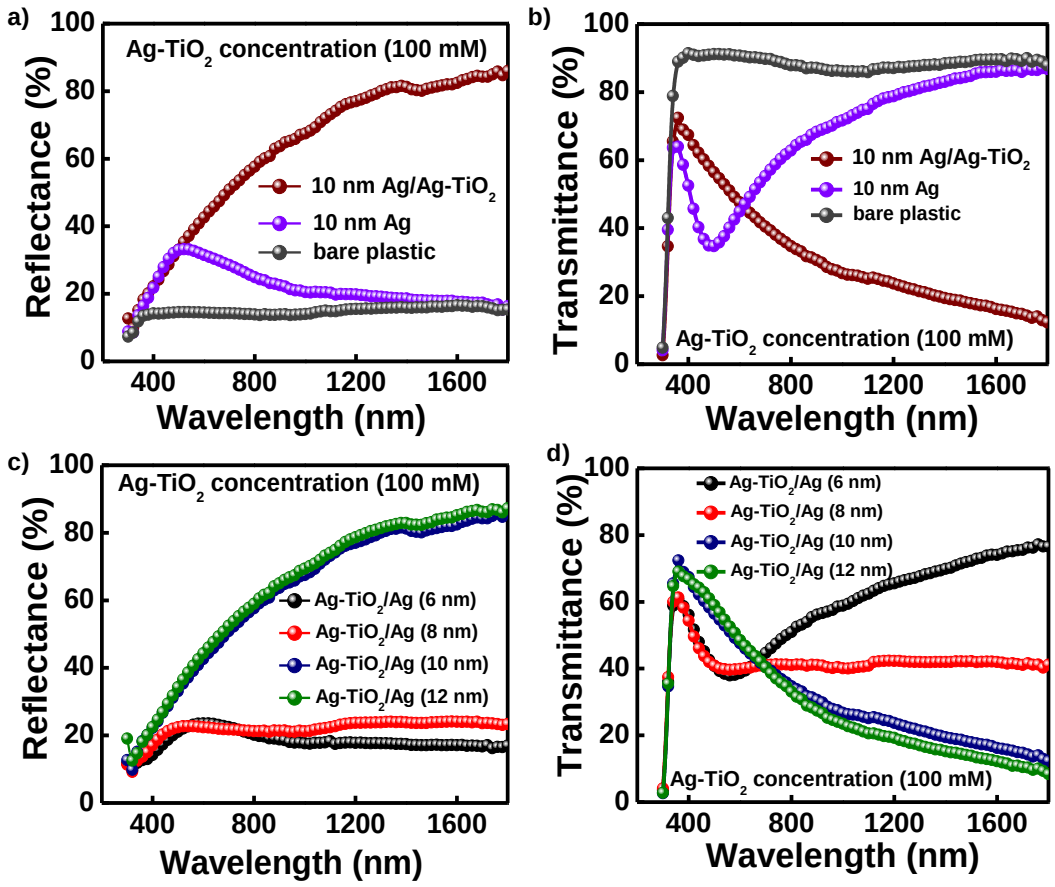

Figure 4.20a&b) Comparison of optical reflectance and transmittance of bare plastic, 10 nm Ag film on bare plastic and 10 nm Ag/Ag-TiO_2 bilayer THR thin film; **c&d)** reflectance &

transmittance data of different thermal evaporated Ag film ranging from 6 nm to 12 nm in present of Ag-TiO_2 thin film.

Figure 4.21a) demonstrates the variation of visual observation of different thickness of Ag/Ag-TiO_2 film. It's clearly shown from the picture that the transparency of 14 nm Ag/Ag-TiO_2 film is significantly lower compared to 10 nm Ag/Ag-TiO_2 film thickness. **Figure 4.21b)** shows the transparency and reflectance of 10 nm Ag/Ag-TiO_2 transparent heat reflecting coating. **Figure 4.21c)** shows the real image of 10 nm Ag/Ag-TiO_2 film with a background of bright color flowers.

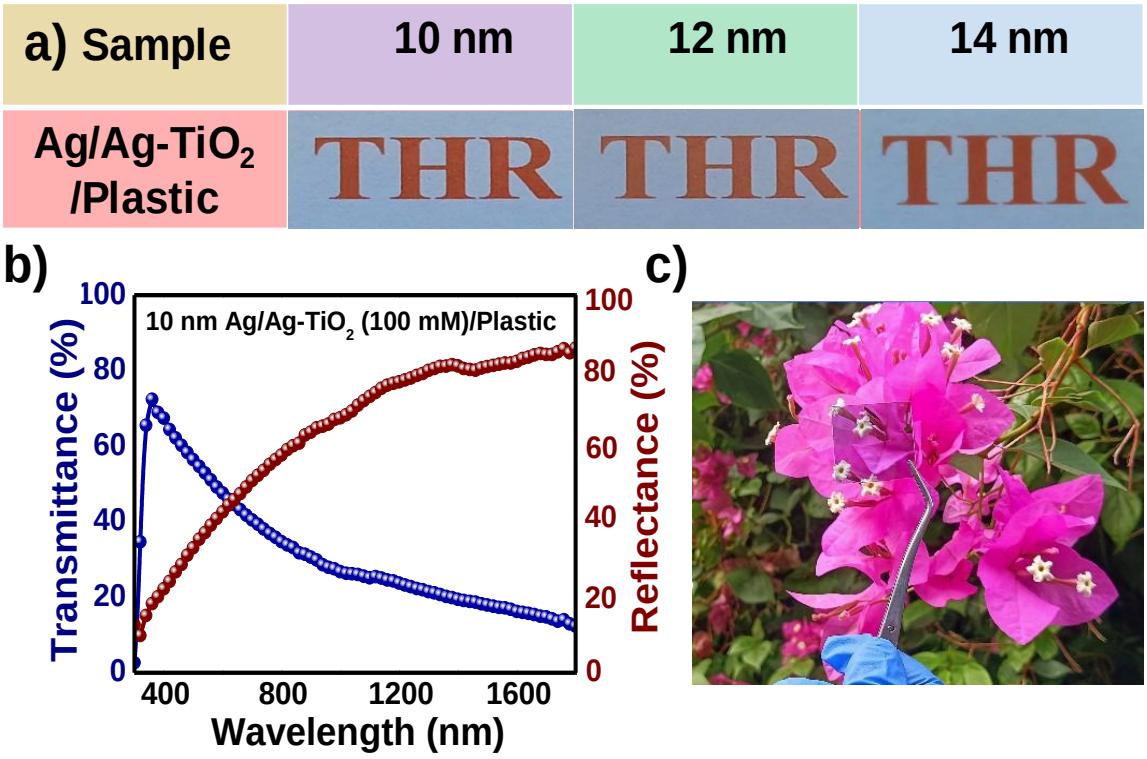

Figure 4.21a) The images of Ag/Ag-TiO_2 transparent heat reflector on plastic substrate at different thickness of Ag film vary from 10 nm to 14 nm with an underlying 'THR' written on a white paper **b)** optical transparency and reflection of 10 nm Ag/Ag-TiO_2 on plastic **c)** practical transparency test with a background of a bight colour flower.

The effectiveness of this 10 nm Ag/Ag-TiO_2 coating as a transparent heat reflector has been investigated throughout a daytime temperature monitoring with a prototype box that has one transparent wall coated with this THR (real photo is attached in **Figure 4.22**. Two identical

thermocol covered wall boxes of dimension 15×15×15 cm^3 with a glass window wall of (10×10 cm^2) have been prepared. In one box, the glass window is coated with 10 nm Ag/Ag-TiO_2 whereas reference box glass window is uncoated. These boxes are kept on a rooftop. Then two identical thermocouples are placed inside the closed boxes for monitoring the inside live temperature. Another thermocouple is attached outside the box to check the live air temperature all over the day. Inner walls of these boxes are coated with white, gray and black papers for three sets of individual experiments. The idea of using different colored inner walls for the experiment of daytime cooling performance is to visualize the effect of temperature difference under different color window wall.

Figure 4.22 Experimental set-up under sunlight outdoor experiment.

The variation of temperature inside the 10 nm Ag/Ag-TiO_2 coating box, reference box and outside air temperature have been monitored throughout the daytime and has been given in **Figure 4.23a,b&c).** The average temperature differences of these three different thermocouples in peak hour of the day (from 12 pm to 1 pm), which is shown in **Figure 4.23d)** for different inner walls. With black insulating inner wall ~15˚C temperature differences have been observed between THR coated and uncoated glass boxes while with white wall this difference becomes ~ 3.5˚C. With the gray wall, there is a temperature difference of ~ 7˚C. Since the boxes are closed, heat is accumulating inside the boxes over the time, which increase the inner temperature. Therefore, the temperature of these boxes is significantly higher than open air temperature.

Besides, heat reflecting property of the 10 nm Ag/Ag-TiO_2 coated window with respect to the glass window has been investigated under steady NIR/IR light (IR lamp) illumination. For this study, one digital thermometer and IR lamp is kept 4 cm behind and 6 cm away from the coated window, respectively. Temperature variations of digital thermometers have been monitored over the time. Same experiment has been also performed for reference uncoated glass window. It is observed that the temperature behind the coated window shows an average ~10-12˚C lower temperature compared to the reference glass window, which is shown in the bar diagram (**Figure 4.23e)**. Real picture of the experiment under the IR lamp is shown in **Figure 4.23f)**.

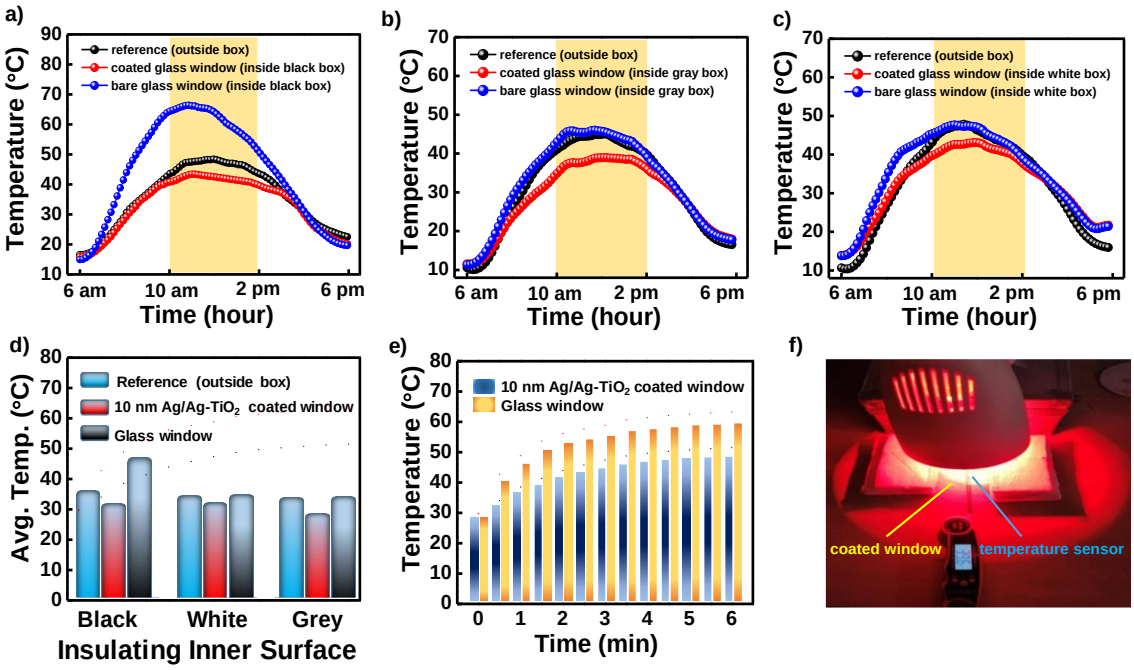

Figure 4.23 Performance of daytime (under sunlight) cooling study of 10 nm Ag/Ag-TiO_2 coated window compare with reference glass window box with inner wall color of **a)** black, **b)** white and **c)** gray; **d)** comparative average temperature difference at the peak hour (12 pm to 1 pm) for different inner color wall of the box; **e)** experimental study (IR lamp) of 10 nm Ag/Ag-TiO_2 coated window compare with glass window; **f)** real image of IR lamp experimental setup

Table 4.6 Comparison of the performance of our develope transparent heat reflector with other material based heat reflecting coating

THR coating	Transmittance at Visible Region	Reflectance at NIR Region	Average Temp. differ. with normal window	Ref.
10 nm Ag/Ag-TiO_2	68-72%	85-90%	6-7ºC	This work
TiO_2/Cu/TiO_2	90%	85-90%	-	[220]
ZnO/Au/ZnO	68-70%	45-50%	-	[125]
TiO_2/VO_2/TiO_2	60-65%	50-55%	-	[126]

4.8 Conclusion

In summary, Ag-based low temperature processed (100˚C) THR has been fabricated on plastic PET substrate. For this deposition, initially Ag-TiO_2 thin film is deposited by a solution processed technique where Ag nanoparticles are grown inside TiO_2 matrix. Subsequently a thermally deposited Ag film is deposited on top of the Ag-TiO_2 thin film. A protective PMMA layer is deposited on top of Ag/Ag-TiO_2 to improve its stability. It is observed that a critical thickness of the 10 nm Ag layer is essential for optimized NIR/IR reflection (~85%) in combination with reasonably high visible light transmittance (~70 % in blue region and ~50-60 % in rest of the visible region). A comparative surface morphology of the Ag/Ag-TiO_2 reveals a morphological phase transition occurs when thermally deposited Ag film reaches 10 nm. During this transition, the circular shape isolated Ag island on Ag-TiO_2 thin film transfers to a percolated finger-like network that has significantly lower roughness than previous stage isolated Ag island film. This phase transition becomes possible due to the lateral growth of Ag induced by pre-existed Ag NPs on TiO_2 matrix. As a consequence, visible transparency of the film increases with an excellent NIR/IR reflectivity. A prototype box with a window coated with Ag/Ag-TiO_2 thin film reveals that a reduction of ~6-7˚C of internal temperature of the box compared to reference glass window, due to the efficient NIR/IR reflectivity of Ag/Ag-TiO_2 thin film. Overall, our approach opens new opportunities to develop highly transparent heat reflecting coating through a low-cost fabrication method which can be utilized for energy saving smart window applications.

Chapter 5

Mechanically Flexible Au-Ag Bimetallic Transparent Conducting Thin Film and its Application as Self-Bias Plasmonic NIR Photodetector

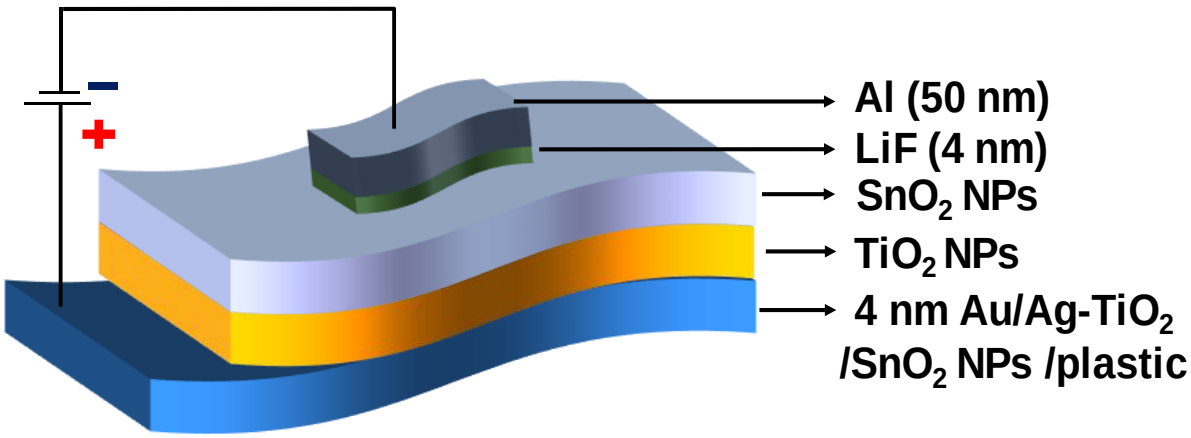

Chapter 5

This chapter mainly focuses on development of a bimetallic Au-Ag TC film fabrication method and its use as a self-bias plasmonic NIR photodetector. This is a follow-up work of the earlier chapter for developing TC and its application. Here, a 4 nm PVD deposited Au is grown on a pre-deposited Ag-TiO_2/SnO_2 (or ZnO NPs) thin film that enhances the transparency, conductivity and environmental stability of the TC. This Ag-TiO_2 thin film is a Ag nanoparticle embedded TiO_2 thin film that has been grown over SnO_2 (or ZnO NPs) which leads to a percolated nano-porous-like structure. Prior to this, surface morphology of the film shows a clear transition from spherical NPs to percolated nano-porous Au-Ag bimetallic nanostructure with random hole formation that result in an abrupt jump of electrical conductivity when deposition reaches to 4 nm mass thickness of Au. This percolated nano-porous structure thin film (4 nm Au/Ag-TiO_2/SnO_2 (or ZnO NPs) /plastic) has a low resistivity of ~ 10-15 ohm/□ and an average visual transmittance around 75-80 % in the visible region. This film has been used to develop a metal-semiconductor-metal (M-S-M) plasmonic hot electron photodetectors where Au-Ag thin film works as a photo-excited hot electron generation as well as transparent bottom electrode. The EQE data reveal that photocurrent of this device is mostly generated in the plasmonic absorption region with a peak detectivity of 1.6×10^{13} Jones at 750 nm under -2V external bias. Besides, the device shows fast response with a response time of ~33 ms.

5.1 Introduction

Plasmonic Transparent Conductors (TCs) are an essential component in many opto-electronic devices, such as touch screens, wearable sensors, memory device, Organic Light-Emitting Diodes (OLED), solar cells, and smart windows.[244-250] Over the past few decades, Indium Tin Oxide (ITO) and Fluorine Tin Oxide (FTO) based materials have played a major role in the current market share due to its high optical transparency (T~90%) and low sheet resistance (R_s <100 Ω/□).[116, 117] On the other hand, indium is not an abundant materials.[119] It has a few limited applications because of its low resistance to mechanical

stress (lack of flexibility) and a difficult manufacturing process.[118] In the last decade, tremendous efforts have been admired for the development of next generation transparent conductive films. Among various options, carbon nanotube or graphene has higher mechanical flexibility as well as optical transparency.[175, 176, 251] Although, the electrical conductivity of these ITO or carbon-based TCs is quite lower with respect to metals like Ag, Cu, and Au. So, metal nanoparticles or metal nanowire networks are emerging as a promising alternative to ITO, especially in flexible and stretchable electronics.[252, 253] This is mainly because of their superior mechanical flexibility, high optical quality, low sheet resistance, and low production costs. Among different metals, Ag has the highest intrinsic conductivity and least refractive index (n) in the visible region compared to Cu or Au. Therefore, the development of TC material is often accomplished in the majority of those investigations using either Ag nanowire or oxide/Ag/oxide multi-stack thin film.[181, 254, 255] Even in so many reports, Cu nanowires are also well studied for developing TC material.[256] But both Ag and Cu individually show poor chemical stability against oxidation.[257, 258] On the other hand, Au shows the highest chemical stability, but it shows the least intrinsic conductivity compared to Ag or Cu. Considerable research has been devoted to solving this issue, mostly by exploiting a core−shell structure that encapsulates metals with an inert shell which is a cost-effective process.[259, 260]

The overgrowth of a metal onto the surface of another metal represents a synthetic challenge. **Yuan et al**. revealed that the galvanic reaction between Ag and $HAuCl_4$ could be blocked in the presence of strong reducing agents.[261] There are very few papers that describe the development of TC material using bimetallic Au-Ag, Ag-Cu, or Au-Cu core structures. Despite the encouraging progress in the literature, it's important to fabricate TC material that shows excellent optical transparency, electrical conductivity, mechanical flexibility as well as chemical stability against oxidation. However, these thin metal films have very strong plasmonic absorption which is a key barrier to achieving high optical transparency of those films.[123, 184]

Although plasmonic absorption is a key bottleneck in developing metal-based highly transparent conductors, it's useful for developing various opto-electronic devices including solar cells, plasmonic photodetectors, gas sensors, and LEDs.[186, 189, 192] So many

reports claim that the plasmonic effect of those transparent electrodes can generate hot-electron induced photocurrent which can be beneficial for photocurrent generation of solar cells, photodetector, and photo-electrochemical H_2 generation.[190, 191] When EM waves interact with MNPs, part of that EM waves is scattered and the rest of the part is absorbed by MNPs due to the SPR. This SPR absorption of MNPs increases whereas scattering reduces with reducing particle size. Besides, the shape of metal NP, the relation of dielectric constant of MNPs, and surrounding are also important parameters for SPR related absorption of MNPs.[81] Due to the SPR, MNPs either generate electron-hole pairs or go through radiative decay to the far field. Again, this generated electron-hole pair can produce hot-electron through non-thermal electron distribution via electron-electron scattering. To utilize this hot-electron for optoelectronics device application, a semiconductor-metal Schottky junction is required through which it can be injected into the semiconductor within a very short period (<100 fs), before non-radiative energy relaxation of hot-electron through electron-phonon scattering. Besides, for efficient electron injection of this hot-electron in the Schottky junction, a low barrier height (Φ_b) Schottky junction is required.[154] In plasmonic devices, this metal-semiconductor Schottky junction has been developed by varsities ways like; by depositing a metal thin film on a nanostructured semiconductor surface followed by inert atmosphere annealing to form MNPs, MNPs-metal oxide thin film, semiconductor-metal thin film hetero-junction etc.[195, 199] Therefore, Au-Ag bimetallic nanostructures can provide a combined effect of both metallic properties. Interestingly, Ag nano-structures allow the growth of Au NPs on their surface due to the same lattice match between their crystal structures, leading to the synthesis of bimetallic nanostructures. The growth of Au NPs onto another metal surface like Ag NPs leads to the creation of different dipolar and multipolar LSPR. Directed overgrowth of Au on Ag can tune nanostructured SPR from visible to NIR region. This overgrowth of Au is highly dependent on the core Ag geometry. By varying the amount of metal NPs used during the growth process, SPR can be tuned towards NIR which leads NIR sensitive plasmonic photodetector, SERS based applications.[262, 263] In addition, several reports claim that the opto-electronic devices performance can be improved by using a plasmonic electrode. In a plasmonic photodetector, the contribution of hot electrons is commonly realized from the external quantum efficiency (EQE) measurement that indicates a strong photocurrent generation in the plasmonic absorption region of MNPs.

However, there are very limited reports that demonstrate identical plasmonic absorption and EQE spectra of the device. Moreover, those devices show quite poor response for different plasmonic photodetector applications.

This chapter reports the synthesis of Au-Ag bimetallic transparent conducting film on plastic substrate at a low processing temperature (100˚C). The as-synthesized Au-Ag bimetallic thin film is highly conductive with sheet resistance as low as 5-10 Ω/□ with more than 80% transparency. At the initial stage of the growth, it has been observed that the nucleation density of Au on this substrate is much higher than bare plastic substrate which are originated by pre-deposited Ag islands of the Ag-TiO_2 film. However, after a critical size growth of those grains, granular film undergoes a solid-state dewetting process which makes it possible to deposit percolated finger-like Au-Ag nanostructured thin film. As a consequence, the resistivity of the film dropped suddenly. Besides, due to the lower mass thickness of Au film, transparency has been maintained over 80% in the visible region. However, it drops to ~50-60% in the higher wavelength region of light due to the plasmonic absorption of the film. To analyze the surface phenomena of this percolated finger-like Au-Ag nanostructured we developed a percolation model which tells about the nature of percolation threshold during growth. Besides, this transparent-conducting Au-Ag bimetallic film has been used as a plasmonic electrode for developing high performance hot-electron photodetectors. The device has been fabricated on the same plastic substrate as well as a highly doped silicon (n^+- Si) substrate that shows extremely high detectivity with fast response speed. The UV-Vis absorption spectra of Au-Ag bimetallic TC film show a strong SPR absorption from visible to NIR region which has an excellent spectral matching with the EQE spectra of the photodetector, implying the major contribution of hot-electron in the photocurrent generation of the device.

.

5.2 Experimental Section

5.2.1 Preparation of Precursor Materials

The preparation process for SnO_2 NPs, ZnO NPs, TiO_2 NPs and ion-conducting dielectric LTO via low temperature solution process technique has been explained in **Chapter 2 Section 2.1.3, 2.1.4, 2.1.6 and 2.1.1.**

5.2.2 Fabrication of Au-Ag TC Film and Plasmonic NIR Photodetector

Bimetallic Au-Ag based TC film has been fabricated on a flexible PET substrate and the fabrication steps has been explained **Chapter 2 Section 2.3.3**, and schematically present in **Figure 2.9**. For fabrication of a photodetector, these optimized mechanically flexible bimetallic Au-Ag TC thin film have been used as transparent bottom electrode to develop NIR active plasmonic photodetector in a photodiode geometry which is schematically present in **Figure 2.10**.

5.3 Results and discussion

5.3.1 Electrical and Optical Characterization of Flexible Au-Ag Bimetallic Transparent Conductor

To measure the electrical conductivity of prepared Au-Ag TC films, parallel Ag electrodes (thickness ~ 50 nm) of separation 0.45 mm have been deposited over the conductive film. **Figure 5.1a)** depicts the semi-log plot of current density vs voltage (J-V) graphs of those 4 nm Au/Ag-TiO_2 thin films with SnO_2 or ZnO NPs. This data implies that conductivity of 4 nm Au/Ag-TiO_2 film with SnO_2 NPs is higher w.r.t ZnO NPs. Besides, it can be noted that a significant quantity of current (~ mA) is produced by applying a relatively modest voltage of 0.05 V. Besides, to test the flexibility of the prepared film, we examined the conductivity of our best performed device (4 nm Au/Ag-TiO_2/SnO_2 NPs) with different bending cycles in **Figure 5.1b)** upto 100 (bending radius ~ 4 mm). This study indicates that conductivity of the film remains almost unaltered even after 100 cycles of bending, which implies this conductor is suitable for fabrication of flexible photo-voltaic devices.

The optical transparency of the 4 nm Au/Ag-TiO_2 thin films with SnO_2 or ZnO NPs has been investigated and is shown in **Figure 5.1c)**. This data implies that the 4 nm Au/Ag-TiO_2/SnO_2

NPs conductor has an excellent optical transparency of ~ 80-82 %, where ZnO NPs based device shows an optical transparency around 76-78 % in the wavelength region of 500-600 nm. As film is showing better transparency and conductivity with SnO_2 NPs compare to ZnO NPs, for other characteristic we mainly go through SnO_2 NPs compatible TC film. For longer wavelengths, films transparency is reduced to ~ 65-70 %. The reduction of transparency arises mainly due to the plasmonic absorption of the film. The phenomena of conductivity and transparency are interconnected for any TC devices. Besides, resistance vs temperature of (4 nm Au/Ag-TiO_2/SnO_2 NPs) samples has been measured by four probe methods. The sample shows moderate drop in resistance upto 200 K which indicates fully metallic behavior of the film **Figure 5.1d)**.

The precise form of this dependency is defined by the impact of varying deposition conditions on the electro-optical characteristics of these layers. However, for any conducting film sheet resistance (R_{sh}) is an important measurement. Our calculated R_{sh} for both films are listed below in **Table 5.1.** The **Figure 5.1e)** shows the real picture of comparative transparency of the 4 nm Au/Ag-TiO_2/SnO_2 NPs w.r.t references. Our reference Device (4 nm Au/plastic) and only plastic film transparency spectra are given in (**Figure 5.2**).

Table 5.1 Electrical Sheet Resistance and Visible Transmittance Value of Mechanically Flexible Au-Ag TC Film

Au-Ag bi-metallic film	Sheet Resistance (Ω/□)	Visible Transmittance (%) λ= 550 nm
4 nm Au/Ag-TiO_2/SnO_2 NPs	5.37	81.48 %
4 nm Au/ Ag-TiO_2/ZnO NPs	14.63	77.69 %

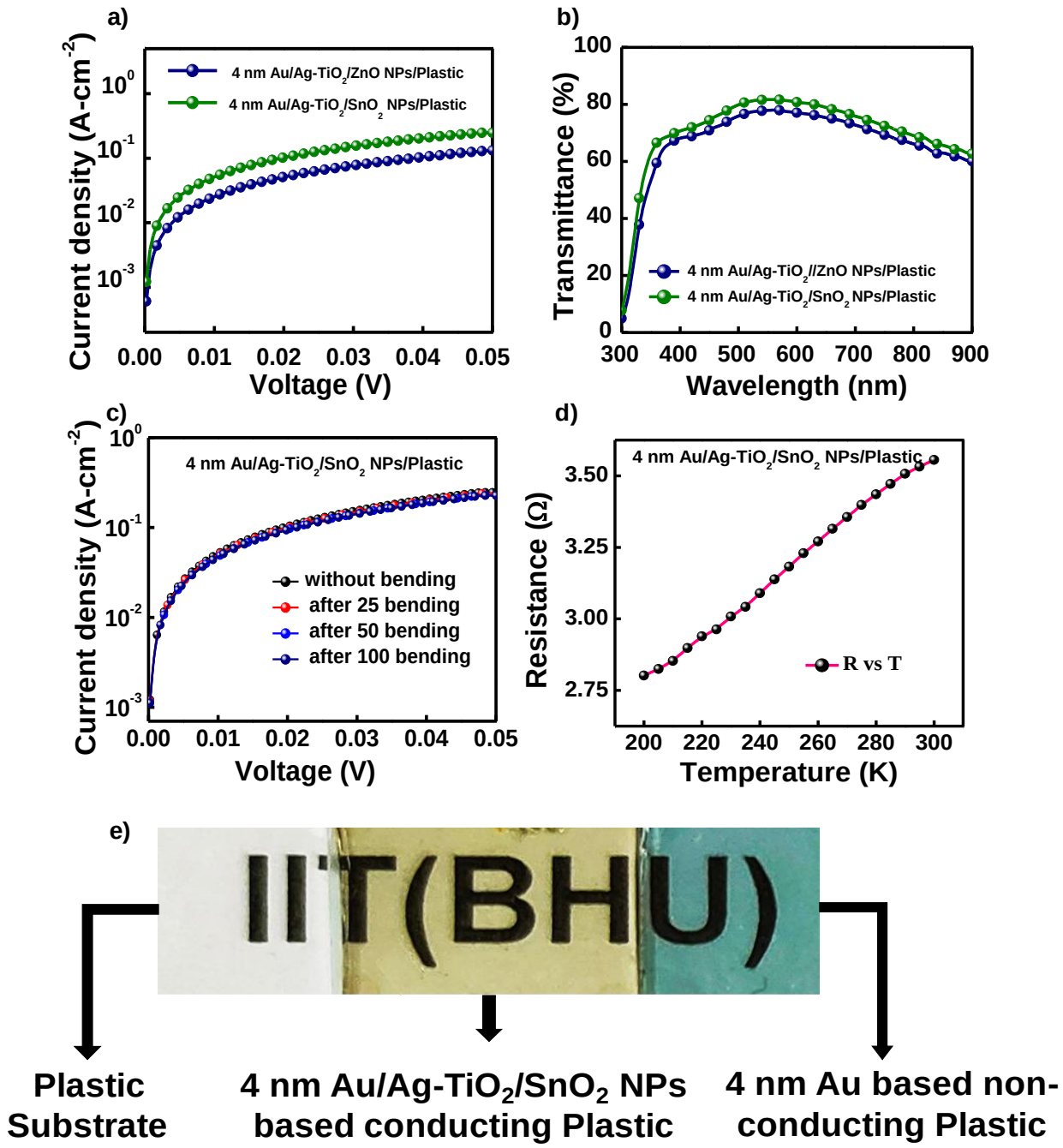

Figure 5.1a) Semi-log graph of electrical current density vs voltage of 4 nm Au/Ag-TiO_2 based transparent conducting film with SnO_2 or ZnO NPs **b)** mechanical flexibility upto 100 bending cycles (bending radius 4 mm) **c)** optical transparency of TC film with two different film, **d)** variation of R vs. T using four-probe low temperature set-up and **e)** real picture of TC film with reference.

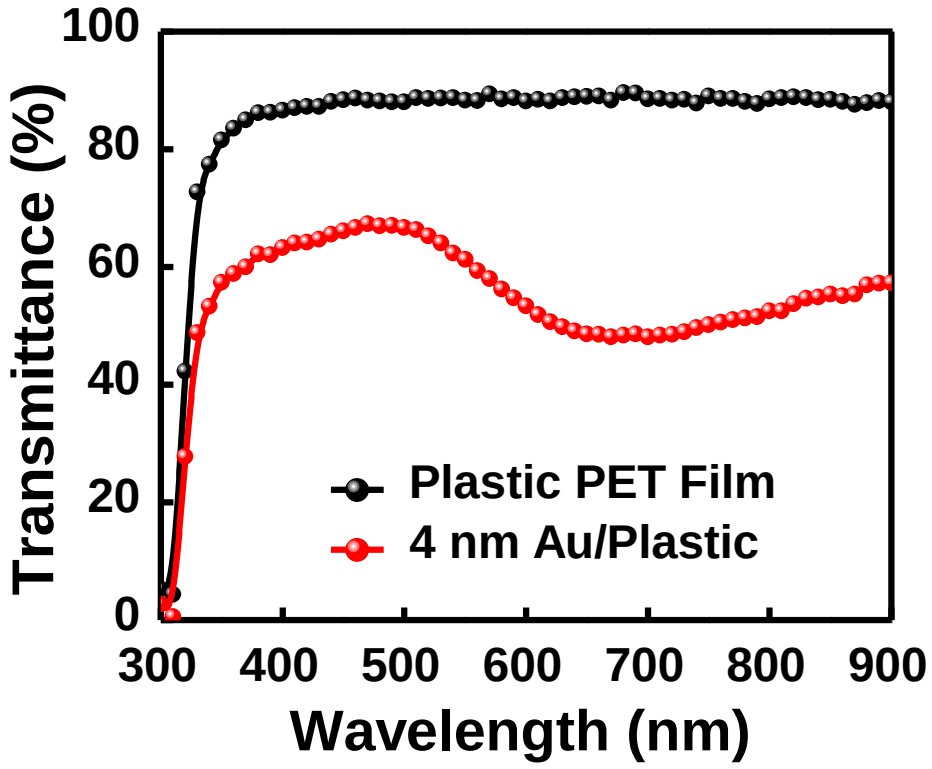

Figure 5.2 Transparency Spectra of 4 nm Au/plastic and plastic PET substrate.

5.3.2 XRD, Raman, UV-NIR absorption & PL Spectra

Figure 5.3a) depicts step-by-steps XRD pattern of the thin films that are deposited in the similar way that followed to fabricate Au-Ag bimetallic based nanostructured thin film. A bare plastic substrate is used as a reference, and the XRD data of the bare plastic is subtracted from sample data to get the actual signal of the sample. The XRD pattern of SnO_2 NPs thin films annealed at 100°C exhibits peak position located at 2θ of 26.17°, 33.58°, 51.47° and 54.45° which corresponds to (110), (101), (211), and (310) planes respectively, indicating the formation of crystalline phase of SnO_2 NPs thin film over the substrate (JCPDS file no. 411445). In next step, thin-film XRD pattern of LTO/SnO_2 NPs shows two additional intense peaks of LTO at 2θ ~ 35.77° and 43.52°, which has come from the reflection planes of (311) and (400) respectively (JCPDS file no. 490207). After ion-exchange process of this, film shows extra three intense peaks at 2θ ~ 25.1°, 37.84° and 44.02° which corresponds to anatase TiO_2 (101), Ag (111) and Ag (200) respectively (JCPDS file no 897322 & 731764). These intense broad peaks of Ag NPs are confirming the formation of Ag

NPs inside TiO_2 matrix after ion-exchange process. At final stage, TC thin film (4 nm Au/Ag-TiO_2 /SnO_2 NPs) thin film shows similar peak positions with much higher intensity at 2θ ~ 37.84˚, and 44.02˚. These peak positions of Au or Ag NPs are common because of their very similar lattice parameters. From this XRD spectra its very clear that the width of the peaks is quite wide, indicates the small size of the metal/metal oxide nanoparticle.

Figure 5.3b) shows the Raman spectra of 4 nm Au/Ag-TiO_2/SnO_2 NPs thin film. From this study an intense peak has been observed at 630 cm^{-1} which originated from the SnO_2 NPs. The peak position at 1086, 1193 and 1616 cm^{-1} which corresponds to Au or Ag NPs and the rest peaks at 705, 865, 995, 1293 and 1729 cm^{-1} corresponds to plastic substrate. This Raman data confirms the formation of Au-Ag bimetallic conducting film on plastic. For optical studies, the thin film of 4 nm Au/Ag-TiO_2/SnO_2 NPs is fabricated on a quartz substrate. The normalized UV-Vis absorbance spectra of Au/Ag-TiO_2/SnO_2 NPs thin films spanning the optical spectral region of 300–1800 nm are shown in **Figure 5.3c)**. The absorption spectrum of as-prepared 4 nm Au/Ag-TiO_2/SnO_2 NPs thin films demonstrate a spectrally broadened spectrum from UV-Vis to NIR region with a plasmonic peak around 750 nm wavelength whereas the reference Au NPs film shows plasmonic peak ~ 520-560 nm in visible range of spectra., implying a red shift of >200 nm of the plasmonic peak due to the Au-Ag bimetallic nanostructure formation (**Figure 5.3c)).** The plasmonic absorption in the NIR region appeared due to the longitudinal plasmon mode of the porous Au-Ag bimetallic nano-film formed during the lateral growth of Au NPs over Ag-TiO_2/SnO_2 NPs surface. The PL spectra of the 4 nm Au/Ag-TiO_2/SnO_2 NPs thin film is shown in **Figure 5.3d)** which is acquired in the range of 320-550 nm with an excitation wavelength of 300 nm, indicating the emission peaks around 370 nm (3.35 eV), which is directly providing the energy band gap of the thin film. The PL peak position at 370 nm suggests specific optical properties that could be attributed to the formation of an Au-Ag bimetallic nanostructure on TiO_2/SnO_2 matrix. Pure Au or Ag NPs typically have PL characteristics with a peak position of much larger wavelength, indicating a possible radiative recombination through intermetallic energy states.

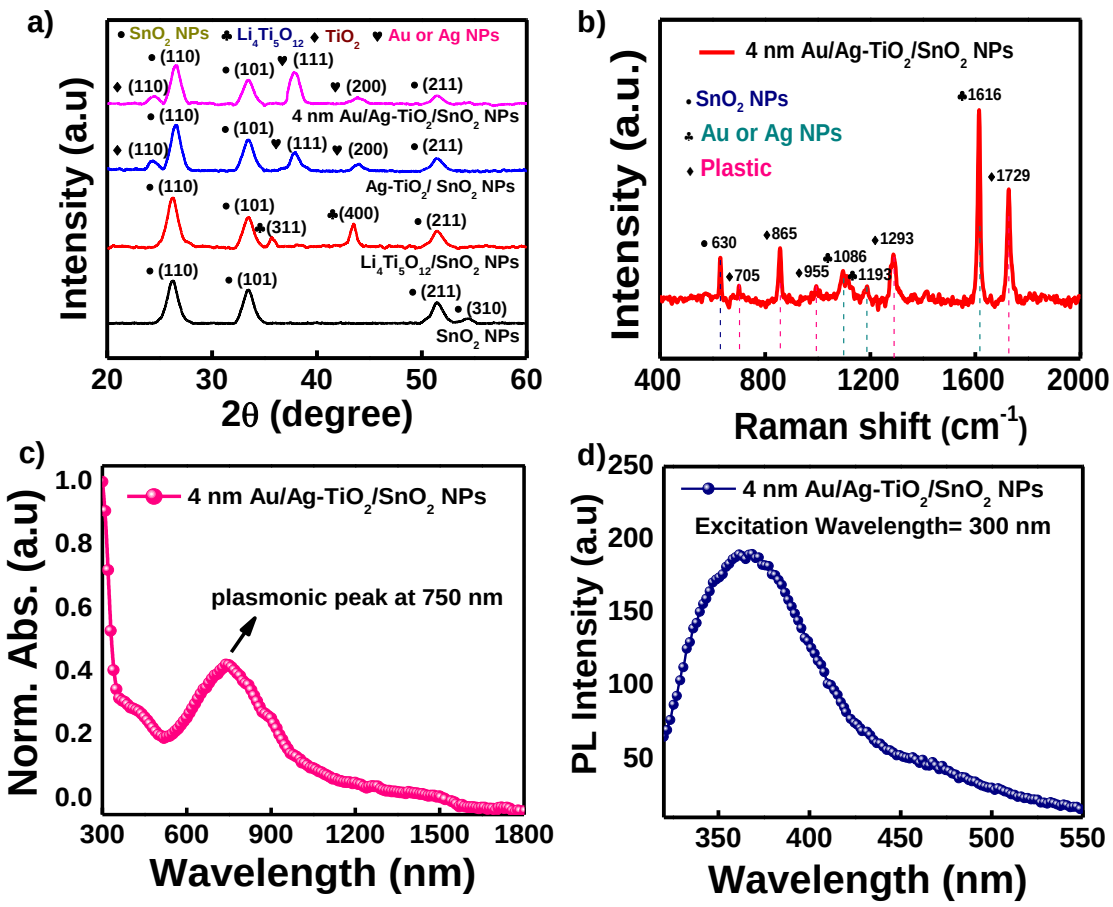

Figure 5.3 Structural analysis of 4 nm Au/Ag-TiO_2/SnO_2 NPs thin film **a)** XRD Spectra **b)** Raman Spectra **c)** UV-Vis-NIR absorption Spectra, and **d)** PL Spectra.

5.3.3 Surface Morphology (HR-SEM & AFM) Study

The surface morphology of Au/Ag-TiO_2/SnO_2 NPs thin film on plastic substrates are studied by HR-SEM. **Figure 5.4a,b&c)** demonstrated the morphological change of the films with the increasing mass thickness of thermally deposited Au film over Ag-TiO_2/ SnO_2 NPs thin film. From this surface morphology study, it's very clear that the individual islands (**Figure 5.4a)** to a percolated network (**Figure 5.4b)** transition is occurring during the process with a critical mass thickness of 4 nm..[200, 201] Although this phase transition of the surface morphology is not observed in the reference 4 nm Au film over bare plastic substrate **(Figure 5.7a)**. From this comparative study, it can be speculated that the morphological phase transition of 4 nm Au/Ag-TiO_2/SnO_2 NPs film occurs due to the coalescence of individual grains with their neighbor which becomes possible due to the pre-existing Ag NPs of Ag-

TiO_2 film which is grown during the ion-exchange process. Due to this low mass thickness of Au film, optical transparency is very high by maintaining its metallic conductivity. Moreover, these nano-porous structures can create intrinsic EM hot spots which leads to produce a highly sensitive plasmonic opto-electronic device. Further deposition of Au film (~ 6 nm) covers the voids (**Figure 5.4c)**), as a result film will become more electrically conducting but transparency decreases drastically. An energy- dispersive X-ray spectrometer (EDX) & color-mapping attached to the HR-SEM instrument is used to figure out the contents and amount of metallic elements present in 4 nm Au/Ag-TiO_2/ SnO_2 NPs is shown in **Figure 5.5**, which confirms the presence of Au, Ag, Ti, Sn and O uniformly throughout the film.

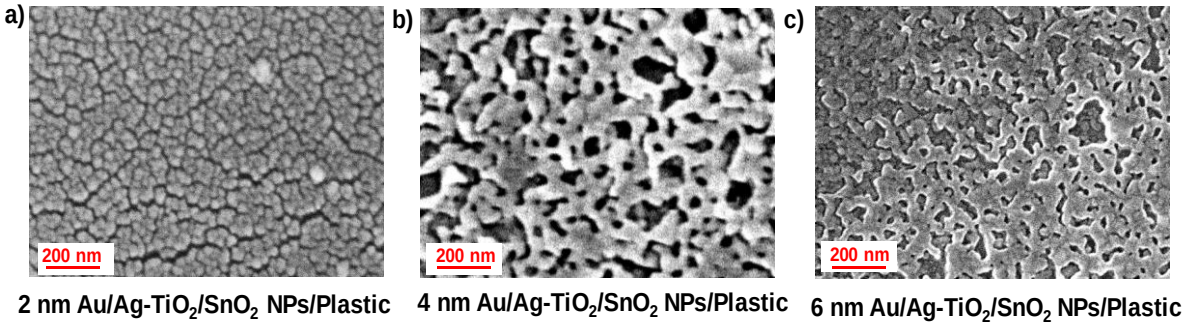

Figure 5.4 FE-SEM photographs of Au/Ag-TiO_2/SnO_2 NPs thin film at room temperature on plastic. Each photograph's average film thickness is listed below. **a)** shows the early stage of growth and coalescence of islands **b)** percolating nano-porous structures **c)** complete percolating structures

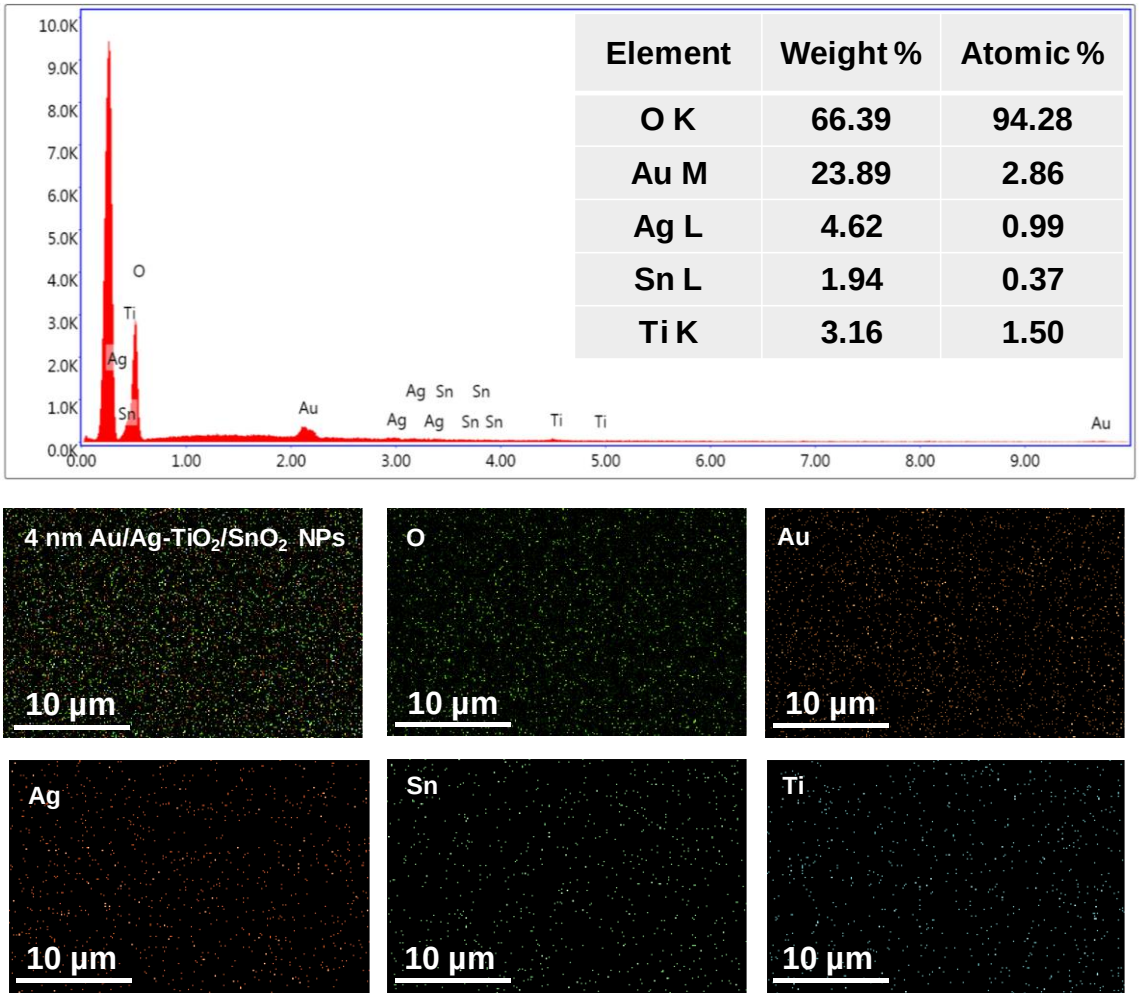

Figure 5.5 Energy dispersive spectra of 4 nm Au/Ag-TiO_2/SnO_2 NPs/plastic thin film, with the elemental composition determined by EDX displayed in the inset. Color mapping of (i) 4 nm Ag/Ag-TiO_2/SnO_2 NPs thin film (ii) O, (iii) Au, (iv) Ag, (v) Sn, (vi) Ti.

Furthermore, AFM has been used for more detailed surface study of Au/Ag-TiO_2/ SnO_2 NPs thin films to recognize the surface roughness (R_{rms}) shown in **Figure 5.6a,b&c)**. These studies show that the surface roughness for 2 nm Au/Ag-TiO_2/SnO_2 NPs is quite low (R_{rms} ~ 1.55 nm) as film is fully covered by individual tiny NPs, but as soon as mass thickness reached 4 nm, film goes through a phase transition from individual metallic islands to a percolated nano-porous type structure which create denser EM hotspot and multipolar resonance effect. As a result, films surface roughness increases quite significantly to 3.91 nm. On the other hand, in case of 6 nm Au/Ag-TiO_2/SnO_2 NPs (R_{rms} ~1.62 nm), further

growth covers the porosity of the film, reduces its surface roughness to 1.62 nm. Besides, **Figure 5.6d,e&f)** shows the 3-D AFM images of the film for more celerity. The 2D-AFM image of reference 4 nm Au (R_{rms} ~ 5.74 nm) on the bare plastic substrate is shown in **Figure 5.7b)**, indicates its larger roughness.

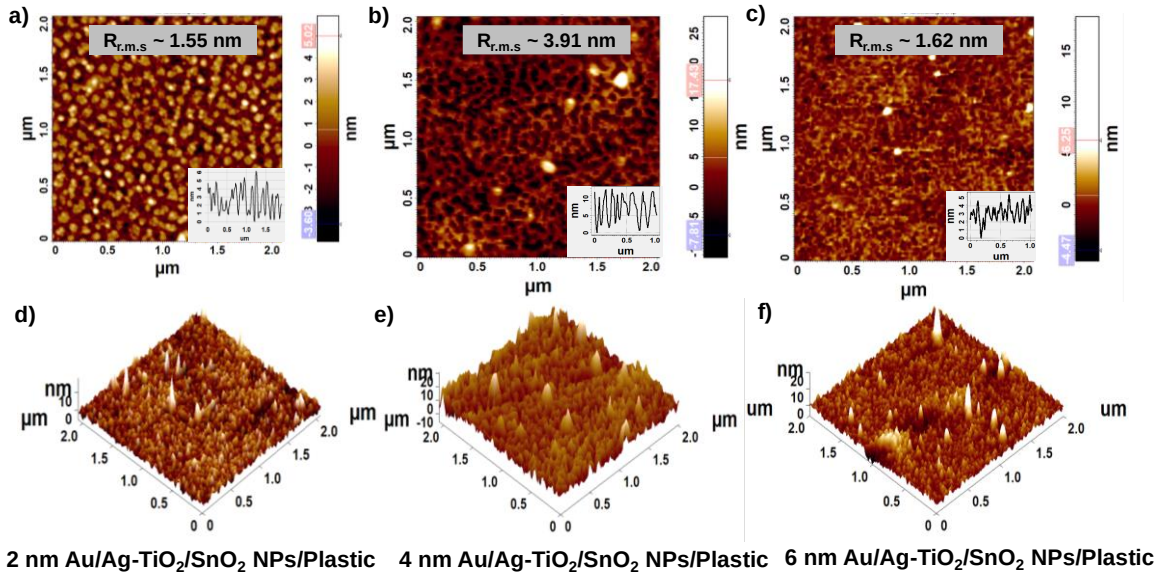

Figure 5.6a,b&c) 2-D AFM & **d,e&f)** 3D-AFM image of (2 or 4 or 6 nm Au)/Ag-TiO_2/SnO_2 NPs. Each rms roughness is listed in the graphics.

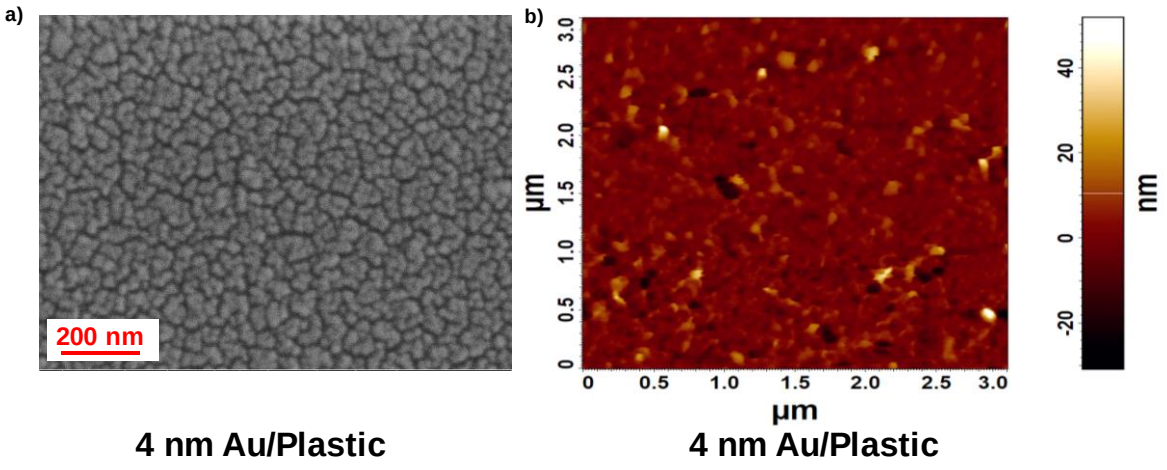

Figure 5.7 a&b) HR-SEM and 2D-AFM image of 4 nm Au reference thin film on plastic.

5.3.4 HR-TEM Study

Figure 5.8a)shows a TEM study of the 4 nm Au/Ag-TiO_2/SnO_2 NPs nanocomposites for further structural analysis. To prepare the TEM sample, the film is scratched off with a clean glass slide and placed on clean paper. Following that, it is dissolved in isopropyl alcohol and dispersed for a few minutes using a probing sonicator. A drop of this dispersed material is then collected and placed on a TEM grid. **Figure 5.8a)** shows that the Au or Ag NPs have grown quite uniformly within the TiO_2/SnO_2 NPs matrix. These data also show that the NPs are predominantly between 5 and 15 nm in size, with an average particle size of 8.84 nm. The particle size distribution of Au or Ag NPs inside the TiO_2/SnO_2 NPs matrix is shown in **Figure 5.8b)**. Higher-magnification TEM analysis **Figure 5.8c)** of 4 nm Au/Ag-TiO_2/SnO_2 NPs sample indicates individual lattice fringe formation of Au or Ag NPs and inside the TiO_2/SnO_2 NPs, implying their own coexistence. The average d spacing's of Au or Ag NPs and SnO_2 NPs are 0.213, 0.242, and 0.348 nm, respectively, which correspond to the Au or Ag (200), Au or Ag (111), and SnO_2 NPs (101) planes. All of these spacing's are also defined by the selected-area electron diffraction (SAED) pattern, as shown in **Figure 5.8d)**. As shown earlier, the XRD pattern of the 4 nm Au/Ag-TiO_2/SnO_2 NPs sample (**Figure 5.3a)**) also reveals the same set of planes.

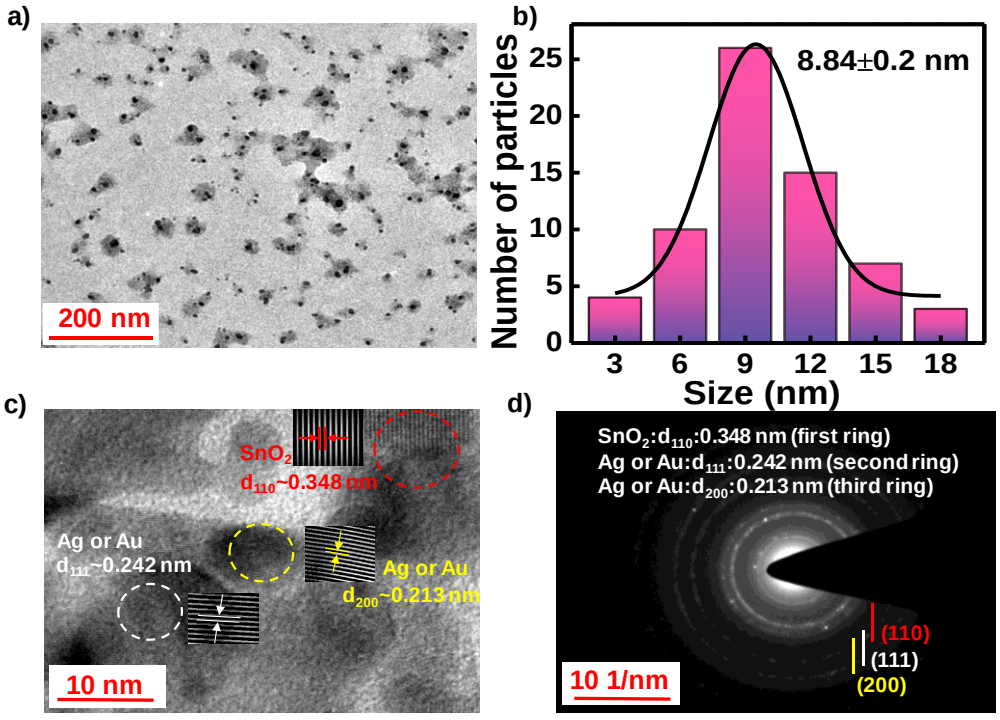

Figure 5.8 a) TEM image of 4 nm Au/Ag-TiO_2/SnO_2 NPs **b)** distribution of the particle sizes of Au or Ag NPs from the TEM image **c&d)** high-resolution TEM image and SAED pattern of 4 nm Au/Ag-TiO_2/SnO_2 NPs film.

5.3.5 Optoelectronics characterization of the photodetectors

As mentioned earlier, plasmonic photodetectors have been fabricated in a cross-bar geometry with the help of multilayer stack-structure of (LiF/Al)/SnO_2 NPs/4 nm Au/Ag-TiO_2/ plastic where 4 nm Au/Ag-TiO_2 works as bottom transparent electrode and LiF/Al works as a top electrode with an active area of 1×1 mm^2. Photocurrent of this device is generated from the hot electron generated due to the LSPRs effect of nano-porous Au-Ag thin film. The surface conduction electrons of Au or Ag NPs that collectively oscillate in response to incident light, leading to enhanced EM fields near the NPs. This enhanced EM field leads to the absorption of incident photons resulting in the generation of hot electrons. During electrical characterization of the device, white light of different intensity has been illuminated from the back side of the device that partly transmits and partly absorbed by 4 nm Au/Ag-TiO_2/SnO_2 NPs electrode due to the semi-transparent nature and plasmonic absorption of the electrode respectively in longer wavelength region. **Figure 5.9a)** shows the semi-log plot of electrical current-voltage parameters of this plasmonic photodetector device under dark and light. From this figure, it is clear that the device is rectifier in nature and reverse photocurrent increases with light intensity. When the light intensity is varied from 0 to 400 W/m^2, with moderate reversed bias current at 1V, increases from ~1.8×10^{-9}A to ~9.98×10^{-8}A, which 55 times w.r.t the dark current. Besides, I−V characterization data are plotted in a linear scale **Figure 5.9b)**, which ensures the device is a diode in nature. Furthermore, it has been observed that the reverse bias photocurrent variation is nearly linear (LDR curve) with the incident light intensity (**Figure 5.9c)**). Barrier height and ideality factor of the proposed device under light condition is calculated using **Equation 2.7** and **2.8** respectively. The calculated value of ideality factor and barrier height under different light intensities are plotted in **Figure 5.10a&b)**. Under dark, the ratio of forward bias to reverse bias current (rectifying ratio) is quite high at 1 V is ~1800. With different light intensities rectifying ratio is plotted in **Figure 5.10c)**. **Figure 5.9d)** shows schematic representations of the relative energy band structure, band bending, and charge separation of these devices under

illumination. As soon, light is illuminated, the bottom 4 nm Au/Ag-TiO_2/SnO_2 NPs electrode generates a hot-electron due to the plasmonic absorption and subsequently transfers to the CB of TiO_2 and SnO_2 NPs and finally reaches to the CB of LiF/Al. Hole, on the other hand, is collected by the Au-Ag bimetallic electrode itself. The concept of using LiF/Al as a top electrode to increase the work function between top and bottom electrode. Al electrode has work function of 4.1 eV but if we use an interface layer of LiF it decreases to 3.75 eV.[264] On the other hand, Au-Ag bimetallic electrode has a work function around 4.9 eV. This generates electron-hole pairs that are separated due to the built-in electric field within the photodiode structure and the different work functions of the electrode materials.

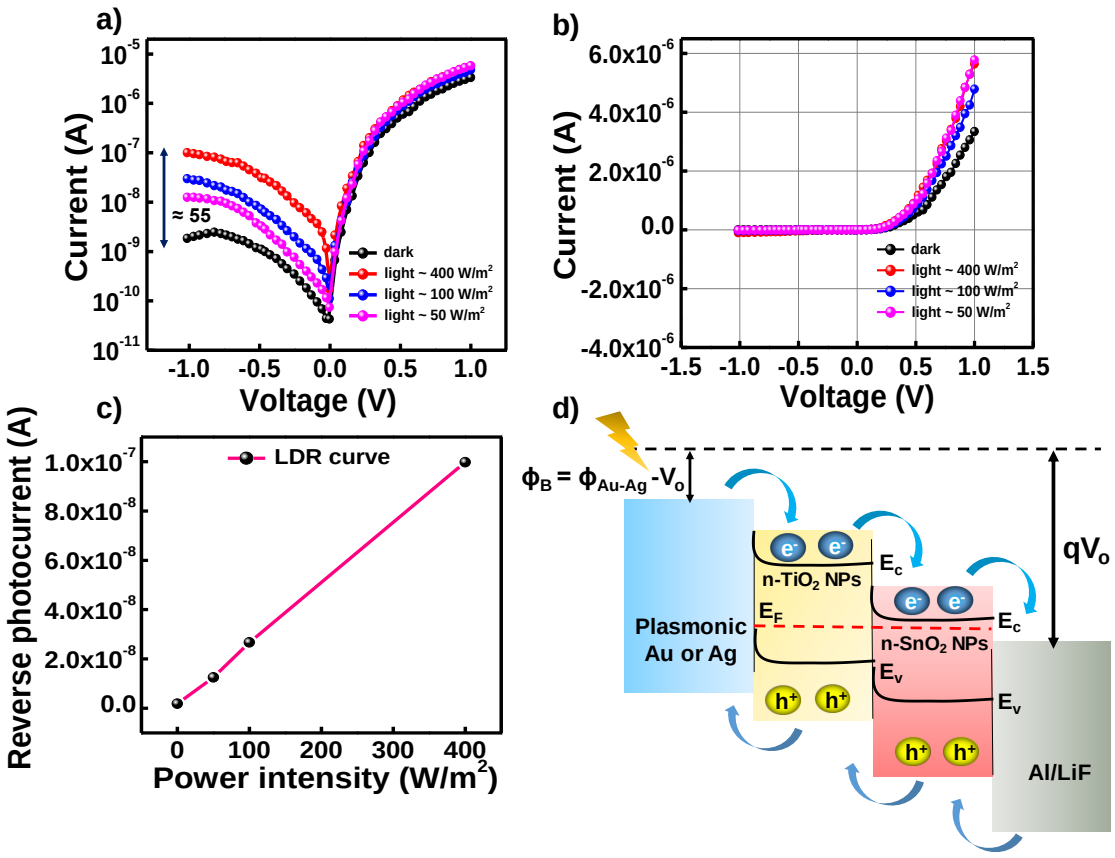

Figure 5.9a) photocurrent generation of plastic compatible Au-Ag transparent plasmonic electrode based photodiode device under dark and light conditions (semi-log plot) **b)** linear I-V plot **c)** reverse photocurrent vs power intensity (LDR curve) **d)** band alignment, band bending and charge separation of this hetero-structure photodiode devices.

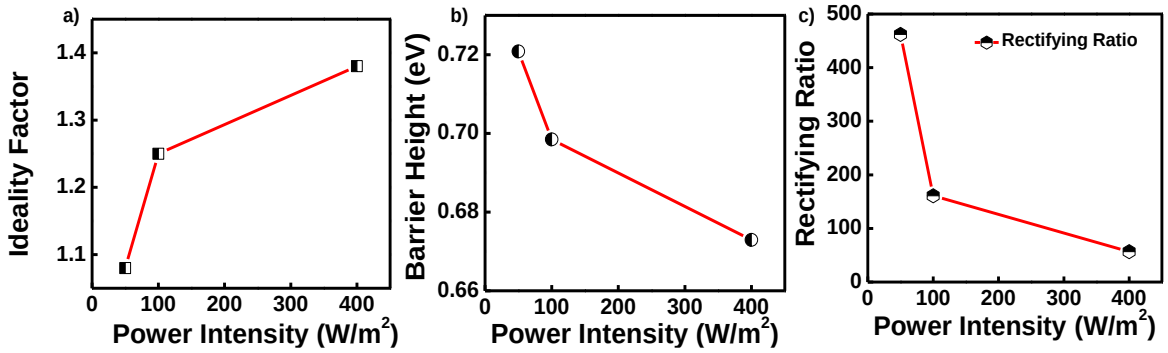

Figure 5.10a) experimental barrier height vs power intensity (Φ_b–P) curve **b)** experimental ideality factor vs power intensity (n-P) curve **c)** experimental rectifying ratio vs power intensity curve of the photodiode

5.3.6 EQE, Responsivity and Detectivity and role of plasmon induced hot electron

The EQE values under different external bias have been measured in the wavelength range of 300 to 1800 nm, as shown in **Figure 5.11a)**. This data implies that EQE value reaches ~ 32.62 % at 750 nm under -2V external bias. Because of the bi-metallic formation of plasmonic Au-Ag NPs, EQE spectra extended upto 1500 nm, which cover entire UV-Vis to NIR spectra region. It can be noted that the EQE spectra of this device is quite similar to the absorption spectra of the 4 nm Au/Ag-TiO_2/SnO_2 NPs film (**Figure 5.3c)**) with exactly same peak position (750 nm) which indicates the photocurrent is mostly generated from the plasmon driven hot electron generation. Responsivity and detectivity of the device is calculated from EQE measurement by using **Equation 1.3** and **1.4** respectively. The variation of photo-responsivity under different external biases is depicted in **Figure 5.11b)**. These results show that a maximum responsivity of 20.23 (A/W) has been achieved at 750 nm with an external bias of -2V. As a plasmonic photodetector, this responsivity data is reasonably higher than earlier reports. Besides, detectivity is another fundamental device parameter that suggests the device sensitivity with respect to the minimum signal that can be detected by the photodetector. The variation of the device's detectivities is shown in **Figure 5.11c)**. The highest detectivity of this heterojunction photodetector that has been calculated is of 1.6×10^{13} Jones at 750 nm under -2 V external bias. As mentioned earlier, there is a

significant amount of photo detection of this plastic based bi-metallic device with a detectivity of 2.33×10^{12} Jones is achievable in the NIR region (wavelength of 1500 nm). It is worth mentioning that the plasmonic absorption peak coincides perfectly with the peak of the detectivity of the device, indicating the hot electron of bimetallic Au-Ag NPs is primarily responsible for this device's photocurrent generation.

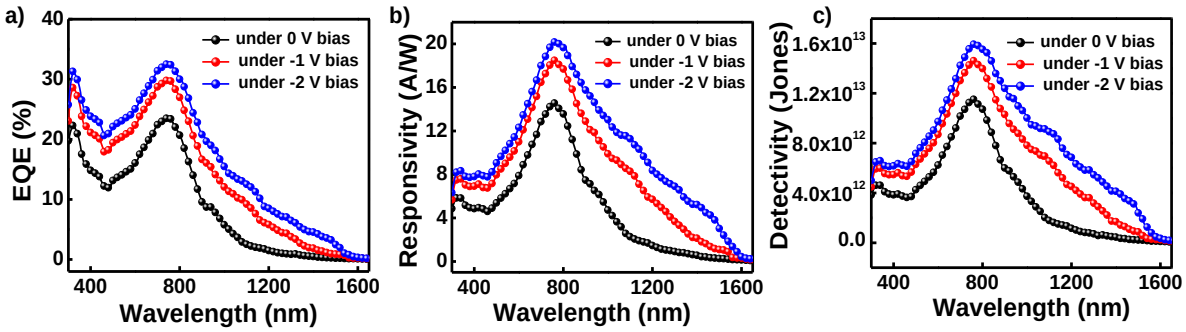

Figure 5.11 device performance of heterostructure photodiode **a)** EQE vs wavelength **b)** extracted R_λ vs wavelength **c)** Extracted D* vs wavelength.

5.3.7 Transient Time Response

Beside device photosensitivity, transient photo response is another key parameter of a photodetector that implies how fast a device can respond and how promptly it can back to its original stage for detecting the next signal. To determine the photo-response of these devices a white light pulse of width and separation of ~ 5 s is illuminated on the device. During this study, the device is subjected to -2V external bias. This transient photocurrent data which is shown in **Figure 5.12a&b)**, reveals that the device's rise and decay time are ~ 16.2 ms and ~ 16.7 ms respectively, indicating the device has fast photo response and recovery time. Furthermore, devices are stored in an ambient atmosphere for a few months, although its photosensitivity and transient time remains almost the same, indicating its very high atmospheric stability.

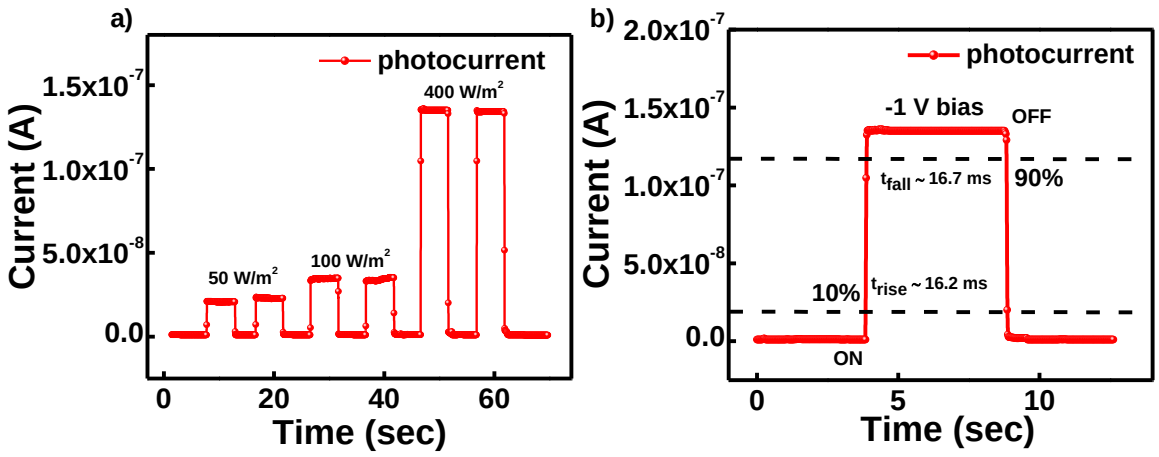

Figure 5.12a) Transient time response of the device **b)** single cycle time response data with rising and decaying times of ~ 16.2 ms and ~ 16.7 ms, respectively.

For a comprehensive assessment of our device's performance, a summary of previously published work on photodetectors based on plasmonic hot electrons is presented in **Table 5.2**. It can be noted that earlier investigations into hot-electron photodetectors have primarily focused on spectral response (R_λ) and the rise-to-fall time ratio (t_{rise}/t_{fall}). Although, important parameters of the hot electron photodetectors are the EQE and D* spectra analysis from where contribution of the hot-electron can be realized, have not been explored in most of the reports. Some earlier works on a hot-electron based photodetector has been listed below. In comparison to other reported hot-electron photodetectors, this flexible plasmonic hot-electron photodetector exhibits a higher responsivity, higher detectivity with fast response speed.

Table 5.2 Comparison of the performance of the current plasmonic hot electrons photodetector with that of other similar devices employing plasmonic hot electrons

Device	λ_{max} (nm)	EQE (%)	R (A/W)	D^* (Jones)	τ_r/τ_f	Ref.
SnO_2 NPs/TiO_2 NPs/(4 nm Au/Ag-TiO_2/SnO_2 NPs)/Plastic	**750**	**32.62**	**20.23**	**1.6×10^{13}**	**16.2/16.7 ms**	**This work**
Porous Ag/TiO_2/Ti	450	–	3.3×10^{-3}	9.8×10^{10}	112/24 µs	[165]
Ag/TiO_2 NTs/FTO	370	–	176.30	–	82/14 s	[172]
Porous Au/Si	–	–	3.5×10^{-3}	–	–	[173]
Au nanorods/Si	–	–	1.0×10^{-5}	–	–	[154]
Au/Pyramid-Si	1200	–	8.2×10^{-3}	1.8×10^{10}	–	[159]

5.4 Conclusions

In conclusion, a cost effective synthesis technique has been developed to fabricate mechanically flexible transparent conductors. For this synthesis, initially a $Li_4Ti_5O_{12}$/SnO_2 NPs heterojunction thin film has been prepared through a solution processed technique with processing temperature of ~100 ^oC. Then, the loosely bound Li^+ of $Li_4Ti_5O_{12}$ thin film has been replaced by Ag^+ through an ion-exchange process that forms a Ag-TiO_2 thin film. Thereafter, a thermally evaporated Au of thickness 4 nm is deposited on top of this Ag-TiO_2/SnO_2 NPs thin film, which shows high electrical conductivity (5-10 ohm/□) with ~ 80% average visible transmittance in the range of 500-600 nm wavelength. The electrical conductivity of this film (4 nm Au/Ag-TiO_2/SnO_2 NPs) is significantly higher w.r.t reference

bare plastic substrate Au film (4 nm Au/plastic). Besides, this film also shows a vibrant plasmonic absorption extended up to 1600 nm. By utilizing combined electrical conductivity, optical transparency and plasmonic absorption features of this thin film, a plasmonic photodetector has been fabricated where 4 nm Au/Ag-TiO_2/SnO_2 thin film works as plasmonic electrode as well as photocurrent harvesting materials and LiF/Al substrate as counter electrode. Device shows a very high photosensitivity to the visible light. Besides, it has been observed that the EQE spectra of this device has a great similarity with the absorption spectra of 4 nm Au/Ag-TiO_2/SnO_2 thin film with same absorption and EQE peak position (750 nm) that reveal the contribution of plasmonic hot electron in the photocurrent generation of the device. Device shows EQE, photo responsiveness, and detectivity of values 32.62%, 20.23 A/W, and 1.6×10^{13} Jones, respectively at (750 nm). Moreover, these devices show fast photo response with a rise and decay times of 16.2 ms and 16.7 ms respectively. Overall performance of this plasmonic photodetector is significantly higher than the previous report that gives a visible way to fabricate reliable hot electron based photodetectors.

Chapter 5

Mechanically Flexible Au-Ag bimetallic Plasmonic Transparent Conductor for Boosting Efficiency of Organic Solar Cell

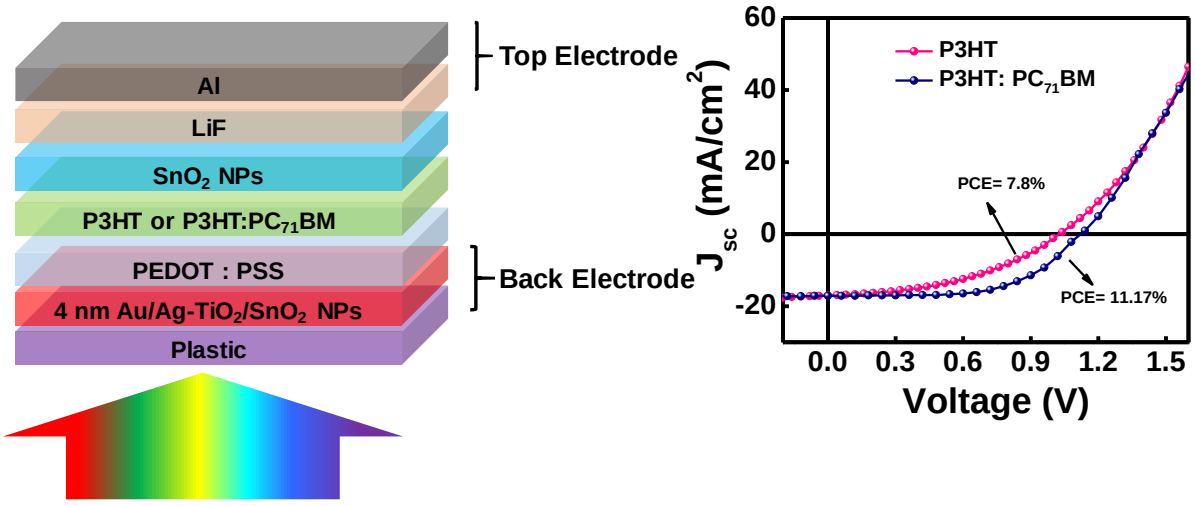

This work is the continuation of previous chapter 5, where bimetallic Au-Ag film is used as a back electrode of plasmonic organic solar cells (POSCs). In recent years, there has been great interest in the utilization of plasmons, or free electron oscillations of MNPs, to increase the efficiency of both organic and inorganic thin film optoelectronic devices. This has been driven by the possibility of employing thin plasmonic MNPs layer in order to increase photo absorption by light trapping in photovoltaic or other opto-electronic devices. In this particular work, I fabricated donor only (P3HT) and donor-acceptor bulk heterojunction (P3HT: PCBM) solar cell using Au-Ag plasmonic thin film as a back electrode. Experimental data indicates a promising enhancement in solar cell performance parameters, including both the open circuit voltage (V_{OC}) and short circuit current density (J_{SC}), has been observed for single layer P3HT and blended P3HT:$PC_{71}BM$ based organic solar cell devices. The observed V_{OC} for donor only and BHJ solar cell reaches to 1.00 and 1.13 V respectively, ensuring tandem cell formation due to the plasmonic Au-Ag film. As a consequence, the PCE values of these two cells reaches to 7.8 % and 11.17% respectively which are record efficiency with these materials combination. These results suggest a unique way to boost PCE of thin film solar cells by utilizing hot carriers of plasmonic Au-Ag thin film that not only works as TC of the device but also increases its V_{OC} by ~ two times.

5.5 Introduction

Transparent conductors (TCs) are in high demand in modern time due to their wide range of applications in electronics, including touch screens, wearable sensors, memory devices, organic light-emitting diodes (OLEDs), solar cells, smart windows etc.[23, 265-269] Traditionally, indium tin oxide (ITO) and fluorine-doped tin oxide (FTO) have dominated the TC market due to their high optical transparency (~ 90%) and low sheet resistance (R_s < 100 Ω/□). However, the scarcity of indium, along other inherent limitations of ITO—such as low mechanical flexibility and complex, costly manufacturing processes has driven the search for alternative TC materials.[116, 117]

To find out the substitute of these metal oxide based TCs, recent studies have focused on next-generation TCs that can provide a balance of transparency, conductivity, mechanical flexibility, and ease of fabrication. Carbon-based materials, including carbon nanotubes and graphene, have garnered attention for their excellent flexibility and optical transparency.[175, 176, 251] However, their electrical conductivity remains lower than that of metals like Ag, Cu, and Au. As a result, metal nanowires and nanoparticle networks have emerged as promising alternatives, particularly for flexible and stretchable electronics, where they offer superior mechanical flexibility, high optical clarity, low sheet resistance, and cost-effective production.[177, 253, 254] Among metals, Ag has emerged as a leading candidate for TCs due to its exceptionally high intrinsic conductivity and low refractive index in the visible spectrum. Ag nanowire networks and oxide/Ag/oxide multilayer films, in particular, have shown significant promise.[181, 255] Copper, though less expensive and conductive, is more chemically reactive, as is Ag, with both materials prone to oxidation.[256, 257] Au, by contrast, offers excellent chemical stability but is limited by lower conductivity and higher cost.[270] To address these stability concerns, researchers have developed core-shell structures that encapsulate metals with chemically inert shells, an approach that enhances the longevity of TCs in a cost-effective manner. Despite advancements, limited studies have explored the use of bimetallic core-shell architectures like Au-Ag, Ag-Cu, and Au-Cu for TC applications, highlighting an area of potential growth.[271, 272]

A critical barrier to achieving high transparency in metal-based TCs is their strong plasmonic absorption, which restricts optical transparency. Nevertheless, plasmonic effects have been harnessed advantageously in solar cells, plasmonic photodetectors, gas sensors, and LEDs.[186, 189] These effects enable hot-electron generation, enhancing photocurrent in devices such as solar cells, photodetectors, and systems for photo-electrochemical hydrogen production.[140, 190] To advance TCs, ongoing research must aim to resolve the balance of optical transparency, electrical conductivity, mechanical durability, and chemical stability. The development of multi-metallic and core-shell nanostructures offers promising pathways to realize high-performance TCs suited to the next generation of flexible and transparent optoelectronic devices.

Plasmonic effects are increasingly explored in solar cell research due to their potential to improve light trapping in organic and inorganic thin-film solar cells, enhancing efficiency.[273-275] The key feature of plasmon resonance is its ability to concentrate conduction electron oscillations within specific spectral ranges. Nevertheless, due to the resonant nature of plasmonic effects, absorption enhancement is limited to specific wavelengths dictated by the NP's size, shape, composition, and local dielectric environment.[76, 276] This enhancement is often offset by parasitic absorption at other wavelengths, reducing efficiency gains. Thus, achieving broadband optical absorption enhancement is essential for advancing plasmonic solar cells beyond the lab.[277, 278] Prior research has focused on theoretical models and experimental setups with random or structured monometallic NPs or gratings requiring precise geometry. While theoretical studies show promising efficiency boosts from metallic NP plasmonic effects, substantial experimental improvements remain elusive, influenced by several factors affecting optical absorption in thin-film solar cells.

Organic photovoltaic devices (OPVs) fabrication is an advancing research field due to their potential as low-cost, lightweight renewable energy sources with promising PCE.[279-281] Since Tang et al.'s 1986 report on the first two-layer OPV[282], significant progress has been made, with continuous improvements in device efficiency through novel materials, device engineering, and architecture. Spin coating is the primary technique for lab-scale OPV fabrication, and state-of-the-art OPVs with donor/acceptor bulk heterojunction (BHJ) or tandem structures now achieve PCEs exceeding 15-20%.[280, 283, 284] The incorporation of plasmonic MNPs has recently been identified as a promising approach to enhance OPV efficiency. This improvement is attributed to increase light trapping and enhanced electrical properties due to the metallic nature of MNPs. Plasmonic NPs can be blended with OPV layers or added as a separate layer, and various synthesis methods, including sol-gel routes and laser nanofabrication, have been explored.[285-288] Numerous studies have examined how factors such as solvent choice, drying rates, annealing, and post-deposition treatments influence layer morphology and PCE. Among these, P3HT:$PC_{71}BM$ BHJs remain prominent in polymer photovoltaic research,[275, 289-291] although new organic polymers are increasingly used to produce efficient BHJs globally.[113, 292] However, literature on achieving high-efficiency P3HT:$PC_{71}BM$ organic solar cells (OSCs) remains limited.

In this section of this chapter, We report the synthesis of Au-Ag bimetallic transparent conducting film on plastic substrate at a low processing temperature (120°C). The as-synthesized Au-Ag bimetallic thin film is highly conductive with sheet resistance as low as 5-6 Ω/□ with more than 80% transparency, which is achieved without any purification steps. Like the earlier section, this Au-Ag film has been developed by depositing 4 nm Au on a pre-deposited Ag-TiO_2/SnO_2 thin film that enables us to achieve a high conducting film with such a low thickness Au deposition. Besides, this transparent-conducting Au-Ag bimetallic film has been used as a back electrode for developing highly efficient organic solar cells. The device has been fabricated on a plastic substrate by using donor only and Donor-acceptor bulk heterojunction geometry. The power conversion efficiency (PCE) of donor only (P3HT) and BHJ (P3HT:PCBM) solar cells are 7.8% and 11.17% respectively, which are record efficiency with this materials combination. These improvements become possible due to enhancement of open circuit voltage by almost double, ensuring a tandem cell formation. Moreover, photocurrent spectra of these devices are broaden from 300 to 1600 nm due to the plasmonic hot carriers of Au-Ag thin film, which is significantly larger w.r.t. it's common photocurrent generation spectral range of 300-700 nm of these organic semiconductor.

5.6 Experimental Section

5.6.1 Preparation of Precursor Solution

The preparation process for ion-conducting dielectric LTO, SnO_2 NPs, PEDOT:PSS, P3HT, and blended P3HT:$PC_{71}BM$ via low cost solution process technique has been explained in **Chapter 2 Section 2.1.1, 2.1.3, 2.1.8, 2.1.9, 2.1.12**.

5.6.2 Fabrication of Au-Ag TC Film and Plasmonic Organic Solar Cells

Bimetallic Au-Ag based TC film has been fabricated on a flexible PET substrate and the fabrication steps has been explained **Chapter 2 Section 2.3.3**, and schematically present in **Figure 2.9**. For fabrication of a photodetector, these optimized mechanically flexible bimetallic Au-Ag TC thin film have been used as transparent bottom electrode to develop NIR active plasmonic photodetector in a photodiode geometry which is schematically present in **Figure 2.11**.

5.7 Results and Discussion

5.7.1 Electrical and Optical Characterization of Flexible Au-Ag Bimetallic Transparent Conductor

Electrical and optical characterization of prepared Au-Ag flexible TC film is discussed earlier in **Chapter 5 Section 5.3.1**.

5.7.2 XRD, Raman, UV-Vis-NIR absorption & PL Spectra

All structural analysis of Au-Ag TC film is discussed in **Chapter 5 Section 5.3.2**.

5.7.3 Surface Morphology (HR-SEM & AFM) & HR-TEM

Surface morphology of prepared film is discussed in details in **Chapter 5 Section 5.3.3.** HR-TEM is done to calculate the particle size of plasmonic NPs and also it tells us about crystal plane of the film which is discussed in **Chapter 5 Section 5.3.4.**

5.7.4 UV-Vis & PL Spectra of P3HT and P3HT: PCBM Film

The UV–Vis absorption spectra of P3HT and blended P3HT:$PC_{71}BM$ are studied in **Figure 5.13a)**. The absorption spectra of P3HT film generally shows a broad absorption in the visible range extended from 450 to 620 nm, while P3HT:$PC_{71}BM$ blend exhibits wider absorption covering from 300 to 620 nm because of $PC_{71}BM$. Interestingly, when these polymers are deposited on top of the prepared TC film (4 nm Au/Ag-TiO_2/SnO_2 NPs), shows a quite broader absorption spectrum, extended up to 1500 nm as shown in **Figure 5.13a).** Here, the LSPR effect of the Au-Ag bimetallic film enhances the light absorption in the stacked film which is realized from the absorption spectra of Au-Ag thin film (Inset of **Figure 5.13a**). The Steady-State Photoluminescence (SSPL) spectra of organic solar cells based on P3HT and blended P3HT: $PC_{71}BM$ provide valuable insights into charge transfer efficiency and quenching mechanism. In pristine P3HT, strong PL is observed in the range of 620–700 nm, corresponding to its excitonic emissions. However, when blended with $PC_{71}BM$, PL is significantly quenched, indicating efficient charge transfer from P3HT (donor) to $PC_{71}BM$ (acceptor), which is essential for effective exciton dissociation. The degree of quenching reflects the efficiency of the heterojunction in facilitating charge

separation. Since $PC_{71}BM$ itself does not exhibit significant PL in the visible range, its presence mainly influences the spectral shape and intensity through its strong electron-accepting properties. Again, as soon organic films are prepared on Au-Ag bimetallic TC film, PL spectrums are blue shifted which is shown in **Figure 5.13b)** as PL peak is observed around 570-590 nm. This observation is mainly due to changes in the local dielectric environment and exciton interactions. The plasmonic effect of the Au-Ag film alters the exciton recombination dynamics, leading to enhanced exciton dissociation and modification of the energy levels.

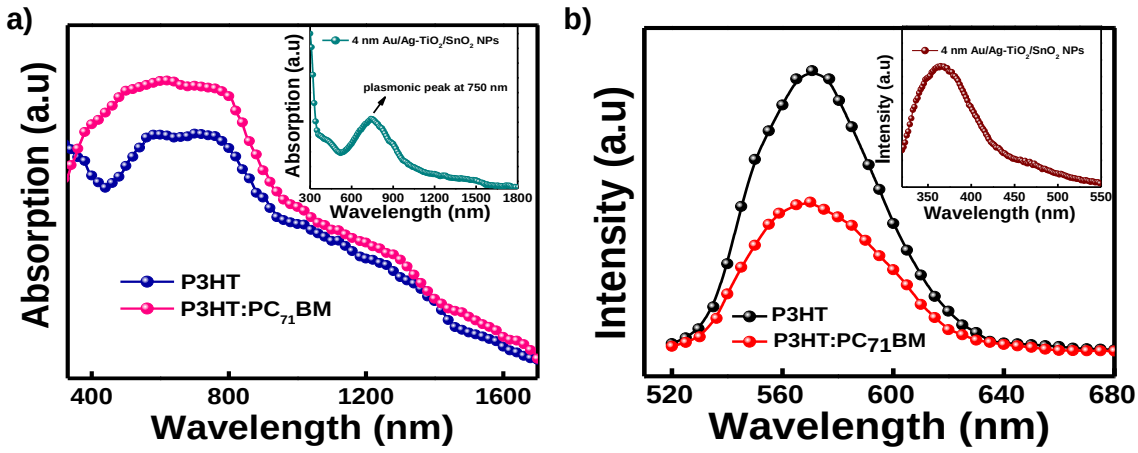

Figure 5.13a) UV-Vis absorption spectra **b)** PL spectra of P3HT and P3HT:PC71BM polymeric film over Au-Ag TC film.

5.7.5 Surface Morphology (HR-SEM & AFM) of P3HT and P3HT: $PC_{71}BM$ Film

Figure 5.14a&b) shows the SEM analysis which reveals significant morphological differences between pure P3HT and P3HT: $PC_{71}BM$ blended films, which directly impacting PCE of solar cells. Pure P3HT films exhibit a smooth morphology with limited charge transport efficiency due to the absence of an acceptor, leading to high recombination losses. Average grain size of P3HT film is around 45-50 nm while in contrast P3HT: $PC_{71}BM$ blends film shows higher average grain size of ~ 50-55 nm, which leads to less grain boundary formation in blended film. Larger grains lead to better polymer crystallinity and improved π-π stacking, which facilitates charge carrier mobility by reducing the trap states. As a result,

it sufficiently reduces recombination losses, result improve J_{sc} and V_{oc} and overall PCE compared to pure P3HT films.

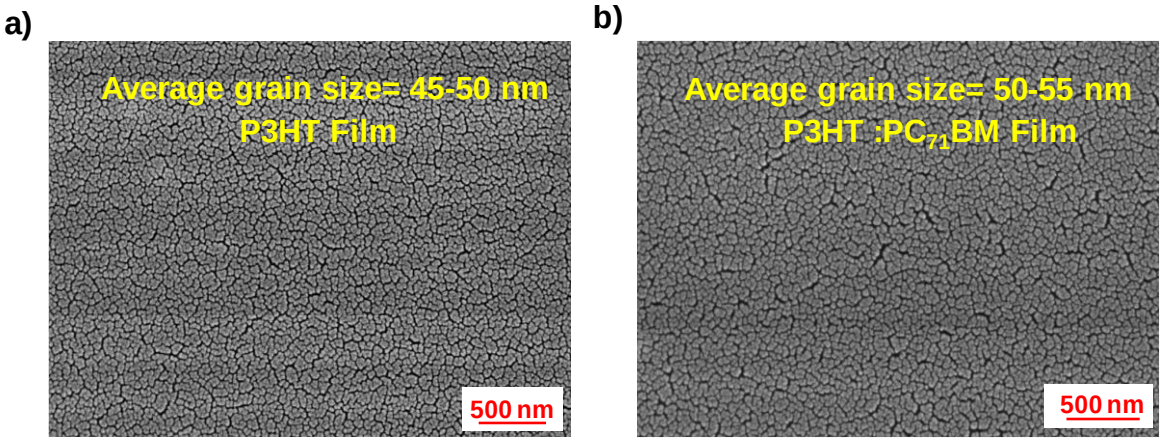

Figure 5.14a&b) HR-SEM image of pure P3HT & blended P3HT: $PC_{71}BM$ polymeric thin film over Au-Ag TC film.

AFM measurement is also performed to investigate the roughness and grown pattern of pure P3HT & blended P3HT: $PC_{71}BM$ polymeric film. The 2D & 3D AFM topographical images of pure P3HT & blended P3HT: $PC_{71}BM$ are shown in **Figure 5.15a,b,c&d**). In pure P3HT films, the AFM image shows a relatively rough surface (r.m.s roughness ~ 3.72 nm) with fine polymer domains, indicating good self-organization but limited charge separation capability. On the other hand, blended P3HT:$PC_{71}BM$ film exhibits distinct nanoscale phase separation, where the surface roughness (r.m.s roughness ~ 3.12 nm) decreases due to the bulk heterojunction formation, leading to a more uniform and compact film morphology. Also, reduced roughness improves the film's contact with the electrode, enhancing charge extraction and reducing interfacial resistance the formation of donor-acceptor domains. Therefore, AFM analysis helps optimize processing conditions to achieve an ideal morphology that enhances charge transport, reduces recombination losses, and improves overall PCE in OPVs.

.

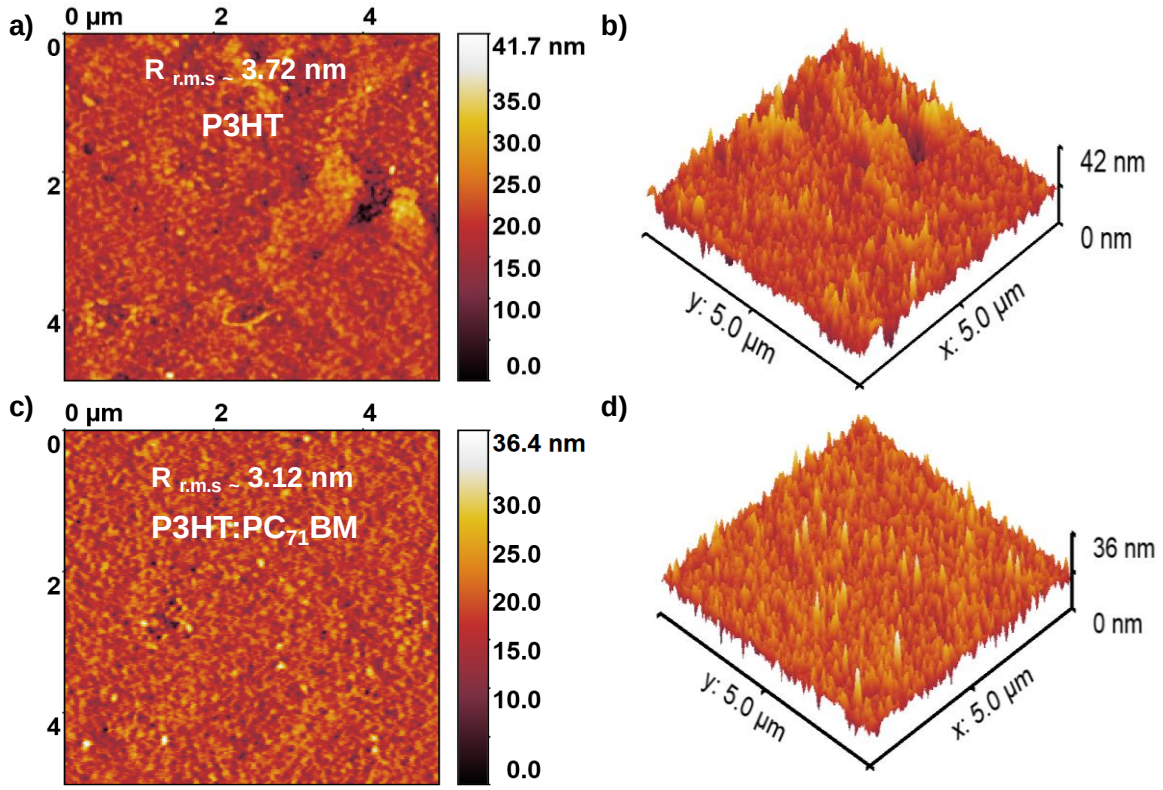

Figure 5.15 Morphological Study by AFM **a)** pure P3HT **b)** blended P3HT:$PC_{71}BM$ film over Au-Ag TC film.

5.7.6 Device Performance of Organic Solar Cells

The photovoltaic properties of pure P3HT and blended P3HT:$PC_{71}BM$ are investigated by fabricating devices with an inverted structure (plastic/SnO_2 NPs/Ag-TiO_2/4 nm Au/PEDOT:PSS/active layer/SnO_2 NPs/LiF/Al) with an active exposure area of 0.09 cm^2. **Figure 5.16a)**, shows a semi-log plot of the dark J–V characteristics for both devices. The ideality factor (η) of the devices are calculated from these plots by using the **Equation 2.8**. As estimated, the η values of are 1.7 and 2.3, for P3HT and P3HT:$PC_{71}BM$ devices, which are moderate to the high bias regions, where space charge limited current (SCLC) is predominant.[79] The photovoltaic performance of these devices are tested under ambient conditions with an illumination 1 sun white light that is shown in **Figure 5.16b).** The details of photovoltaic device parameters for both devices are shown in **Table 5.3,** indicating devices have very similar short circuit current with a density of ~17.5 mA/cm^2 which is reasonably high. Besides, it is very worth to note that the V_{OC} of the P3HT:$PC_{71}BM$ devices

is ~1.13 V which is almost double reported w.r.t the reported works on this class of organic solar cell. Again, V_{OC} of the P3HT is ~1.0 V which is hardly reported in literature. As a consequence, the PCE of P3HT and P3HT: $PC_{71}BM$ devices reaches to ~7.8% and 11.2% respectively which are record efficiency solar cell that are reported with these molecules. We have repeatedly tested the device under identical conditions and consistently observed similar performance, confirming the reliability of the results. The unusually high power conversion efficiency (PCE) primarily originates from the plasmonic bottom electrode. Unlike a conventional transparent or metallic electrode, the plasmonic electrode not only facilitates charge collection but also actively absorbs incident light through LSPR. This plasmonic absorption contributes directly to the photocurrent generation, in addition to the photocurrent produced by the active organic layer (P3HT:$PC_{71}BM$). Because both the plasmonic electrode and the organic layer act as photoactive components, the device essentially behaves like a tandem solar cell without requiring two separate junctions. The plasmonic electrode enhances light–matter interactions and broadens the absorption window, while the organic layer provides the standard excitonic contribution. The combined effect leads to an improvement in both photocurrent and photovoltage. In particular, the open-circuit voltage (Voc) shows a remarkable increase compared to that of a standard P3HT:$PC_{71}BM$ device, highlighting the synergistic role of the plasmonic electrode in boosting overall device efficiency.

In addition to the J−V characteristics, I investigated the EQE spectra of the devices which is shown in **Figure 5.16c).** It also can be noted that spectral range of these devices are extended up to 1500 nm wavelength which is very significantly higher than the reported EQE spectra of the P3HT:$PC_{71}BM$ BHJ devices that commonly exist within the spectral range of 700 nm. This broadening of the EQE spectra originates from the hot carriers of the plasmonic Au-Ag film, present as a back electrode. To validate the NIR sensitivity of the devices, IR light of peak emission spectra of ~ 980 nm is illuminated on both the devices that shows a large variation of photocurrent. The transient photoresponse of the P3HT:$PC_{71}BM$ devices is with a time interval of ~ 5 sec is shown in **Figure 5.16d),** indicating large variation of device current with reasonably fast device response, gave us evidence of generating photocurrent in NIR region.

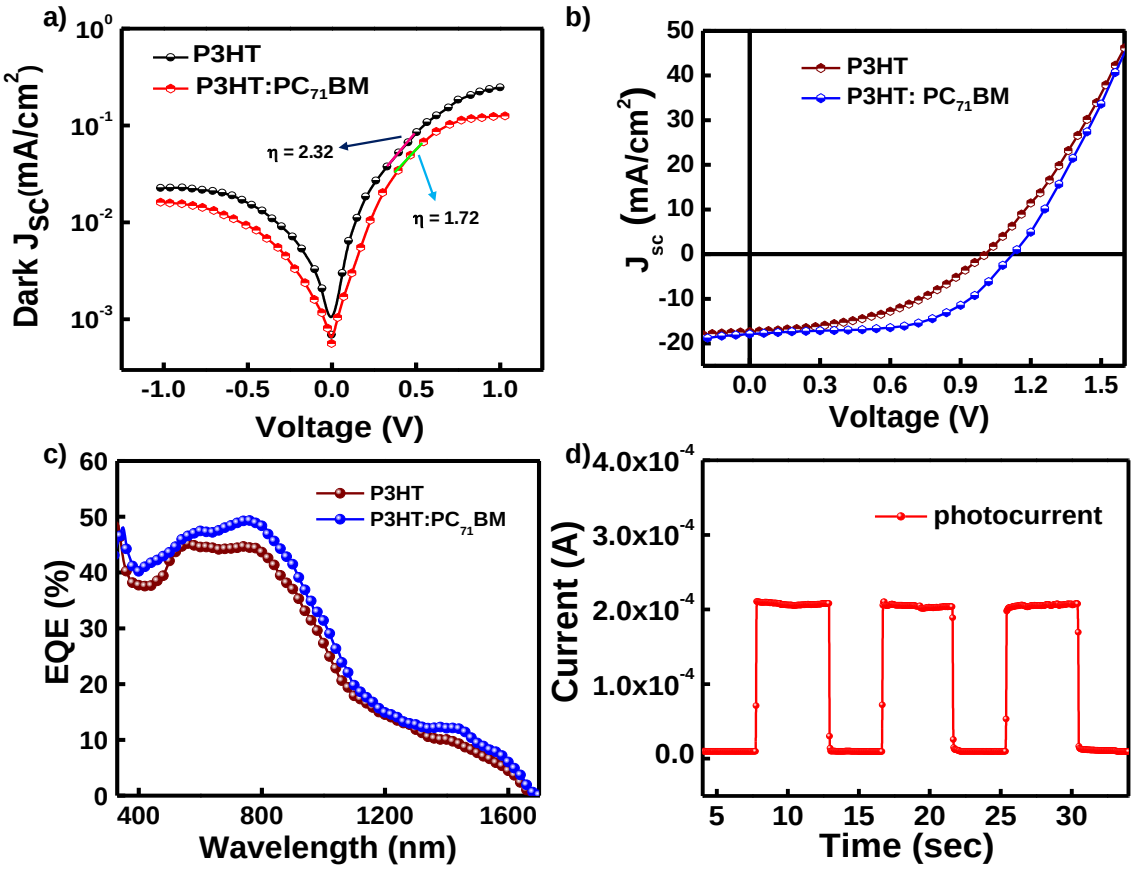

Figure 5.16 device characterization result **a)** dark J-V **b)** J-V under 1 Sun light **c)** EQE vs wavelength **d)** photoresponse with IR light.

Table 5.3 Device Parameter of Calculated Plasmonic Organic Photovoltaics

Active Material	J_{sc} (mA/cm^2)	V_{oc} (V)	FF (%)	PCE (%)
P3HT	17.42	1.01	44.32	7.8
P3HT:$PC_{71}BM$	17.89	1.13	55.25	11.17

To realize the origin of enhancement of V_{OC} of these devices, I fabricated a reference device without any organic semiconductor, keeping all other components same. The schematic presentation of this reference device is given in the inset of the **Figure 5.17a)**. The J-V

characteristics of this reference device is shown in **Figure 5.17a)**, indicating without any organic semiconductor it can works as a solar cell with a J_{sc} and V_{oc} and PCE of 9.56 ma/cm^2, 0.44 v and 1.36% respectively shown in **Table 5.4**. The EQE spectra of this reference device shows an intense photocurrent generation up to the wavelength of ~1600 nm which is similar to the P3HT and P3HT:$PC_{71}BM$ devices (**Figure 5.17b)**). The J-V characteristics and the EQE spectra of the reference device, clearly implies a tandem cell formation in both the P3HT and P3HT:$PC_{71}BM$ based device where 4 nm Au/Ag-TiO_2/SnO_2 NPs/PEDOT:PSS works as 1st cell which is connected in series with the P3HT:$PC_{71}BM$ (or P3HT)/SnO_2/LiF/Al that works as 2nd cell, resulting an addition of V_{OC} and enhancement photocurrent spectra up to 1600 nm.

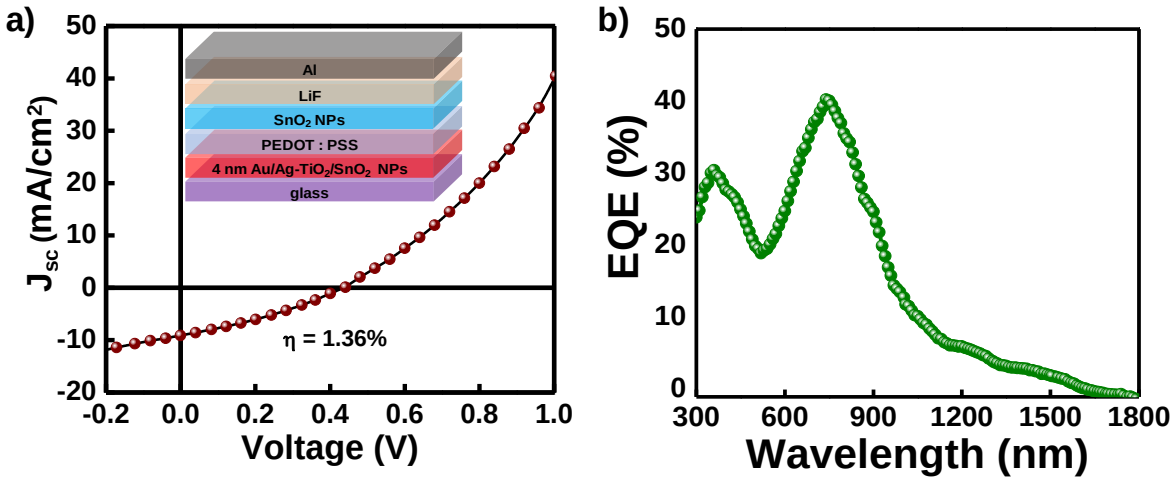

Figure 5.17 device performance of Au-Ag TC film based solar cell without active organic layer **a)** J-V curve under 1 sun light **b)** EQE vs wavelength.

Table 5.4 Device Parameter of Calculated Au-Ag TC Film Based Photovoltaics

J_{sc} (mA/cm^2)	V_{oc} (V)	FF(%)	PCE (%)
9.36	0.44	33.28	1.36

Despite tremendous gains in photovoltaic performance in OSCs, increased stability and repeatability remain a critical concern for practical applications. For that, we checked

reproducibility of the device performance by fabricating atleast 15 small area (0.25 cm^2) P3HT & P3HT:$PC_{71}BM$ based devices. Here, we have shown the histogram plots in **Figure 5.18a)** and the distribution of the data points for champion devices based on P3HT & P3HT:$PC_{71}BM$ active layer. From figure, we found that P3HT based device shows a PCE ranging 7.3 to 8.1%, whereas blended P3HT:$PC_{71}BM$ shows a distribution of PCE ranging from 10.8 to 11.6%. The distribution peak of blended BHJ devices is a little bit higher than that of single organic layer based devices. So, from the overall results, we can conclude that blended BHJ polymeric devices shows better reproducibility and, performance wise, can compete with other air stable organic photovoltaics.

The stability of the fabricated solar cells is an important topic to consider. We analyzed the self-life-testing experiment, which demonstrated the long-term stability of the fabricated cells. The self-life of the produced cells is determined by evaluating and recording the PCE of devices after exposing them to ambient air and room temperature. All the devices are stored in an ambient desiccator (humidity <40% and room temperature 25°C). The J−V measurement is carried out over 720 hours until the produced cell revealed a PCE drop of more than 20% from the initial value. All measurements are typically taken every five days, with the cells exposed to the solar simulator's light for less than one minute to avoid the degrading effect of POSCs. **Figure 5.18b)** shows the change in PCE of the devices with time (t) in ambient circumstances. Blended film shows a better stability where it maintains PCE of 80% up to 600 h.

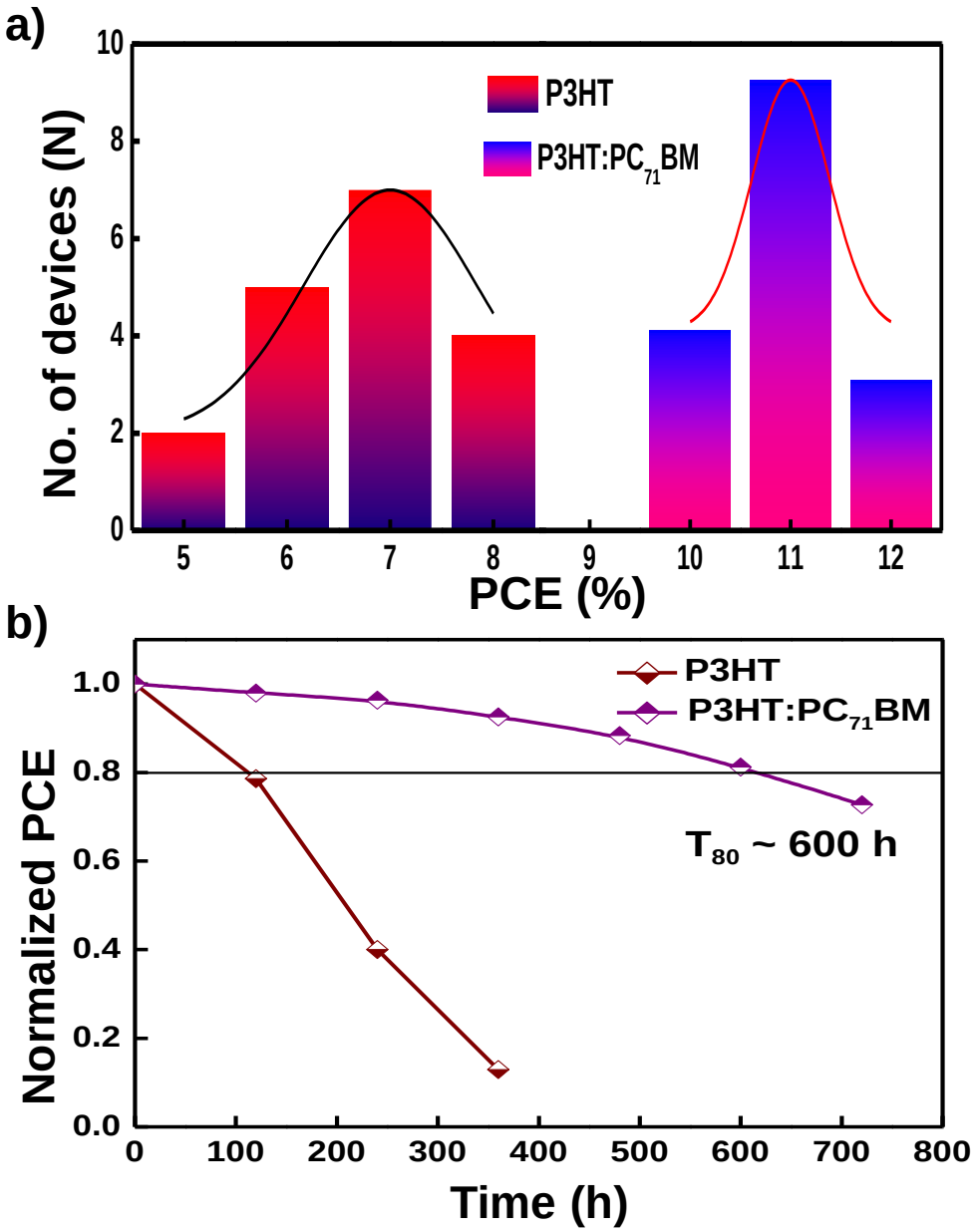

Figure 5.18a) reproducibility and **b)** air stability data of prepared plasmonic organic solar cell devices

5.8 Conclusion

We have successfully developed a solution process low-cost synthesis technique by depositing LTO/SnO_2 NPs based thin film on mechanically flexible plastic substrate at low

temperature by combined heating (at 100 ^{o}C) and UV illumination. Then, the loosely bound Li^{+} of this thin film has been replaced by Ag^{+} through an ion-exchange process that forms a Ag-TiO_2 thin film. A thermally evaporated 4 nm Au is deposited on top of this Ag-TiO_2/SnO_2 NPs thin film, which shows high electrical conductivity (5-10 ohm/□) and over 80% average visible transmittance in the range of 500-600 nm wavelength. This high electrical conductivity of the film appears due to the percolated growth of nanostructure Au-Ag NPs film during thermal evaporation. This film also shows a vibrant plasmonic absorption in the UV-Vis-NIR region. By utilizing combined optical transparency and plasmonic absorption features of this thin film, a plasmonic organic solar cell has been fabricated using this transparent electrode as a bottom electrode, where 4 nm Au/Ag-TiO_2/SnO_2 thin film works as plasmonic electrode and LiF/Al substrate as top electrode. Device shows a record PCE of 7.8% with pure P3HT and 11.17% with blended P3HT:PC_{71}BM based film, which is unusually high w.r.t the ITO coated device. A reference device without the organic semiconducting layer shows a solar cell behavior with a PCE of 1.36% to ensure a separate cell formation by the plasmonic Au-Ag based TC which is connected in series with the fabricated organic solar cell. As a result, V_{oc} improved by 1.5 times which ensures tandem cell formation in presence of an organic active layer. This P3HT: PCBM BHJ organic layer shows an excellent ambient (25 °C, 40–60% RH) stability (retained 80% of the initial PCE) up to 600 h of storage without encapsulation.

Chapter 6

Plasmonic Au-Ag Bimetallic Nanoporous Film as Flexible SERS Substrate for Detection of Molecular Level R6G dye and Vitamin B_{12}

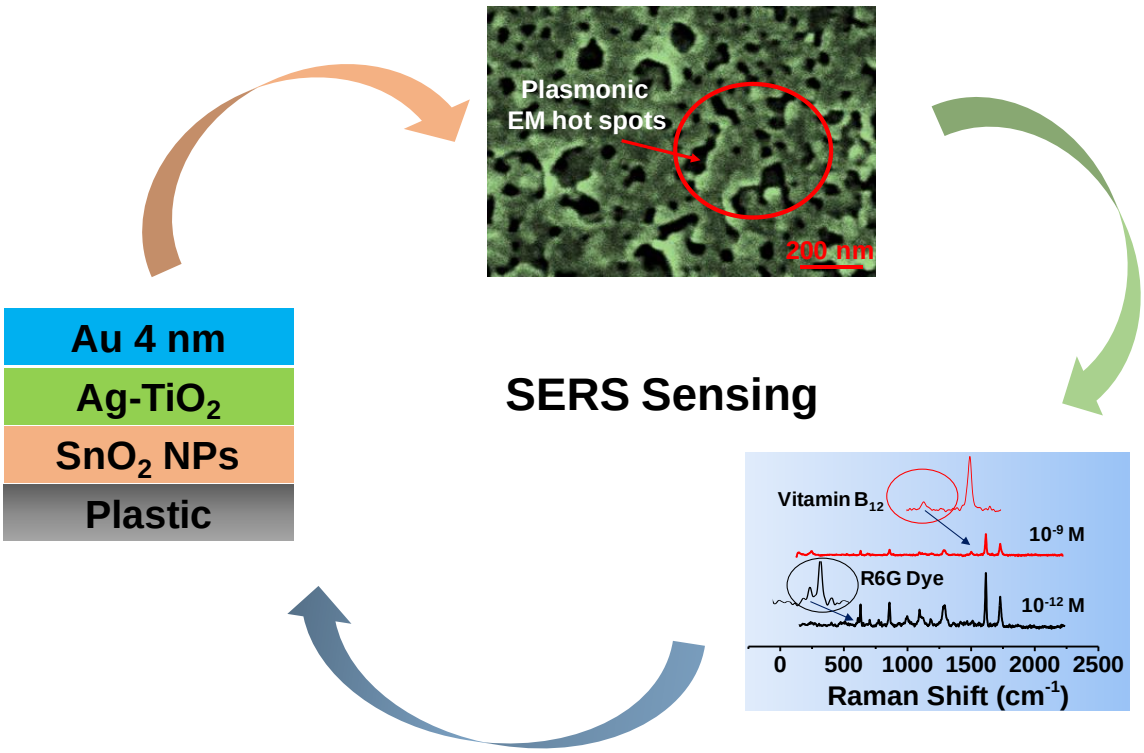

Chapter 6

This chapter also mainly focuses on development of a bimetallic Au-Ag TC film and then used that film for the detection of low molecule via Surface-Enhanced Raman Scattering (SERS) study. It is known that the surface roughness and nanostructures of novel metal thin film plays the major role in SERS study due to their intrinsic EM hotspots, multipolar resonance, and other factors. Based on that knowledge, I developed a low cost and scalable method to fabricate a nano-porous Au-Ag bimetallic thin film on a plastic substrate. This percolated and conducting Au-Ag nanostructured thin film is developed by thermally deposited Au film (4 nm mass thickness) onto a pre-deposited Ag-TiO_2 thin film. This Ag-TiO_2 film, consisting of Ag nanoparticles (NPs) embedded in TiO_2, is grown on SnO_2 nanoparticle (NPs) thin film, forming a nano-porous structure with an average roughness of 3.9 nm. Moreover, this Au-Ag nanostructured is grown inside/over TiO_2 that helps plasmon induced hot electrons transfer from Au-Ag nanostructure to the conduction band of TiO_2, which can enhance the SERS sensitivity of the substrate. This flexible Au (4 nm)/Ag-TiO_2/SnO_2 (NPs) substrate demonstrates efficient SERS-based sensing, detecting Rhodamine 6G (R6G) dye and Vitamin B_{12} down to 1 pM and 1 nM concentrations, respectively. Detailed investigation of the Au (4 nm)/Ag-TiO_2/SnO_2 NPs substrate for R6G detection shows its capability to detection limit up to a single molecule level where as it can detect vitamin B_{12} up to 89 molecules. These observations are attributable due to improved photo induced charge transfer (PICT) processes. This typical porous nature of the bimetallic thin film aids in dispersing the analytes, thus lowering particle density for single molecule optical detection, and enabling low-concentration measurements.

6.1 Introduction

SERS is an efficient analytic technique which amplifies the Raman signal on a metallic nanostructured surface to identify the highly sensitive chemical and biological molecules or structures.[298] This technique enables molecule level detection [263, 299]with an

enhancement factors up to ~10^{13}-10^{14}.[300, 301] Recently, novel metal-based plasmonic NPs such as Au, Ag, Cu have emerged as key players in various scientific and technological fields due to their multifunctional properties, including tunable optical, electrical, and catalytic behaviors.[262, 302-304] These NPs find wide applications in plasmonic photodetectors, photo catalysis, transparent conductor & heat reflector, memory devices, chemical and gas sensing, bio imaging, SERS and so on.[305-309] The size, shape, composition and surrounding medium of these mono-metallic, bimetallic, or multicomponent NPs are the key factors of their plasmonic properties.[310, 311] For SERS substrate application, bimetallic or metal/metal oxide heterostructures are gaining attention for their enhanced optical properties compared to single-metal nanostructures. Particularly, Au-Ag bimetallic nanostructures are gaining interest due to the enhanced plasmonic effect of Ag NPs and superior chemical stability of Au component.[312-315] Advantageously, Ag nano-structures may allow the growth of Au on its surface without alloy formation due to their same set of lattice parameters if processing temperature is restricted <50 °C, leading to the synthesis of bimetallic nanostructures.[316] The growth of Au on Ag leads to the creation of various LSPR, which can be tuned from visible to near-infrared regions, depending on the core Ag geometry and atomic ratio of Ag and Au.[317, 318] This tunability extends the applications of SERS sensing and biomedical fields, especially in NIR regions where background fluorescence is minimal.[319, 320] Instead of the advantages SERS enhancement factors of these Ag-Au based bimetallic plasmonic NPs is limited for practical applications that required further research.

SERS enhancement relies on EM and chemical mechanisms. EM enhancement, the primary component, arises due to the electric field generated on the surface of novel metal nanostructures by excited surface plasmons (SPs), while chemical enhancement involves charge transfer between nanostructures and adsorbed molecules.[321, 322] In both case, analytes required an accessible surface for strong molecule-metal interaction.[323] However, most of the colloidal plasmonic NP synthesis required organic ligands which limit that molecule-metal interaction. Besides, a metal oxide semiconductor contact of plasmonic NP helps light induced hot electron transfer from metal NP to semiconductor that effectively enhances chemical mechanism.[324] Therefore, an ideal SERS system would be ligand free metal NP/metal oxide heterostructure to maximize enhancement factors. However, only few

studies have successfully combined these components into a stable, low-cost, highly sensitive, and flexible SERS substrate.[325, 326] Besides, plasmonic hot electron of novel MNPs can efficiently transfer to a conduction band (CB) of a metal oxide semiconductor like TiO_2.[194, 196] This energy charge transfer (CT) phenomena from metal NPs to the CB of oxide semiconductor can largely improve the enhancement factor of SERS signal.[327, 328] This concept has been explored mostly with the Ag/TiO_2 system due to the strong SPR of Ag and very fast charge transfer from Ag NPs to TiO_2.[329] However, the environmental stability of Ag NPs is not that high. Therefore, in-depth research is required to develop a stable metal/metal-oxide SERS substrate with high enhancement factor.

Herein, this study demonstrated the fabrication strategy of environmentally stable and highly sensitive SERS substrate by using Au-Ag bimetallic nanostructured based plasmonic thin film grown on a mechanically flexible plastic substrate. These plasmonic Au-Ag nanostructured is grown in the TiO_2 matrix that improve the enhancement factor of SERS signal by efficient CT phenomena. For this synthesis, 4 nm mass-thickness of Au has been deposited by thermal evaporation on a pre-deposited Ag-TiO_2/SnO_2 NPs thin film which is grown by a low temperature solution processed technique. This Au/Ag-TiO_2/SnO_2 NPs substrate is not only mechanically flexible, but also optically transparent and electrically high conducting. The SERS study has been investigated by using this substrate with R6G dye and vitamin B_{12} biomolecules as analytes, indicating their detection limits of 10^{-12} M and 10^{-9} M, with an enhancement factor of 3.4×10^8 and 2.2×10^5 respectively.

6.2 Experimental Section

6.2.1 Preparation of Precursor Materials

The preparation process for ion-conducting dielectric LTO and SnO_2 NPs via low temperature solution process technique has been explained in **Chapter 2 Section 2.1.1 and 2.1.3.** Preparation method of analytic solution R6G dye and Vitamin B_{12} is reported in **Chapter 2 Section 2.1.12.**

6.2.2 Fabrication of Au-Ag SERS Substrate

Bimetallic Au-Ag based SERS substrate has been fabricated on a flexible PET substrate and the fabrication steps has been explained **Chapter 2 Section 2.3.3**, and schematically present in **Figure 2.9**.

6.3 Results and Discussion

6.3.1 Surface Morphology (HR-SEM & AFM)

The surface morphology of (4 or 6 nm Au)/Ag-TiO_2/SnO_2 NPs thin film is studied by HR-SEM. **Figure 6.1a&b)** demonstrated the morphological change of the films with different mass thickness of thermally deposited Au film over Ag-TiO_2/SnO_2 NPs thin film. At a critical Au deposition, a percolated Au nanostructure formation is observed which is realized from the sudden change of its morphology. At the initial stage of this growth, thin films are composed of metallic Au islands which forms interconnecting paths of Au as growth is progressed and the residual voids are filled up with additional deposition.[330] The percolated growth of Au during thermally grown Au becomes possible due enhanced lateral growth rate of Au which is promoted by the pre-deposited Ag-TiO_2/SnO_2 NPs thin film due to the pre-existing highly dense Ag-NP that works a nucleation point of Au growth. This possible phenomenon has been realized from the Au film growth on a reference clean plastic substrate which is shown in **Figure 5.7a)**. Reference sample clearly show an isolated grain-like Au growth over the plastic substrate upto 10 nm mass thickness, implying the importance of pre-deposited Ag-TiO_2/SnO_2 NPs as an initial layer which helps to reach percolated nano-porous structure at 4 nm Au mass thickness. Moreover, the nano-porous structure of this SERS substrate (**Figure 6.1a)**) can create intrinsic EM hot spots which effectively enhance the sensitivity of the film. Further deposition of Au film (~ 6 nm) covers the voids, results less effective sensitivity which is shown in **Figure 6.1b)**, is used as a reference film to study side by side of the actual film. EDX and color-mapping attached to the HR-SEM instrument is used to figure out the contents and amount of metallic elements present in both type of film 4 nm Au/Ag-TiO_2/ SnO_2 NPs (**Figure 5.5**) and 6 nm Au/Ag-TiO2/SnO2 NPs (**Figure 6.2**) which confirms the presence of Au, Ag, Ti, Sn and O uniformly throughout the thin film.

Further, AFM has been used for more detailed surface study of Au/Ag-TiO_2/SnO_2 NPs thin films to recognize the surface roughness (R_{rms}) in **Figure 6.1c&d)**. Surface roughness for 4 nm Au/Ag-TiO_2/SnO_2 NPs is quite high (R_{rms}~3.91 nm) compared to 6 nm Au/Ag-TiO_2/ SnO_2 NPs (rms~1.62 nm). Besides, 4 nm Au/Ag-TiO_2/SnO_2 NPs film has larger porosity compared to the 6 nm Au/Ag-TiO_2/SnO_2 NPs which is beneficial for generating hotspot and multipolar resonance effect during the interaction with EM wave that essentially enhanced the SERS significantly. The height profile of these two films are shown in the inset of **Fig. Figure 6.1c&d)** whereas **Figure 6.1e&f)** shows the 3-D AFM image of these two respective films.

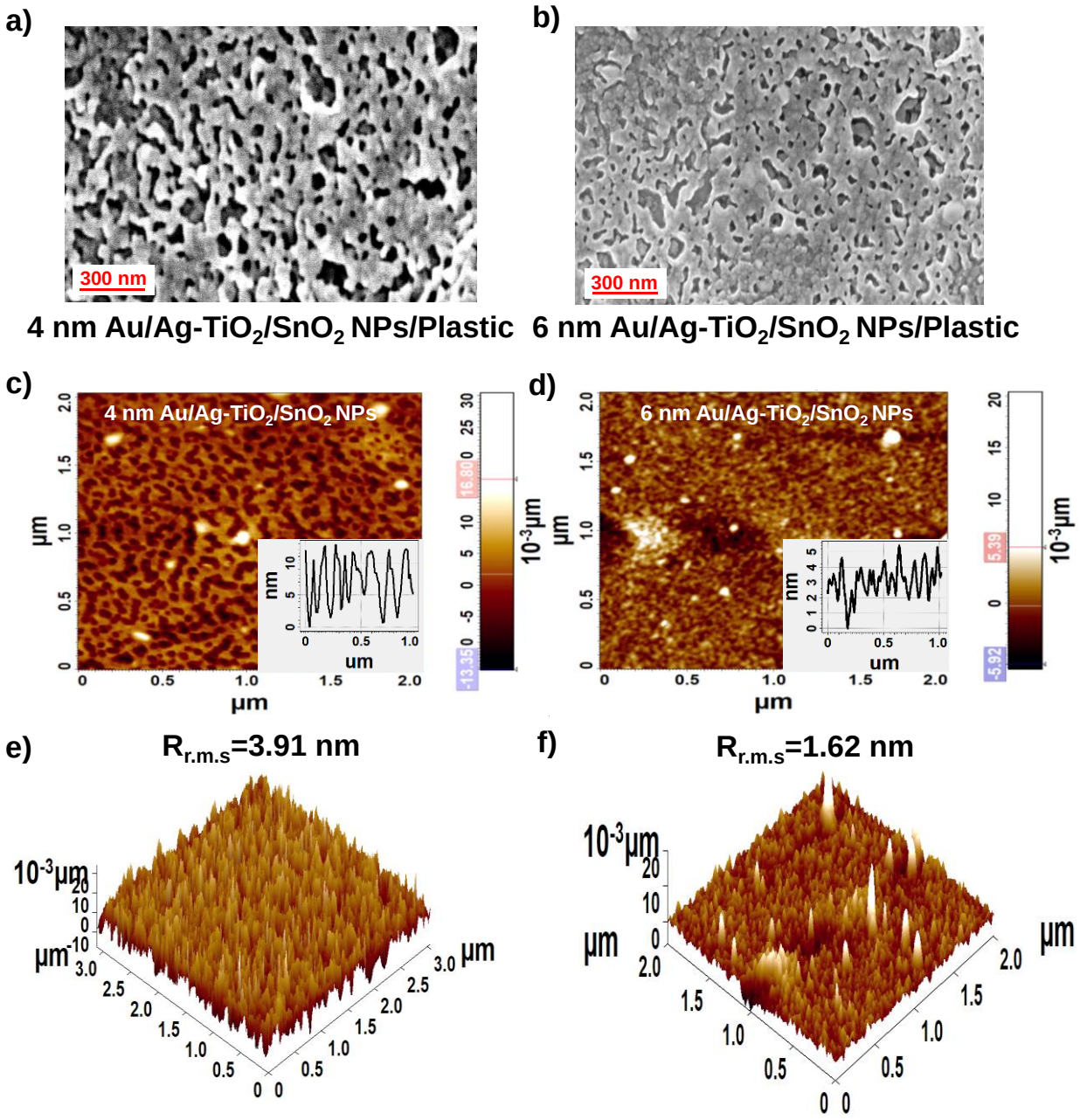

Figure 6.1 FE-SEM photographs of Au/Ag-TiO_2/SnO_2 NPs thin film at room temperature on plastic. Each photograph's average film thickness is listed below. **a)** percolating nano-porous structures **b)** complete percolating structures **c&d)** 2-D AFM image of (4 or 6 nm Au)/Ag-TiO_2/SnO_2 NPs. Each image height profile is listed in the inset **e&f)** 3-D AFM image of (4 or 6 nm Au)/Ag-TiO_2/SnO_2 NPs. R.M.S Roughness of each film is listed in the graphics.

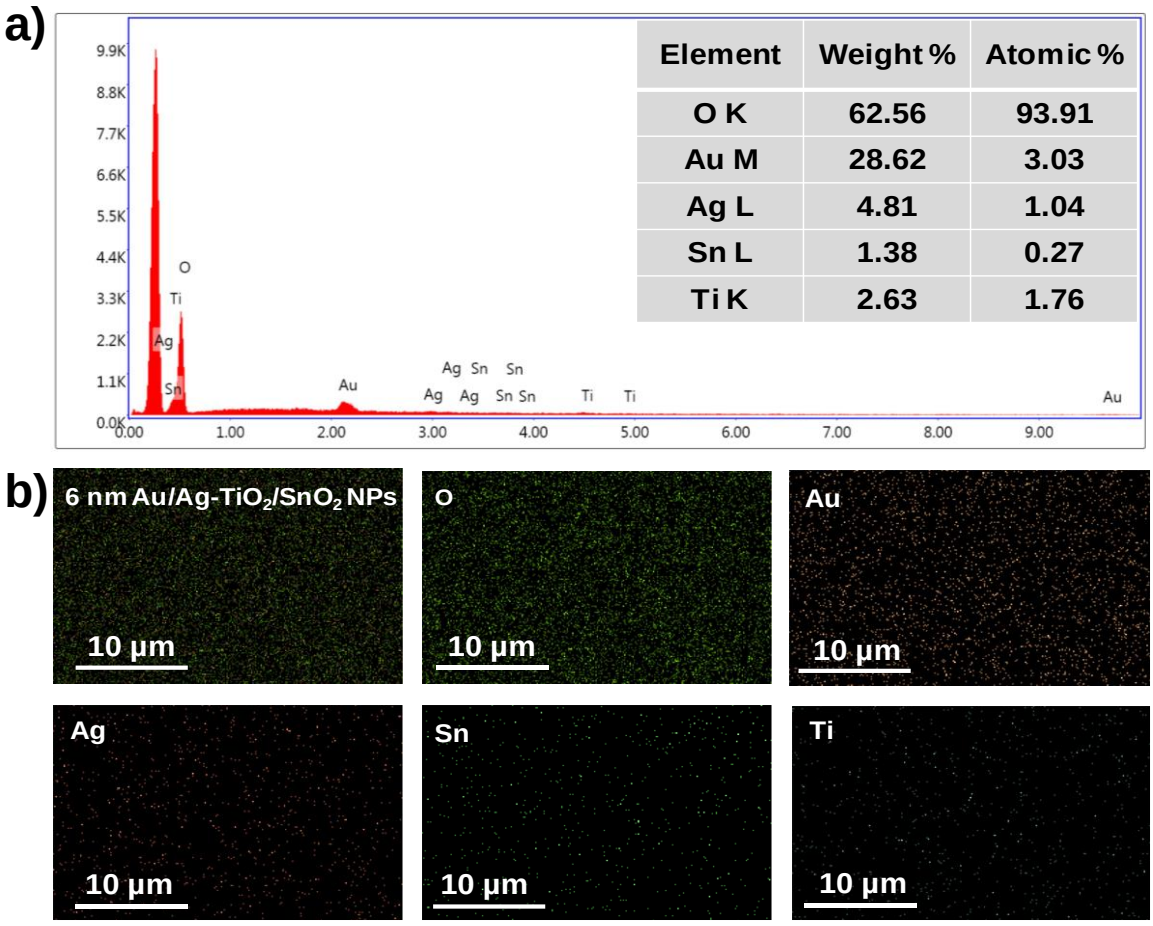

Figure 6.2 EDX and color mapping image of 6 nm Au/Ag-TiO_2/SnO_2 NPs on plastic.

6.3.2 XRD, Raman, UV-Vis Absorption, and PL Spectra

Figure 6.3a) depicts XRD pattern of the thin films that are deposited in the similar way as of Au-Ag based bimetallic nano films fabrication This figure clearly shows the XRD patterns of both substrates (4 or 6 nm Au)/Ag-TiO_2/SnO_2 NPs) exhibits identical XRD pattern but with different intensities. In both cases, the peak position is located at 2θ of 26.17˚, 33.58˚, 51.47˚ and 54.45˚ which corresponds to (110), (101), (211), and (310) planes respectively, indicating the formation of SnO_2 NPs thin film over the substrate (JCPDS file no. 411445). Also, the peak position of TiO_2 at 2θ ~ 24.52˚ corresponds to (110) planes (JCPDS file no. 731764). Besides, the peak position of Au or Ag NPs are located at 2θ ~ 37.83˚ and 44.02˚ which corresponds to (111) and (200) planes respectively (JCPDS file no. 897322). The XRD peak positions of Au or Ag NPs are common because of their very similar lattice parameters.

From this XRD spectra its very clear that the width of the peaks is quite wide, indicating the small size of the metal/metal oxide nanoparticle.

The synthesized 4 nm and 6 nm Au/Ag-TiO_2/SnO_2 NPs thin film are characterized using Raman spectroscopy with 532 nm excitation laser sources. The Raman spectra of both samples, collected using a green laser (532 nm), are displayed in **Figure 6.3b).** The presence of various characteristic phonon modes at ~628 cm^{-1} is arising due to the SnO_2 NPs, at ~ 856,1287 and ~1725 cm^{-1} are observed for plastic substrate, and Raman modes observed at ~1098 & 1613 cm^{-1} are because of Au/Ag NPs. Raman Spectra of reference plastic substrate is given in **Figure 6.4a)**.

For optical studies, thin film of (4 or 6 nm Au)/Ag-TiO_2/SnO_2 NPs is fabricated on a quartz substrate. **Figure 6.3c)** displays the normalized UV-Vis absorbance spectrum of Au/Ag-TiO_2/SnO_2 NPs thin films throughout the optical spectral range of 300–1800 nm. The absorption spectra of as-prepared (4 or 6 nm Au)/Ag-TiO_2/SnO_2 NPs thin films demonstrate strong plasmonic absorption with wide spectral broadening extended from UV-Vis to NIR region up to 1600 nm with a peak position ~ 750 nm. However, reference pure Ag NPs film has a plasmonic peak situated in the blue region around 420-440 nm, while reference Au NPs film has a plasmonic peak of around 520-550 nm. Therefore, it can be concluded that the bimetallic Au-Ag NP formation causes the absorption peak shift to ~750 nm with a large broadening of spectra extended up to 1500 nm, particularly for the longitudinal plasmon mode of this metallic network. The photoluminescence (PL) spectra of the (4 or 6 nm Au)/Ag-TiO_2/SnO_2 NPs thin film is shown in **Figure 6.3d)** which is acquired in the range of 320-550 nm with an excitation wavelength of 300 nm, indicating the emission peaks of around 370 nm (3.35 eV), with a FWHM of 55 nm. The PL peak position at 370 nm suggests specific optical properties that could be attributed to the formation of an Au-Ag NP on TiO_2/SnO_2 matrix. We also observed that the reference pure Au NPs also have PL with the same peak position (~370 nm) but with much lower intensity (**Figure 6.4b)**).

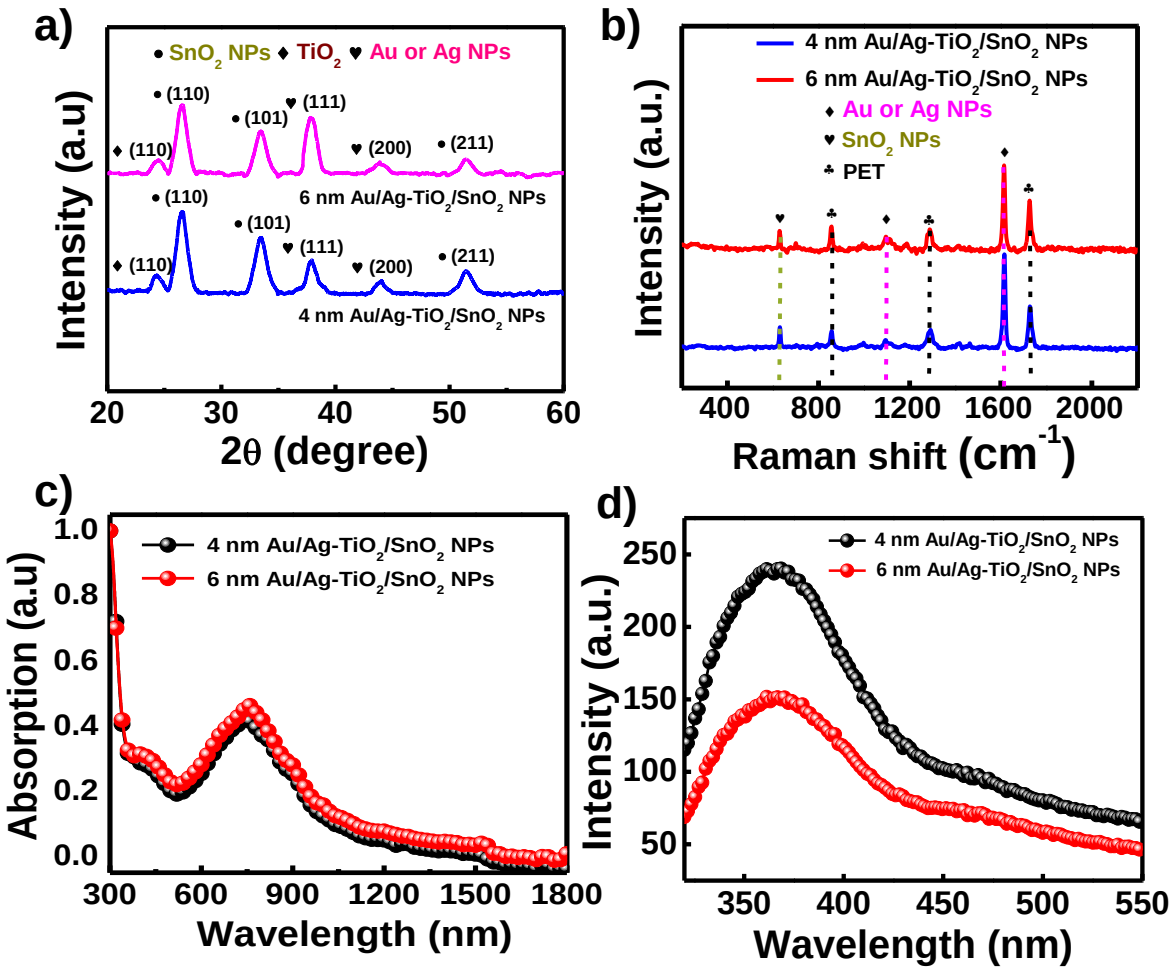

Figure 6.3 structural analysis of (4 or 6 nm Au/Ag-TiO_2/SnO_2 NPs/plastic) **a)** XRD **b)** Raman **c)** UV-Vis **d)** PL spectra.

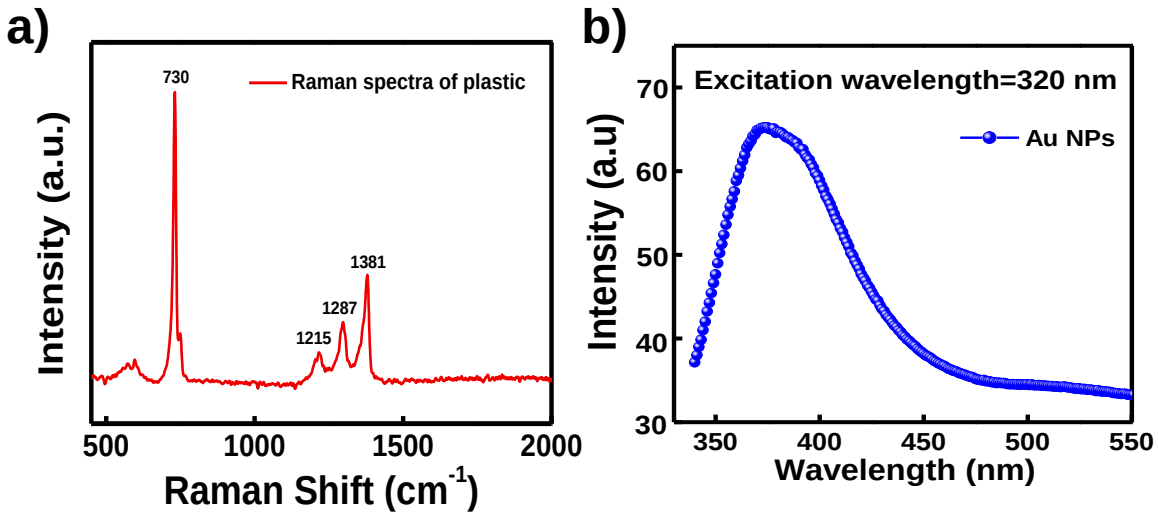

Figure 6.4a) raman spectra of plastic PET **b)** PL spectra of reference 4 nm Au/plastic.

6.3.3 SERS Study

We have performed a SERS study to detect R6G dye using 4 nm and 6 nm Au/Ag-TiO_2/SnO_2 NPs thin films as SERS substrates, which is shown in **Figure 6.5a&b)**. The limit of detection for R6G, adsorbed over 4 nm and 6 nm Au/Ag-TiO_2/SnO_2 NPs thin films substrates are found to be 10^{-12} M and 10^{-9} M, respectively, which is an excellent SERS activity at room temperature. With increasing dye concentrations, the SERS peaks for R6G become more intense. **Figure 6.5c&d)** displays the linear response curve of a prominent peak (~ 611 cm^{-1}) intensity with dye concentration. A notable intensity at picomolar concentration indicates that R6G is highly detectable. The most intense peak, centered around 611 cm^{-1} for R6G dye, is due to the aromatic C-C stretching of the R6G molecule.

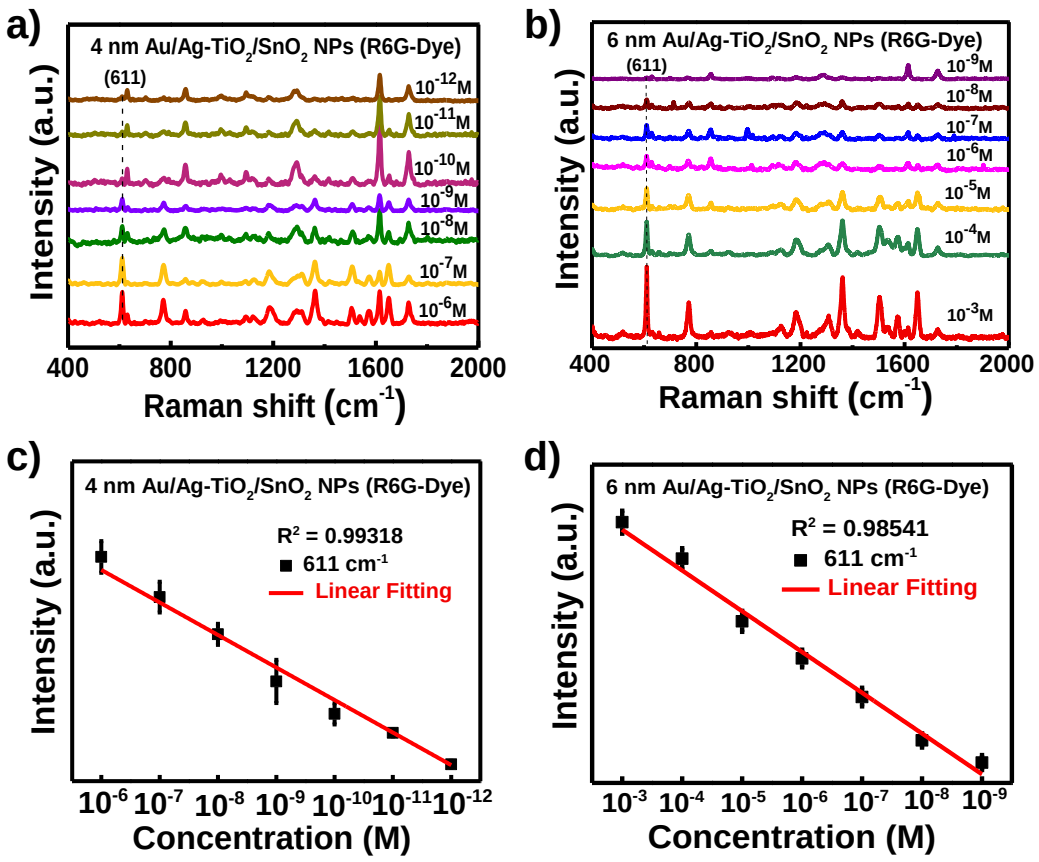

Figure 6.5 SERS spectra of R6G dye of different concentrations on **a)** 4 nm Au/Ag-TiO_2/SnO_2 NPs/plastic substrate (10^{-6} to 10^{-12} M) **b)** 6 nm Au/Ag-TiO_2/SnO_2 NPs/plastic substrate (10^{-3} to 10^{-9} M**) c)** linear fitting curve of 4 nm Au/Ag-TiO_2/SnO_2 NPs/plastic

substrate (10^{-6} to 10^{-12} M) and **d)** linear fitting curve of 6 nm Au/Ag-TiO_2/SnO_2 NPs/plastic substrate (10^{-3} to 10^{-9} M).

We have also performed a SERS study to detect vitamin B_{12} using 4 nm and 6 nm Au/Ag-TiO_2/SnO_2 NPs thin film substrates, as shown in **Figure 6.6a&b)**. The limit of detection for vitamin B_{12} adsorbed over 4 nm Au/Ag-TiO_2/SnO_2 NPs thin films and 6 nm Au/Ag-TiO_2/SnO_2 NPs thin films are found to be 10^{-9} M and 10^{-7} M, respectively, which indicates strong SERS activity at ambient temperature. The most intense peak centered at ~1501 cm^{-1} for the 4 nm thin film and 6 nm thin film (assigned to the stretching of C=C and C=N bonds of the corrins with mild contributions from CH, CH_2, and CH_3 bending modes) is preferred here for vitamin B_{12} detection. It's found that a lower SERS signal is detected as the vitamin B_{12} concentration decreases. The linear variation of peak intensity at 1501 cm^{-1} of vitamin B_{12} with concentration on the 4 nm and 6 nm thin film substrates, respectively, is displayed in **Figure 6.6c&d)**. The notable peak intensity even at a nanomolar (10^{-9} M) concentration of vitamin B_{12} on the 4 nm Au/Ag-TiO_2/SnO_2 NPs thin film substrate indicates the ultrasensitive detection, which is better than the 6 nm thin film used as a SERS substrate.

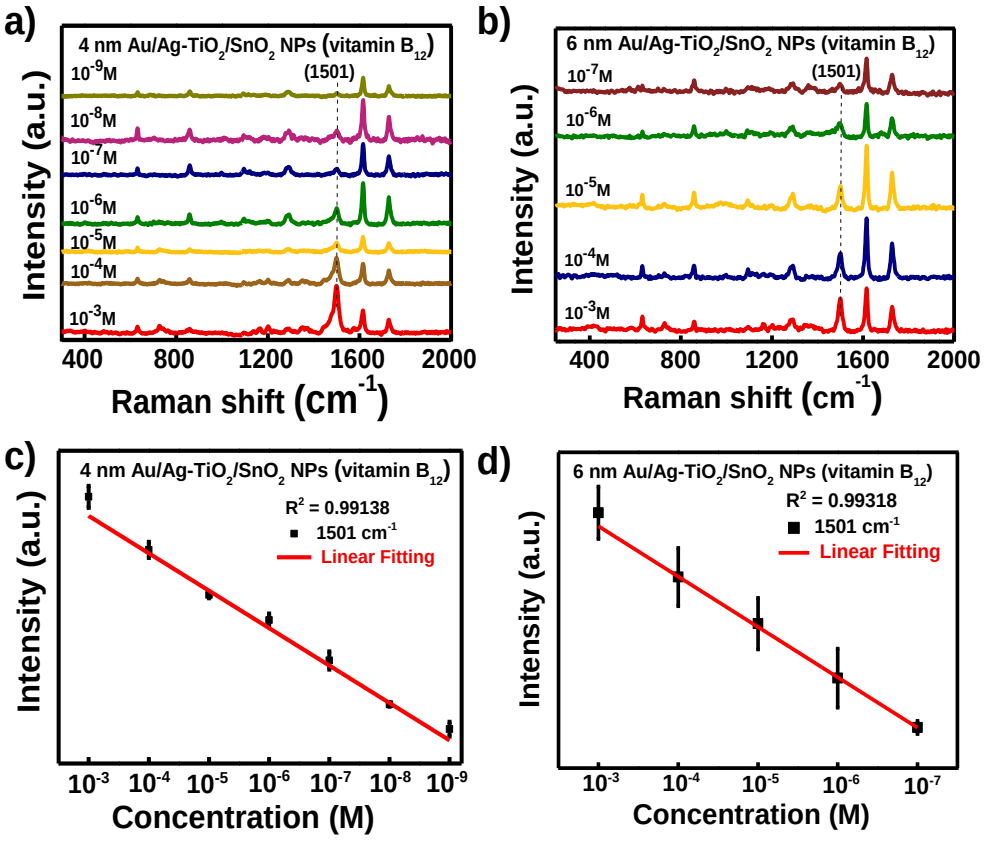

Figure 6.6 SERS spectra of vitamin B_{12} at different concentrations on **a)** 4 nm Au/Ag-TiO_2/SnO_2 NPs/plastic substrate (10^{-3} to 10^{-9} M) **b)** 6 nm Au/Ag-TiO_2/SnO_2 NPs/plastic substrate (10^{-3} to 10^{-7} M) **c)** linear fitting curve of 4 nm Au/Ag-TiO_2/SnO_2 NPs/plastic substrate (10^{-3} to 10^{-9} M) and d) linear fitting curve of 6 nm Au/Ag-TiO_2/SnO_2 NPs/plastic substrate (10^{-3} to 10^{-7} M).

To check the uniform distribution of analyte molecule molecules over SERS substrate, we have performed the SERS mapping corresponding to Raman intensity ratio of SERS substrate to analytic molecule. **Figure 6.7a&c)** shows the SERS mapping ratio or 4nm and 6nm Au/Ag-TiO_2/SnO_2 NPs corresponding to R6G dye. Additionally, the SERS uniformity is also verified by plotting the histograms showing the SERS intensity at ten different locations shown in **Figure 6.7c&d)**. The calculated coefficient of variation is ~0.017 for R6G on 4 nm Au/Ag-TiO_2/SnO_2 NPs and 0.028 for R6G on 6 nm Au/Ag-TiO_2/SnO_2 NPs. Similarly, we have performed for SERS mapping ratio corresponding vitamin B_{12} over 4nm and 6nm Au/Ag-TiO_2/SnO_2 NPs as shown in **Figure 6.8a&c)** and the histograms plot corresponding to SERS data point at ten different locations for vitamin B_{12} on 4 nm and 6nm Au/Ag-TiO_2/SnO_2 NPs as shown in **Figure 6.8b&d)**.

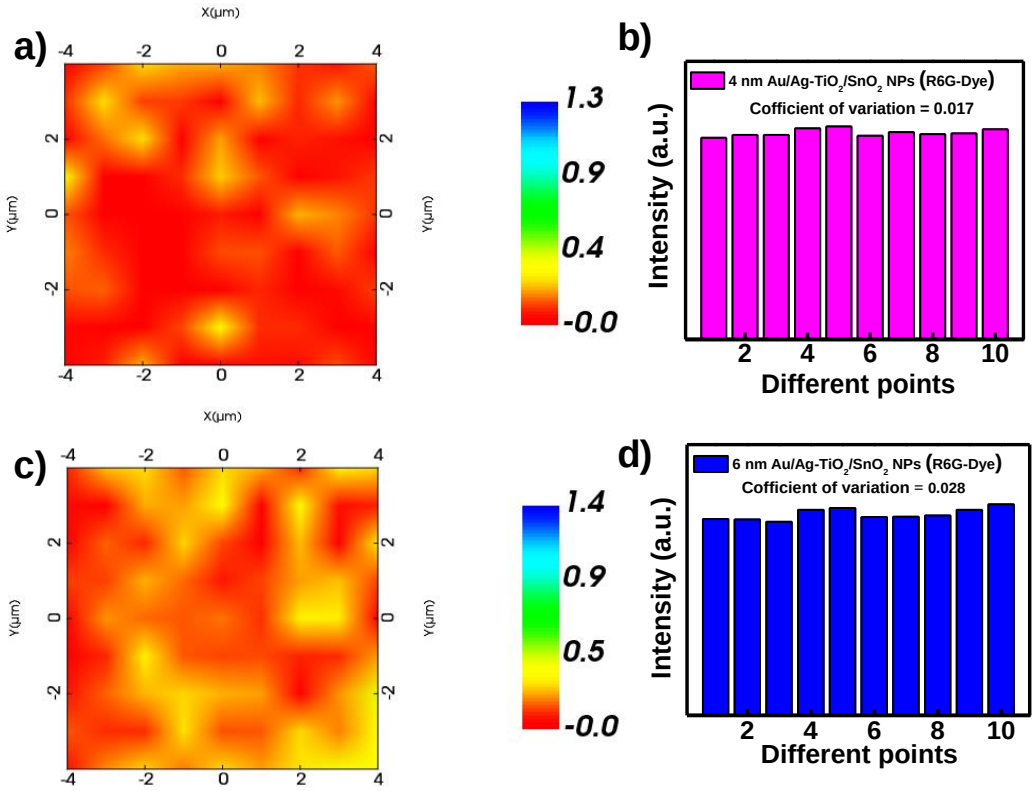

Figure 6.7 mapping images of the ratios of Raman intensities of the SERS substrate to R6G on **a)** 4 nm Au/Ag-TiO_2/SnO_2 NPs and **c)** 6 nm Au/Ag-TiO_2/SnO_2 NPs **b&d)** histograms depicting the distribution of SERS intensities at different locations for corresponding substrates, along with their coefficients of variation.

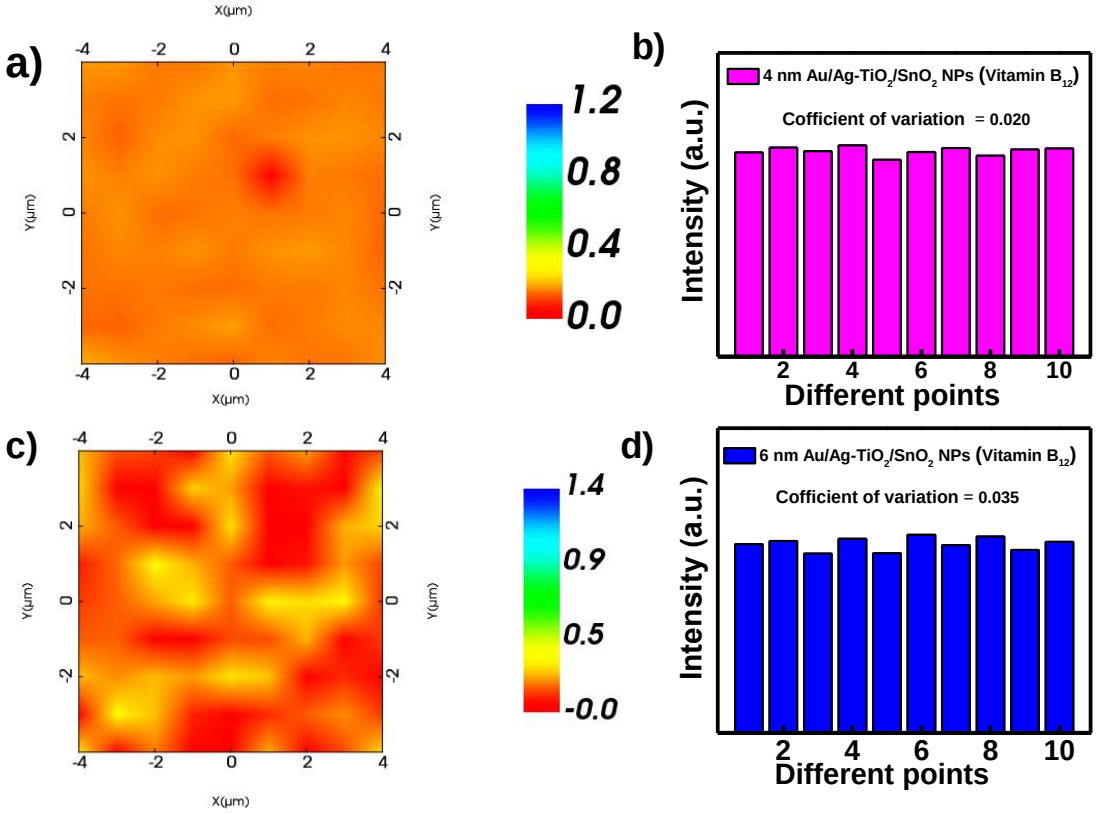

Figure 6.8 mapping images of the ratios of Raman intensities of the SERS substrate to vitamin B_{12} **a)** 4 nm Au/Ag-TiO_2/SnO_2 NPs **c)** 6 nm Au/Ag-TiO_2/SnO_2 NPs **b,d)** histograms depicting the distribution of SERS intensities at different locations for corresponding substrates, along with their coefficients of variation.

We have also performed SERS mapping at three different regions of SERS sample to check SERS uniformity throughout. The SERS ratio mapping for three different regions of R6G and vitamin B_{12} at two orders of magnitude lower than the highest detection limit is presented in **Figure 6.9** & **Figure 6.10**. This mapping clearly demonstrates the uniform distribution of these analytic molecules across both SERS substrates used for detection.

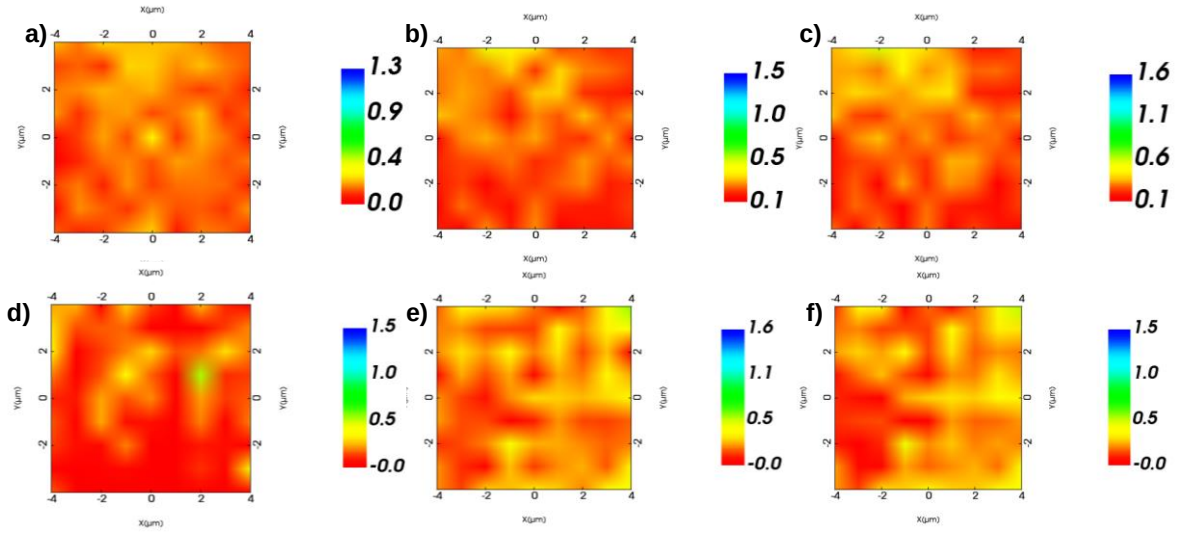

Figure 6.9 Mapping images of the ratios of Raman intensities of **a-c)** 4 nm Ag-TiO_2/SnO_2 NPs substrate to R6G and **d-f)** 6 nm Ag-TiO_2/SnO_2 NPs substrate to R6G.

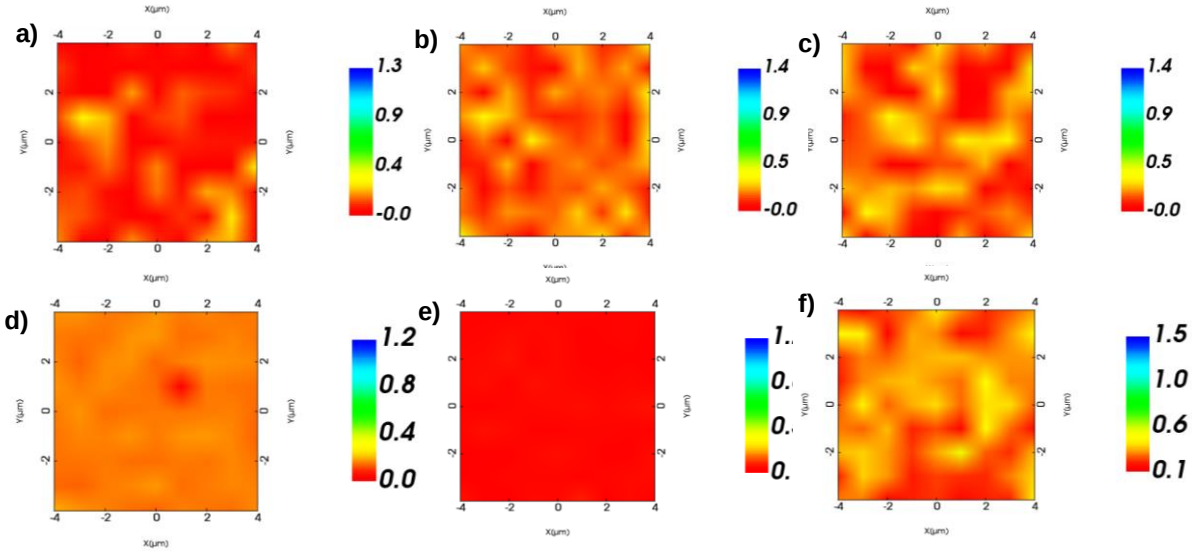

Figure 6.10 mapping images of the ratios of raman intensities of **a-c)** 4 nm Ag-TiO_2/SnO_2 NPs substrate to vitamin B_{12} and **d-f)** 6 nm Ag-TiO_2/SnO_2 NPs substrate to vitamin B_{12}.

Long-term stability of the SERS substrate is investigated at room temperature. The SERS spectra of analytes vitamin B_{12}, and R6G at the lowest detected concentration are collected after 1,2 and 3 months, as shown in **Figure 6.11a,b,c&d)**. The SERS spectra of the substrate on the 1st day and after 1,2 and 3 months show small variation, which may be due to the slight changes in measuring environments. The measured signal intensities of characteristic

peaks from the SERS substrate demonstrated the proposed substrate maintained its fine features and intensities up to months.

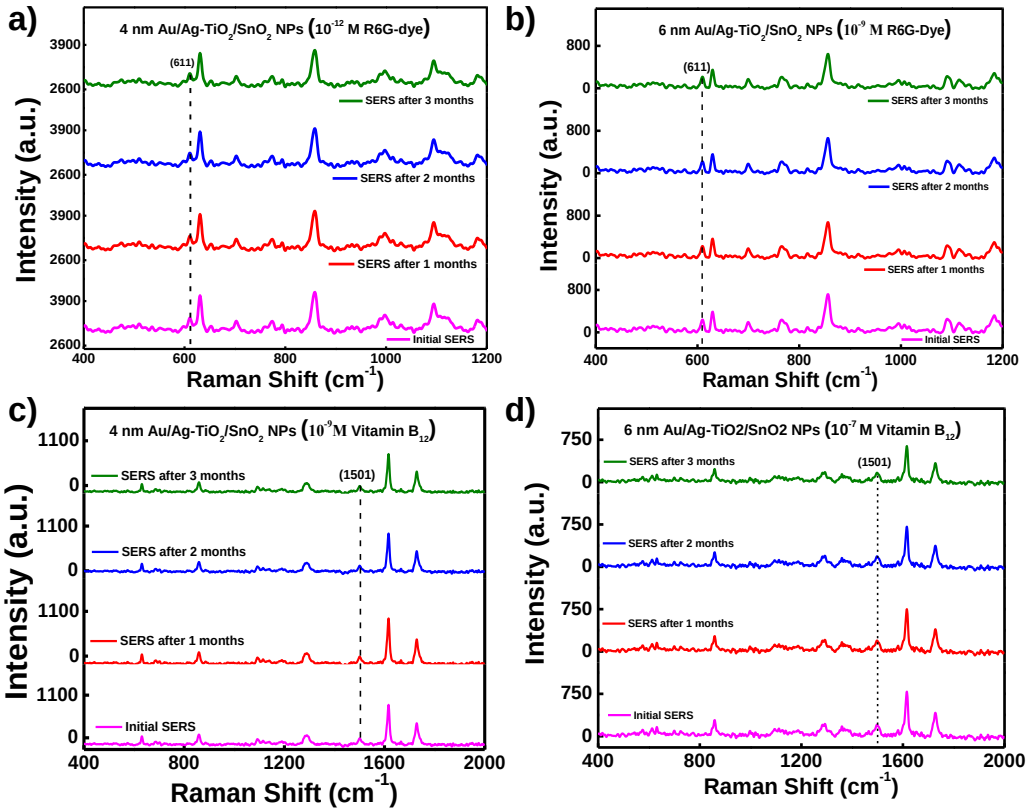

Figure 6.11 SERS spectra after 1-3 months, comparing with initial SERS initial preserved substrate **a,b)** R6G on 4 nm and 6 nm Au/Ag-TiO_2/SnO_2 and **c,d**) vitamin B_{12} on 4 nm and 6 nm Au/Ag-TiO_2/SnO_2 .

The most significant impact to SERS enhancement comes from the EM mechanism, which is predominantly due to the excitation of LSPR on the metal nanostructures. LSPR are collective oscillations of conducting electrons in the plasmonic materials, which occur when the incoming light matches the natural frequency of the outermost electrons vibrating against the restoring force of positive nuclei. When localized surface plasmons are excited, they generate intense EM fields at the surface of the nanostructures, particularly at "hot spots" such as sharp edges, tips, and interparticle junctions. The Raman scattering signal of molecules located in these hot spots is significantly enhanced due to the increased local electromagnetic field (**Figure 6.12a)**). The enhancement factor is highly dependent on the size, shape, and interparticle distance of the metal nanostructures. Optimizing these

parameters can lead to very high local field enhancements and, consequently, substantial SERS signals.[331, 332]

The other mechanism involved is chemical enhancement, wherein charge transfer (CT) between adsorbed molecules and the metal oxide semiconductor layer is considered to be crucial in plasmon driven chemical reactions. Semiconductors possess an energy gap between an empty conduction band (CB) and a full valence band (VB), and the CT between the semiconductor and molecules is dependent on the vibronic coupling of the CB or VB with the excited and ground states of the molecule. In this case, a chemical transition between the HOMO and LUMO of adsorbed molecules might take place. CT can happen from semiconductors to molecules or the other way[333] around (**Figure 6.12b)**). The key variable in the Raman scattering enhancement metal/metal oxide hybrid nanostructure (**Figure 6.12c**) is believed to be the combination of the EM mechanism (e.g., mie resonance) and chemical effects (e.g., band gap resonance). This complex enhancement mechanism includes plasmon-derived enhancement or CT from metals/metal oxide heterostructure.[334]

We used Albrecht's methods, adding Herzberg-Teller vibronic coupling into the polarizability formula, to establish an analytical expression for the Raman intensity near single or bi-metal nanoparticles. This method allows for breakdowns in the Born-Oppenheimer approximation and is extended to second order in perturbation theory. By considering the molecule-metal system as connected and including the occupied and unoccupied levels of the metal conduction band in the Herzberg-Teller expansion to improve Albrecht's estimates. We showed that the largest enhancement happens when transitions to or from the metal levels are at the energy level of Fermi by substituting an integral for the sum over metal states. The resultant polarizability (R) expression is similar to Albrecht's and can be expressed as R = A + B + C, which is the sum of three components. In this case, term A has solely Franck-Condon integrals as numerators. This factor disappears well away from resonance; nevertheless, one of the terms in A may become important close to resonance, permitting only completely symmetric Raman lines. This term is usually attributed to resonance Raman spectra. The B and C terms are Herzberg-Teller contributions resulting from metal-to-molecule or molecule-to-molecule charge-transfer transitions, respectively; these transitions "borrow" intensity from adjacent allowed molecular transitions via the

Herzberg-Teller coupling constant (h). SPR or CT processes can improve the intensity of the resultant vibrational modes, and the B and C components permit transitions to both fully symmetric and non-totally symmetric modes. The presence of any or both of the B or C factors is required when SERS spectra show intensity in non-totally symmetric normal modes.[335, 336] These components, along with the A term, may also contribute to completely symmetric bands. A term is given by-

$$\boldsymbol{R_{IC}(\omega)} = \frac{\boldsymbol{\mu_{IC}\,\mu_{IC}\,\langle i|k\rangle\langle k|f\rangle}}{\{(\boldsymbol{\epsilon_1(\omega)+2\epsilon_0})^2+\boldsymbol{\epsilon_2^2\,(\omega)}\}\boldsymbol{C}\,\{(\boldsymbol{\omega_{IC}^2-\omega^2})+\boldsymbol{\Upsilon_{IC}^2}\}} \quad \text{--------- (6.1)}$$

In the denominator, the first term represents the valence band plasmon resonance, a feature present in all subsequent expressions. For the A-terms, an additional resonance occurs, which can be attributed to either the charge transfers from the HOMO to the conduction band edge (at $\omega = \omega_{IC}$) or from the valence band edge to the LUMO of the molecule (at $\omega = \omega_{VK}$). The numerator includes the oscillator strength of these charge-transfer transitions, governed by Franck- Condon selection rules, which are nonzero only for totally symmetric normal modes and allow for overtones (f = i + 1, i + 2, i + 3, ...). Consequently, when the A-term dominates, one would expect extensive progressions in totally symmetric modes. Nevertheless, such long progressions are infrequently observed in SERS spectra, indicating that the intensities of even the totally symmetric modes may result from B- or C-term contributions.[337] Both analytical formula for B and C are quite difficult since they entail infinite sums over every state of the molecule-metal system. Still, just one or a few factors will predominate in the total when the excitation wavelength is close to a CT or molecular resonance in addition to SPR. One of these dominant B terms can be expressed as:

$$\boldsymbol{R_{ICV}(\omega)} = \frac{\boldsymbol{\mu_{mol}\mu_{CT}h\,\langle i|Q_k|f\rangle}}{\{(\boldsymbol{\epsilon_1(\omega)+2\epsilon_0})^2+\boldsymbol{\epsilon_2^2\,(\omega)}\}\,\{(\boldsymbol{\omega_{mol}^2-\omega^2})+\boldsymbol{\Upsilon_{mol}^2}\}\,\{(\boldsymbol{\omega_{CT}^2-\omega^2})+\boldsymbol{\Upsilon_{CT}^2}\}} \text{-------- (6.2)}$$

The surface-enhanced Raman intensity is proportional to the square of the polarizability, so for a single dominant term. In this expression, i, f, and k represent the ground state, a charge-transfer state, and an excited molecular state of the molecule-metal system, respectively.

The denominator of the expression involves the sum of three terms, each representing a different resonance contribution to SERS. This shows how various resonant interactions, including CT and molecular resonances, in conjunction with SPR, contribute to the enhanced Raman signal.

Apart from the metals to semiconductors CT pathway, photosensitive molecules may also facilitate the reverse direction of CT from semiconductors to metals. In these situations, depending on how the building blocks and SERS probes are assembled, CT either begins with the semiconductors or the adsorbed molecules.[338] In the case of Au/Ag-TiO_2/SnO_2 NPs grown over the plastic substrate, used analytic molecules R6G & B_{12} (HOMO levels are -5.7, -5.5 eV, LUMO levels are -3.4, -3.5 eV respectively) are expected to lie as per literature reports.[339] For both analytic molecules, electrons are first excited from the HOMO level to the LUMO level (**Figure 6.12d&e)**), then subsequently transferred to lower level of the Ag-TiO_2/SnO_2 NPs complex due to the energy level equilibration (band position of semiconductor are collected from literature review) and then injected into the Fermi levels of Au (W_f ~ -5.1 eV) via the Ag NPs (W_f ~ -4.7 eV).[294, 295, 324] The introduction of bi-metallic Au-Ag NPs, decreased the CT threshold, extended the CT response to NIR region, and enhanced the CT efficiency in the high-energy region.

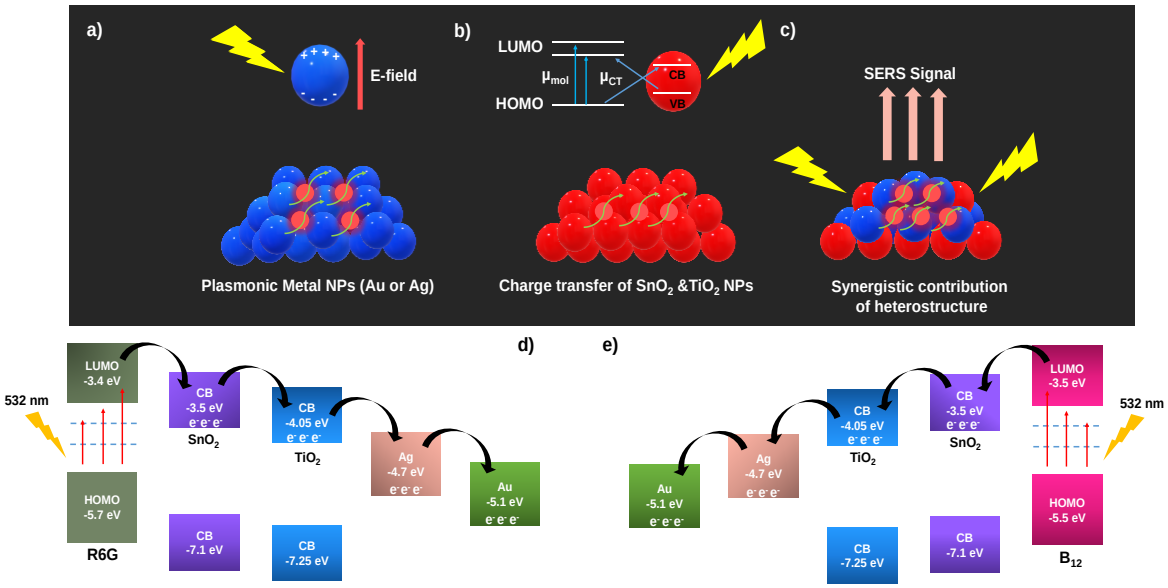

Figure 6.12a,b&c) SERS mechanisms: plasmon-induced enhancement on metals, CT on semiconductors, and the synergistic contribution of plasmons and CT on metal–semiconductor heterostructures. Mechanisms of the photo induced CT process in Au-Ag based metal–semiconductor heterostructures: **d&e)** Au/Ag-TiO_2/SnO_2 NPs heterostructures for R6G dye and vitamin B_{12} respectively.

For further investigations of CT mechanism, we examined the change in the ambient temperature PL spectrum of (4 or 6 nm Au)/Ag-TiO_2/SnO_2 NPs on plastic substrates with and without R6G dye & vitamin B_{12} biomolecules (**Figure 6.13a&b)**). Ambient temperature PL spectra and its quenching for R6G dye demonstrate that the PL intensities of substrates treated with the dye (10^{-3} M) decreased drastically (~ 60–70%) when compared to the PL intensities of the same SERS substrates without the dye. In case of vitamin B_{12} (10^{-3} M) PL almost quenched completely compared to the original substrate. This experiment demonstrates that the CT process has been confirmed since the greatest number of electrons are transported from SERS substrates to R6G dye and vitamin B_{12} biomolecules, and only a small number of electrons return from the CB to the VB.

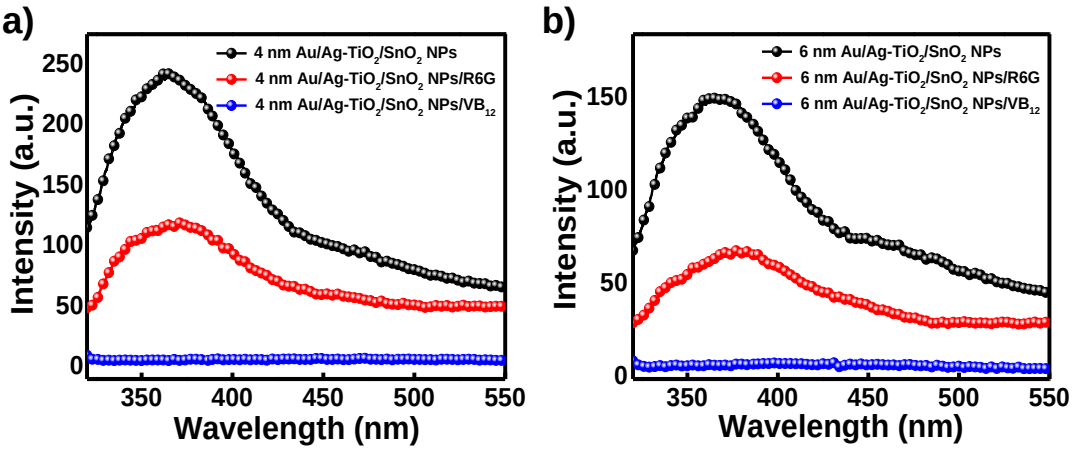

Figure 6.13 PL spectra of **a)** 4 nm Au/Ag-TiO_2/SnO_2 NPs and **b)** 6 nm Au/Ag-TiO_2/SnO_2 NPs on plastic substrate with and without R6G dye & vitamin B_{12}.

Additionally, we have determined the number of biomolecules involved in SERS as well as in normal Raman scattering N_{SERS} and N_{Raman} respectively. Using this calculation, we further estimated the SERS enhancement factor (EF) by using the following equations:

$$N_{Raman} = \frac{CVN_A A_{Raman}}{A_{Sub}} \qquad \text{--------- (6.3)}$$

$$N_{SERS} = \frac{\rho h N_A A_{Raman}}{M} \qquad \text{--------- (6.4)}$$

$$\mathbf{EF} = \frac{I_{SERS}\, N_{Raman}}{I_{Raman}\, N_{SERS}} \qquad \text{--------- (6.5)}$$

Here, C denotes the molar concentration of the biomolecule in solution, V is the volume of the irradiated solution, and N_A is Avogadro number. The laser spot area is denoted by A_{Raman} , while A_{sub} represents the effective area of the substrate. The density and molecular weight of the bulk biomolecule are indicated by ρ and M, respectively. I_{SERS} represents the intensity of the Raman signal obtained with the SERS substrate, while I_{Raman} is the intensity of the normal Raman signal recorded without any enhancement. N_{Raman} refers to the number of molecules contributing to the normal Raman signal and N_{SERS} indicates the number of molecules interacting directly with the SERS-active surface, usually limited to those located at or near the substrate's hot spots.

In the SERS studies, 1 and 116 molecules for R6G are detected on 4 nm and 6nm Au/Ag-TiO_2/SnO_2 NPs at the lowest concentrations of 10^{-12} M and 10^{-9} M, respectively. For vitamin $B_{12,}$ 89 and 6120 molecules are detected on 4 nm and 6 nm Au/Ag- TiO_2/SnO_2 NPs substrates at 10^{-9} M and 10^{-7} M, respectively. After calculating and substituting all parameters into **Equation 6.5**, the EF values for R6G at ~ 611 cm^{-1}, and vitamin B_{12} at ~1501 cm^{-1} on the 4 nm Au/Ag-TiO_2/SnO_2 NPs substrate are found to be 3.4 $\times 10^8$ and 2.2 $\times 10^5$, respectively. Similarly, for the 6 nm Au/Ag-TiO_2/SnO_2 NPs substrate, the EF values are 4.8 $\times 10^5$ for R6G and for vitamin B_{12} 5.1$\times 10^3$. The calculated number of molecules, and EF are provided in **Table 6.1** and **Table 6.2**.

Table 6.1 Calculated No. of Molecules for SERS Substrate

Substrates	R6G	Vitamin B_{12}
4 nm Au/Ag-TiO_2/SnO_2 NPs	1	89
6 nm Au/Ag-TiO_2/SnO_2 NPs	116	6120

Table 6.2 Calculated EF for SERS Substrate

Substrates	R6G	Vitamin B_{12}
4 nm Au/Ag-TiO_2/SnO_2 NPs	2.07×10^8	2.2×10^5
6 nm Au/Ag-TiO_2/SnO_2 NPs	6.024×10^5	6.38×10^3

Table 6.3 presents a comparison of detection limits for different analytes on various SERS substrates reported in literature. The detection limits achieved in this study notably surpass those reported for pristine metal/metal oxide substrates.

Table 6.3 Comparison Table of SERS Detection Limits for Different Substrates with Different Analytical Methods

SERS Substrate	Preparation Method	Detection method	Analyte molecules	Detection limit (M)	Ref.
MoS_2@ZnO@Ag	Hydrothermal	SERS	Bilirubin	10^{-8}	[340]
Ag@Fe_2O_3	Hydrothermal	SERS	R6G	9.3×10^{-10}	[341]
			Bilirubin	2.3×10^{-8}	
Ag/SnO_2 nanocore composite/glass	Spray-pyrolysis/PVD	SERS	R6G	10^{-12}	[342]
Au/SnO_2/glass	PVD	SERS	Ciprofloxacin (CIP)	10^{-8}	[294]
10 nm Ag/$Ag_4Ti_5O_{12}$ /glass	Chemical method/PVD	SERS	MB	10^{-9}	[343]
Ag@SiO_2-Au NPs	Chemical Method	SERS	RhB	5×10^{-9}	[344]
4 nm Au/Ag-TiO_2 /plastic	**Chemical method/PVD**	**SERS**	**R6G**	**10^{-12}**	**This work**
			Vitamin B_{12}	**10^{-9}**	

6.4 Conclusion

In summary, we have successfully synthesized nano-porous Au-Ag bi-metallic thin film on a pre-deposited solution processed Ag-TiO_2/SnO_2 NPs film of different mass thickness of Au NPs and used them as SERS substrates for detecting different analytes like R6G dye and

vitamin B_{12} biomolecules. Morphological study shows the 4 nm Au/Ag-TiO_2/SnO_2 NPs/plastic sample has a percolated metallic nanostructure that has high porosity with high surface roughness but uniformly distributed throughout the sample. This typical Au-Ag nanostructure has high environmental stability due to its typical Au-embedded Ag nanostructure, also has high density EM hotspots originating from its nanoporous structure and high roughness which is an essential condition for developing a highly sensitive SERS substrate. Besides, Au-Ag nanostructure is grown inside TiO_2 matrix that helps charge transfer of plasmon induced hot electrons from Au-Au nanostructure to TiO_2, which can enhance the SERS sensitivity. The SERS detection limits of R6G dye on 4 or 6 nm Au/Ag-TiO_2/SnO_2 NPs/plastic substrates are 10^{-12} & 10^{-9} with EF values of 2.07×10^8 and 6.02×10^5 respectively. While SERS detection limits of vitamin B_{12} on 4 or 6 nm Au/Ag-TiO_2/SnO_2 NPs/plastic substrates are 10^{-9} & 10^{-7} M with EF values of 2.2×10^5 and 6.38×10^3 respectively. These superior SERS performances of Au-Ag thin films are due to strong coupling of LSPR effect of plasmonic metal NPs with molecular resonance & CT process from metal/metal oxide layer to analytic molecule and this CT mechanism is verified by observing the decline of ambient temperature PL of R6G dye & vitamin B_{12} molecule adsorbed SERS substrates.

Chapter 7

7.1 Conclusions

My PhD thesis is primarily built upon three key findings that have significantly shaped my research progress;

1. Development of a cost-effective, scalable synthesis technique of Plasmonic thin film by utilizing solution processed ion-conducting oxide as initial material.

2. Development of a mechanically flexible Ag based transparent conductor and transparent heat reflector and its application as a self-bias plasmonic photodetector and heat reflecting coat for smart window applications.

3. Fabrication of a novel bimetallic Au-Ag transparent conducting thin film and used that new technique in diverse fields of solar cells, plasmonic photodetector and biosensors applications.

I have leveraged these three key findings for multiple applications in photonic technologies. The striking features of this thesis work are the improvement of transparency and electrical conductivity of plasmonic NPs based transparent conducting film as an alternative of ITO coated film. A brief discussion of these applications follows in the subsequent section-

Firstly, the thesis addresses the oxidation issue of the plasmonic thin films that arises in Ag-based plasmonic devices due to open air instability. Till now researchers basically focus on colloidal or composite synthesis route for the fabrication of Ag-plasmonic film, but all these techniques have critical issues related to atmospheric stability. To mitigate this, we have introduced a novel low cost where lithium titanate ($Li_4Ti_5O_{12}$), an ion-conducting oxide is used as the initial material. This ceramic contains light ions like Li^+ and this mobile ion can move through the crystal channel easily. By taking advantage of these mobile ions, we have chemically replaced Li^+ by Ag^+ inside the dielectric matrix to form a stable Ag-TiO_2 thin

film. This new innovation helps to fabricate plasmonic thin film with much more stability, making it feasible for multi-functional photonic applications. Using Ag-TiO_2 thin film, I have successfully fabricated a narrowband plasmonic hot electron based photodetector in photoconductor geometry. Device shows a very good detectivity of 3.19×10^{11} Jones with conclusive evidence of hot electron generation from the plasmonic part. This approach shows a record detectivity of a plasmonic photodetector with a photoconductor geometry.

Secondly, the concept of low cost and scalable synthesis of Plasmonic thin film is extended further by depositing Ag based transparent conducting film on a flexible PET (plastic) substrate via low temperature synthesis route. Initially, I demonstrated the development of Ag nanostructured based flexible transparent conductor and its application as a self-biased plasmonic photodetector. Moreover, I used this film to fabricate a cost-effective flexible transparent heat reflector for energy-efficient smart window applications. The integration of an Ag-TiO_2 thin layer, derived from a solution-processed LTO precursor via ion exchange, facilitated lateral Ag growth, enabling a percolated Ag network at ultrathin thickness (~10 nm) of Ag film. The resulting Ag/Ag-TiO_2 thin film exhibited a low sheet resistance of ~50 Ω/sq with >70% transmittances in the visible range, making it a promising candidate for transparent electrode applications. This nanostructured Ag film is successfully employed in a plasmonic hot electron photodetector, leveraging its surface plasmon absorption to achieve a peak detectivity of 2.84×10^{12} Jones at 510 nm with a fast response time of ~25 ms. In parallel, the same Ag/Ag-TiO_2 bilayer structure is utilized to develop a flexible and environmentally stable THR coating, exhibiting high IR/NIR reflectivity (~85–90%) while maintaining 50–70% visible transmittance. A polymer overcoat (PMMA) further enhanced its durability. The effectiveness of this THR film is demonstrated in a real-world prototype, where its application on a glass window led to an internal temperature reduction of ~ 6–7°C under daylight conditions, underscoring its potential for smart window technologies.

Thirdly, I have extended these findings in the next level by developing a mechanically flexible and highly transparent bimetallic Au-Ag transparent conductor, which is comparable to commercially available ITO coated film. This work presents a scalable approach for fabricating highly transparent and conductive Au-Ag bimetallic nanostructures via PVD, utilizing a pre-deposited Ag-TiO_2/SnO_2 (or ZnO) NP seed layer with 4 nm Au deposition

over it to induce percolated nano-porosity. The prepared film shows a sheet resistance of 5–10 Ω/□ and visible transmittance of 75–80%, enabling its application in plasmonic photodetectors, solar cells and biosensors. Film works as a transparent electrode as well as plasmonic hot electron generator in an M-S-M photodetector device configuration that achieves a peak detectivity of 1.6×10^{13} Jones at 750 nm with a fast response (~33 ms), demonstrating its efficacy for IR-sensitive optoelectronics. Additionally, its integration as a back electrode in inverted plasmonic organic solar cells (POSCs) yields record efficiencies of 7.8% (P3HT) and 11.17% (P3HT: $PC_{71}BM$) due to enhancement of open-circuit voltage in presence of plasmonic film, confirmed tandem cell formation. Furthermore, the porous Au-Ag nanostructured film serves as an ultrasensitive SERS substrate, detecting R6G and Vitamin B_{12} up to 1 pM & 1 nM, respectively. Overall, this study demonstrates the multi-functionality of Au-Ag nanostructures, offering a cost-effective and high-performance alternative for plasmonic optoelectronics, energy conversion, and molecular sensing applications.

7.2 Future Perspectives

The developed Ag and Au-Ag nanostructured films hold significant potential for advanced photonic applications beyond their current utilizations. Future research can be focused on optimizing their plasmonic properties for next-generation transparent photodetectors, extending their spectral sensitivity into the NIR and shortwave infrared (SWIR) regions for low-light imaging and night vision technologies. Additionally, their integration into ultrathin and flexible optoelectronic devices will be explored, including transparent touch sensors, wearable photodetectors, and smart windows with dynamic optical modulation. In energy applications, further engineering of these films could enhance light trapping in tandem and perovskite solar cells, improving energy conversion efficiency. Their unique SERS capabilities also make them promising for real-time biosensing and environmental monitoring, enabling label-free molecular detection with ultrahigh sensitivity. Furthermore, the nano-porous architecture of these films could facilitate surface plasmon-driven photocatalysis for sustainable chemical synthesis and pollutant degradation. The scalability and compatibility of these films with solution-processed techniques will also be explored for roll-to-roll fabrication, enabling cost-effective manufacturing of large-area photonic devices.

Overall, these advancements will position Ag and Au-Ag films as key materials for future photonic technologies spanning optoelectronics, energy harvesting, sensing, and environmental applications.

References

[1] P. Mulvaney, "Nanoscience vs Nanotechnology Defining the Field," vol. 9, ed: ACS Publications, 2015, pp. 2215-2217.

[2] M. Karkare, *Nanotechnology: fundamentals and applications*. IK International Pvt Ltd, 2013.

[3] J. Tarafdar and R. Raliya, *Nanotechnology*. Scientific Publishers, 2012.

[4] M. T. Bohr, "Nanotechnology goals and challenges for electronic applications," *IEEE Transactions on Nanotechnology*, vol. 1, no. 1, pp. 56-62, 2002.

[5] E. Serrano, G. Rus, and J. Garcia-Martinez, "Nanotechnology for sustainable energy," *Renewable and Sustainable Energy Reviews*, vol. 13, no. 9, pp. 2373-2384, 2009.

[6] A. K. Hussein, "Applications of nanotechnology in renewable energies—A comprehensive overview and understanding," *Renewable and Sustainable Energy Reviews*, vol. 42, pp. 460-476, 2015.

[7] A. Surendiran, S. Sandhiya, S. Pradhan, and C. Adithan, "Novel applications of nanotechnology in medicine," *Indian Journal of Medical Research*, vol. 130, no. 6, pp. 689-701, 2009.

[8] G. A. Silva, "Introduction to nanotechnology and its applications to medicine," *Surgical neurology*, vol. 61, no. 3, pp. 216-220, 2004.

[9] J. Weiss, P. Takhistov, and D. J. McClements, "Functional materials in food nanotechnology," *Journal of food science*, vol. 71, no. 9, pp. R107-R116, 2006.

[10] L. Dai, "Carbon nanotechnology: recent developments in chemistry, physics, materials science and device applications," 2006.

[11] E. Pomerantseva, F. Bonaccorso, X. Feng, Y. Cui, and Y. Gogotsi, "Energy storage: The future enabled by nanomaterials," *Science*, vol. 366, no. 6468, p. eaan8285, 2019.

[12] M. O. Emeje, I. C. Obidike, E. I. Akpabio, and S. I. Ofoefule, "Nanotechnology in drug delivery," *Recent advances in novel drug carrier systems*, vol. 1, no. 4, pp. 69-106, 2012.

[13] W. Jiang, B. Y. Kim, J. T. Rutka, and W. C. Chan, "Advances and challenges of nanotechnology-based drug delivery systems," *Expert opinion on drug delivery*, vol. 4, no. 6, pp. 621-633, 2007.

[14] M. Rafique, M. B. Tahir, M. S. Rafique, and M. Hamza, "History and fundamentals of nanoscience and nanotechnology," in *Nanotechnology and photocatalysis for environmental applications*: Elsevier, 2020, pp. 1-25.

[15] B. Zhang, *Physical fundamentals of nanomaterials*. William Andrew, 2018.

[16] S. Cuenot, C. Frétigny, S. Demoustier-Champagne, and B. Nysten, "Surface tension effect on the mechanical properties of nanomaterials measured by atomic force microscopy," *Physical Review B*, vol. 69, no. 16, p. 165410, 2004.

[17] D. Vollath, F. D. Fischer, and D. Holec, "Surface energy of nanoparticles–influence of particle size and structure," *Beilstein journal of nanotechnology*, vol. 9, no. 1, pp. 2265-2276, 2018.

[18] W. Luo, W. Hu, and S. Xiao, "Size effect on the thermodynamic properties of silver nanoparticles," *The Journal of Physical Chemistry C*, vol. 112, no. 7, pp. 2359-2369, 2008.

[19] A. B. Asha and R. Narain, "Nanomaterials properties," in *Polymer science and nanotechnology*: Elsevier, 2020, pp. 343-359.

[20] R. Koole, E. Groeneveld, D. Vanmaekelbergh, A. Meijerink, and C. de Mello Donegá, "Size effects on semiconductor nanoparticles," *Nanoparticles: Workhorses of Nanoscience*, pp. 13-51, 2014.

[21] A. Fernando, K. D. M. Weerawardene, N. V. Karimova, and C. M. Aikens, "Quantum mechanical studies of large metal, metal oxide, and metal chalcogenide nanoparticles and clusters," *Chemical reviews,* vol. 115, no. 12, pp. 6112-6216, 2015.
[22] K. Wang *et al.*, "Advances in energy-efficient plasmonic electrochromic smart windows based on metal oxide nanocrystals," *Advanced Energy and Sustainability Research,* vol. 2, no. 12, p. 2100117, 2021.
[23] C. G. Granqvist, "Electrochromics for smart windows: Oxide-based thin films and devices," *Thin solid films,* vol. 564, pp. 1-38, 2014.
[24] T. Zhai *et al.*, "A comprehensive review of one-dimensional metal-oxide nanostructure photodetectors," *Sensors,* vol. 9, no. 8, pp. 6504-6529, 2009.
[25] W. Ouyang, F. Teng, J. H. He, and X. Fang, "Enhancing the photoelectric performance of photodetectors based on metal oxide semiconductors by charge-carrier engineering," *Advanced Functional Materials,* vol. 29, no. 9, p. 1807672, 2019.
[26] K. McNamara and S. A. Tofail, "Nanoparticles in biomedical applications," *Advances in Physics: X,* vol. 2, no. 1, pp. 54-88, 2017.
[27] M. P. Nikolova and M. S. Chavali, "Metal oxide nanoparticles as biomedical materials," *Biomimetics,* vol. 5, no. 2, p. 27, 2020.
[28] P. C. Nagajyothi, S. V. Prabhakar Vattikuti, K. C. Devarayapalli, K. Yoo, J. Shim, and T. V. M. Sreekanth, "Green synthesis: photocatalytic degradation of textile dyes using metal and metal oxide nanoparticles-latest trends and advancements," *Critical Reviews in Environmental Science and Technology,* vol. 50, no. 24, pp. 2617-2723, 2020.
[29] M. Faraday, "X. The Bakerian Lecture.—Experimental relations of gold (and other metals) to light," *Philosophical transactions of the Royal Society of London,* no. 147, pp. 145-181, 1857.
[30] W. Hergert and T. Wriedt, *The Mie theory: basics and applications*. Springer, 2012.
[31] T. Wriedt, "Mie theory: a review," *The Mie theory: Basics and applications,* pp. 53-71, 2012.
[32] J. M. George, A. Antony, and B. Mathew, "Metal oxide nanoparticles in electrochemical sensing and biosensing: a review," *Microchimica Acta,* vol. 185, pp. 1-26, 2018.
[33] Z. Zhang, J. Liu, J. Gu, L. Su, and L. Cheng, "An overview of metal oxide materials as electrocatalysts and supports for polymer electrolyte fuel cells," *Energy & Environmental Science,* vol. 7, no. 8, pp. 2535-2558, 2014.
[34] N. Jung, D. Y. Chung, J. Ryu, S. J. Yoo, and Y.-E. Sung, "Pt-based nanoarchitecture and catalyst design for fuel cell applications," *Nano today,* vol. 9, no. 4, pp. 433-456, 2014.
[35] V. Mazumder, Y. Lee, and S. Sun, "Recent development of active nanoparticle catalysts for fuel cell reactions," *Advanced Functional Materials,* vol. 20, no. 8, pp. 1224-1231, 2010.
[36] A. Biswas, I. S. Bayer, A. S. Biris, T. Wang, E. Dervishi, and F. Faupel, "Advances in top–down and bottom–up surface nanofabrication: Techniques, applications & future prospects," *Advances in colloid and interface science,* vol. 170, no. 1-2, pp. 2-27, 2012.
[37] W. K. Choi *et al.*, "A combined top-down and bottom-up approach for precise placement of metal nanoparticles on silicon," *small,* vol. 4, no. 3, pp. 330-333, 2008.
[38] N. Abid *et al.*, "Synthesis of nanomaterials using various top-down and bottom-up approaches, influencing factors, advantages, and disadvantages: A review," *Advances in Colloid and Interface Science,* vol. 300, p. 102597, 2022.
[39] V. Arole and S. Munde, "Fabrication of nanomaterials by top-down and bottom-up approaches-an overview," *J. Mater. Sci,* vol. 1, pp. 89-93, 2014.
[40] S. Iravani, H. Korbekandi, S. V. Mirmohammadi, and B. Zolfaghari, "Synthesis of silver nanoparticles: chemical, physical and biological methods," *Research in pharmaceutical sciences,* vol. 9, no. 6, pp. 385-406, 2014.
[41] K. B. Narayanan and N. Sakthivel, "Biological synthesis of metal nanoparticles by microbes," *Advances in colloid and interface science,* vol. 156, no. 1-2, pp. 1-13, 2010.

[42] I. Ijaz, E. Gilani, A. Nazir, and A. Bukhari, "Detail review on chemical, physical and green synthesis, classification, characterizations and applications of nanoparticles," *Green chemistry letters and reviews,* vol. 13, no. 3, pp. 223-245, 2020.
[43] J. Kimling, M. Maier, B. Okenve, V. Kotaidis, H. Ballot, and A. Plech, "Turkevich method for gold nanoparticle synthesis revisited," *The Journal of Physical Chemistry B,* vol. 110, no. 32, pp. 15700-15707, 2006.
[44] M. Wuithschick *et al.*, "Turkevich in new robes: key questions answered for the most common gold nanoparticle synthesis," *ACS nano,* vol. 9, no. 7, pp. 7052-7071, 2015.
[45] B. Pinho, K. Zhang, R. L. Hoye, and L. Torrente-Murciano, "Importance of Monitoring the Synthesis of Light-Interacting Nanoparticles–A Review on In Situ, Ex Situ, and Online Time-Resolved Studies," *Advanced Optical Materials,* vol. 10, no. 14, p. 2200524, 2022.
[46] S. K. Ghosh and T. Pal, "Interparticle coupling effect on the surface plasmon resonance of gold nanoparticles: from theory to applications," *Chemical reviews,* vol. 107, no. 11, pp. 4797-4862, 2007.
[47] M. A. García, "Surface plasmons in metallic nanoparticles: fundamentals and applications," *Journal of Physics D: Applied Physics,* vol. 44, no. 28, p. 283001, 2011.
[48] H. S. Sehmi, W. Langbein, and E. A. Muljarov, "Optimizing the Drude-Lorentz model for material permittivity: Method, program, and examples for gold, silver, and copper," *Physical Review B,* vol. 95, no. 11, p. 115444, 2017.
[49] D. Bohm and D. Pines, "A collective description of electron interactions. I. Magnetic interactions," *Physical Review,* vol. 82, no. 5, p. 625, 1951.
[50] Y. Wang, E. Plummer, and K. Kempa, "Foundations of plasmonics," *Advances in Physics,* vol. 60, no. 5, pp. 799-898, 2011.
[51] C. F. Bohren and D. R. Huffman, *Absorption and scattering of light by small particles*. John Wiley & Sons, 2008.
[52] A. Rider, K. Ostrikov, and S. Furman, "Plasmas meet plasmonics: Everything old is new again," *The European Physical Journal D,* vol. 66, pp. 1-19, 2012.
[53] K. A. Willets and R. P. Van Duyne, "Localized surface plasmon resonance spectroscopy and sensing," *Annu. Rev. Phys. Chem.,* vol. 58, no. 1, pp. 267-297, 2007.
[54] S. Peiris, J. McMurtrie, and H.-Y. Zhu, "Metal nanoparticle photocatalysts: emerging processes for green organic synthesis," *Catalysis Science & Technology,* vol. 6, no. 2, pp. 320-338, 2016.
[55] M. L. Brongersma, N. J. Halas, and P. Nordlander, "Plasmon-induced hot carrier science and technology," *Nature nanotechnology,* vol. 10, no. 1, pp. 25-34, 2015.
[56] J. Hofmann and W. Steinmann, "Plasma resonance in the photoemission of silver," *physica status solidi (b),* vol. 30, no. 1, pp. K53-K56, 1968.
[57] J. Sipe and J. Becher, "Surface-plasmon-assisted photoemission," *Journal of the Optical Society of America,* vol. 71, no. 10, pp. 1286-1288, 1981.
[58] C. F. Bohren, "How can a particle absorb more than the light incident on it?," *American Journal of Physics,* vol. 51, no. 4, pp. 323-327, 1983.
[59] S. Oldenburg, R. Averitt, S. Westcott, and N. Halas, "Nanoengineering of optical resonances," *Chemical Physics Letters,* vol. 288, no. 2-4, pp. 243-247, 1998.
[60] M. Moskovits, "Surface-enhanced spectroscopy," *Reviews of modern physics,* vol. 57, no. 3, p. 783, 1985.
[61] J. I. Gersten and A. Nitzan, "Photophysics and photochemistry near surfaces and small particles," *Surface Science,* vol. 158, no. 1-3, pp. 165-189, 1985.
[62] X. Li, D. Xiao, and Z. Zhang, "Landau damping of quantum plasmons in metal nanostructures," *New Journal of Physics,* vol. 15, no. 2, p. 023011, 2013.
[63] A. Manjavacas, J. G. Liu, V. Kulkarni, and P. Nordlander, "Plasmon-induced hot carriers in metallic nanoparticles," *ACS nano,* vol. 8, no. 8, pp. 7630-7638, 2014.

[64] K. Watanabe, D. Menzel, N. Nilius, and H.-J. Freund, "Photochemistry on metal nanoparticles," *Chemical reviews,* vol. 106, no. 10, pp. 4301-4320, 2006.
[65] M. Lisowski, P. Loukakos, U. Bovensiepen, J. Stähler, C. Gahl, and M. Wolf, "Ultra-fast dynamics of electron thermalization, cooling and transport effects in Ru (001)," *Applied Physics A,* vol. 78, pp. 165-176, 2004.
[66] X.-C. Ma, Y. Dai, L. Yu, and B.-B. Huang, "Energy transfer in plasmonic photocatalytic composites," *Light: Science & Applications,* vol. 5, no. 2, pp. e16017-e16017, 2016.
[67] C. Burda, X. Chen, R. Narayanan, and M. A. El-Sayed, "Chemistry and properties of nanocrystals of different shapes," *Chemical reviews,* vol. 105, no. 4, pp. 1025-1102, 2005.
[68] J. Lehmann, M. Merschdorf, W. Pfeiffer, A. Thon, S. Voll, and G. Gerber, "Surface plasmon dynamics in silver nanoparticles studied by femtosecond time-resolved photoemission," *Physical review letters,* vol. 85, no. 14, p. 2921, 2000.
[69] H. Hövel, S. Fritz, A. Hilger, U. Kreibig, and M. Vollmer, "Width of cluster plasmon resonances: bulk dielectric functions and chemical interface damping," *Physical Review B,* vol. 48, no. 24, p. 18178, 1993.
[70] M. Valenti *et al.*, "Hot carrier generation and extraction of plasmonic alloy nanoparticles," *ACS photonics,* vol. 4, no. 5, pp. 1146-1152, 2017.
[71] M. Bernardi, J. Mustafa, J. B. Neaton, and S. G. Louie, "Theory and computation of hot carriers generated by surface plasmon polaritons in noble metals," *Nature communications,* vol. 6, no. 1, p. 7044, 2015.
[72] C. Clavero, "Plasmon-induced hot-electron generation at nanoparticle/metal-oxide interfaces for photovoltaic and photocatalytic devices," *Nature Photonics,* vol. 8, no. 2, pp. 95-103, 2014.
[73] S. Linic, P. Christopher, and D. B. Ingram, "Plasmonic-metal nanostructures for efficient conversion of solar to chemical energy," *Nature materials,* vol. 10, no. 12, pp. 911-921, 2011.
[74] C. Sönnichsen *et al.*, "Drastic reduction of plasmon damping in gold nanorods," *Physical review letters,* vol. 88, no. 7, p. 077402, 2002.
[75] T. P. White and K. R. Catchpole, "Plasmon-enhanced internal photoemission for photovoltaics: theoretical efficiency limits," *Applied Physics Letters,* vol. 101, no. 7, 2012.
[76] L. Wang, M. Hasanzadeh Kafshgari, and M. Meunier, "Optical properties and applications of plasmonic-metal nanoparticles," *Advanced Functional Materials,* vol. 30, no. 51, p. 2005400, 2020.
[77] S. T. Kochuveedu, Y. H. Jang, and D. H. Kim, "A study on the mechanism for the interaction of light with noble metal-metal oxide semiconductor nanostructures for various photophysical applications," *Chemical Society Reviews,* vol. 42, no. 21, pp. 8467-8493, 2013.
[78] G. Xu *et al.*, "Plasmonic graphene transparent conductors," *Advanced Materials,* vol. 24, no. 10, pp. OP71-OP76, 2012.
[79] S. Ezendam *et al.*, "Hybrid plasmonic nanomaterials for hydrogen generation and carbon dioxide reduction," *ACS Energy Letters,* vol. 7, no. 2, pp. 778-815, 2022.
[80] L. Song, J. Chen, B. B. Xu, and Y. Huang, "Flexible plasmonic biosensors for healthcare monitoring: Progress and prospects," *ACS nano,* vol. 15, no. 12, pp. 18822-18847, 2021.
[81] J. A. Huang and L. B. Luo, "Low-dimensional plasmonic photodetectors: recent progress and future opportunities," *Advanced Optical Materials,* vol. 6, no. 8, p. 1701282, 2018.
[82] X. Shan *et al.*, "Plasmonic optoelectronic memristor enabling fully light-modulated synaptic plasticity for neuromorphic vision," *Advanced Science,* vol. 9, no. 6, p. 2104632, 2022.
[83] F. Enrichi, A. Quandt, and G. C. Righini, "Plasmonic enhanced solar cells: Summary of possible strategies and recent results," *Renewable and sustainable energy reviews,* vol. 82, pp. 2433-2439, 2018.
[84] S. Jana *et al.*, "Halloysite nanotubes with immobilized silver nanoparticles for anti-bacterial application," *Colloids and Surfaces B: Biointerfaces,* vol. 151, pp. 249-254, 2017.

[85] K. Khurana and N. Jaggi, "Localized surface plasmonic properties of Au and Ag nanoparticles for sensors: a review," *Plasmonics,* vol. 16, no. 4, pp. 981-999, 2021.
[86] D. E. Mustafa, T. Yang, Z. Xuan, S. Chen, H. Tu, and A. Zhang, "Surface plasmon coupling effect of gold nanoparticles with different shape and size on conventional surface plasmon resonance signal," *Plasmonics,* vol. 5, pp. 221-231, 2010.
[87] S. Kundu, "A new route for the formation of Au nanowires and application of shape-selective Au nanoparticles in SERS studies," *Journal of Materials Chemistry C,* vol. 1, no. 4, pp. 831-842, 2013.
[88] H. Yuan *et al.*, "Shape and SPR evolution of thorny gold nanoparticles promoted by silver ions," *Chemistry of materials,* vol. 19, no. 7, pp. 1592-1600, 2007.
[89] K.-S. Lee and M. A. El-Sayed, "Gold and silver nanoparticles in sensing and imaging: sensitivity of plasmon response to size, shape, and metal composition," *The journal of physical chemistry B,* vol. 110, no. 39, pp. 19220-19225, 2006.
[90] J. Jana, M. Ganguly, and T. Pal, "Enlightening surface plasmon resonance effect of metal nanoparticles for practical spectroscopic application," *RSC advances,* vol. 6, no. 89, pp. 86174-86211, 2016.
[91] Y. Y. Cai, Y. C. Choi, and C. R. Kagan, "Chemical and Physical Properties of Photonic Noble-Metal Nanomaterials," *Advanced Materials,* vol. 35, no. 34, p. 2108104, 2023.
[92] M. B. Cortie and A. M. McDonagh, "Synthesis and optical properties of hybrid and alloy plasmonic nanoparticles," *Chemical reviews,* vol. 111, no. 6, pp. 3713-3735, 2011.
[93] J. Z. Zhang and C. Noguez, "Plasmonic optical properties and applications of metal nanostructures," *Plasmonics,* vol. 3, pp. 127-150, 2008.
[94] J. Lim and S. A. Majetich, "Composite magnetic–plasmonic nanoparticles for biomedicine: Manipulation and imaging," *Nano Today,* vol. 8, no. 1, pp. 98-113, 2013.
[95] S. Linic, P. Christopher, H. Xin, and A. Marimuthu, "Catalytic and photocatalytic transformations on metal nanoparticles with targeted geometric and plasmonic properties," *Accounts of chemical research,* vol. 46, no. 8, pp. 1890-1899, 2013.
[96] S. M. Morton, D. W. Silverstein, and L. Jensen, "Theoretical studies of plasmonics using electronic structure methods," *Chemical reviews,* vol. 111, no. 6, pp. 3962-3994, 2011.
[97] D. J. de Aberasturi, A. B. Serrano-Montes, and L. M. Liz-Marzán, "Modern applications of plasmonic nanoparticles: from energy to health," *Advanced Optical Materials,* vol. 3, no. 5, pp. 602-617, 2015.
[98] H. Matsui *et al.*, "Infrared plasmonic metamaterials based on transparent nanoparticle films of In2O3: Sn for solar-thermal shielding applications," *ACS Applied Materials & Interfaces,* vol. 14, no. 43, pp. 49313-49325, 2022.
[99] E. S. Arinze, B. Qiu, G. Nyirjesy, and S. M. Thon, "Plasmonic nanoparticle enhancement of solution-processed solar cells: practical limits and opportunities," *Acs Photonics,* vol. 3, no. 2, pp. 158-173, 2016.
[100] W. Wang *et al.*, "Advances in emerging photonic memristive and memristive-like devices," *Advanced Science,* vol. 9, no. 28, p. 2105577, 2022.
[101] P. Berini, "Surface plasmon photodetectors and their applications," *Laser & Photonics Reviews,* vol. 8, no. 2, pp. 197-220, 2014.
[102] R. T. Hill, "Plasmonic biosensors," *Wiley Interdisciplinary Reviews: Nanomedicine and Nanobiotechnology,* vol. 7, no. 2, pp. 152-168, 2015.
[103] A. Loiseau, V. Asila, G. Boitel-Aullen, M. Lam, M. Salmain, and S. Boujday, "Silver-based plasmonic nanoparticles for and their use in biosensing," *Biosensors,* vol. 9, no. 2, p. 78, 2019.
[104] I. Urries *et al.*, "Magneto-plasmonic nanoparticles as theranostic platforms for magnetic resonance imaging, drug delivery and NIR hyperthermia applications," *Nanoscale,* vol. 6, no. 15, pp. 9230-9240, 2014.

[105] R. Abbasi, G. Shineh, M. Mobaraki, S. Doughty, and L. Tayebi, "Structural parameters of nanoparticles affecting their toxicity for biomedical applications: a review," *Journal of Nanoparticle Research*, vol. 25, no. 3, p. 43, 2023.
[106] S. Hazra, S. V. Singh, S. Dahiya, P. K. Aich, and B. N. Pal, "Solution-processed Ag-TiO2 nanostructure-based Schottky junction thin films for narrowband hot-electron photodetectors," *ACS Applied Nano Materials*, vol. 6, no. 16, pp. 15119-15127, 2023.
[107] P. Maity, S. V. Singh, S. Biring, B. N. Pal, and A. K. Ghosh, "Selective near-infrared (NIR) photodetectors fabricated with colloidal CdS: Co quantum dots," *Journal of Materials Chemistry C*, vol. 7, no. 25, pp. 7725-7733, 2019.
[108] X. Zheng and L. Zhang, "Photonic nanostructures for solar energy conversion," *Energy & Environmental Science*, vol. 9, no. 8, pp. 2511-2532, 2016.
[109] W. Ye, R. Long, H. Huang, and Y. Xiong, "Plasmonic nanostructures in solar energy conversion," *Journal of Materials Chemistry C*, vol. 5, no. 5, pp. 1008-1021, 2017.
[110] C.-H. Chou and F.-C. Chen, "Plasmonic nanostructures for light trapping in organic photovoltaic devices," *Nanoscale*, vol. 6, no. 15, pp. 8444-8458, 2014.
[111] K. ElKhamisy, H. Abdelhamid, E.-S. M. El-Rabaie, and N. Abdel-Salam, "A comprehensive survey of silicon thin-film solar cell: challenges and novel trends," *Plasmonics*, vol. 19, no. 1, pp. 1-20, 2024.
[112] L. Huang *et al.*, "Temperature-Gradient Solution Deposition Amends Unfavorable Band Structure of Sb2 (S, Se) 3 Film for Highly Efficient Solar Cells," *Angewandte Chemie*, vol. 136, no. 36, p. e202406512, 2024.
[113] A. G. Waketola, N. A. Tegegne, and F. G. Hone, "Recent Progress in Silver and Gold Nanoparticle-Based Plasmonic Organic Solar Cells," *Plasmonics*, pp. 1-36, 2024.
[114] Y. Ding *et al.*, "Metal nanowire-based transparent electrode for flexible and stretchable optoelectronic devices," *Chemical Society Reviews*, 2024.
[115] W. Song, Q. Ye, Z. Chen, J. Ge, L. Xie, and Z. Ge, "Advances in stretchable organic photovoltaics: flexible transparent electrodes and deformable active layer design," *Advanced Materials*, vol. 36, no. 37, p. 2311170, 2024.
[116] C. Yuan *et al.*, "Stable indium tin oxide with high mobility," *ACS Applied Materials & Interfaces*, vol. 14, no. 44, pp. 49937-49944, 2022.
[117] J. Shi, J. Zhang, L. Yang, M. Qu, D. C. Qi, and K. H. Zhang, "Wide bandgap oxide semiconductors: from materials physics to optoelectronic devices," *Advanced materials*, vol. 33, no. 50, p. 2006230, 2021.
[118] A. Kumar and C. Zhou, "The race to replace tin-doped indium oxide: which material will win?," *ACS nano*, vol. 4, no. 1, pp. 11-14, 2010.
[119] K. Ellmer, "Past achievements and future challenges in the development of optically transparent electrodes," *Nature Photonics*, vol. 6, no. 12, pp. 809-817, 2012.
[120] B. Joshi, E. Samuel, S. An, S. Kim, A. L. Yarin, and S. S. Yoon, "Review of indium-free, transparent and flexible metallic fibers for wearable electronics," *Chemical Engineering Journal*, vol. 475, p. 146189, 2023.
[121] S. De, P. J. King, P. E. Lyons, U. Khan, and J. N. Coleman, "Size effects and the problem with percolation in nanostructured transparent conductors," *ACS nano*, vol. 4, no. 12, pp. 7064-7072, 2010.
[122] S. Schubert, J. Meiss, L. Müller-Meskamp, and K. Leo, "Improvement of transparent metal top electrodes for organic solar cells by introducing a high surface energy seed layer," *Advanced Energy Materials*, vol. 3, no. 4, pp. 438-443, 2013.
[123] M. R. Azani, A. Hassanpour, and T. Torres, "Benefits, problems, and solutions of silver nanowire transparent conductive electrodes in indium tin oxide (ITO)-free flexible solar cells," *Advanced Energy Materials*, vol. 10, no. 48, p. 2002536, 2020.
[124] K. Kim, K. Hong, B. Koo, I. Lee, and J.-L. Lee, "Transparency controllable silver-based electrode for flexible optoelectronics," *Applied Physics Letters*, vol. 102, no. 8, 2013.

[125] M. Rabizadeh, M. H. Ehsani, and M. M. Shahidi, "ZnO/metal/ZnO (metal= Ag, Pt, Au) films for energy-saving in windows application," *Scientific Reports*, vol. 12, no. 1, p. 15575, 2022.
[126] J. Zheng, S. Bao, and P. Jin, "TiO2 (R)/VO2 (M)/TiO2 (A) multilayer film as smart window: Combination of energy-saving, antifogging and self-cleaning functions," *Nano Energy*, vol. 11, pp. 136-145, 2015.
[127] J. Y. Mao, L. Zhou, X. Zhu, Y. Zhou, and S. T. Han, "Photonic memristor for future computing: a perspective," *Advanced Optical Materials*, vol. 7, no. 22, p. 1900766, 2019.
[128] Z. Shen *et al.*, "Emerging optical in-memory computing sensor synapses based on low-dimensional nanomaterials for neuromorphic networks," *Advanced Intelligent Systems*, vol. 4, no. 9, p. 2100236, 2022.
[129] P. A. Mosier-Boss, "Review of SERS substrates for chemical sensing," *Nanomaterials*, vol. 7, no. 6, p. 142, 2017.
[130] U. Dinish, F. C. Yaw, A. Agarwal, and M. Olivo, "Development of highly reproducible nanogap SERS substrates: Comparative performance analysis and its application for glucose sensing," *Biosensors and Bioelectronics*, vol. 26, no. 5, pp. 1987-1992, 2011.
[131] C. Dincer *et al.*, "Disposable sensors in diagnostics, food, and environmental monitoring," *Advanced materials*, vol. 31, no. 30, p. 1806739, 2019.
[132] F. Fung, H.-S. Wang, and S. Menon, "Food safety in the 21st century," *Biomedical journal*, vol. 41, no. 2, pp. 88-95, 2018.
[133] E. C. Alocilja and S. M. Radke, "Market analysis of biosensors for food safety," *Biosensors and Bioelectronics*, vol. 18, no. 5-6, pp. 841-846, 2003.
[134] M. Hoseinnejad, S. M. Jafari, and I. Katouzian, "Inorganic and metal nanoparticles and their antimicrobial activity in food packaging applications," *Critical reviews in microbiology*, vol. 44, no. 2, pp. 161-181, 2018.
[135] A. Yakoubi and C. E. B. Dhafer, "Advanced plasmonic nanoparticle-based techniques for the prevention, detection, and treatment of current COVID-19," *Plasmonics*, vol. 18, no. 1, pp. 311-347, 2023.
[136] F. Paladini and M. Pollini, "Antimicrobial silver nanoparticles for wound healing application: progress and future trends," *Materials*, vol. 12, no. 16, p. 2540, 2019.
[137] M. Moritz and M. Geszke-Moritz, "The newest achievements in synthesis, immobilization and practical applications of antibacterial nanoparticles," *Chemical Engineering Journal*, vol. 228, pp. 596-613, 2013.
[138] S. V. Singh, A. Sharma, S. Biring, and B. N. Pal, "Solution processed Cu2S/TiO2 heterojunction for visible-near infrared photodetector," *Thin Solid Films*, vol. 710, p. 138275, 2020.
[139] N. Pal, A. Sharma, V. Acharya, N. K. Chourasia, S. Biring, and B. N. Pal, "Gate interface engineering for subvolt metal oxide transistor fabrication by using ion-conducting dielectric with Mn2O3 gate interface," *ACS Applied Electronic Materials*, vol. 2, no. 1, pp. 25-34, 2019.
[140] S. V. Singh, M. P. Kumar, S. Anantharaj, B. Mukherjee, S. Kundu, and B. N. Pal, "Direct evidence of an efficient plasmon-induced hot-electron transfer at an in situ grown Ag/TiO2 interface for highly enhanced solar H2 generation," *ACS Applied Energy Materials*, vol. 3, no. 2, pp. 1821-1830, 2020.
[141] S. Habashyani, A. Özmen, S. Aydogan, and M. Yilmaz, "An examination of correlation between characteristic and device performance of ZnO films as a function of La content," *Vacuum*, vol. 157, pp. 497-507, 2018.
[142] M. Yilmaz, A. Kocyigit, S. Aydogan, U. Incekara, A. Tursucu, and H. Kacus, "Light-sensing behaviors of organic/n-Si bio-hybrid photodiodes based on malachite green (MG) organic dye," *Journal of Materials Science: Materials in Electronics*, vol. 31, pp. 21548-21556, 2020.

[143] Ş. Aydoğan, M. L. Grilli, M. Yilmaz, Z. Çaldiran, and H. Kaçuş, "A facile growth of spray based ZnO films and device performance investigation for Schottky diodes: Determination of interface state density distribution," *Journal of Alloys and Compounds,* vol. 708, pp. 55-66, 2017.
[144] R. Sundararaman, P. Narang, A. S. Jermyn, W. A. Goddard III, and H. A. Atwater, "Theoretical predictions for hot-carrier generation from surface plasmon decay," *Nature communications,* vol. 5, no. 1, p. 5788, 2014.
[145] L. Amirav and M. Wächtler, "Nano Schottky?," vol. 22, ed: ACS Publications, 2022, pp. 9783-9785.
[146] J. A. Lee *et al.*, "Schottky nanocontact of one-dimensional semiconductor nanostructures probed by using conductive atomic force microscopy," *Nanotechnology,* vol. 27, no. 42, p. 425711, 2016.
[147] C. F. Tan *et al.*, "Inverse stellation of CuAu-ZnO multimetallic-semiconductor nanostartube for plasmon-enhanced photocatalysis," *ACS nano,* vol. 12, no. 5, pp. 4512-4520, 2018.
[148] P. Zhang, T. Wang, and J. Gong, "Mechanistic understanding of the plasmonic enhancement for solar water splitting," *Advanced Materials,* vol. 27, no. 36, pp. 5328-5342, 2015.
[149] D. Thrithamarassery Gangadharan, Z. Xu, Y. Liu, R. Izquierdo, and D. Ma, "Recent advancements in plasmon-enhanced promising third-generation solar cells," *Nanophotonics,* vol. 6, no. 1, pp. 153-175, 2017.
[150] W. Li and J. G. Valentine, "Harvesting the loss: surface plasmon-based hot electron photodetection," *Nanophotonics,* vol. 6, no. 1, pp. 177-191, 2017.
[151] I. Goykhman *et al.*, "On-chip integrated, silicon–graphene plasmonic Schottky photodetector with high responsivity and avalanche photogain," *Nano letters,* vol. 16, no. 5, pp. 3005-3013, 2016.
[152] J. E. Lee, S. Bera, Y. S. Choi, and W. I. Lee, "Size-dependent plasmonic effects of M and M@ SiO2 (M= Au or Ag) deposited on TiO2 in photocatalytic oxidation reactions," *Applied Catalysis B: Environmental,* vol. 214, pp. 15-22, 2017.
[153] Y.-H. Qiu *et al.*, "Size-dependent plasmon relaxation dynamics and saturable absorption in gold nanorods," *Journal of Physics D: Applied Physics,* vol. 49, no. 18, p. 185107, 2016.
[154] M. W. Knight, H. Sobhani, P. Nordlander, and N. J. Halas, "Photodetection with active optical antennas," *Science,* vol. 332, no. 6030, pp. 702-704, 2011.
[155] X. Ding, Y. Zhao, H. Xiao, and L. Qiao, "Engineering Schottky-to-Ohmic contact transition for 2D metal–semiconductor junctions," *Applied Physics Letters,* vol. 118, no. 9, 2021.
[156] Y. Park, J. Choi, M. Kang, H. Lee, H. Ihee, and J. Y. Park, "Relaxation dynamics of enhanced hot-electron flow on perovskite-coupled plasmonic silver schottky nanodiodes," *The Journal of Physical Chemistry C,* vol. 125, no. 4, pp. 2575-2582, 2021.
[157] B. Liu *et al.*, "Schottky junction made from a nanoporous Au and TiO2 film for plasmonic photodetectors," *ACS Applied Nano Materials,* vol. 6, no. 6, pp. 4619-4625, 2023.
[158] A. Pescaglini *et al.*, "Hot-electron injection in Au nanorod–ZnO nanowire hybrid device for near-infrared photodetection," *Nano letters,* vol. 14, no. 11, pp. 6202-6209, 2014.
[159] Z. Qi *et al.*, "Au nanoparticle-decorated silicon pyramids for plasmon-enhanced hot electron near-infrared photodetection," *Nanotechnology,* vol. 28, no. 27, p. 275202, 2017.
[160] L. V. Besteiro, X.-T. Kong, Z. Wang, G. Hartland, and A. O. Govorov, "Understanding hot-electron generation and plasmon relaxation in metal nanocrystals: quantum and classical mechanisms," *Acs Photonics,* vol. 4, no. 11, pp. 2759-2781, 2017.
[161] Q. Guo, C. Zhou, Z. Ma, and X. Yang, "Fundamentals of TiO2 photocatalysis: concepts, mechanisms, and challenges," *Advanced Materials,* vol. 31, no. 50, p. 1901997, 2019.
[162] A. J. Frank, N. Kopidakis, and J. Van De Lagemaat, "Electrons in nanostructured TiO2 solar cells: transport, recombination and photovoltaic properties," *Coordination Chemistry Reviews,* vol. 248, no. 13-14, pp. 1165-1179, 2004.

[163] J. Zou, Q. Zhang, K. Huang, and N. Marzari, "Ultraviolet photodetectors based on anodic TiO2 nanotube arrays," *The Journal of Physical Chemistry C*, vol. 114, no. 24, pp. 10725-10729, 2010.
[164] A. Furube, L. Du, K. Hara, R. Katoh, and M. Tachiya, "Ultrafast plasmon-induced electron transfer from gold nanodots into TiO2 nanoparticles," *Journal of the American Chemical Society*, vol. 129, no. 48, pp. 14852-14853, 2007.
[165] X. D. Gao *et al.*, "Porous Ag/TiO2-Schottky-diode based plasmonic hot-electron photodetector with high detectivity and fast response," *Nanophotonics*, vol. 8, no. 7, pp. 1247-1254, 2019.
[166] P. Joshna, A. Hazra, K. N. Chappanda, P. K. Pattnaik, and S. Kundu, "Fast response of UV photodetector based on Ag nanoparticles embedded uniform TiO2 nanotubes array," *Semiconductor Science and Technology*, vol. 35, no. 1, p. 015001, 2019.
[167] H. Ferhati, F. Djeffal, and N. Martin, "Highly improved responsivity of self-powered UV–Visible photodetector based on TiO2/Ag/TiO2 multilayer deposited by GLAD technique: Effects of oriented columns and nano-sculptured surface," *Applied Surface Science*, vol. 529, p. 147069, 2020.
[168] T. Yan, S. Cai, Z. Hu, Z. Li, and X. Fang, "Ultrafast speed, dark current suppression, and self-powered enhancement in TiO2-based ultraviolet photodetectors by organic layers and Ag nanowires regulation," *The Journal of Physical Chemistry Letters*, vol. 12, no. 40, pp. 9912-9918, 2021.
[169] H. Tang *et al.*, "Plasmonic hot electrons for sensing, photodetection, and solar energy applications: A perspective," *The Journal of Chemical Physics*, vol. 152, no. 22, 2020.
[170] H. Chalabi, D. Schoen, and M. L. Brongersma, "Hot-electron photodetection with a plasmonic nanostripe antenna," *Nano letters*, vol. 14, no. 3, pp. 1374-1380, 2014.
[171] G. Tagliabue *et al.*, "Quantifying the role of surface plasmon excitation and hot carrier transport in plasmonic devices," *Nature communications*, vol. 9, no. 1, p. 3394, 2018.
[172] L. Wang *et al.*, "Efficient ultraviolet photodetectors based on TiO 2 nanotube arrays with tailored structures," *RSC Advances*, vol. 5, no. 65, pp. 52388-52394, 2015.
[173] K.-T. Lin, H.-L. Chen, Y.-S. Lai, and C.-C. Yu, "Silicon-based broadband antenna for high responsivity and polarization-insensitive photodetection at telecommunication wavelengths," *Nature communications*, vol. 5, no. 1, p. 3288, 2014.
[174] T. Matsui *et al.*, "Highly stable plasmon induced hot hole transfer into silicon via a SrTiO3 passivation interface," *Advanced Functional Materials*, vol. 28, no. 17, p. 1705829, 2018.
[175] P. Wan *et al.*, "Flexible transparent films based on nanocomposite networks of polyaniline and carbon nanotubes for high-performance gas sensing," *Small*, vol. 11, no. 40, pp. 5409-5415, 2015.
[176] T. Gao *et al.*, "Hierarchical graphene/metal grid structures for stable, flexible transparent conductors," *Acs Nano*, vol. 9, no. 5, pp. 5440-5446, 2015.
[177] Y. Zhu, Y. Deng, P. Yi, L. Peng, X. Lai, and Z. Lin, "Flexible transparent electrodes based on silver nanowires: material synthesis, fabrication, performance, and applications," *Advanced Materials Technologies*, vol. 4, no. 10, p. 1900413, 2019.
[178] M. Lagrange, D. Langley, G. Giusti, C. Jiménez, Y. Bréchet, and D. Bellet, "Optimization of silver nanowire-based transparent electrodes: effects of density, size and thermal annealing," *Nanoscale*, vol. 7, no. 41, pp. 17410-17423, 2015.
[179] F. Sun *et al.*, "An autonomously ultrafast self-healing, highly colourless, tear-resistant and compliant elastomer tailored for transparent electromagnetic interference shielding films integrated in flexible and optical electronics," *Materials Horizons*, vol. 8, no. 12, pp. 3356-3367, 2021.
[180] R. Zhu *et al.*, "Fused silver nanowires with metal oxide nanoparticles and organic polymers for highly transparent conductors," *ACS nano*, vol. 5, no. 12, pp. 9877-9882, 2011.

[181] C. F. Guo and Z. Ren, "Flexible transparent conductors based on metal nanowire networks," *Materials Today,* vol. 18, no. 3, pp. 143-154, 2015.
[182] S. Vedraine, A. El Hajj, P. Torchio, and B. Lucas, "Optimized ITO-free tri-layer electrode for organic solar cells," *Organic Electronics,* vol. 14, no. 4, pp. 1122-1129, 2013.
[183] X. Wang *et al.*, "Assembly of silver nanowires and PEDOT: PSS with hydrocellulose toward highly flexible, transparent and conductivity-stable conductors," *Chemical Engineering Journal,* vol. 392, p. 123644, 2020.
[184] J. H. Im, K.-T. Kang, S. H. Lee, J. Y. Hwang, H. Kang, and K. H. Cho, "Bulk-like Al/Ag bilayer film due to suppression of surface plasmon resonance for high transparent organic light emitting diodes," *Organic Electronics,* vol. 33, pp. 116-120, 2016.
[185] H. Lu, D. Zhang, J. Cheng, J. Liu, J. Mao, and W. C. Choy, "Locally welded silver nano-network transparent electrodes with high operational stability by a simple alcohol-based chemical approach," *Advanced Functional Materials,* vol. 25, no. 27, pp. 4211-4218, 2015.
[186] W. Cui, F. Chen, Y. Li, X. Su, and B. Sun, "Status and perspectives of transparent conductive oxide films for silicon heterojunction solar cells," *Materials Today Nano,* vol. 22, p. 100329, 2023.
[187] R. Chakraborty *et al.*, "Fabrication of non-volatile memory transistor by charge compensation of interfacial ionic polarization of a ferroelectric gate dielectric," *Applied Materials Today,* vol. 33, p. 101862, 2023.
[188] T. Lee, E. Choi, J.-O. Park, and D. Bang, "Tunable and highly accessible plasmonic gap nanostructures on flexible film as a high-performance surface-enhanced Raman scattering sensor," *Materials Today Nano,* vol. 23, p. 100370, 2023.
[189] L. Ferrari *et al.*, "Design and analysis of blue InGaN/GaN plasmonic LED for high-speed, high-efficiency optical communications," *ACS Photonics,* vol. 5, no. 9, pp. 3557-3564, 2018.
[190] T. Echtermeyer *et al.*, "Strong plasmonic enhancement of photovoltage in graphene," *Nature communications,* vol. 2, no. 1, p. 458, 2011.
[191] H.-Y. Hou *et al.*, "Boosted radiative energy transfer of plasmonic electrodes enables flexible organic photovoltaics with efficiency over 18%," *Chemical Engineering Journal,* vol. 450, p. 138181, 2022.
[192] Y. H. Jang, Y. J. Jang, S. Kim, L. N. Quan, K. Chung, and D. H. Kim, "Plasmonic solar cells: from rational design to mechanism overview," *Chemical reviews,* vol. 116, no. 24, pp. 14982-15034, 2016.
[193] J. Ma and S. Gao, "Plasmon-induced electron–hole separation at the Ag/TiO2 (110) interface," *ACS nano,* vol. 13, no. 12, pp. 13658-13667, 2019.
[194] C. Pang *et al.*, "Ultrafast electron transfer dynamics in Ag/TiO2 nanocomposite for tailoring of optical nonlinearity," *Applied Surface Science,* vol. 539, p. 148258, 2021.
[195] L. B. Luo *et al.*, "The effect of plasmonic nanoparticles on the optoelectronic characteristics of CdTe nanowires," *Small,* vol. 10, no. 13, pp. 2645-2652, 2014.
[196] J. Song *et al.*, "Highly efficient plasmon induced hot-electron transfer at Ag/TiO2 interface," *ACS Photonics,* vol. 8, no. 5, pp. 1497-1504, 2021.
[197] C. Ng *et al.*, "Hot carrier extraction with plasmonic broadband absorbers," *Acs Nano,* vol. 10, no. 4, pp. 4704-4711, 2016.
[198] F. P. García de Arquer, A. Mihi, and G. Konstantatos, "Large-area plasmonic-crystal–hot-electron-based photodetectors," *ACS photonics,* vol. 2, no. 7, pp. 950-957, 2015.
[199] A. Sobhani *et al.*, "Narrowband photodetection in the near-infrared with a plasmon-induced hot electron device," *Nature communications,* vol. 4, no. 1, p. 1643, 2013.
[200] X. Yu, P. Duxbury, G. Jeffers, and M. Dubson, "Coalescence and percolation in thin metal films," *Physical Review B,* vol. 44, no. 23, p. 13163, 1991.
[201] D. Kim, A. L. Giermann, and C. V. Thompson, "Solid-state dewetting of patterned thin films," *Applied Physics Letters,* vol. 95, no. 25, 2009.

[202] H. Galinski, T. Ryll, P. Elser, J. Rupp, A. Bieberle-Hütter, and L. Gauckler, "Agglomeration of Pt thin films on dielectric substrates," *Physical Review B—Condensed Matter and Materials Physics*, vol. 82, no. 23, p. 235415, 2010.
[203] J. W. Essam, "Percolation theory," *Reports on progress in physics*, vol. 43, no. 7, p. 833, 1980.
[204] S. Chu and A. Majumdar, "Opportunities and challenges for a sustainable energy future," *nature*, vol. 488, no. 7411, pp. 294-303, 2012.
[205] K. R. Abbasi, M. Shahbaz, J. Zhang, M. Irfan, and R. Alvarado, "Analyze the environmental sustainability factors of China: The role of fossil fuel energy and renewable energy," *Renewable Energy*, vol. 187, pp. 390-402, 2022.
[206] M. T. Kartal, "The role of consumption of energy, fossil sources, nuclear energy, and renewable energy on environmental degradation in top-five carbon producing countries," *Renewable Energy*, vol. 184, pp. 871-880, 2022.
[207] N. Kabalina, M. Costa, W. Yang, and A. Martin, "Impact of a reduction in heating, cooling and electricity loads on the performance of a polygeneration district heating and cooling system based on waste gasification," *Energy*, vol. 151, pp. 594-604, 2018.
[208] K. Zhu, M. Victoria, G. B. Andresen, and M. Greiner, "Impact of climatic, technical and economic uncertainties on the optimal design of a coupled fossil-free electricity, heating and cooling system in Europe," *Applied Energy*, vol. 262, p. 114500, 2020.
[209] S. D. Rezaei, S. Shannigrahi, and S. Ramakrishna, "A review of conventional, advanced, and smart glazing technologies and materials for improving indoor environment," *Solar Energy Materials and Solar Cells*, vol. 159, pp. 26-51, 2017.
[210] S. K. Kang, D. H. Ho, C. H. Lee, H. S. Lim, and J. H. Cho, "Actively operable thermoresponsive smart windows for reducing energy consumption," *ACS Applied Materials & Interfaces*, vol. 12, no. 30, pp. 33838-33845, 2020.
[211] Y. Niu *et al.*, "Energy saving and energy generation smart window with active control and antifreezing functions," *Advanced Science*, vol. 9, no. 6, p. 2105184, 2022.
[212] J. Zhou *et al.*, "VO2 thermochromic smart window for energy savings and generation," *Scientific reports*, vol. 3, no. 1, p. 3029, 2013.
[213] M. Kamalisarvestani, R. Saidur, S. Mekhilef, and F. Javadi, "Performance, materials and coating technologies of thermochromic thin films on smart windows," *Renewable and Sustainable Energy Reviews*, vol. 26, pp. 353-364, 2013.
[214] Y. Ke *et al.*, "Two-dimensional SiO2/VO2 photonic crystals with statically visible and dynamically infrared modulated for smart window deployment," *ACS applied materials & interfaces*, vol. 8, no. 48, pp. 33112-33120, 2016.
[215] S.-W. Oh, S.-M. Nam, S.-H. Kim, T.-H. Yoon, and W. S. Kim, "Self-regulation of infrared using a liquid crystal mixture doped with push–pull azobenzene for energy-saving smart windows," *ACS Applied Materials & Interfaces*, vol. 13, no. 4, pp. 5028-5033, 2021.
[216] H. Khandelwal, A. P. Schenning, and M. G. Debije, "Infrared regulating smart window based on organic materials," *Advanced Energy Materials*, vol. 7, no. 14, p. 1602209, 2017.
[217] S. Nundy, A. Mesloub, B. M. Alsolami, and A. Ghosh, "Electrically actuated visible and near-infrared regulating switchable smart window for energy positive building: A review," *Journal of Cleaner Production*, vol. 301, p. 126854, 2021.
[218] J. Mandal *et al.*, "Hierarchically porous polymer coatings for highly efficient passive daytime radiative cooling," *Science*, vol. 362, no. 6412, pp. 315-319, 2018.
[219] X. Lu, P. Xu, H. Wang, T. Yang, and J. Hou, "Cooling potential and applications prospects of passive radiative cooling in buildings: The current state-of-the-art," *Renewable and Sustainable Energy Reviews*, vol. 65, pp. 1079-1097, 2016.
[220] G. K. Dalapati *et al.*, "Color tunable low cost transparent heat reflector using copper and titanium oxide for energy saving application," *Scientific reports*, vol. 6, no. 1, p. 20182, 2016.

[221] G. K. Dalapati *et al.*, "Transparent heat regulating (THR) materials and coatings for energy saving window applications: Impact of materials design, micro-structural, and interface quality on the THR performance," *Progress in materials science,* vol. 95, pp. 42-131, 2018.
[222] J. H. Kwon, S. Choi, Y. Jeon, H. Kim, K. S. Chang, and K. C. Choi, "Functional design of dielectric–metal–dielectric-based thin-film encapsulation with heat transfer and flexibility for flexible displays," *ACS Applied Materials & Interfaces,* vol. 9, no. 32, pp. 27062-27072, 2017.
[223] M. Butt, S. Fomchenkov, and S. Khonina, "Dielectric-Metal-Dielectric (DMD) infrared (IR) heat reflectors," in *Journal of Physics: Conference Series*, 2017, vol. 917, no. 6: IOP Publishing, p. 062007.
[224] M. Al-Kuhaili, A. Al-Aswad, S. Durrani, and I. Bakhtiari, "Energy-saving transparent heat mirrors based on tungsten oxide–gold WO3/Au/WO3 multilayer structures," *Solar energy,* vol. 86, no. 11, pp. 3183-3189, 2012.
[225] T. D. Nguyen *et al.*, "Electrochromic smart glass coating on functional nano-frameworks for effective building energy conservation," *Materials Today Energy,* vol. 18, p. 100496, 2020.
[226] Y. Yang *et al.*, "Triboelectric nanogenerator enabled wearable sensors and electronics for sustainable internet of things integrated green earth," *Advanced Energy Materials*, vol. 13, no. 1, p. 2203040, 2023.
[227] D. Wang, G. Chen, and J. Fu, "Multifunctional thermochromic smart windows for building energy saving," *Journal of Materials Chemistry A,* vol. 12, no. 22, pp. 12960-12982, 2024.
[228] H. Peng *et al.*, "Dynamically Tunable Thermochromic Smart Windows for Building Energy Conservation," *ACS Materials Letters,* vol. 6, no. 8, pp. 3404-3413, 2024.
[229] Z. Shao *et al.*, "Tri-band electrochromic smart window for energy savings in buildings," *Nature Sustainability,* vol. 7, no. 6, pp. 796-803, 2024.
[230] X. Geng *et al.*, "Tuning phase transition and thermochromic properties of vanadium dioxide thin films via cobalt doping," *ACS Applied Materials & Interfaces,* vol. 14, no. 17, pp. 19736-19746, 2022.
[231] L. Calvi *et al.*, "A comparative study on the switching kinetics of W/VO2 powders and VO2 coatings and their implications for thermochromic glazing," *Solar Energy Materials and Solar Cells,* vol. 224, p. 110977, 2021.
[232] Y. Ke *et al.*, "Cephalopod-inspired versatile design based on plasmonic VO2 nanoparticle for energy-efficient mechano-thermochromic windows," *Nano Energy,* vol. 73, p. 104785, 2020.
[233] Z. Zhao *et al.*, "Sn–W Co-doping improves thermochromic performance of VO2 films for smart windows," *ACS Applied Energy Materials,* vol. 3, no. 10, pp. 9972-9979, 2020.
[234] M. Azmat *et al.*, "Samarium-doped vanadium dioxide thin films to modulate the thermochromic properties for energy-saving smart windows," *ACS Applied Energy Materials,* vol. 7, no. 9, pp. 3776-3786, 2024.
[235] S. Barinova, Y.-W. Wu, S.-H. Yang, and I. Abdulhalim, "Metamaterial hybrid smart window based on nanoporous VO2 microparticles in liquid crystal for heat blocking and visibility control," *ACS Applied Energy Materials,* vol. 6, no. 14, pp. 7587-7595, 2023.
[236] L. Wu *et al.*, "Kirkendall effect induced ultrafine VOOH nanoparticles and their transformation into VO 2 (M) for energy-efficient smart windows," *Materials Horizons,* vol. 11, no. 4, pp. 1098-1107, 2024.
[237] N. Wang, Q. S. Goh, P. L. Lee, S. Magdassi, and Y. Long, "One-step hydrothermal synthesis of rare earth/W-codoped VO2 nanoparticles: Reduced phase transition temperature and improved thermochromic properties," *Journal of Alloys and Compounds,* vol. 711, pp. 222-228, 2017.
[238] R. Guo *et al.*, "Phase-change materials for intelligent temperature regulation," *Materials Today Energy,* vol. 23, p. 100888, 2022.

[239] J. Li *et al.*, "A photosynthetically active radiative cooling film," *Nature Sustainability*, vol. 7, no. 6, pp. 786-795, 2024.
[240] Y. Jiao *et al.*, "Flexible tri-state-regulated thermochromic smart window based on WxV1-xO2/paraffin/PVA composite film," *Chemical Engineering Journal*, vol. 497, p. 154578, 2024.
[241] S. Lin *et al.*, "Direct spray-coating of highly robust and transparent Ag nanowires for energy saving windows," *Nano Energy*, vol. 62, pp. 111-116, 2019.
[242] Y. Li, X. Chen, L. Yu, D. Pang, H. Yan, and M. Chen, "Janus interface engineering boosting visibly transparent radiative cooling for energy saving," *ACS Applied Materials & Interfaces*, vol. 15, no. 3, pp. 4122-4131, 2023.
[243] S. H. Kim, M. Kim, J. H. Lee, and S.-J. Lee, "Self-cleaning transparent heat mirror with a plasma polymer fluorocarbon thin film fabricated by a continuous roll-to-roll sputtering process," *ACS applied materials & interfaces*, vol. 10, no. 12, pp. 10454-10460, 2018.
[244] H.-C. Chu *et al.*, "Spray-deposited large-area copper nanowire transparent conductive electrodes and their uses for touch screen applications," *ACS applied materials & interfaces*, vol. 8, no. 20, pp. 13009-13017, 2016.
[245] J. Lee *et al.*, "Room-temperature nanosoldering of a very long metal nanowire network by conducting-polymer-assisted joining for a flexible touch-panel application," *Advanced Functional Materials*, vol. 23, no. 34, pp. 4171-4176, 2013.
[246] T. Shimura *et al.*, "A high-resolution, transparent, and stretchable polymer conductor for wearable sensor arrays," *Advanced Materials Technologies*, vol. 8, no. 12, p. 2201992, 2023.
[247] X.-Y. Yin, Y. Zhang, X. Cai, Q. Guo, J. Yang, and Z. L. Wang, "3D printing of ionic conductors for high-sensitivity wearable sensors," *Materials Horizons*, vol. 6, no. 4, pp. 767-780, 2019.
[248] Z. H. Chen, R. Fang, W. Li, and J. Guan, "Stretchable transparent conductors: from micro/macromechanics to applications," *Advanced Materials*, vol. 31, no. 35, p. 1900756, 2019.
[249] J. Lee *et al.*, "Semitransparent perovskite solar cells with enhanced light utilization efficiencies by transferable Ag nanogrid electrodes," *ACS Applied Materials & Interfaces*, vol. 13, no. 49, pp. 58475-58485, 2021.
[250] S. Lin *et al.*, "Roll-to-roll production of transparent silver-nanofiber-network electrodes for flexible electrochromic smart windows," *Advanced materials*, vol. 29, no. 41, p. 1703238, 2017.
[251] J. K. Wassei and R. B. Kaner, "Graphene, a promising transparent conductor," *Materials today*, vol. 13, no. 3, pp. 52-59, 2010.
[252] C. Mancarella, M. Sygletou, B. R. Bricchi, F. Bisio, and A. Li Bassi, "Tunable optical and plasmonic response of Au nanoparticles embedded in Ta-doped TiO 2 transparent conducting films," *Physical Review Materials*, vol. 6, no. 2, p. 025201, 2022.
[253] T. Kim, A. Canlier, C. Cho, V. Rozyyev, J.-Y. Lee, and S. M. Han, "Highly transparent Au-coated Ag nanowire transparent electrode with reduction in haze," *ACS applied materials & interfaces*, vol. 6, no. 16, pp. 13527-13534, 2014.
[254] T.-B. Song *et al.*, "Highly robust silver nanowire network for transparent electrode," *ACS applied materials & interfaces*, vol. 7, no. 44, pp. 24601-24607, 2015.
[255] B. Bari *et al.*, "Simple hydrothermal synthesis of very-long and thin silver nanowires and their application in high quality transparent electrodes," *Journal of Materials Chemistry A*, vol. 4, no. 29, pp. 11365-11371, 2016.
[256] A. R. Rathmell, S. M. Bergin, Y. L. Hua, Z. Y. Li, and B. J. Wiley, "The growth mechanism of copper nanowires and their properties in flexible, transparent conducting films," *Advanced materials*, vol. 22, no. 32, pp. 3558-3563, 2010.
[257] X. Lu, Y. Zhang, and Z. Zheng, "Metal-based flexible transparent electrodes: challenges and recent advances," *Advanced Electronic Materials*, vol. 7, no. 5, p. 2001121, 2021.

[258] J. Liu, D. Jia, J. M. Gardner, E. M. Johansson, and X. Zhang, "Metal nanowire networks: Recent advances and challenges for new generation photovoltaics," *Materials Today Energy*, vol. 13, pp. 152-185, 2019.
[259] X. Ma, Y. Li, I. Hussain, R. Shen, G. Yang, and K. Zhang, "Core–shell structured nanoenergetic materials: preparation and fundamental properties," *Advanced Materials*, vol. 32, no. 30, p. 2001291, 2020.
[260] Z. Ren *et al.*, "Core-shell TiO2@ Au nanofibers derived from a unique physical coating strategy for excellent capacitive energy storage nanocomposites," *Advanced Functional Materials*, vol. 34, no. 36, p. 2401907, 2024.
[261] S. Yuan, X. Li, X. Zhang, and Y. Jia, "Fabrication of Au–Ag bimetallic nanostructures through the galvanic replacement reaction of block copolymer-stabilized Ag nanoparticles with HAuCl4," *Science of Advanced Materials*, vol. 7, no. 5, pp. 918-923, 2015.
[262] A. N. Koya *et al.*, "Nanoporous metals: From plasmonic properties to applications in enhanced spectroscopy and photocatalysis," *ACS nano*, vol. 15, no. 4, pp. 6038-6060, 2021.
[263] P. Singh, T. A. König, and A. Jaiswal, "NIR-active plasmonic gold nanocapsules synthesized using thermally induced seed twinning for surface-enhanced raman scattering applications," *ACS applied materials & interfaces*, vol. 10, no. 45, pp. 39380-39390, 2018.
[264] U. Pandey, A. K. Yadav, N. Pal, P. K. Aich, and B. N. Pal, "Enhanced sub-band gap photosensitivity by an asymmetric source–drain electrode low operating voltage oxide transistor," *Journal of Materials Chemistry C*, vol. 11, no. 43, pp. 15276-15287, 2023.
[265] J. Miao and T. Fan, "Flexible and stretchable transparent conductive graphene-based electrodes for emerging wearable electronics," *Carbon*, vol. 202, pp. 495-527, 2023.
[266] D. S. Ginley and J. D. Perkins, "Transparent conductors," in *Handbook of transparent conductors*: Springer, 2010, pp. 1-25.
[267] M. Morales-Masis, S. De Wolf, R. Woods-Robinson, J. W. Ager, and C. Ballif, "Transparent electrodes for efficient optoelectronics," *Advanced Electronic Materials*, vol. 3, no. 5, p. 1600529, 2017.
[268] Q. Tai and F. Yan, "Emerging semitransparent solar cells: materials and device design," *Advanced Materials*, vol. 29, no. 34, p. 1700192, 2017.
[269] D. Won *et al.*, "Transparent electronics for wearable electronics application," *Chemical Reviews*, vol. 123, no. 16, pp. 9982-10078, 2023.
[270] K. Salimi, A. Atilgan, M. Y. Aydin, H. Yildirim, N. Celebi, and A. Yildiz, "Plasmonic mesoporous core-shell Ag-Au@ TiO2 photoanodes for efficient light harvesting in dye sensitized solar cells," *Solar Energy*, vol. 193, pp. 820-827, 2019.
[271] R. Borah and S. W. Verbruggen, "Silver–gold bimetallic alloy versus core–shell nanoparticles: implications for plasmonic enhancement and photothermal applications," *The Journal of Physical Chemistry C*, vol. 124, no. 22, pp. 12081-12094, 2020.
[272] X. Liu *et al.*, "Synthesis of thermally stable and highly active bimetallic Au− Ag nanoparticles on inert supports," *Chemistry of Materials*, vol. 21, no. 2, pp. 410-418, 2009.
[273] Z. Tang, W. Tress, and O. Inganäs, "Light trapping in thin film organic solar cells," *Materials today*, vol. 17, no. 8, pp. 389-396, 2014.
[274] A. Peter Amalathas and M. M. Alkaisi, "Nanostructures for light trapping in thin film solar cells," *Micromachines*, vol. 10, no. 9, p. 619, 2019.
[275] E. L. Lim, C. C. Yap, M. A. M. Teridi, C. H. Teh, A. R. bin Mohd Yusoff, and M. H. H. Jumali, "A review of recent plasmonic nanoparticles incorporated P3HT: PCBM organic thin film solar cells," *Organic Electronics*, vol. 36, pp. 12-28, 2016.
[276] K. L. Kelly, E. Coronado, L. L. Zhao, and G. C. Schatz, "The optical properties of metal nanoparticles: the influence of size, shape, and dielectric environment," vol. 107, ed: ACS Publications, 2003, pp. 668-677.

[277] R. A. Pala, J. White, E. Barnard, J. Liu, and M. L. Brongersma, "Design of plasmonic thin-film solar cells with broadband absorption enhancements," *Adv. Mater,* vol. 21, no. 34, pp. 3504-3509, 2009.
[278] X. Huang, S. Han, W. Huang, and X. Liu, "Enhancing solar cell efficiency: the search for luminescent materials as spectral converters," *Chemical Society Reviews,* vol. 42, no. 1, pp. 173-201, 2013.
[279] E. K. Solak and E. Irmak, "Advances in organic photovoltaic cells: a comprehensive review of materials, technologies, and performance," *RSC advances,* vol. 13, no. 18, pp. 12244-12269, 2023.
[280] J. Panidi, D. G. Georgiadou, T. Schoetz, and T. Prodromakis, "Advances in organic and perovskite photovoltaics enabling a greener Internet of Things," *Advanced Functional Materials,* vol. 32, no. 23, p. 2200694, 2022.
[281] G. Bernardo, T. Lopes, D. G. Lidzey, and A. Mendes, "Progress in upscaling organic photovoltaic devices," *Advanced Energy Materials,* vol. 11, no. 23, p. 2100342, 2021.
[282] C. W. Tang, "Two-layer organic photovoltaic cell," *Applied physics letters,* vol. 48, no. 2, pp. 183-185, 1986.
[283] S. Park, T. Kim, S. Yoon, C. W. Koh, H. Y. Woo, and H. J. Son, "Progress in materials, solution processes, and long-term stability for large-area organic photovoltaics," *Advanced Materials,* vol. 32, no. 51, p. 2002217, 2020.
[284] G. Wang, M. A. Adil, J. Zhang, and Z. Wei, "Large-area organic solar cells: material requirements, modular designs, and printing methods," *Advanced Materials,* vol. 31, no. 45, p. 1805089, 2019.
[285] N. Kalfagiannis *et al.*, "Plasmonic silver nanoparticles for improved organic solar cells," *Solar Energy Materials and Solar Cells,* vol. 104, pp. 165-174, 2012.
[286] J. Wang *et al.*, "Effect of plasmonic Au nanoparticles on inverted organic solar cell performance," *The Journal of Physical Chemistry C,* vol. 117, no. 1, pp. 85-91, 2013.
[287] M. Notarianni, K. Vernon, A. Chou, M. Aljada, J. Liu, and N. Motta, "Plasmonic effect of gold nanoparticles in organic solar cells," *Solar Energy,* vol. 106, pp. 23-37, 2014.
[288] X. Li, W. C. H. Choy, H. Lu, W. E. Sha, and A. H. P. Ho, "Efficiency enhancement of organic solar cells by using shape-dependent broadband plasmonic absorption in metallic nanoparticles," *Advanced Functional Materials,* vol. 23, no. 21, pp. 2728-2735, 2013.
[289] M. Omrani, H. Fallah, K.-L. Choy, and M. Abdi-Jalebi, "Impact of hybrid plasmonic nanoparticles on the charge carrier mobility of P3HT: PCBM polymer solar cells," *Scientific reports,* vol. 11, no. 1, p. 19774, 2021.
[290] L. Tzounis, C. Gravalidis, A. Papamichail, and S. Logothetidis, "Enhancement of P3HT: PCBM photovoltaic shells efficiency incorporating core-shell Au@ Ag plasmonic nanoparticles," *Materials Today: Proceedings,* vol. 3, no. 3, pp. 832-839, 2016.
[291] H. Kaçuş, M. Biber, and Ş. Aydoğan, "Role of the Au and Ag nanoparticles on organic solar cells based on P3HT: PCBM active layer," *Applied Physics A,* vol. 126, no. 10, p. 817, 2020.
[292] S. Sanad, A. M. Ghanim, N. Gad, M. El-Aasser, A. Yahia, and M. A. Swillam, "Enhanced light harvesting in PM6: Y6 organic solar cells using plasmonic nanostructures," in *Smart Materials for Opto-Electronic Applications*, 2023, vol. 12584: SPIE, pp. 133-137.
[293] T. Das, A. Kumar, S. Rani, A. Guchhait, and D. S. Ghosh, "Fabrication of highly efficient and ambient stable planar MAPbI3 perovskite solar cells via defect passivation through crosslinking strategy," *Advanced Engineering Materials,* vol. 26, no. 8, p. 2302078, 2024.
[294] D. Li, Y. Sun, J. Pei, X. Yu, Z. Tian, and H. Xu, "Au-SnO2 resonator for SERS detection of ciprofloxacin," *Microchemical Journal,* vol. 203, p. 110830, 2024.
[295] A. M. Ismail, E. Csapó, and C. Janáky, "Correlation between the work function of Au–Ag nanoalloys and their electrocatalytic activity in carbon dioxide reduction," *Electrochimica Acta,* vol. 313, pp. 171-178, 2019.

[296] M. Abdallaoui, N. Sengouga, A. Chala, A. Meftah, and A. Meftah, "Comparative study of conventional and inverted P3HT: PCBM organic solar cell," *Optical Materials,* vol. 105, p. 109916, 2020.
[297] A. Iwan *et al.*, "Electrochemical and photocurrent characterization of polymer solar cells with improved performance after GO addition to the PEDOT: PSS hole transporting layer," *Solar Energy,* vol. 146, pp. 230-242, 2017.
[298] X. X. Han, R. S. Rodriguez, C. L. Haynes, Y. Ozaki, and B. Zhao, "Surface-enhanced Raman spectroscopy," *Nature Reviews Methods Primers,* vol. 1, no. 1, p. 87, 2021.
[299] A. Korkmaz, M. Kenton, G. Aksin, M. Kahraman, and S. Wachsmann-Hogiu, "Inexpensive and flexible SERS substrates on adhesive tape based on biosilica plasmonic nanocomposites," *ACS Applied Nano Materials,* vol. 1, no. 9, pp. 5316-5326, 2018.
[300] J. Bar *et al.*, "Silicon microchannel-driven Raman scattering enhancement to improve gold nanorod functions as a SERS substrate toward single-molecule detection," *ACS Applied Materials & Interfaces,* vol. 13, no. 30, pp. 36482-36491, 2021.
[301] K. Kneipp *et al.*, "Single molecule detection using surface-enhanced Raman scattering (SERS)," *Physical review letters,* vol. 78, no. 9, p. 1667, 1997.
[302] L. Zhang, C. Guan, Y. Wang, and J. Liao, "Highly effective and uniform SERS substrates fabricated by etching multi-layered gold nanoparticle arrays," *Nanoscale,* vol. 8, no. 11, pp. 5928-5937, 2016.
[303] S. Huang, C. Wu, Y. Wang, X. Yang, R. Yuan, and Y. Chai, "Ag/TiO2 nanocomposites as a novel SERS substrate for construction of sensitive biosensor," *Sensors and Actuators B: Chemical,* vol. 339, p. 129843, 2021.
[304] X. Zhao *et al.*, "High-performance SERS substrate based on hierarchical 3D Cu nanocrystals with efficient morphology control," *Small,* vol. 14, no. 38, p. 1802477, 2018.
[305] L. Zhang, T. Liu, K. Liu, L. Han, Y. Yin, and C. Gao, "Gold nanoframes by nonepitaxial growth of Au on AgI nanocrystals for surface-enhanced Raman spectroscopy," *Nano letters,* vol. 15, no. 7, pp. 4448-4454, 2015.
[306] H. Zhang *et al.*, "Physical deposition improved SERS stability of morphology controlled periodic micro/nanostructured arrays based on colloidal templates," *Small,* vol. 11, no. 7, pp. 844-853, 2015.
[307] Y.-J. Yeh, C.-J. Cho, J.-S. Benas, K.-L. Tung, C.-C. Kuo, and W.-H. Chiang, "Plasma-engineered plasmonic nanoparticle-based stretchable nanocomposites as sensitive wearable SERS sensors," *ACS Applied Nano Materials,* vol. 6, no. 12, pp. 10115-10125, 2023.
[308] T.-J. Wang, N. R. Barveen, Z.-Y. Liu, C.-H. Chen, and M.-H. Chou, "Transparent, flexible plasmonic Ag NP/PMMA substrates using chemically patterned ferroelectric crystals for detecting pesticides on curved surfaces," *ACS Applied Materials & Interfaces,* vol. 13, no. 29, pp. 34910-34922, 2021.
[309] J. Wang, K. M. Koo, Y. Wang, and M. Trau, "Engineering state-of-the-art plasmonic nanomaterials for SERS-based clinical liquid biopsy applications," *Advanced Science,* vol. 6, no. 23, p. 1900730, 2019.
[310] B. A. Yusuf *et al.*, "Rational design of noble metal-based multimetallic nanomaterials: A review," *Nano Energy,* vol. 104, p. 107959, 2022.
[311] G. Sharma *et al.*, "Revolution from monometallic to trimetallic nanoparticle composites, various synthesis methods and their applications: A review," *Materials Science and Engineering: C,* vol. 71, pp. 1216-1230, 2017.
[312] M. Fan, F.-J. Lai, H.-L. Chou, W.-T. Lu, B.-J. Hwang, and A. G. Brolo, "Surface-enhanced Raman scattering (SERS) from Au: Ag bimetallic nanoparticles: the effect of the molecular probe," *Chemical Science,* vol. 4, no. 1, pp. 509-515, 2013.
[313] K. Liu *et al.*, "Porous Au–Ag nanospheres with high-density and highly accessible hotspots for SERS analysis," *Nano letters,* vol. 16, no. 6, pp. 3675-3681, 2016.

[314] H.-l. Hao, J. Zhu, G.-j. Weng, J.-j. Li, Y.-b. Guo, and J.-w. Zhao, "Exclusive core-Janus satellite assembly based on Au–Ag Janus self-aligned distributions with abundant hotspots for ultrasensitive detection of CA19-9," *ACS sensors,* vol. 9, no. 2, pp. 942-954, 2024.
[315] H. Kang *et al.*, "Stabilization of silver and gold nanoparticles: preservation and improvement of plasmonic functionalities," *Chemical reviews,* vol. 119, no. 1, pp. 664-699, 2018.
[316] Y. Yang *et al.*, "Controlled growth of Ag/Au bimetallic nanorods through kinetics control," *Chemistry of Materials,* vol. 25, no. 1, pp. 34-41, 2013.
[317] D. Chateau *et al.*, "From gold nanobipyramids to nanojavelins for a precise tuning of the plasmon resonance to the infrared wavelengths: experimental and theoretical aspects," *Nanoscale,* vol. 7, no. 5, pp. 1934-1943, 2015.
[318] W. Xiong, R. Mazid, L. W. Yap, X. Li, and W. Cheng, "Plasmonic caged gold nanorods for near-infrared light controlled drug delivery," *Nanoscale,* vol. 6, no. 23, pp. 14388-14393, 2014.
[319] M. Mayer, M. J. Schnepf, T. A. König, and A. Fery, "Colloidal Self-Assembly Concepts for Plasmonic Metasurfaces," *Advanced Optical Materials,* vol. 7, no. 1, p. 1800564, 2019.
[320] C. Li, L. Sun, Y. Sun, and T. Teranishi, "One-pot controllable synthesis of Au@ Ag heterogeneous nanorods with highly tunable plasmonic absorption," *Chemistry of Materials,* vol. 25, no. 13, pp. 2580-2590, 2013.
[321] C. L. Haynes, A. D. McFarland, and R. P. Van Duyne, "Surface-enhanced Raman spectroscopy," ed: ACS Publications, 2005.
[322] A. Campion and P. Kambhampati, "Surface-enhanced Raman scattering," *Chemical society reviews,* vol. 27, no. 4, pp. 241-250, 1998.
[323] S. Abalde-Cela, S. Carregal-Romero, J. P. Coelho, and A. Guerrero-Martínez, "Recent progress on colloidal metal nanoparticles as signal enhancers in nanosensing," *Advances in colloid and interface science,* vol. 233, pp. 255-270, 2016.
[324] Y. Liu, H. Ma, X. X. Han, and B. Zhao, "Metal–semiconductor heterostructures for surface-enhanced Raman scattering: synergistic contribution of plasmons and charge transfer," *Materials horizons,* vol. 8, no. 2, pp. 370-382, 2021.
[325] K. Zhang *et al.*, "Synthesis of a Gold–Metal Oxide Core–Satellite Nanostructure for In Situ SERS Study of CuO-Catalyzed Photooxidation," *Angewandte Chemie,* vol. 132, no. 41, pp. 18159-18165, 2020.
[326] S. Cong *et al.*, "Noble metal-comparable SERS enhancement from semiconducting metal oxides by making oxygen vacancies," *Nature communications,* vol. 6, no. 1, p. 7800, 2015.
[327] L. Yang *et al.*, "Charge-transfer-induced surface-enhanced Raman scattering on Ag− TiO2 nanocomposites," *The Journal of Physical Chemistry C,* vol. 113, no. 36, pp. 16226-16231, 2009.
[328] Y. Huang, S. Zhang, S. Jiang, and J. Xu, "Improved SERS Performance on Ag-Coated Amorphous TiO2 Random Nanocavities by the Enhanced Light–Matter Coupling Effect," *ACS Sustainable Chemistry & Engineering,* vol. 12, no. 8, pp. 3234-3242, 2024.
[329] Y. Wang *et al.*, "Effect of TiO2 arrays on surface enhanced Raman scattering (SERS) performance for Ag/TiO2 substrates," *Nanotechnology,* vol. 32, no. 7, p. 075708, 2020.
[330] J. Colin *et al.*, "In situ and real-time nanoscale monitoring of ultra-thin metal film growth using optical and electrical diagnostic tools," *Nanomaterials,* vol. 10, no. 11, p. 2225, 2020.
[331] L. Zhu, Z. Meng, S. Hu, T. Zhao, and B. Zhao, "Understanding metal–semiconductor plasmonic resonance coupling through surface-enhanced Raman scattering," *ACS Applied Materials & Interfaces,* vol. 15, no. 18, pp. 22730-22736, 2023.
[332] X. Wang, E. Zhang, H. Shi, Y. Tao, and X. Ren, "Semiconductor-based surface enhanced Raman scattering (SERS): from active materials to performance improvement," *Analyst,* vol. 147, no. 7, pp. 1257-1272, 2022.

[333] J. R. Lombardi and R. L. Birke, "Theory of surface-enhanced Raman scattering in semiconductors," *The Journal of Physical Chemistry C,* vol. 118, no. 20, pp. 11120-11130, 2014.
[334] X. X. Han, W. Ji, B. Zhao, and Y. Ozaki, "Semiconductor-enhanced Raman scattering: active nanomaterials and applications," *Nanoscale,* vol. 9, no. 15, pp. 4847-4861, 2017.
[335] B. P. Majee, V. Srivastava, and A. K. Mishra, "Surface-enhanced Raman scattering detection based on an interconnected network of vertically oriented semiconducting few-layer MoS2 nanosheets," *ACS Applied Nano Materials,* vol. 3, no. 5, pp. 4851-4858, 2020.
[336] J. R. Lombardi and R. L. Birke, "A unified view of surface-enhanced Raman scattering," *Accounts of chemical research,* vol. 42, no. 6, pp. 734-742, 2009.
[337] A. Singh and A. K. Mishra, "Large area CVD-grown vertically and horizontally oriented MoS 2 nanostructures as SERS biosensors for single molecule detection," *Nanoscale,* vol. 15, no. 40, pp. 16480-16492, 2023.
[338] Y. Wang, J. Liu, Y. Ozaki, Z. Xu, and B. Zhao, "Effect of TiO2 on Altering Direction of Interfacial Charge Transfer in a TiO2-Ag-MPY-FePc System by SERS," *Angewandte Chemie International Edition,* vol. 58, no. 24, pp. 8172-8176, 2019.
[339] H. Kim, D.-H. Lee, and Y.-A. Son, "Electrochemical study on rhodamine 6G-indole based dye for HOMO and LUMO energy levels," *Textile Coloration and Finishing,* vol. 25, no. 1, pp. 7-12, 2013.
[340] Y. Quan *et al.,* "Interface synthesis of MoS2@ ZnO@ Ag SERS substrate for the ultrasensitive determination of bilirubin," *Applied Surface Science,* vol. 598, p. 153750, 2022.
[341] D. Xu, L. Duan, W. Jia, G. Yang, and Y. Gu, "Fabrication of Ag@ Fe2O3 hybrid materials as ultrasensitive SERS substrates for the detection of organic dyes and bilirubin in human blood," *Microchemical Journal,* vol. 161, p. 105799, 2021.
[342] A. R. Paloly, K. Anju, and M. J. Bushiri, "High sensitive and reusable SERS substrate based on Ag/SnO2 nanocone arrayed thin film," *Plasmonics,* vol. 17, no. 5, pp. 2187-2196, 2022.
[343] U. Qamar, S. Hazra, C. Kant, U. U. Ghosh, B. N. Pal, and S. Das, "Two-dimensional silver nanonetwork on Ag4Ti5O12 film as highly efficient SERS substrate," *Microchemical Journal,* vol. 196, p. 109686, 2024.
[344] S. Mao *et al.,* "Detection of trace Rhodamine B using stable, uniformity, and reusable SERS substrate based on Ag@ SiO2-Au nanoparticles," *Colloids and Surfaces A: Physicochemical and Engineering Aspects,* vol. 657, p. 130595, 2023.

List of Publications and Patents

Publications:

1. **Hazra S,** Singh SV, Dahiya S, Aich PK, Pal BN. Solution Processed Ag-TiO_2 Nanostructure-Based Schottky Junction Thin Films for Narrowband Hot-Electron Photodetectors. **ACS Applied Nano Materials. 2023;6(16):15119-15127**

2. **Hazra S,** Dahiya S, Singh SV, Pandey U, Suman S, Swaminathan P, Pal BN. Flexible Transparent Conductors with a percolated Ag nanostructure and its Application as Efficient Self-bias Plasmonic Photodetector. **Chemical Engineering Journal. 2024; 498;155313.**

3. **Hazra S,** Dahiya S, Bijarniya JP, Pramanik S, Pal BN. Cost Efficient Ag/Ag-TiO_2 Coating Based Flexible Transparent Heat Reflector for Energy-Saving Smart Window. **ACS Applied Energy Materials. 2024;7(17);7316-7324.**

4. Qamar U#, **Hazra S#**, Kant C, Ghosh UU, Pal BN, Das S. Two-dimensional silver nanonetwork on $Ag_4Ti_5O_{12}$ film as highly efficient SERS substrate. **Microchemical Journal. 2024;196;109686 (# Equal Contribution)**

5. Pradhan L, **Hazra S#**, Manna S, Pal BN, Mukherjee S. Screening of Lithium substituted Ag-TiO_2 nanoparticles coating for antibiofilm application. **ACS applied Bio Materials. 2024. (# Equal Contribution)**

6. **Hazra S,** Dahiya S, Pramanik S, Chakraborty R, Pal BN. Visible to IR Active Highly Transparent Plasmonic Au-Ag Bimetallic Conducting Film and its Application as an efficient Plasmonic Photodetector on Plastic Substrate **(under review)**

7. **Hazra S#,** Jangra P#, Dahiya S, Mishra AK, Pal BN. Highly Sensitive Plasmonic Au-Ag Bimetallic Nano-Film as Flexible SERS Biosensors for Detection of single molecule R6G dye & multi-molecules Vitamin B_{12} **(under review)**

8. **Hazra S,** Dahiya S, Pramanik S, Chetri P, Pal BN. Improve efficiency of Plasmonic organic solar cell using Au-Ag bimetallic transparent conducting film as a Back Electrode **(under review)**

9. Singh SV**, Hazra S,** Dahiya S, Pandey U, Pal BN. Plasmonic hot-electron induced narrowband photodetector by using in-situ grown Ag/TiO_2 nano heterojunction thin films. **Optical Materials. 2024; 148:114874.**

10. Thakurta B**, Hazra S,** Samanta A, Singh AK, Nasir A, Mourya D, Mandal BC, Giri A, Pal BN, Pal M. One-Step Room Temperature Synthesis of Printable Carbon Quantum Dots Ink for Visual Encryption and High Performance Photodetector. **Advanced Optical Material. 2024; 202401886.**

11. Pradhan L**, Hazra S,** Singh SV, Bajrang, Upadhaya A, Pal BN, Mukherjee S. Surface Modification of Medical Grade Biomaterials by Using Low-Temperature Processed Dual Functional Ag-TiO_2 coating for preventing Biofilm Formation. **Journal of Material Chemistry B. 2024,12, 10093-10109.**

12. Pramanik S, Chakraborty **R, Hazra S,** Pandey U, Pal BN. Enhanced memory performance with ion exchange and reduction in Ag-doped Memristors**. Journal of Material Chemistry C. 2024,12,16145-16155.**

13. Dahiya S**, Hazra S,** Pandey U, Pramanik S, Dahiya P, Singh SV, Kumari N, Pal BN. Enhancement in photo-response of CuZnS nanocrystals-based photodetector using asymmetric work function electrode**s. Optical Materials, 2024; 157(1),116182.**

14. Dahiya S, Singh SV, Pandey U, **Hazra S,** Pal BN. Microwave-Assisted Synthesis of CuZnS Nanocrystals for Spectrally Flat Visible Light Photodetector Application Using a ZnO/CuZnS Heterojunctio**n. ACS Applied Optical Materials. 2024;2(5):776-783.**

15. Suresh S, Subramaniam MR**, Hazra S,** Pal BN, Batabyal SK. Solvent evaporation induced large-scale synthesis of Cs_4PbBr_6 and $CsPbBr_3$ microcrystals: Optical properties and backlight application for LEDs**. ACS omega. 2023;8(5):4616-4626.**

16. Dahiya S, Pandey U, **Hazra S,** Chakraborty R, Pramanik S, Maurya P.P, Pal BN. High-Performance Broadband Photodetector with Lateral Contact of n^+-Si Wafer by Two Asymmetric Work-Function Electrode**s. Advanced Materials Technologies. 2024; 2401532.**

17. Pandey U, Pal N, Dahiya S**, Hazra S,** Pal BN. Self-Biased Silicon Transistor with a Piezoelectric Gate for Efficient Mechanical Energy Harvesting Device**. Nanoscale. 2025.**

18. Gupta N, Anamika, Maurya A, **Hazra S,** Pal BN, Kuila BK. Donor acceptor hybrid between a conjugated linear polymer and conjugated polymer network: Improved charge separation and application to high-performance all polymer photodetector. **(accepted in ACS Appl. Polym. Mater. 2025)**

19. Pandey U, Dahiya S, Chakraborty R, Pramanik S, **Hazra S,** Pal BN. Piezopotential Gated Self-Biased Conducting Polymer based Printable Transistor for Efficient Mechanical Energy Harvesting Device. **ACS Appl. Mater. Interfaces. 2025.**

20. Majhi S, **Hazra S,** Pal BN, Giri D. Inverse Vulcanized Sulfur with Vinylic Monomer: A Thin Film Polymer for Photodetector Application. **(under review)**

21. Pramanik S, Chakraborty R, **Hazra S,** Pal BN. Emulating synaptic plasticity in brain-inspired optoelectronic Ag-based oxide memristor for high-accuracy neuromorphic computing **(under review)**

22. Pramanik S, Chakraborty R, **Hazra S,** Panpalia S, Pal BN. LiV_3O_8 thin film for Non-Volatile Resistive Memory Devices and Broadband Photodetectors**. (manuscript under process)**

23. Pramanik S, Chakraborty R, **Hazra S,** Dahiya S, Pal BN. Emulating High Memory Performance in Ionic and Metallic Ag-doped Oxide Memristors. **(manuscript under process)**

Patents:

1. **Hazra S,** Pal BN. "A SUPERCONDUCTIVE MESOSCOPIC FILM AND A METHOD OF FABRICATION THERE OF"; 2023/7/10; P.2780.IN; **Application No-202311046399; Grant No-558639**
2. **Hazra S,** Dahiya S, Pal BN**.** "A METHOD OF FABRICATION OF A MULTILAYERED TRANSPARENT FILM AND A PRODUCT THEREOF"; 2024/6/13; P.3042.IN**; Application No-202411045664; Grant No-569634**
3. **Hazra S,** Pradhan L, Pal BN**,** Mukherjee S**. "**AN ANTI-BACTERIAL AND ANTI-BIOFILM SURFACE COATING AND A METHOD OF FABRICATION THEREOF"; 2024/12/30; P.3254.IN; **Application No- 202411045664**